

MECHANISTIC STUDIES ON THE METHIONINE
AMINOPEPTIDASE AND PEPTIDE DEFORMYLASE
CATALYZED REACTIONS

A Dissertation
Submitted to the Graduate Faculty
of the
North Dakota State University
of Agriculture and Applied Science

By

Nitesh Vivekananda Sule

In Partial Fulfillment of the Requirements
for the Degree of
DOCTOR OF PHILOSOPHY

Major Department:
Chemistry and Biochemistry

November 2013

Fargo, North Dakota

North Dakota State University
Graduate School

Title

Mechanistic studies on the methionine aminopeptidase and peptide
deformylase catalyzed reactions

By

Nitesh Vivekananda Sule

The Supervisory Committee certifies that this *disquisition* complies with North
Dakota State University's regulations and meets the accepted standards for the
degree of

DOCTOR OF PHILOSOPHY

SUPERVISORY COMMITTEE:

D. K. Srivastava

Chair

Wenfang Sun

Guodong Liu

Birgit Pruess

Approved:

11/04/2013

Date

Gregory Cook

Department Chair

ABSTRACT

In the search for novel antibiotic and therapeutic targets, methionine aminopeptidase (MetAP) and peptide deformylase (PDF) have recently been identified as eminently compelling. These enzymes are involved in the co-translational modification of nascent polypeptides, affecting majority of the cellular proteome across all the kingdoms of living organisms. As a result, the various isoforms of MetAP and PDF have been successfully targeted by antimalarial and anti-cancer drugs. However, in spite of great interest in the bacterial forms of these enzymes as potent antibiotic targets, efforts to develop such agents have failed. This investigation is a study of the biochemical and biophysical features of the *E. coli* isoforms of MetAP and PDF in order to understand the unique characteristics of these bacterial enzymes.

The catalytic properties of these enzymes were studied using a combination of direct and coupled spectrometric assays. Potent inhibitors of MetAP were identified by screening a focused library of compounds and potential pharmacophores were determined. The inhibitor-enzyme interactions were further studied via steady-state and transient kinetic methods. While attempting to enhance the solubility of the tight-binding inhibitors using cyclodextrins, a novel substrate-driven mode of enzyme inhibition by 2-hydroxypropyl- β -cyclodextrin was discovered. The metal-ion binding properties of MetAP were studied and in this effort, the luminescence of the trivalent lanthanide ion europium was identified as a convenient signal for monitoring metal-ion binding to the enzyme. Moreover, europium was found to catalytically activate

MetAP. These properties allowed the characterization of MetAP–metal-ion binding with various metals, and this represents the most comprehensive study of the MetAP metal-ion interactions. The C-terminal domain of PDF is implicated in imparting highly unusual properties to PDF, hence the stability of PDF was characterized with respect to this domain. The truncated form of PDF lacking the C-terminal domain was found to be remarkably robust with the secondary structure as well as catalytic activity being very resistant to loss by heat. The evidence suggests additional roles for the C-terminal domain in regulating PDF. Overall, the work described here provides new understanding and avenues for enzymological pursuits of MetAP, PDF and similar valuable targets.

ACKNOWLEDGMENTS

The ideas and discussions presented in this thesis have gratefully been influenced and vetted by Dr. D.K. Srivastava and his extensive research group. In addition, I received valuable input from several faculty members at NDSU, particularly members of my committee, Dr. G. Liu, Dr. B. Pruess and Dr. W. Sun, and including (in no particular order) Dr. E. Esposito, Dr. S. Mallick, Dr. A. Ugrinov and Dr. S. Kilina. The work conducted in this research undertaking was supported by funds made available by the NIH and the Department of Chemistry and Biochemistry. However, it would have been very difficult to complete without the support as well as financial assistance provided by my close friends the Balakrishnans, the Chandwalkers and the Nagarajans, as well as my immediate and extended family, who remain unlisted only to effect brevity. The preparation of this document has been possible due to the excellent applications made available free of charge, including MiKTeX and in particular, chemscheme, ChemFig and pgfmolbio. Finally, typesetting this document would not have been accomplished without help from the community and members of various web forums, including latex-community.org, tex.stackexchange.com and tex.ac.uk.

DEDICATION

To Preeti

who accompanied me through this thrilling ride
even as she rode her own roller coaster.

CONTENTS

ABSTRACT	iii
ACKNOWLEDGMENTS	v
DEDICATION	vi
LIST OF TABLES	viii
LIST OF FIGURES	ix
LIST OF SCHEMES	xiii
1. INTRODUCTION	1
2. STATEMENT OF PROBLEM	58
3. MATERIALS	59
4. METHODS	60
5. RESULTS	81
6. DISCUSSION	199
REFERENCES	226
APPENDIX	250

LIST OF TABLES

<u>Table</u>	<u>Page</u>
1.1 Steady state kinetic parameters of selected PDF isoforms.	30
1.2 Steady state kinetic parameters of selected MetAP isoforms	46
1.3 PDF and MetAP as antibiotic targets	54
1.4 PDF and MetAP as therapeutic targets	57
5.1 Metal content of PDFs	92
5.2 Lead inhibitor compounds	110
5.3 Oxobarbiturate derivatives	113
5.4 Barbiturate based lead compounds	118
5.5 Thiobarbiturate derivatives	119
5.6 Dimethylbarbiturate derivatives	121
5.7 Inhibition constants of selected MetAP inhibitors	128
5.8 Changes in MH-5-53 spectra.	136
5.9 Model discrimination analysis	148
5.10 Interaction energies from MD simulations	155
5.11 Metallospecific inhibition of <i>EcMetAP</i> by DCPF.	158
5.12 K_d and K_a values of various metals for <i>EcMetAP</i>	186
5.13 Steady-state kinetic parameters of various metalloforms of <i>EcMetAP</i> ..	187
6.1 Comparison of the binding affinities of Mn^{2+} and Co^{2+} for <i>EcMetAP</i> determined in this study with those reported in literature.	213

LIST OF FIGURES

<u>Figure</u>	<u>Page</u>
1.1 Sequence Alignment of representative PDFs.	7
1.2 Phylogenetic tree of PDFs.	9
1.3 X-ray crystal structure of <i>Ec</i> PDF.	10
1.4 Structures of representative PDF isoforms	12
1.5 Conformations of extended C–D loop in PDF.	13
1.6 Sequence Alignment of representative MetAPs.	14
1.7 Phylogenetic tree of MetAPs	15
1.8 X-ray crystal structure of <i>Ec</i> MetAP.	18
1.9 Structures of representative MetAP isoforms	19
1.10 X-ray crystal structure of <i>E. coli</i> PDF active site pocket	22
1.11 Structure based mechanism for Fe ²⁺ -PDF.	24
1.12 Structure based mechanism for Zn ²⁺ -PDF	26
1.13 Metal dependent binding of formate in PDF.	27
1.14 X-ray crystal structure of dinuclear metal center of <i>Ec</i> MetAP	33
1.15 X-ray crystal structure of bestatin derivative bound at the di-metalated <i>Ec</i> MetAP active site.	34
1.16 Structure based mechanism for di-metalated MetAP.	35
1.17 Transition analogue based mechanism for di-metalated MetAP.	37
1.18 Mechanism for di-metalated MetAP based on H178A mutation	39
1.19 X-ray crystal structure of mono-nuclear metal center of <i>Ec</i> MetAP.	40
1.20 Structure based mechanism for mono-metalated <i>Ec</i> MetAP	42
1.21 Mechanism for di-metalated MetAP based on H79A mutation	43

5.1	SDS-PAGE analysis of purified MetAPs	82
5.2	BSA standard plot for the Bradford assay	83
5.3	SDS-PAGE analysis of purified EcPDF-C Δ 21	86
5.4	DNA sequence of the MBP-TEV-EcPDF-C Δ 21 construct	87
5.5	EcPDF absorbance spectrum	93
5.6	Spectral features of Met-AMC and AMC	95
5.7	Fluorescence parameters for the direct MetAP assay	96
5.8	Fluorescence spectra of DCPF	98
5.9	CD spectra of native and truncated PDFs	99
5.10	Steady state parameters of ProAP	101
5.11	MetAP steady-state parameters with substrate Met-Pro-pNA	102
5.12	MetAP activity measured by the coupled assay	103
5.13	ProAP inhibition by Met-Pro-pNA	104
5.14	AMC standard plot	105
5.15	Catalytic features of MetAP with fluorogenic substrate MetAMC	106
5.16	Comparison of catalytic features of native and truncated PDFs	107
5.17	Catalytic features of the Zn ²⁺ forms of native and truncated PDFs	109
5.18	Determination of K_i for MetAP inhibitors	127
5.19	MH-5-74 inhibition constants for EcMetAP and hmap	130
5.20	Spectral changes in MH-5-53 upon binding to EcMetAP and HsMetAP	132
5.21	Effect of solvent and pH on MH-5-53 spectra	133
5.22	pH dependent reversibility of MH-5-53 spectra	134
5.23	Change in MH-5-53 spectra over time	135
5.24	Absorbance spectra of free and encapsulated MH-5-75	137

5.25	Inhibition of <i>EcMetAP</i> by free and encapsulated MH-5-75	138
5.26	Effect of cyclodextrin on <i>MetAP</i> activity	140
5.27	Effect of CD on <i>MetAMC</i> fluorescence spectra	141
5.28	Binding affinity of the <i>Met-AMC</i> - CD complex	142
5.29	<i>MetAMC</i> standard plot	143
5.30	Catalytic features of <i>EcMetAP</i> with fluorogenic substrate <i>Met-AMC</i> ..	144
5.31	Experimental vs. simulated data for the inhibition of <i>EcMetAP</i> by HP- β -CD	146
5.32	CD dependent inhibition profile of <i>EcMetAP</i>	149
5.33	Molecular docking of HP- β -CD and <i>Met-AMC</i>	151
5.34	X-ray crystal structure of the <i>Met-AMC</i> - β -CD	152
5.35	<i>Met-AMC</i> RMSD over the course of MD trajectories	154
5.36	MD simulation of the <i>EcMetAP</i> - <i>Met-AMC</i> -HP- β -CD complex	156
5.37	Inhibition of Mn^{2+} - <i>EcMetAP</i> by DCPF	158
5.38	Inhibition of different metalloforms of <i>EcMetAP</i> by DCPF	159
5.39	Effect of <i>EcMetAP</i> on DCPF fluorescence	160
5.40	<i>EcMetAP</i> metalloform dependent spectra of DCPF	161
5.41	Reversibility of DCPF metallo-specific spectral properties	162
5.42	Effect of solvent polarity on the fluorescence spectra of DCPF	163
5.43	DCPF- Mn^{2+} - <i>EcMetAP</i> association kinetics	165
5.44	Concentration dependence of DCPF- Mn^{2+} - <i>EcMetAP</i> binding phases ..	166
5.45	DCPF association kinetics with Co^{2+} & Ca^{2+} <i>EcMetAP</i>	167
5.46	DCPF-apo- <i>EcMetAP</i> association kinetics	168
5.47	Extended DCPF-apo- <i>EcMetAP</i> association kinetics	169
5.48	Change in Eu^{3+} luminescence spectra on binding to <i>EcMetAP</i>	171

5.49	Binding affinity of the Eu^{3+} -MetAP complex	173
5.50	Determination of metal binding affinity by Eu^{3+} displacement	174
5.51	Absorption spectra of FeCl_3 species in solution	178
5.52	Spectrophotometric determination of FeCl_3 concentration in solution ..	179
5.53	Determination of FeCl_3 hydrolysis in aqueous solution	180
5.54	Activation of <i>EcMetAP</i> by different metal ions	182
5.55	Determination of the activation constant of Eu^{3+} for <i>EcMetAP</i>	183
5.56	Determination of <i>EcMetAP</i> activation constants for various metal ions.	185
5.57	Determination of steady-state kinetic parameters of various <i>EcMetAP</i> metalloforms	188
5.58	Interaction of <i>EcPDF</i> with <i>EcMetAP</i>	190
5.59	Temperature dependent unfolding of native <i>EcPDF</i>	192
5.60	Temperature dependent unfolding of <i>EcPDF-CΔ21</i>	193
5.61	Unfolding kinetics of native <i>EcPDF</i>	194
5.62	Unfolding kinetics of <i>EcPDF-CΔ21</i>	195
5.63	Temperature dependent inactivation of native <i>EcPDF</i>	196
5.64	Temperature dependent inactivation of <i>EcPDF-CΔ21</i>	197
5.65	Steady-state parameters of heat stable <i>EcPDF-CΔ21</i>	198
6.1	MH-5-74 docked within the <i>EcMetAP</i> active site.....	200
6.2	Selected examples of compounds showing the effect of various molecular properties on their inhibitory potency against <i>EcMetAP</i>	202
6.3	Protonation states of MH-5-53	205
6.4	Relationship between ionic size and K_d of metal ions	216
6.5	Effect of substrate concentration on Cd inhibited <i>EcMetAP</i> activity ...	220
6.6	Comparison of full length and truncated PDF structures.....	225

LIST OF SCHEMES

<u>Scheme</u>	<u>Page</u>
1.1 Reaction catalyzed by PDF	20
1.2 Reaction catalyzed by MetAP	29
1.3 MetAP assay using tetrapeptide substrate	44
4.1 Coupled spectrophotometric assay for MetAP.	69
4.2 Direct fluorometric assay for MetAP.	71
4.3 Coupled spectrophotometric assay for PDF.	72
5.1 Mechanism of inhibition by cyclodextrin	145
5.2 Caption for scheme	147

1. INTRODUCTION

The evolution of life on earth has given rise to a vast assortment of organisms more diverse than ever imaginable. Arising from the common building blocks of nucleic acids, proteins, lipids and carbohydrates, these organisms have adapted themselves for survival and propagation via a widely varied plethora of molecular mechanisms. Yet in spite of the contrasting means employed by living systems for their goals, some mechanisms have remained seemingly immutable across the millennia. One such enduring system is the use of formylmethionine (fmet) and methionine (met), by prokaryotes and eukaryotes respectively, to initiate protein synthesis. All known proteins are generated with either of these amino acids at N-terminal end. However in a large number of cases, these amino acids are soon removed from the nascent polypeptide chain. This removal of the N-terminal met/fmet is an essential step in the maturation of functional proteins and is specifically and sequentially catalyzed by the enzymes peptide deformylase (PDF) and Methionine aminopeptidase (MetAP). As these processes occur during the translation of the nascent polypeptide chain, they are termed co-translational modification, and are in fact the very first modifications taking place, often to be followed by numerous other co-translational as well as post-translational modifications. The following sections present a review of the literature concerning these two enzymes involved in the first co-translational modification step of proteins: PDF and MetAP.

1.1. Discovery of PDF and MetAP

The field of molecular biology took roots in the late 19th century as Albrecht Kossel determined the composition of nucleic acids and paved the way to understanding the chemical nature of proteins. In the mid-20th century, RNAs and ribosomes were

identified as the machinery responsible for the formation of peptide bonds. Following this revelation, extensive research was conducted to study the process of protein biosynthesis. The subsequent use of cell-free systems to study this process greatly accelerated the advance of further research.

The path to the discovery of the co-translational N-terminal processing enzymes essentially began in the early 1960s with the groundbreaking observations that (a) proteins were synthesized in a sequential chain starting at the NH₂-terminal end [1, 2] and (b) the distribution of the N-termini of proteins was not random, but predominantly populated by methionine and alanine [3, 4]. These were shown to be true in both prokaryotic and eukaryotic systems. The use of radioisotope-labeled amino acids in cell free systems, which lead to the initial observation, was also instrumental in the next milestone which followed soon after in 1964 with the discovery of formylmethionyl-tRNA by Marcker and Sanger [5]. While studying the formation of methionyl-tRNA in cell free *E. coli* extracts using [³⁵S]methionine, they observed a second species of labeled aminoacyl-tRNA being produced. The authors were not only able to identify the species as formylmethionyl-tRNA, but also found that (a) the formylation occurs after the formation of Met-tRNA, (b) no other aminoacyl-tRNAs are formylated, and (c) fMet-tRNA is incorporated into proteins during protein biosynthesis.

Following these results, through studies involving *in vitro* phage protein synthesis (and *E. coli* extracts later), Adams and Capecchi [6], Capecchi [7] showed that fMet-tRNA was incorporated at the N-termini of polypeptides, often followed by alanine. From their observations they were able to arrive at the profound conclusion that (a) there exists an initiation signal for protein synthesis, AUG, encoding methionine, and (b) there exists an enzyme that cleaves the N-formyl or N-fMet group from nascent

proteins, resulting in the occurrence of methionine and alanine as the most common N-terminal amino acids respectively. This initiated the search for the enzymes that catalyzed the removal of N-terminal residues from growing polypeptide chains.

The existence of such a specific catalytic activity was first shown towards the removal of the N-terminal formyl group in *E. coli* by Fry and Lamborg [8] in 1967, through the use of synthetic peptide substrates. Adams [9] later confirmed the presence of the peptide deformylase enzyme. The author noted particular difficulty in isolating the enzyme (presumably due to acute instability), and was unable to observe any catalytic activity specific for the removal of N-terminal methionine. In 1970, Yoshida et al. [10] showed that while nascent hemoglobin polypeptides up to 16 amino acids in length retained an N-terminal methionine, the residue invariably was lost by the time the chain grew longer than 30 amino acids. Further results from hemoglobin synthesis in cell free extracts conducted by Housman et al. [11] indicated that the initiating residue in eukaryotic systems was met and not fmet. The existence of specific methionine aminopeptidase activity was eventually shown in 1972 by Yoshida and Lin [12].

The methionine aminopeptidase (MetAP) enzyme was not isolated until much later, in the late 1980s by Ben-Bassat et al. [13] who also identified the *map* gene encoding the enzyme in *E. coli*. However similar success with peptide deformylase took even longer as the enzyme was isolated and the *def* gene encoding it was identified in the mid 1990s [14, 15].

1.2. Physiological Roles of PDF and MetAP

The universal assignment of fmet or met as the initiating N-terminal amino acid translates into the ubiquitous requirement of PDF and MetAP for N-terminal processing of proteins. Commonly called the N-terminal Methionine Excision (NME) pathway, it involves either one or two steps: (a) the cleavage of the formyl group, in prokaryotes and the eukaryotic organelles mitochondria and plastids, and (b) the cleavage of the methionine group, the only step in case of eukaryotic cytoplasm. The removal of the N-terminal formyl residue occurs in almost 100 % of the proteins [16, 17]. This systematic processing of the nascent polypeptide chain suggests a close association of the PDF enzyme with ribosomes. Co-purification of the enzyme had been observed in early studies and definitive proof of this association was reported recently [18]. MetAP catalyzed removal of the N-terminal methionine occurs in at least 60 % to as high as 80 % of all proteins [19] and studies suggest that this enzyme may also be associated with the ribosome [20, 21].

The modification of proteins is an integral operation needed for their proper function, localization and regulation. Indeed the different types of modifications are the biggest source of cellular complexity and are too numerous to list here. The co-translational excision of N-terminal formyl and methionine residues is of particular significance to all known organisms. Perhaps the most obvious is that these modifications are the most widespread in the proteome as indicated above. Another indication of their importance arises from the fact that these modifications are the very first to occur on a protein being newly synthesized. As a consequence, they affect all subsequent N-terminal processing of the protein. In fact, when the nascent polypeptide is about 40 to 70 amino acids long, the N-terminus undergoes acetylation in majority of the proteins in eukaryotes [19, 22]. N-terminal myristoylation is another

process suspected to occur later during the translation process. The activities of N^α-acetyltransferase A and N-myristoyltransferase are dependent on the removal of N-terminal methionine.

The selective removal of N-terminal methionine also appears to play a major albeit indirect role in the stability of the protein by affecting its half-life. It has been noted that MetAP only removes the N-terminal methionine when the penultimate residue is not destabilizing to the protein. This observation stems from the fact that the specificity of protein degradation as given by the N-end rule coincides with that of MetAP [23]. The removal of methionine has also been implicated in recycling the residue considering that methionine is the most energetically expensive amino acid to synthesize. Further support for this theory comes from the observation that certain archaea substitute internal methionine residues in proteins under conditions of sulfur limitation, but continue to use methionine at the N-terminal position.

Eukaryotic MetAPs have been found to play additional roles in the process of protein synthesis and maturation. MetAP2 has been implicated in protecting the initiation factor eIF-2 α from inactivation, thus promoting protein synthesis via an additional mechanism [24]. The enzyme has also been suggested to act as a molecular chaperone for sarcoplasmic reticulum Ca²⁺-ATPase [25]. However further studies corroborating these observations are currently lacking. MetAP2 has been identified as a target for the S100A4 protein which is known to regulate various cellular processes as well as tumor metastasis [26]. Activity of the isoform has been shown to be important for the Wnt planar cell polarity signaling pathway which is required for normal function of endothelial cells [27]. An unidentified MetAP isoform from Barley (*H. vulgare*) has been found to play a role in freezing tolerance [28].

The removal of N-terminal methionine has been shown to be necessary for proper protein function and subcellular localization [29–31]. Given their widespread function affecting nearly all cellular activity, it is not surprising that both PDF and MetAP have been found to be essential to the survival of all organisms [32–35].

1.3. Classification and Structure

1.3.1. Classification of PDFs

The various known isoforms of peptide deformylase have been found to have very low sequence similarity as seen from a sequence alignment of representative PDF isoforms (Figure 1.1). They do however retain the conserved motifs (indicated in violet): (a) G Φ G Φ AAXQ (b) L Φ NP ξ I/L (c) EGCLS Φ (d) VXR and (e) QHE Φ DHL ξ G where Φ , ξ and X are hydrophobic, hydrophilic and any amino acids respectively [36]. Contained within the last motif is the equivalent of the Zn²⁺ binding HEXXH domain. Sequences indicated in green represent the signal peptides of the PDFs found in eukaryotic organelles.

Despite the low sequence similarity, a comparison of the sequences as well as three dimensional structures indicate a close relationship between the PDF isoforms as seen from the phylogenic tree (Figure 1.2). The isoform classes delineated by the branches are identified as types I, II and III. The most common type I PDFs are found in both prokaryotes and eukaryotes and further classified into subtypes A–D. Type IA are found in mitochondria (representatives Human and *Drosophila*), with the equivalent plastids containing type IB (representatives *Arabidopsis* and *Plasmodium*). The latter subtype is also found in bacteria. While gram-negative bacterial PDFs are

```

A._thaliens_(1A)  MG LHRDEA TAME TIFRVS LR LIPVSAAV -----TCRS IRFFVSRP -----GSSHLNRRKLYN LP TSSS --SLSTKAGM L ---LGLG -----EKRRKVD LPE IVASGDEV LHEKARVDFGE I----- 103
H._sepiens_(1A)  ---MARLWG -ALS LMP LMAAVPWWGGAAGVYRACSS TAAPDQVE -----G-----PA LRRSYWR -H LRR IV -----LGPPEPESHVCOVGGDEV LRGVAAEVEAQA L----- 87
A._thaliens_(1B)  ---MAYCNCF LQAPPE LSR ILPVLRRATILSAGYGLKSLVIFCSIVNRT -SP -LITSSVRA -EVKRSRDKKVASA TDVQFETE LK IVEYVDF IIRAKNR ID IFDE ----- 103
B._ceruus_(1)    -----MAY LE I KHHPNEV LETFCERV INFDK -----MSV LQV LH IPDER LRKVKAKPVEEVNA ----- 26
E._coli         -----MSV LQV LH IPDER LRKVKAKPVEEVNA -----MAY LE I KHHPNEV LETFCERV INFDK ----- 26
H._sapien_(1D)  -----MAY LE I KHHPNEV LETFCERV INFDK -----MSV LQV LH IPDER LRKVKAKPVEEVNA ----- 85
B._ceruus_(2)   -----MAY LE I KHHPNEV LETFCERV INFDK -----MSV LQV LH IPDER LRKVKAKPVEEVNA ----- 85
M._thermoautotrophii  -----MLTKMDV IRESGDP ILRNVAEVS LPASEDIT I 33 -----HDDAD 5
A._thaliens_(1A)  ---GSEER IQK IIDD M IKVNR LAL EVGLA ---APQ IGV -----PLR IIVLED TKEY ISYAPKEE ILAQERRHFD LMVWVDFV LK RSN ---KK -ALFF P GGLSVQD G----- 193
H._sepiens_(1A)  ---GGPE LQR LQRLQV QMRRRRCVGLS ---APQ IGV -----FRQV LIA LELPEA ICRECFPRQA LRQMEFFP URVEVAFS URV LDS ---R L -VTFP P GGE SWAG----- 177
A._thaliens_(1B)  ---N LKN LVDMDFVMYK TQ IGLS ---APQVGL -----NQV LIA LELPEA ICRECFPRQA LRQMEFFP URVEVAFS URV LDS ---R L -VTFP P GGE SWAG----- 176
B._ceruus_(1)    ---KLVK LKDMHE TML IADGVGLA ---APQVGV -----SLQVAVVDVDDD -----GEGKE IVLVNPK KK YSD ---K L -VFFD P GCLSPFG----- 176
E._coli         ---E IQR IVDDMFE TMAAES IGLA ---ATVD I -----HQR IIV IDVSEN R -----TGR IEL I NPS ILEKRG -E --QVGP E GCLSPFG----- 95
H._sapien_(1D)  ---EVKNEQD IQ GLHACQ LARH V LLL -A-----GKS LKVD M TIEE -----DER LV I IPELE LKSG -E --TG IE E GCLS IPE----- 96
B._ceruus_(2)   LKEM IEPV INSODPEMAEKYS LRPE IGLA ---APQ IGV -----GKS LKVD M TIEE -----DA L V HRE I ISHNAY SP LGYGGFP KSV I SNVNLCHG IPDSRP LQDGD I IN IDV TVYNYGHGDISETF 194
M._thermoautotrophii  LKEM IEPV INSODPEMAEKYS LRPE IGLA ---APQ IGV -----GKS LKVD M TIEE -----DA L V HRE I ISHNAY SP LGYGGFP KSV I SNVNLCHG IPDSRP LQDGD I IN IDV TVYNYGHGDISETF 115
A._thaliens_(1A)  ---FRALG EYIEVVVTGYDQGKR IEVNASGWAAR I-----L DHEGCHL I GNLVYDKAVPR TFR TVDN LD L P LA -----EGCFK LGPQ----- 269
H._sepiens_(1A)  ---F LACVE FQAVQ ISGLDFNGEQVWQASGWAAR I-----L DHEGCHL I GNLVYDKAVPR TFR TVDN LD L P LA -----EGCFK LGPQ----- 243
A._thaliens_(1B)  ---IYAEVYFQSVK IDARD ITGERES ISLRKLPAR I-----F DHEYDHLGQV LFDKMDR IFR INVMKRVND -----YEERTGLFSPER ---VEARQRRKAGVGFGRK----- 273
B._ceruus_(1)    ---LYGEVEADY IKVRAQNRKQVF LLEAEGL LARA -----DHE IDR IHGV LFTSKV TRYYENE LE -----KARA----- 156
E._coli         ---QRALVERAEKVK IRA LORDDKPEE LEADGLLA IC -----DHEMDR LYGK LFM DY LSP LKQR IRQKVEK LDR L----- 169
H._sapien_(1D)  LVGNVDECKRLVEA RCRDEA IAA CRAGAPESV IGMT ISH ITH QNGFQVCPHEVHG -IGSYFHGH --PE IMHARDSD LPEMEGMAF I HEP IITEGSPFEKV LE DAW TVVS LD NQSAQFEH TVL ITRGAQ ILTKLPHEA 335
B._ceruus_(2)   ---EVP GYVESYR ITVKA TS INGEVVK LRKGLPFA IV -----F DHE IDR IHGV LFTSKV TRYYENE LE -----KARA----- 184
M._thermoautotrophii  ---LRAV LDP LD -LK IR LKRLKPK LRF TGSG-----AYGVAHEMERLEGESEGT-----PFWSEFEVE IEE----- 175

```

Figure 1.1. Sequence Alignment of representative PDFs. The protein sequences of representative isoforms were obtained from UniProt [37], aligned using Clustal Omega [38] and annotated using Jalview [39]. Conserved motifs are shown in violet and N-terminal targeting sequences are shown in green.

typically of the IB subtype (representatives *E. coli* and *Bacillus*), type 2 have also been observed in gram-positive bacteria (representatives *Bacillus* and *Enterococcus*). Type III have been identified in *Trypanosomas* and archaea.

1.3.2. Structure of PDFs

The *E. coli* type IB PDF is structurally the simplest and hence qualifies as the typical representative of the different isoforms of PDFs. The full length crystal structure of *Ec*PDF is shown in Figure 1.3. The enzyme contains three major helices (α A, α I and α J), a short 3_{10} -helix and seven β -strands (β B– β H arranged into three antiparallel β -sheets). These altogether form a hand-like fold with α A, β B and β C forming the fingers, the β D, β G and β H sheet forming the palm and β E, β F and α J forming the thumb. The hand is wrapped around the highly conserved central helix, α I, which contains the QHE Φ DHL ξ G motif.

Site-directed mutagenesis of the Zn^{2+} form of PDF indicated that His132, His136 and Cys90 are involved in coordinating with the metal ion. As a consequence of its structure and metal ligands, PDF is classified as member of a new subfamily of the clan MA and MB metalloprotease superfamily, along with the similar S-ribosylhomocysteinase LuxS. No significant differences have been observed between the structures of Zn^{2+} , Fe^{2+} , Ni^{2+} or Co^{2+} forms of PDF.

Most PDFs (type IB and type II) have been found to be monomeric, however type IA PDFs (as well as type IB PDFs from *L. interrogans* and *M. tuberculosis*) have been suggested to function as dimers. The dimerization has been attributed to hydrophobic interactions as well as a network of hydrogen bonds and salt bridges. In addition, type IA PDFs differ from the type IB and type II PDFs in the following features: (a) the C–D loop (b) the C-terminal domain and (c) the S1' and S3' subsites. The C–D loop, which connects the β strands C and D, is located near the entrance

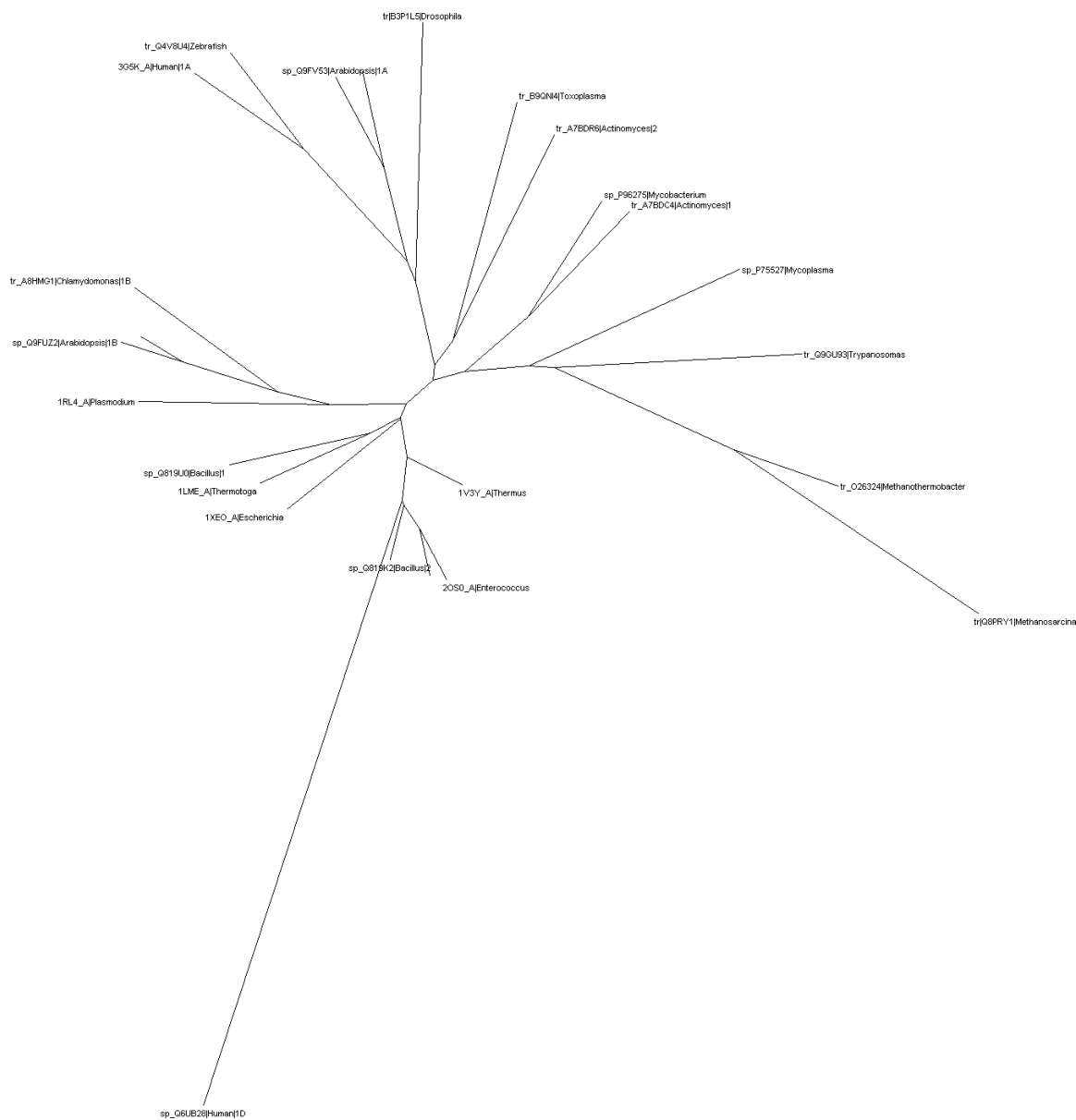


Figure 1.2. Phylogenetic tree of PDFs. Amino acid sequences of selected representative PDFs were obtained from the UniProt database [37] and aligned using Clustal Omega [38]. Phylogenetic representation was prepared in Dendroscope [40].

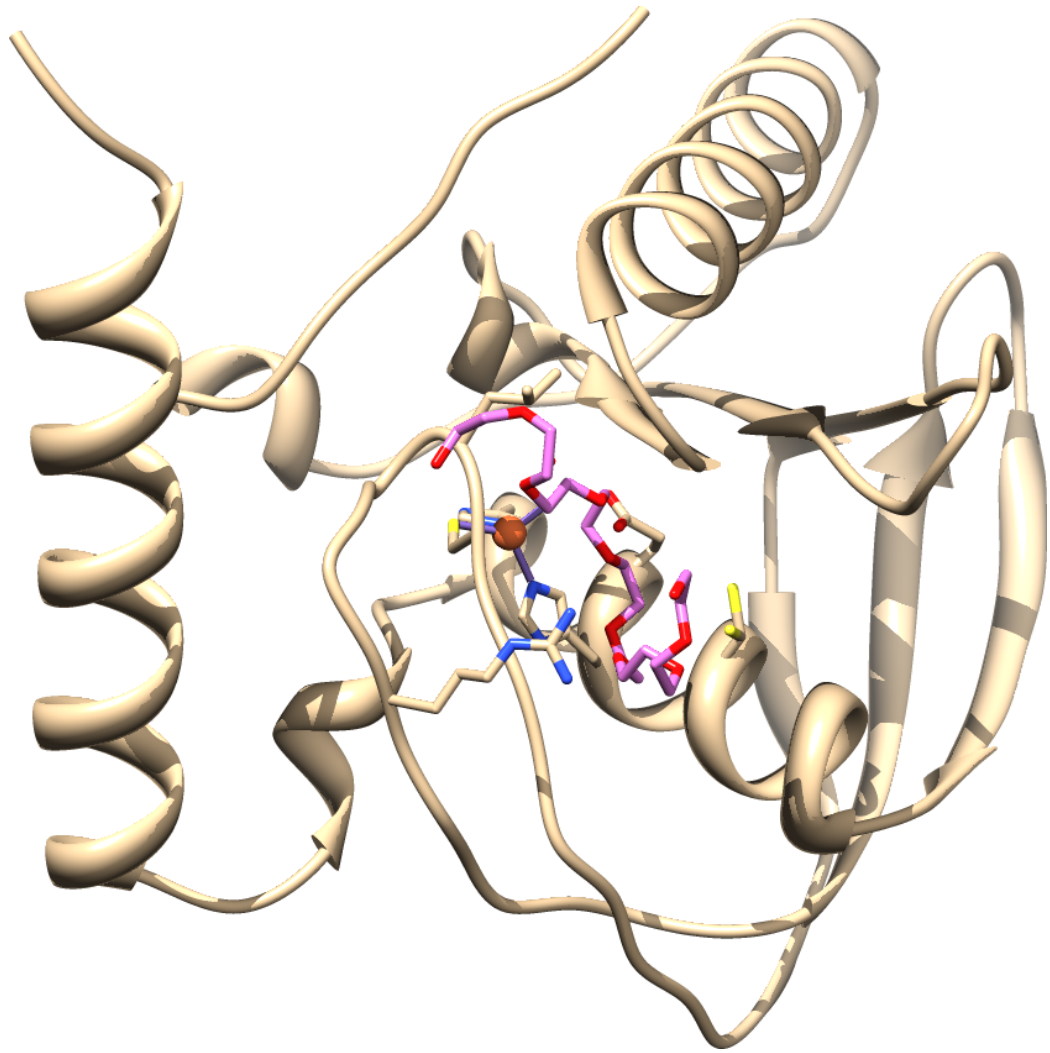


Figure 1.3. X-ray crystal structure of *EcPDF*.

to the active site and is 10 amino acids in length in the type IB PDFs. In type IA PDFs however, an insertion in this region leads to a C–D loop of 15 to 20 amino acids in length, containing two small α -helices (see Figure 1.4). This extended structure partially covers the active site entrance and is involved in forming a S3' subsite that is absent in the type IB PDFs. As an exception, the type IB PDF from *L. interrogans* also contains an extended C–D loop, but without the small α -helices. With the resulting conformational flexibility, this extended loop is seen to adopt “closed” and “open” conformations, named depending on its position relative to (and its effect upon) the active site entrance (see Figure 1.5).

The C-terminal domain typically consists of a disordered loop, with an α -helix in type IB PDFs. Whereas the C-terminus in type IB PDFs is positioned towards the N-terminus, in type IA PDFs it is positioned adjacent to the β E strand. In contrast, the C-terminus in type II PDFs ends in a conserved β -strand (β J) which forms a mixed parallel-antiparallel β -sheet with β E. Additionally, the type II PDFs contain three insertions near the N-terminus, forming a small α -helix ($\alpha A'$) between αA and αB .

1.3.3. Classification of MetAPs

Unlike PDFs, the MetAP sequences appear to be significantly conserved across the various organisms suggesting common ancestors to the current isoforms. This is clearly seen in a sequence alignment of MetAPs from representative sources (Figure 1.6) where the conserved regions are indicated in violet. In fact a phylogenic representation shows that the distance between the nodes of all the different branches is very small (Figure 1.7).

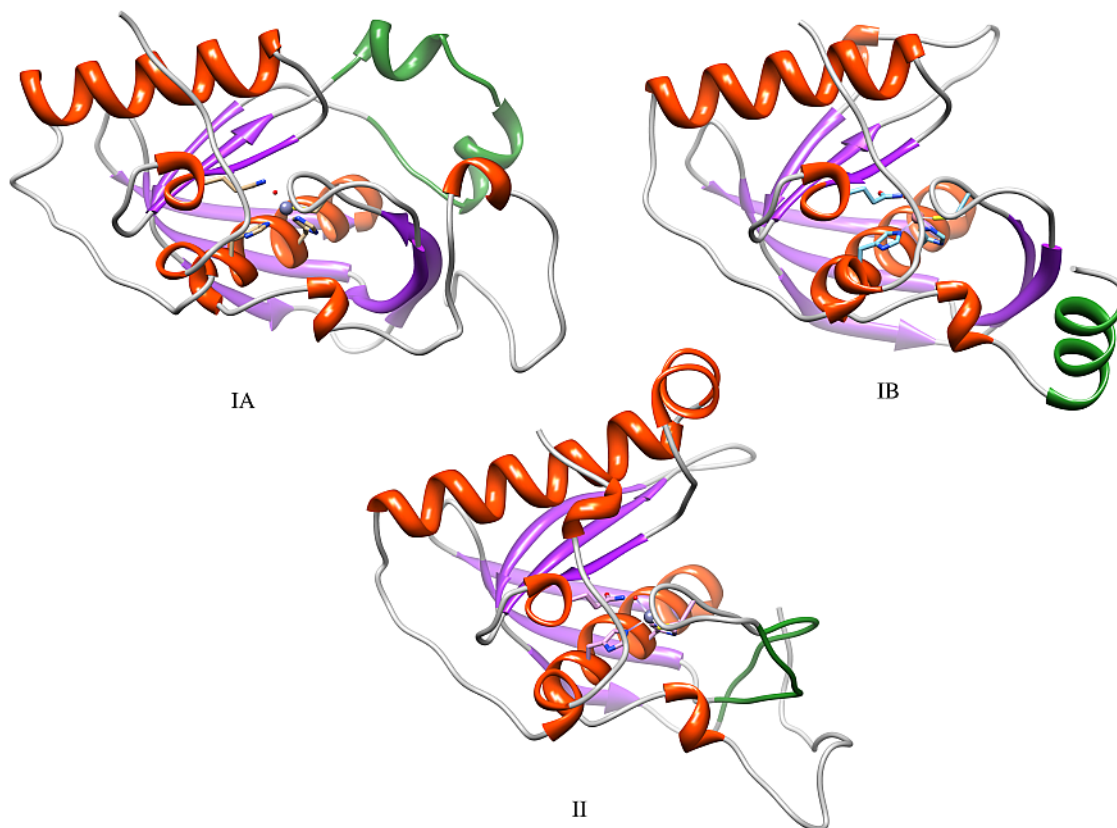


Figure 1.4. Structures of representative PDF isoforms. Type IA from *A. thaliana* (1ZXZ), type IB from *H. pylori* (2EW7) and type II from *S. aureus* (1LQW). Distinctive features of each type are indicated in green.

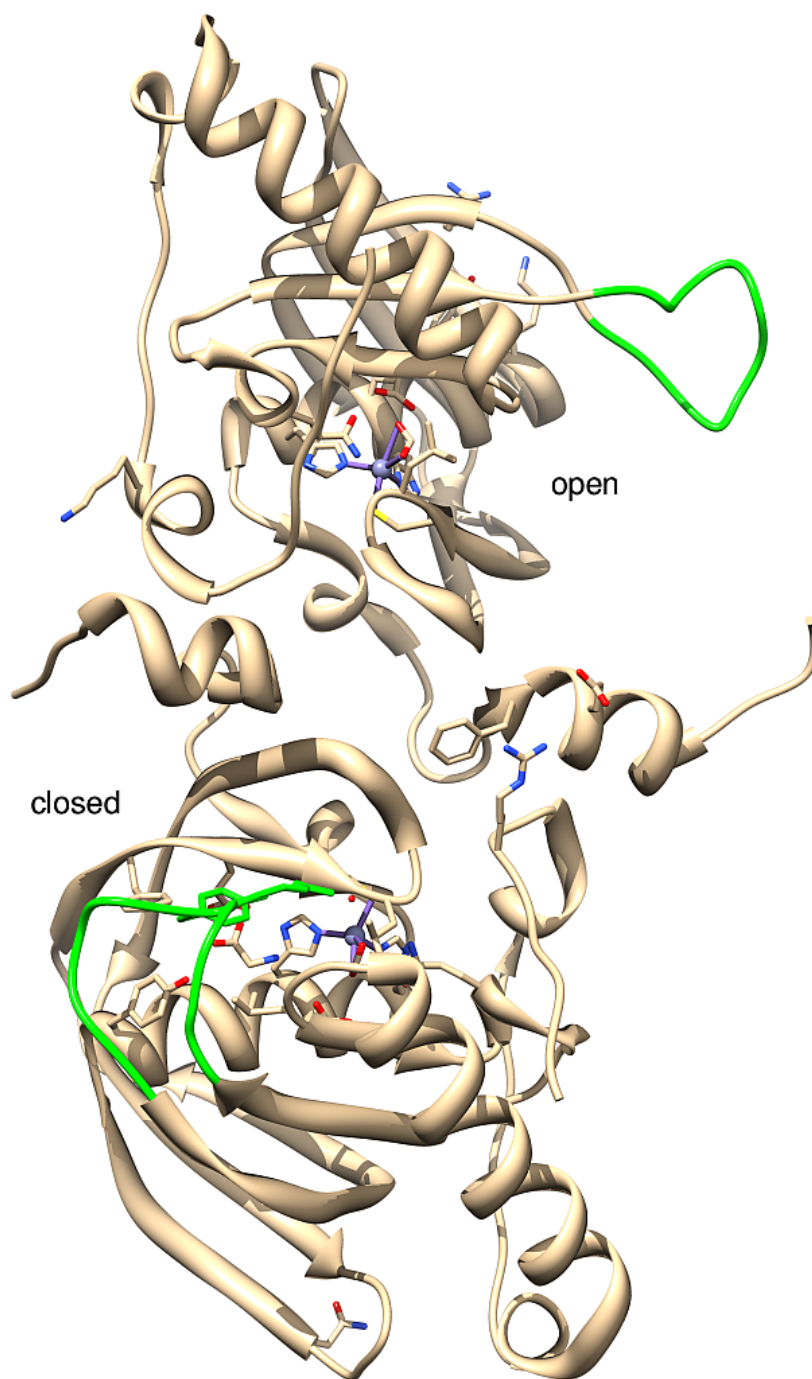


Figure 1.5. Conformations of extended C–D loop in PDF. The C–D loop in *L. interrogans* PDF dimer (1Y6H) is formed by amino acids 66 to 76. The monomer unit on top shows the open conformation with the active site exposed, whereas the monomer unit at the bottom shows the closed conformation with no access to the active site.

Additionally it can be seen from the sequence alignment that all eukaryotic MetAPs have large N-terminal extensions, and some eukaryotic MetAPs also have C-terminal inserts. Based on these amino acid sequence features and their sequence homology, MetAPs are classified into two main types. Type I and II MetAPs are differentiated by the presence of a C-terminal insert in the latter. The two types occupy two halves of the phylogenetic tree in Figure 1.7 with type I on the top and type II at the bottom.

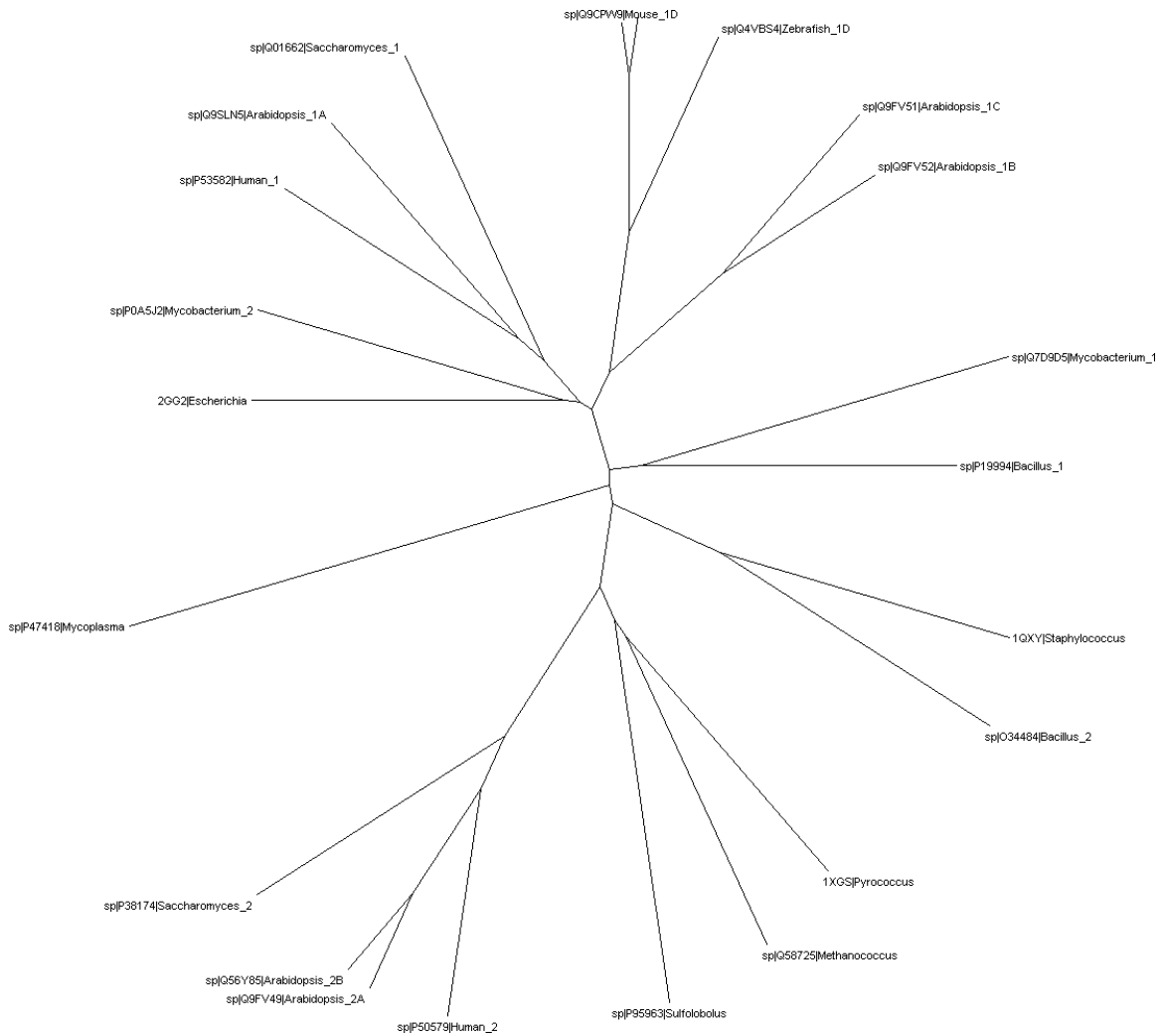


Figure 1.7. Phylogenetic tree of MetAPs. Amino acid sequences of selected representative MetAPs were obtained from the UniProt database [37] and aligned using Clustal Omega [38]. Phylogenetic representation was prepared in Dendroscope [40].

Each MetAP type is further classified into subtypes a and b depending on the absence or presence of an N-terminal extension. While prokaryotes typically contain only type Ia and archaea contain only type IIa MetAPs, eukaryotes are found to contain both type Ib and IIb MetAPs. It is interesting to note that eukaryotic type Ib and IIb MetAPs are closely related to the prokaryotic type Ia and archaeal type IIa MetAPs respectively. This observation has led to the suggestion that prokaryotic and archaeal MetAPs are the ancestors of eukaryotic MetAPs [41]. Thus the presence of N-terminal extensions in eukaryotic MetAPs may be evolved for cellular functions that do not exist in their ancestral counterparts.

In addition to the above major isoforms of MetAPs, two subtypes c and d have also been identified more recently. Subtype c is distinguished by the presence of a very short N-terminal extension 40 amino acids in length (as opposed to 100 amino acids in the case of subtype b). Type Ic has been found in plants and actinomyces [21] and type IIc has been identified in Microsporidia [42]. MetAPs of subtype 1d have been identified as dedicated enzymes of mitochondria and plastids [43, 44]. More recently, a novel MetAP was identified in *H. vulgare* that contained a nuclear localization signal in the C-terminal region [28]. While this isoform remains to be classified, it bears 90 % sequence identity with several other as yet unidentified proteins in plants, suggesting a new subtype of MetAPs.

1.3.4. Structure of MetAPs

As in the case of PDFs, the MetAP from *E. coli* (type Ia) is the simplest of the various MetAPs and ideally suited as the structural representative of the enzyme isoforms. A representation of the crystal structure of *EcMetAP* is shown in Figure 1.8. The structure of MetAP is described as a “pita-bread” fold also seen in creatinase and aminopeptidase P [45]. It consists of pseudo two-fold-related N and C-terminal

domains, each with two α -helices and two antiparallel β -strands. Together, they form a cylindrical structure with a curved antiparallel β -sheet in the center with four α -helices on one face, and connecting loops on the other.

The active site is asymmetrically formed primarily by the N-terminal domain with two metal ions coordinated by monodentate His171 and Glu204, and bidentate Asp97, Asp108 and Glu235. Although majority of MetAP structures have been reported with a dinuclear metal center, several studies have indicated that the enzyme may be monometalated *in vivo*. The mononuclear active site is shown in Figure 1.19. A comparison of the structures of various MetAP isoforms is shown in Figure 1.9. The C-terminal insert differentiating type 1 and 2 MetAPs forms two α -helices (indicated in green), whereas the N-terminal extension differentiating subtypes a and b is indicated in yellow. The N-terminal extension consists of two zinc-finger motifs in the type Ib MetAP replaced by stretches of polybasic and acidic amino acids in the type IIb MetAPs connected to the catalytic domain by a linker. Note that the large N-terminal extension is not obvious from the representation of the human type IIb MetAP in Figure 1.9 as the structure only contains the residues 110–468, with residues 139–152 also missing, attributed to a disordered structure [46]. In the type IIc MetAP from *M. tuberculosis* the N-terminal extension appears to be a mostly disordered loop but in fact contains a polyproline II helix that may be involved in interaction with the SH3 binding domains on the ribosome [21]. Although the above features strongly support the evolutionary relationship of type 1a and 2a with 1b and 2b respectively, it is interesting to note that MetAPs of type 1a share a structural feature with those of type 2b that is absent in the other types of MetAPs. The loop between α -helix 4 and β -strand 4, consisting of residues 160–199 in MetAP type 1a, contains two β -strands which form a part of the central curved β -sheet and include the conserved metal coordinating residue His171. While this loop forms a random coil in the other types,

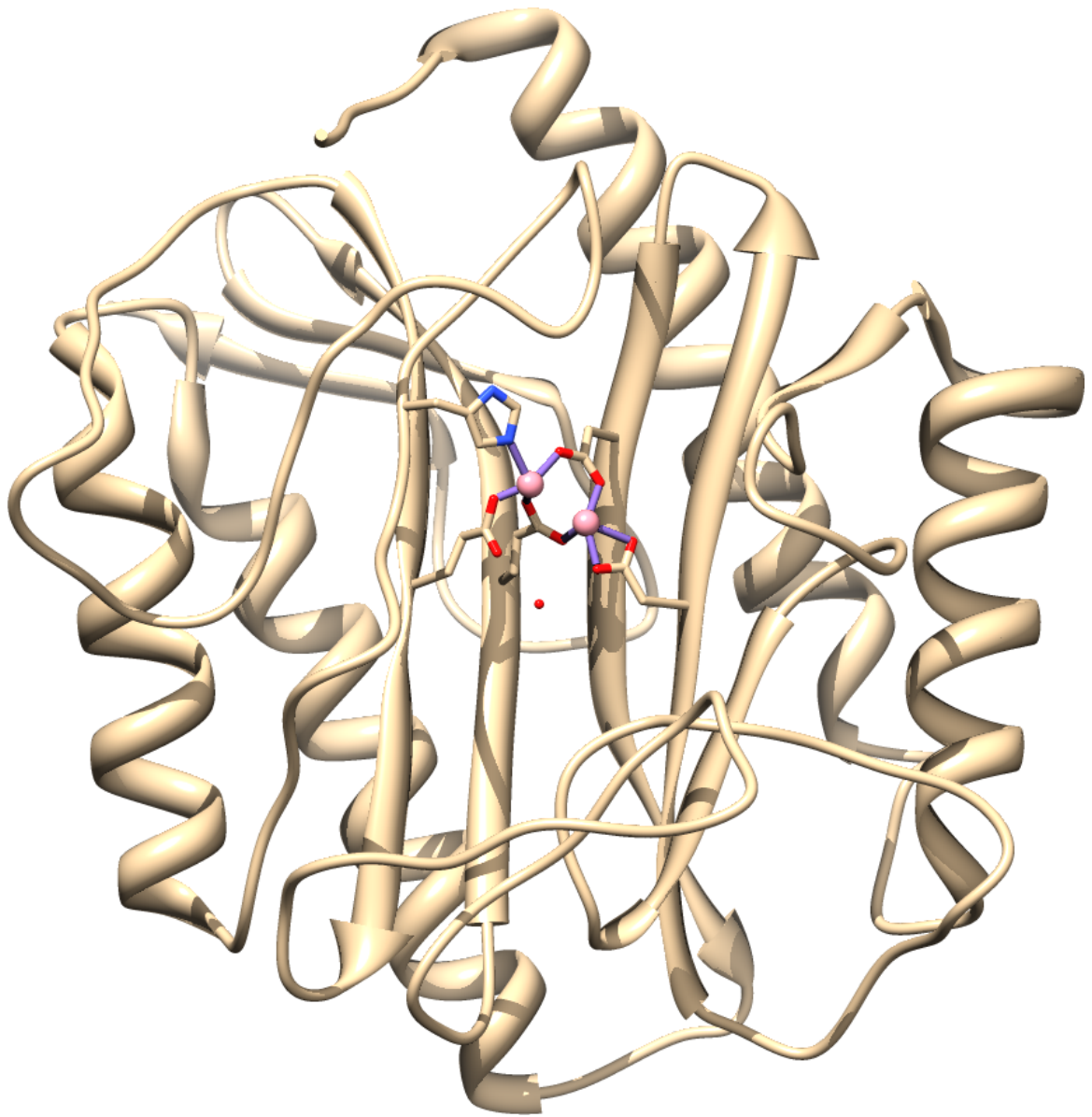


Figure 1.8. X-ray crystal structure of *EcMetAP*

type 2b contains a similar β -sheet with an additional insert (residues 312–321) that also forms a pair of β -strands. The significance of this structure has not yet been realized, but the similarity points towards additional complexity in the evolutionary path of the type 2b MetAPs.

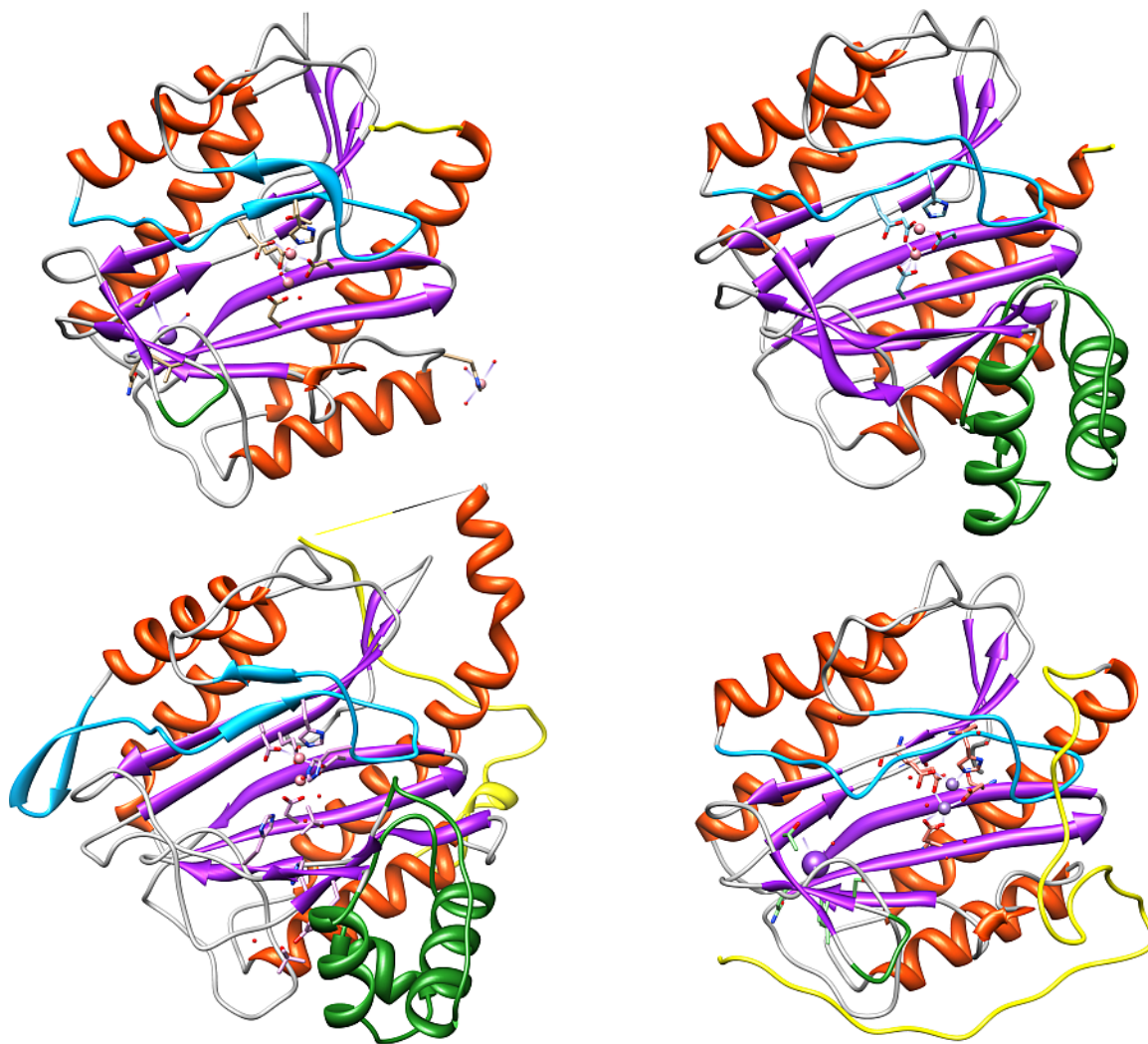
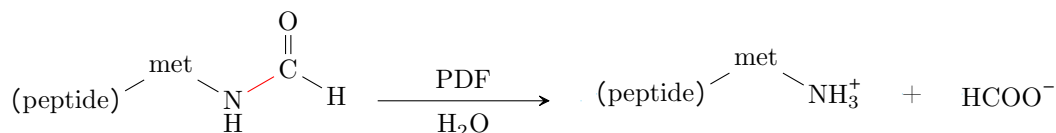


Figure 1.9. Structures of representative MetAP isoforms. Type 1a from *E. coli* (2MAT) [47], type 2a from *P. furiosus* (1XGS) [48], type 2b from Human (1BN5) [21] and type 1c from *M. tuberculosis* (3PKA) [49]. Common α -helices and β -sheets are shown in orange and magenta respectively, while distinctive internal features are shown in cyan and green, and the N-terminal domain is indicated in yellow.

1.4. Biochemical and Biophysical Properties

1.4.1. The reaction catalyzed by PDF

Peptide deformylase catalyzes the irreversible hydrolytic removal of the formyl group from the N-terminal methionine of nascent polypeptides (see Scheme 1.1). It is thus classified as formyl-L-methionyl peptide amidohydrolase (EC 3.5.1.88).



Scheme 1.1. Reaction catalyzed by peptide deformylase.

In addition it has been shown to exhibit some esterase activity and extremely poor deacetylase activity, although these activities probably have no physiological relevance since the enzyme would never encounter such substrates at its position on the ribosome.

1.4.1.1. Substrate specificity of PDF

While PDF acts on a broad range of fmet-peptides, it shows drastically varied rates for different substrates. It was predicted early on that PDF would ideally act on short peptides, as the length of the natural substrate of the enzyme, the nascent polypeptides exiting the ribosome tunnel, would be less than 10 amino acids. Using *E. coli* extract and N-formyl peptides up to 3 amino acids long (fmet-ala-ser), Adams [9] found that the rate of release of the formyl group increased with the length of the peptide substrate, with very poor activity against fmet. Rajagopalan et al. [17] noted that the enzyme pocket interacted with up to 4 amino acids when they observed that the increase in reaction rate as a function of peptide length plateaued at tetrapeptides.

The authors also found that while PDF was highly specific towards f-L-methionine at the N-terminus, also acting on the stereoisomer f-L-norleucine, it could tolerate D amino acids at the penultimate position. Hu et al. [50] employed a combinatorial library of tetrapeptides to reveal the optimal consensus sequence for PDF substrates as fMX(F/Y/K/R)Y where X is not Asp or Glu. Interestingly, the authors found that the enzyme also efficiently catalyzed the deformylation of fFY(F/Y)X peptides. The overall bias towards these substrates is explained by the predominantly hydrophobic active site of PDF (see Figure 1.10). The flexibility of amino acids at the P1' position is presumed to be due the fact the this amino acid interacts with the hydrophobic Leu91 on one side but is completely solvent exposed on the other. The specificity towards the formyl group as compared to the acetyl moiety is explained by the dual factors of lower electrophilicity and steric hindrance in the case of the latter. Fluoro substituted acetyl-peptides increased the catalytic rate indicating the role of electrophilicity, where as increasing the substitution to three fluorines decreased the rate indicating greater steric hindrance.

1.4.1.2. Mechanism of PDF catalyzed reaction

As a metalloprotease, PDF catalyzes the cleavage of an amide bond by the nucleophilic action of a water molecule bound to the active site metal ion. The enzyme has been suggested to employ two different catalytic mechanisms depending on the identity of the bound metal ion [51–53]. Based on structural data and its similarity to thermolysin, the general features of the catalytic mechanism are proposed as follows: (a) the metal ion functions as a Lewis acid to reduce the pK_a of the bound water molecule, thus facilitating its activation as a nucleophile (b) Glu133 forms a hydrogen bond with the metal-bound water molecule and acts as a general base to activate it as a nucleophile (c) the metal-bound water molecule makes a nucleophilic attack on

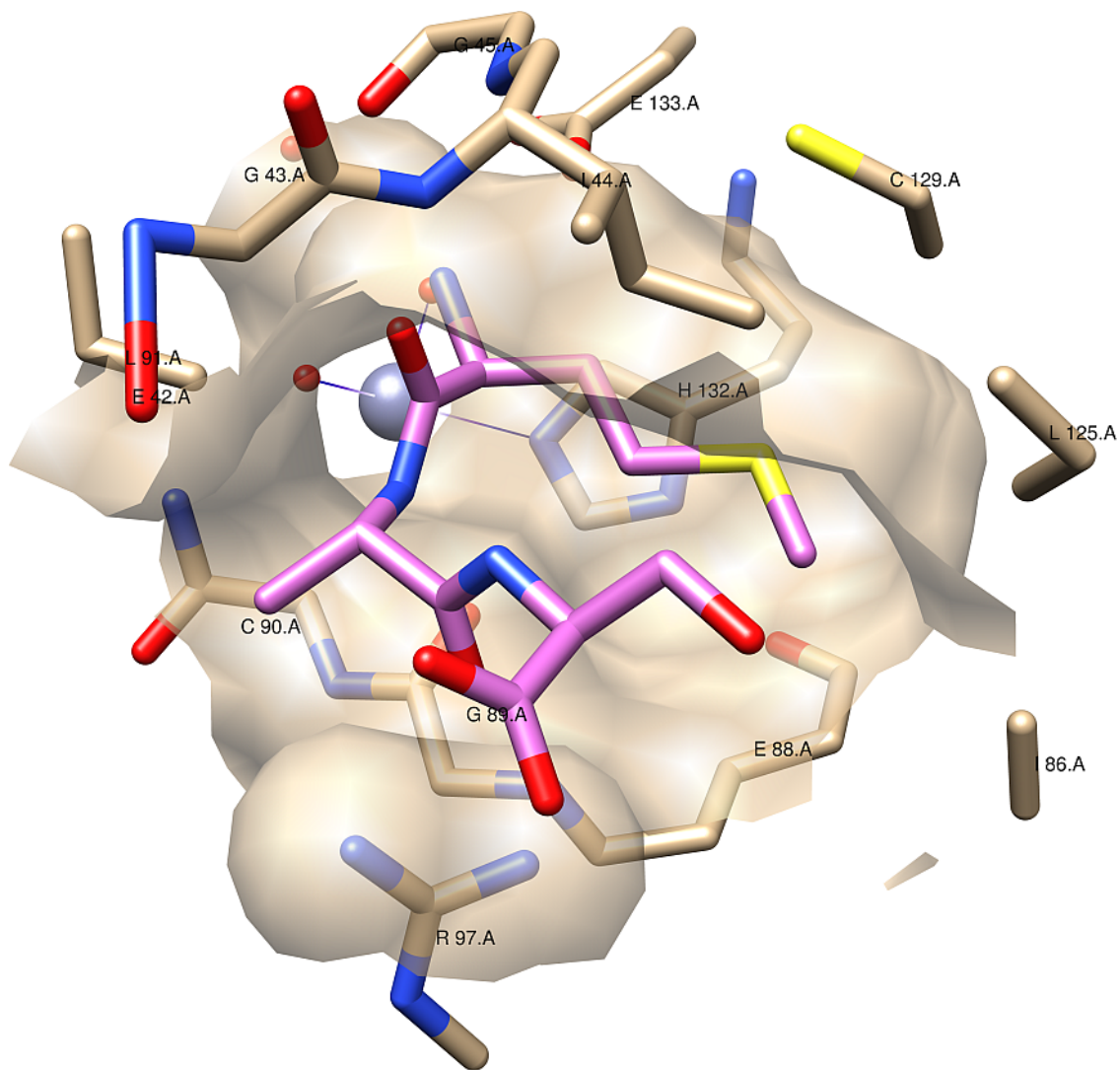


Figure 1.10. X-ray crystal structure of *E. coli* PDF active site pocket. The peptide substrate met-ala-ser, indicated in stick, is bound at the active site.

the carbonyl carbon of the formyl group to form the tetrahedral intermediate which is stabilized through hydrogen bonding by Gly45, Gln50 and Leu91 (d) a proton is shuttled via Glu133 (acting as a general acid) to the P1' amine facilitating the collapse of the tetrahedral intermediate [54, 55].

The proposed catalytic mechanism of the Fe^{2+} and Co^{2+} forms of PDF is shown in Figure 1.11. Besides the above features, the carbonyl oxygen O_C of the formyl group is proposed to coordinate with the metal ion increasing the tetrahedral coordination to pentacoordinate. The metal ion functions as a Lewis acid to activate both, the bound formyl group (increasing the electrophilicity of the carbonyl carbon) and the bound water molecule (making it more nucleophilic). The subsequent nucleophilic attack results in formation of the tetrahedral intermediate INT_1 via the transition state $\text{TS}_{\text{O-C}}$ which is the rate limiting step. The metal bound alcohol, Glu133 and the peptide amine share a proton which requires the formation of the intermediate INT_2 . This step occurs via the transition state $\text{TS}_{\text{H-N}}$ in which the hydrogen bond between the proton and the alcohol is broken and a hydrogen bond between Glu133 and the alcohol hydrogen is formed. As a proton is transferred from Glu133 to the amine group, the second intermediate collapses to form EP in which the cleaved formate is bound to the metal ion in a bidentate fashion (Figure 1.13, Top) while the deacylated peptide dissociates. The formate is finally displaced by a water molecule to regenerate the enzyme active site.

Alternatively, the catalytic mechanism of the Zn^{2+} form of PDF is shown in Figure 1.12. In contrast to the previous mechanism, the O_C does not interact directly with the metal ion, but forms hydrogen bonds with Gln50 and Leu91. As a result the carbonyl carbon is placed in close proximity (2.9 Å) to the metal bound water molecule [56, 57]. A nucleophilic attack by the water molecule on the carbonyl carbon results in the formation of the tetrahedral intermediate INT_1 similar to the previous

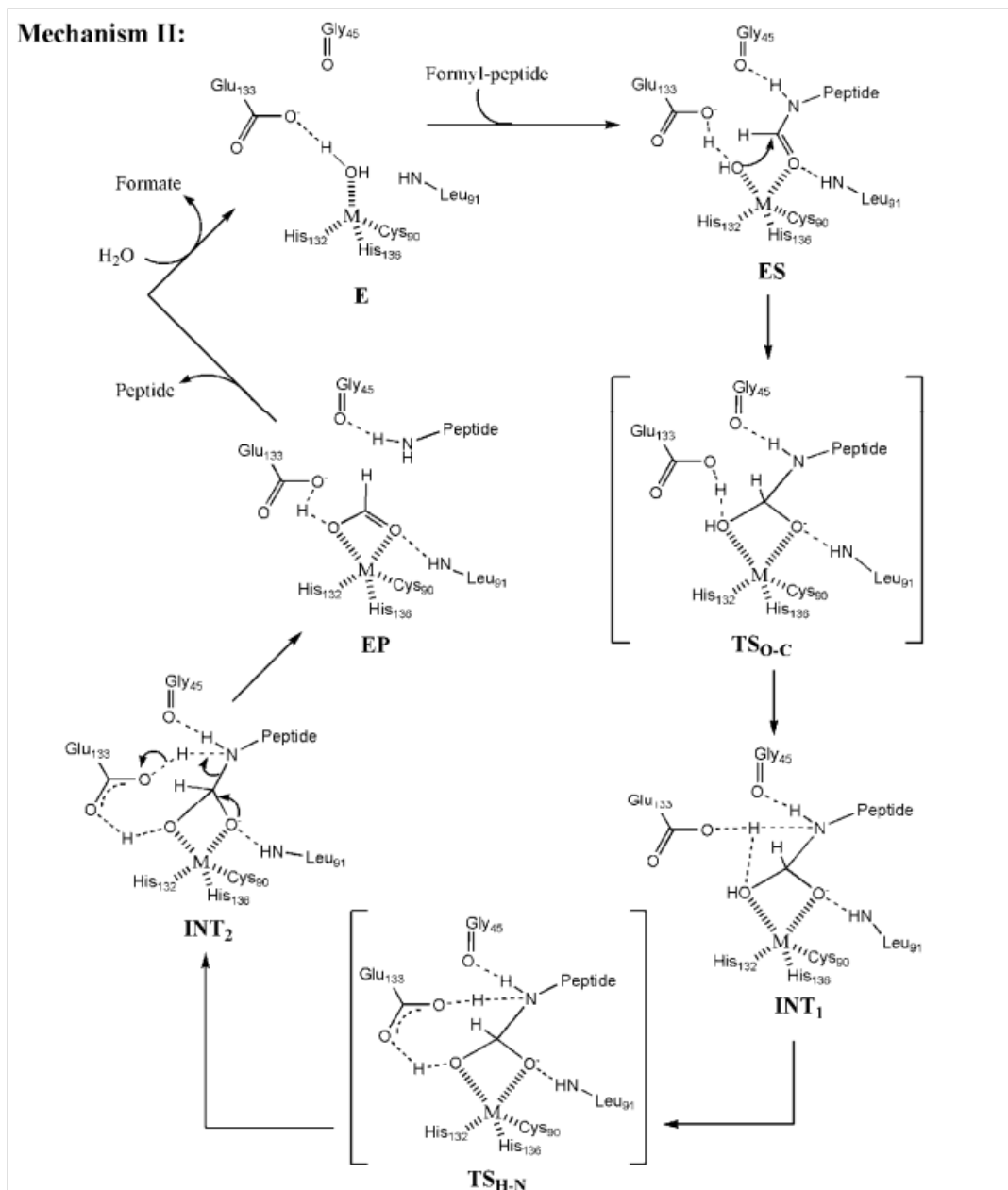


Figure 1.11. Structure based mechanism for Fe^{2+} -PDF.

mechanism. However unlike the previous mechanism, the proton is not shared but transferred completely from the water molecule to Glu133. The resulting proximity of the proton to the P1' amine allows the latter to be protonated and act as a leaving group to collapse the intermediate, thus bypassing the need for the formation of the second intermediate described in the previous mechanism. The cleaved formate is now bound to the metal ion in a monodentate fashion (Figure 1.13, Bottom), and the subsequent regeneration of the enzyme active site proceeds as described earlier. The transition state energy of $\text{TS}_{\text{O-C}}$ in this mechanism is suggested to be about 7kcal mol^{-1} higher than that of the equivalent state in the previous mechanism as a result of an increase in the coordination of metal ion (Zn^{2+}) from tetrahedral to pentacoordinate during the substrate binding step. This difference may explain the poor catalytic efficiency of the Zn^{2+} form of PDF as compared to the Fe^{2+} and Co^{2+} forms.

1.4.1.3. Steady-state characterization of PDF

Much of the understanding of the catalytic mechanisms described above was gained through quantitative measurement of the reaction catalyzed by the enzyme. Indeed the use of synthetic substrates (fmet and fmet-ala) to assay enzyme activity was instrumental in obtaining the evidence for the existence of PDF [8]. As with any enzyme assay, the activity of PDF is measured by quantitating the product(s) formed by a known concentration of the enzyme, as a function of time. In the case of the PDF catalyzed reaction, the end products are formate and peptide (with N-terminal methionine) as described in Scheme 1.1. Early measurements of the PDF catalyzed reaction were conducted with discontinuous (*aka* end-point) assays, where the reaction is stopped at a fixed time and the product is then quantified. Typical discontinuous assays involved the quantification of the product formed upon cleavage of the substrate

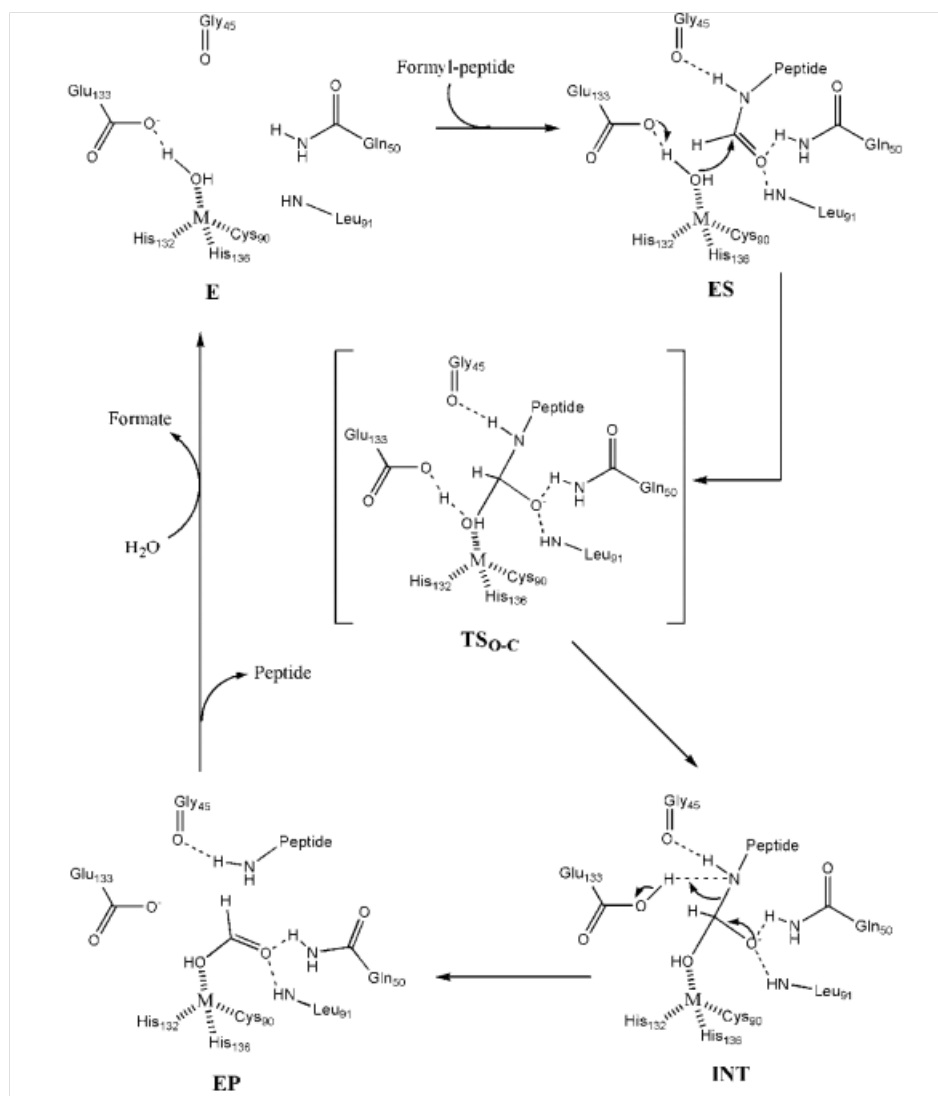


Figure 1.12. Structure based mechanism for Zn²⁺-PDF.

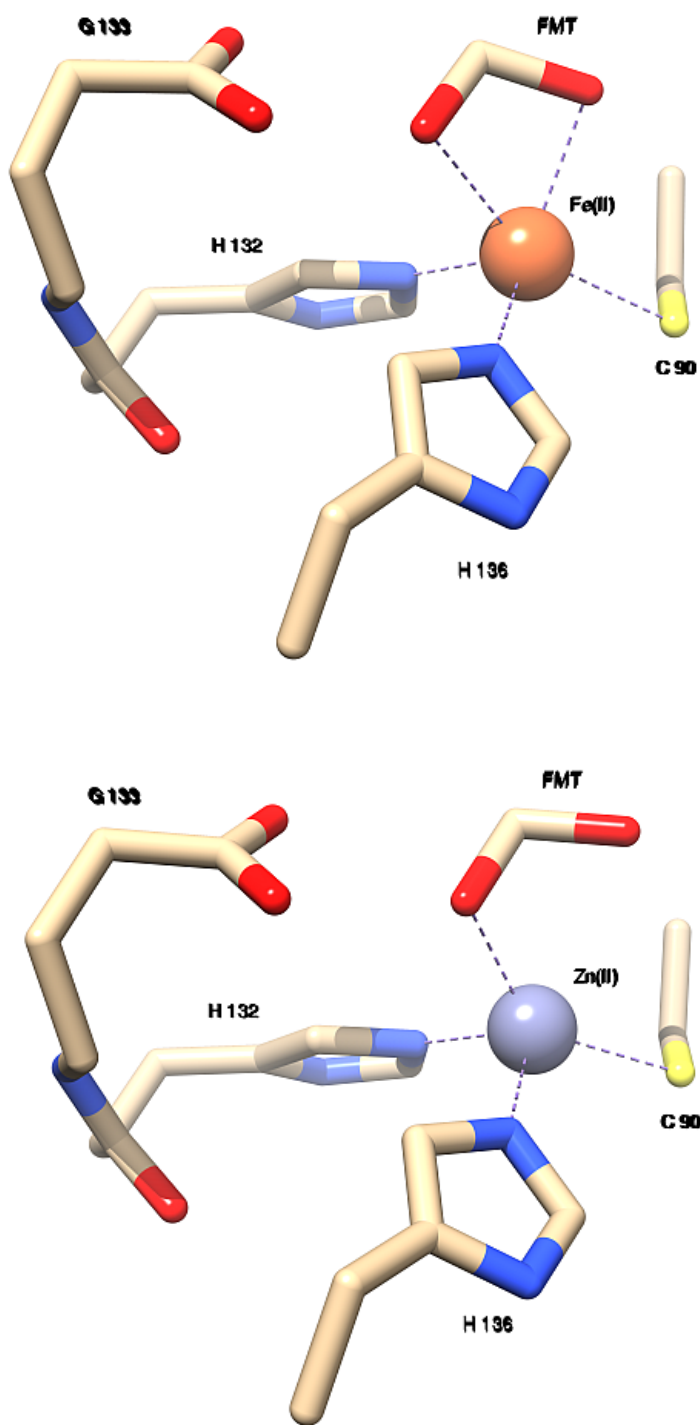


Figure 1.13. Metal dependent binding of formate in PDF. The cleaved formate binds in a bidentate fashion in Fe^{2+} form of PDF (1XEN, Top) and in a monodentate fashion in Zn^{2+} form of PDF (1XEM, Bottom).

fmet-ala-ser using either (a) amine-reactive chromogenic probes that react with the newly exposed N-terminal group of the peptide product or (b) chromogenic reactions involving the formate product. The reactions were stopped after an incubation period ranging from 30 s to 30 min at room temperature (RT) and the product concentration determined by adding the specific reagent. The different assay systems included amine-reacting probes such as fluorescamine [58] or trinitrobenzene sulfonic acid [59] (measured at the absorbance maxima of 380 and 335 nm respectively). Alternatively formate was quantified by initiating a dehydrogenase reaction by adding formate dehydrogenase and NAD^+ , the resulting change in absorbance being monitored at 340 nm [17].

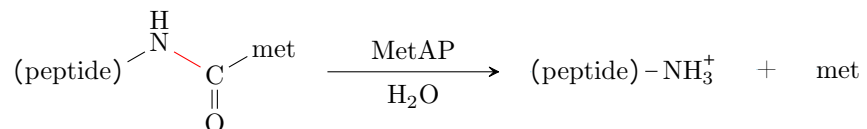
However, a much more convenient and revealing method is the use of continuous assays and these have been more commonly used in later studies. The end-point assay involving the quantification of the formate product was in fact the first continuous assay developed for monitoring PDF reactions in real time, where formate dehydrogenase (with NAD^+) and PDF were added simultaneously to the reaction mixture [60]. The rate of conversion of NAD^+ to NADH in the secondary (coupled) reaction is directly proportional to the amount of formate produced by the first reaction catalyzed by PDF, thus the rate of NADH formation (as determined by change in absorbance at 340 nm) is a measure of the PDF reaction rate. Other continuous assays use similar coupled systems to quantify the production of deformylated peptide instead. These include the use of chromogenic or fluorogenic substrates such as fmet-leu-pNA [61] or fmet-lys-AMC [62], with the deformylated product being coupled to a peptidase reaction using *Aeromonas* aminopeptidase (AAP) or dipeptidyl peptidase I (DPPI) respectively. The pNA or AMC residues are produced in the coupled reaction in two steps as each amino acid is hydrolyzed, and the release is monitored by the absorbance change at 405 nm or fluorescence change at 460 nm ($\lambda_{\text{ex}} = 360 \text{ nm}$) respectively. In a

separate continuous assay, the need for a coupling enzyme is obviated by the use of thiol releasing substrates (N-formyl-(β -thiophenylalanyl)-peptides) [63]. Deformylation results in release of thiophenol from the destabilized product which is quantified by Ellman's reagent (DTNB), producing an absorbance change monitored at 412 nm. While the complications of using a coupling enzyme (such as sensitivity to pH, metal chelators, PDF inhibitors) are avoided by this assay, it suffers from the fact that substrate is tedious to synthesize, commercially unavailable and only moderately stable in solution [62].

More recently a direct continuous assay has been reported that circumvents the coupled system altogether by using the chromogenic substrate formyl-*p*NA, where deformylation by PDF releases the chromophore *p*nitroaniline [64]. While the substrate was found to be very poor as compared to other commonly used substrates, it has facilitated the characterization of PDF inhibition by metal chelating agents. The kinetic parameters of selected PDF isoforms for some of the above substrates are listed in Table 1.1

1.4.2. The reaction catalyzed by MetAP

Methionine aminopeptidase (EC 3.4.11.18) catalyzes the irreversible hydrolytic cleavage of the N-terminal methionine from nascent polypeptides (see scheme 1.2).



Scheme 1.2. Reaction catalyzed by methionine aminopeptidase.

Table 1.1. Steady state kinetic parameters of selected PDF isoforms.

Substrate	Enzyme	Metal	k_{cat} (s^{-1})	K_{m} (μM)	Ref	
fMet-Ala-Aer	<i>E. coli</i>	Ni^{2+}	210	3.9	[65]	
		Zn^{2+}	6	70		
	<i>A. thaliana</i> 1A	Zn^{2+}	22	0.25	[66]	
		1B	Ni^{2+}	75	5.6	
	<i>L. pneumophila</i>	A	Ni^{2+}	151	21	[67]
		C		34	2.4	
		B	Zn^{2+}	0.6	0.34	
	<i>H. sapiens</i> N Δ 62	Ni^{2+}	0.26	3.6	[43]	
	<i>B. burgdorferi</i>	Zn^{2+}	20	0.51	[68]	
	fMet-Leu-pNA	<i>E. coli</i>	Fe^{2+}	70	0.02	[54]
Co^{2+}			19	0.02		
G133A			4	0.03		
<i>H. sapiens</i> N Δ 58		Co^{2+}	0.17	0.03	[69]	
<i>B. burgdorferi</i>		Zn^{2+}	5	0.003	[68]	
formyl-pNA	<i>E. coli</i>	Ni^{2+}	0.03	29.4	[64]	

1.4.2.1. Substrate specificity of MetAP

From the observation that a fraction of the proteome retains an N-terminal methionine, it would be expected that MetAP is more selective towards the peptide sequence of substrates as compared to PDF. The removal of N-terminal methionine by MetAP is in fact strongly dependent on the penultimate residue. The enzyme catalyzes this reaction only if the side chain of the P1' amino acid is neutral and has a radius of gyration of 1.29 Å or less (Gly, Ala, Ser, Cys, Thr, Pro and Val) [70], alternatively described as side chains with length less than 3.68 Å [71]. This model of specificity has been observed with MetAP from bacterial as well as eukaryotic sources [13, 72]. The type II enzyme however has a very high preference for Val and Thr at the P1' position, with the activity being two orders of magnitude higher than type I for Met-Val peptides. Studies with mutant MetAP type I have shown that Met329 and Gln356 of the S1' subsite are responsible for the selectivity and changing them

to Ala resulted in catalytic activity against substrates with large amino acids such as Met, Leu and Phe, as well as charged ones such as His, Asn and Gln [73]. It is interesting to note that in spite of the mutations, no activity was observed with acidic residues. In fact acidic residues are disfavored up to the P5' position of the substrate [74]. Surprisingly, although MetAP is able to cleave the imide bond with proline at the P1' position, it is unable to do so when Pro is present at the P2' position [71, 72]. However most other residues are accepted at this position. Although no other obvious selectivity is observed for positions P2' to P5', the overall efficiency of methionine cleavage is significantly affected by the identity of residues up to the P5' position. For example, while acidic residues are poor candidates at most positions, the activity towards substrates with Asp or Glu at the P2' position is enhanced by the presence of Ser or Thr at the P1' position [74]. In the human type I MetAP the N-terminal extension, while dispensable for catalysis, has been shown to affect substrate specificity at the P1 position against substrates smaller than tripeptides [75]. No explanation has been forwarded as yet for these observed complexities of substrate selectivity in MetAPs.

1.4.2.2. Mechanism of MetAP catalyzed reaction

The catalytic mechanism of MetAP has been studied with considerable interest, using a combination of structural and kinetic data from native and site specific mutants of the *E. coli* enzyme. It is interesting to note the progressive development of the proposed model in response to new experimental data. Having been identified as an enzyme with a di-cobalt active site, the mechanism first proposed was based on this model. The di-nuclear metal system with a bridging water observed through x-ray crystallographic structure determination was thought to be consistent with other aminopeptidases such as LeuAP and ProAP.

The use of bestatin based substrate analogue provided the first structure based insight into the catalytic mechanism of MetAP [47]. According to this structure, one of the metal ions, Co1, is penta coordinated (Asp108, His171, Glu204, Glu235 and a bridging solvent) in a distorted trigonal bipyramidal geometry, whereas the other metal ion, Co2, is hexa coordinated (bidentate Asp97, Asp108, Glu235, the bridging solvent and a second solvent molecule) in a distorted octahedral geometry (see Figure 1.14).

The structure of the substrate analog (*3R*)-amino-(*2S*)-hydroxyheptanoyl-L-Ala-L-Leu (AHHpA-Ala-Leu) bound at the *Ec*MetAP active site is shown in Figure 1.15. His79, Cys59, Cys70, Tyr62, Tyr65, Phe177 and Trp221 form the conical hydrophobic S1 subsite which is complementary to the methionine side chain. The S1' subsite, formed by Glu204, Gln233, Met206 and Tyr168 is shallow, corresponding to the requirement of small side chains at the P1' position of substrate.

It is proposed that the amino terminal of the substrate displaces the second water molecule from Co2 and the carbonyl oxygen (O_C) of the scissile peptide bond interacts with Glu204. In addition, the bridging solvent (μ OH) is assumed to be the nucleophile (O_N) leading to the formation of non-covalent tetrahedral gem-diolate intermediate. Based on the probable transition states two variant reaction mechanisms were proposed analogous to the mechanism of other aminopeptidases (Figure 1.16). In mechanism I, solvent amine ligand exchange facilitates proton transfer from the μ OH to the O_C , resulting in a hydrogen bonding interaction with Glu204. The O_N attacks the scissile bond carbonyl carbon leading to the formation of a tetrahedral intermediate with His79 orienting the substrate in the correct manner. Collapse of the intermediate is then mediated by His178 acting as a proton donor to the nitrogen of the leaving amino group.

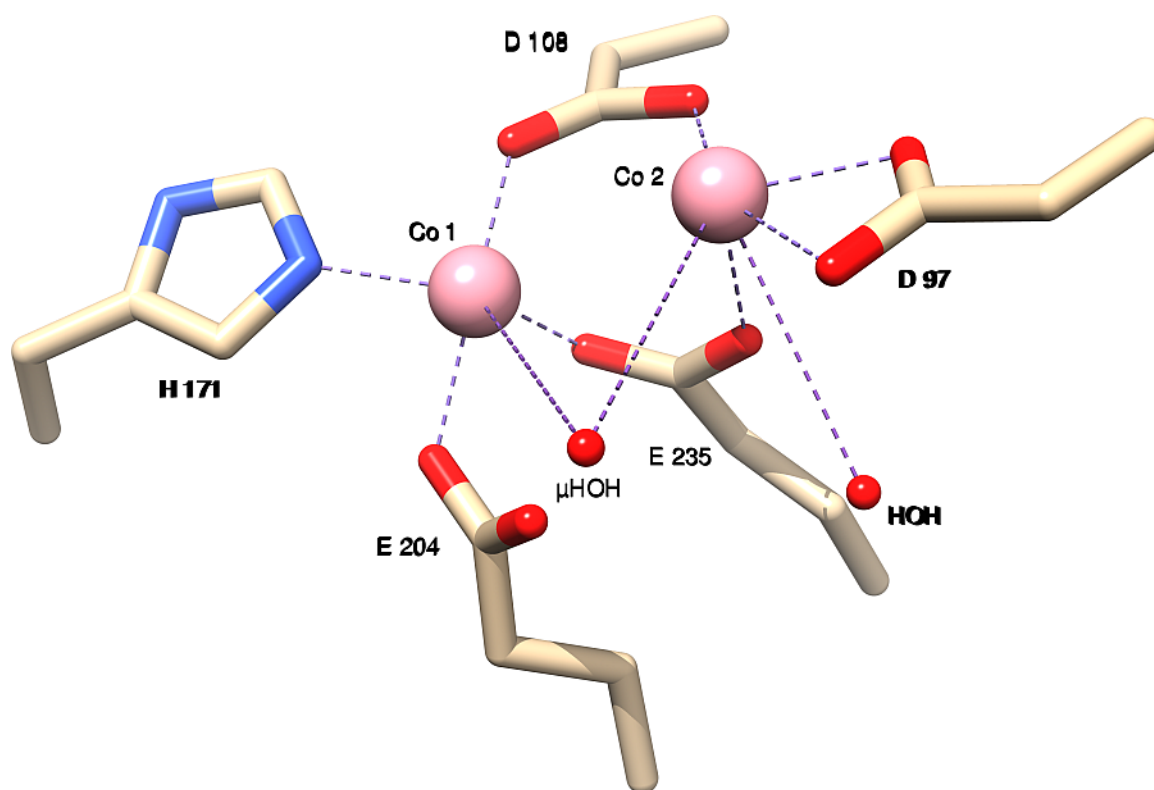


Figure 1.14. X-ray crystal structure of dinuclear metal center of *EcMetAP*. Co1 is penta coordinated with the ligands Asp108, His171, Glu204, Glu235 and a bridging solvent in a distorted trigonal bipyramidal geometry. Co2 is hexa coordinated with the ligands Asp97 (bidentate), Asp108, Glu235, the bridging solvent and a second solvent molecule in a distorted octahedral geometry

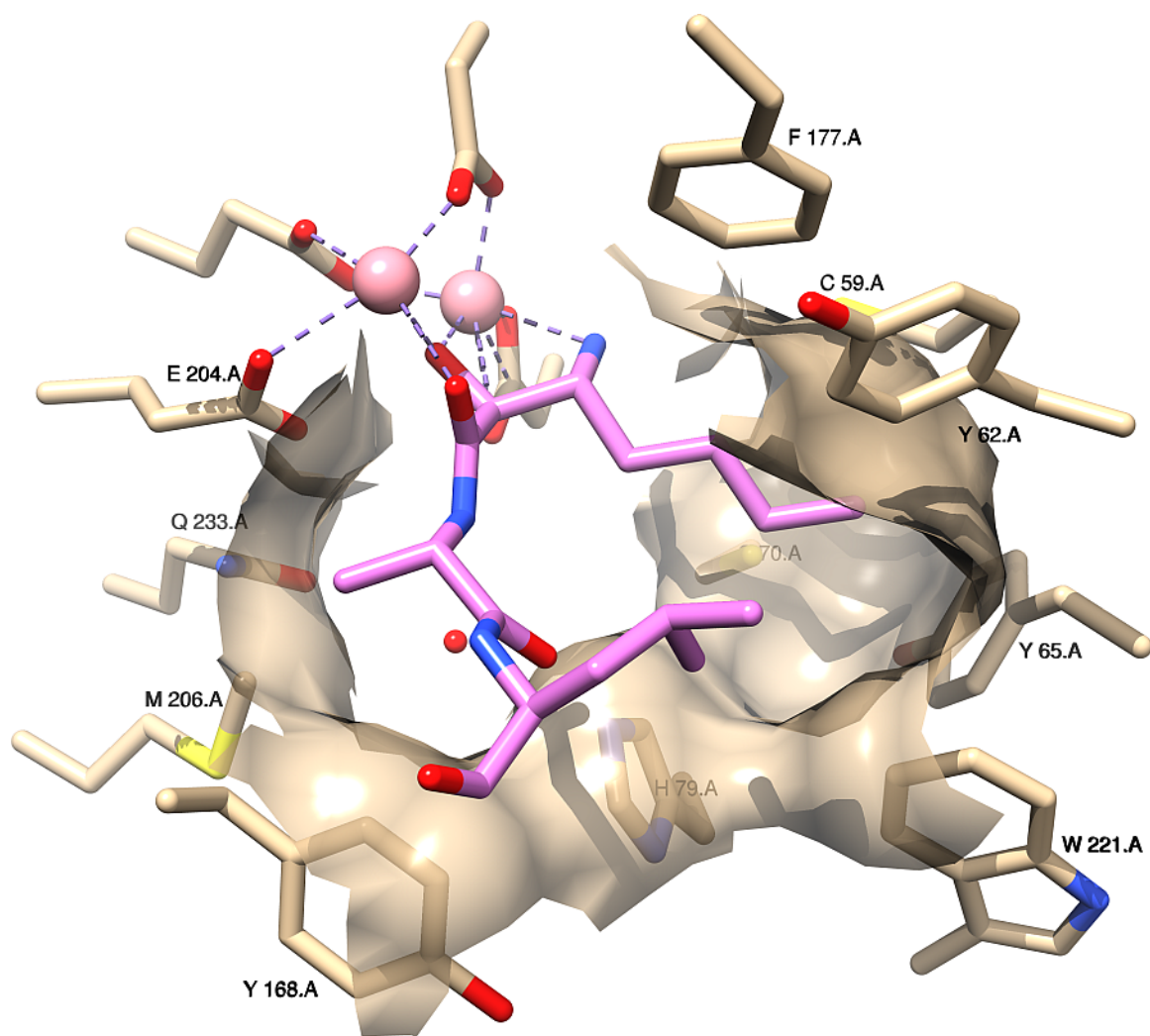


Figure 1.15. X-ray crystal structure of bestatin derivative bound at the di-metalated *EcMetAP* active site.

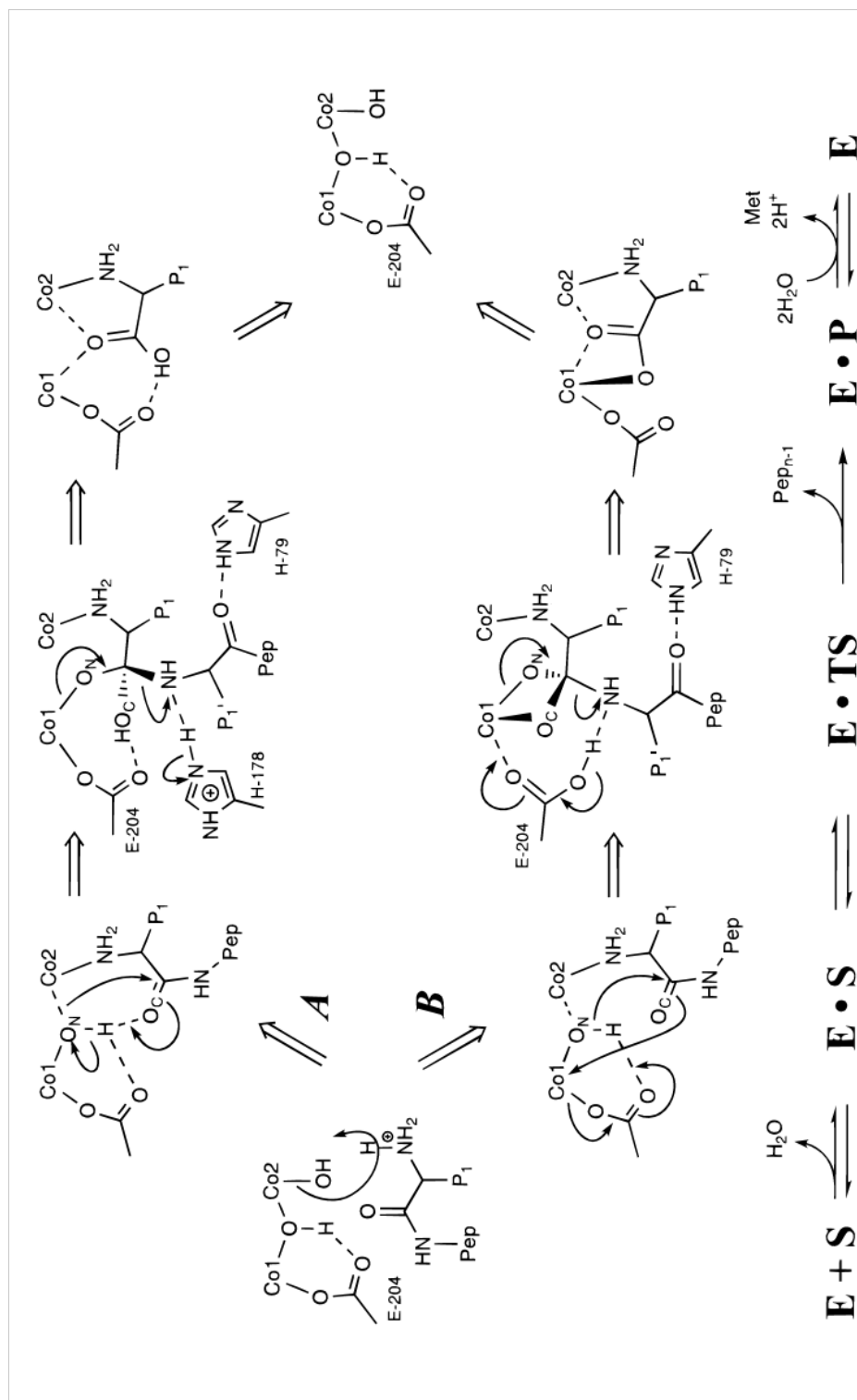


Figure 1.16. Structure based mechanism for di-metalated MetAP.

In mechanism II, ligand exchange at the metal center activates the μOH for nucleophilic attack which results in the tetrahedral intermediate. In addition to orientation by His79 as in mechanism I, the intermediate is stabilized by coordinating with Co1 and possibly hydrogen bonding with His178. Glu204 shuttles a proton from the attacking μOH to the nitrogen of the leaving amino group leading to collapse of the intermediate.

While the bestatin based substrate analog provided insight into the binding mode of the N-terminal methionine of substrates, it was unable to clarify the interaction between the metal center and the scissile peptide bond. A later study with phosphorous-based transition-state analogs (1-amino-3-(methylmercapto)-propylphosphonic acid, norleucine phosphonic acid) sought to resolve this mechanism. Results from the study supported mechanism II described above, but indicated that His79 hydrogen bonded with the nitrogen of the scissile bond (Figure 1.17) rather than with the carbonyl oxygen of the penultimate residue as suggested previously [76].

The hydrogen bonding of His79 occurred via movement of the residue by 1.2 Å which appeared to be facilitated by the overall movement of an extended loop region (residues 75–81 and 216–223) towards the metal site. Interestingly, the proposed function of His79 (use of a conserved hydrogen bond to recognize a small portion of a larger substrate) is similar to the case of peptide deformylase. In addition to updating the role of His79, this mechanism also suggested a definitive function for His178 in stabilizing the substrate by hydrogen bonding with O_C , to account for its highly conserved nature in the MetAP family as well as the effect of its mutation on significantly reducing the catalytic activity [47]. In order to further elucidate the role of His178 in the catalytic mechanism kinetic studies were conducted with the H178A mutant *EcMetAP*. The results from pH dependent activities and electronic absorption spectra of WT and H178A MetAP indicated that the the pK_a of the μOH

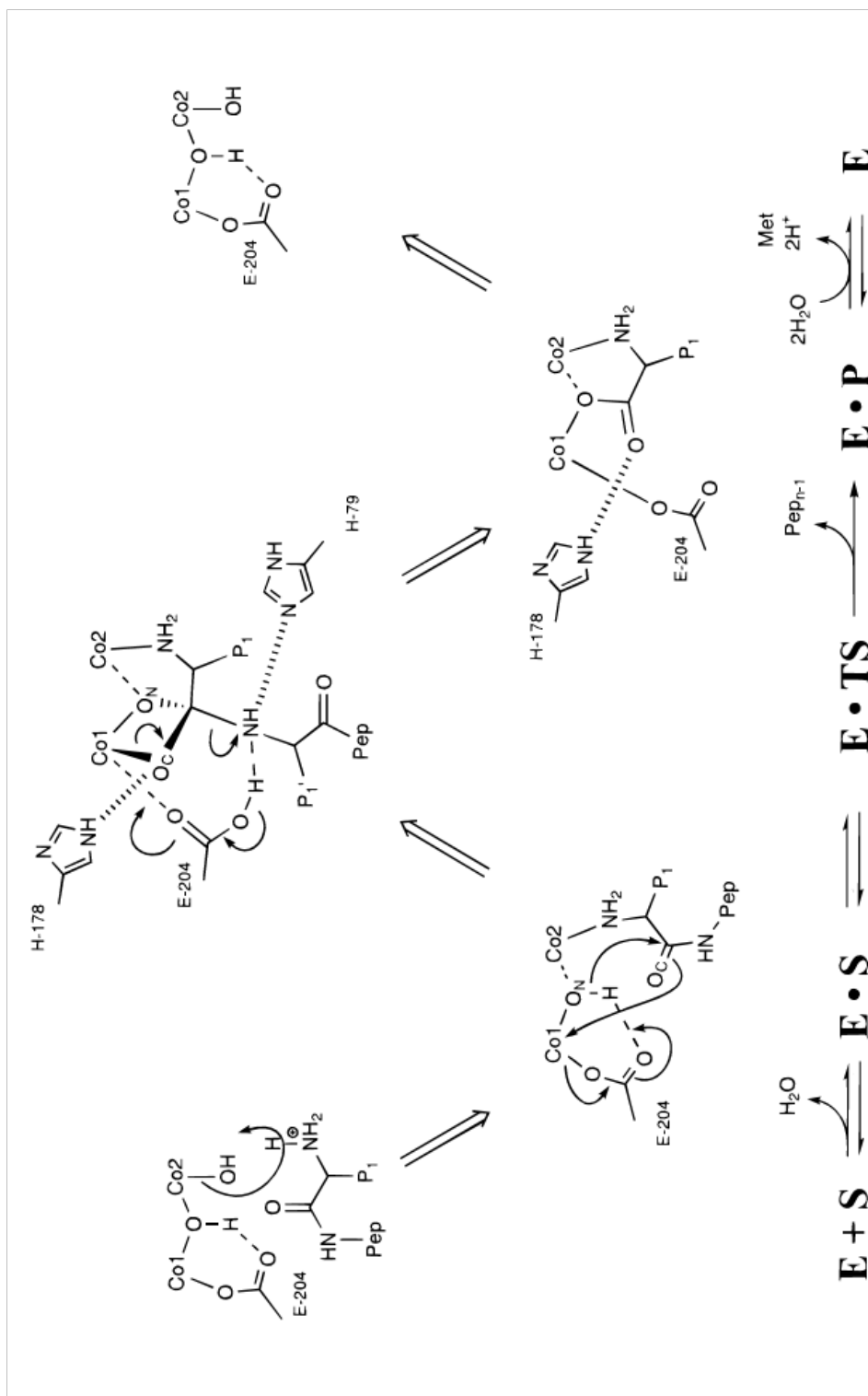


Figure 1.17. Transition analogue based mechanism for di-metalated MetAP.

was more acidic by 0.5 pH units in the mutant, suggesting that His178 may indirectly stabilize the μOH therefore facilitating the binding of the O_C to the metal ion and its activation for nucleophilic attack [77]. In cognizance of these observations, the catalytic mechanism was modified (Figure 1.18) to the following steps: (a) recognition of the N-terminal methionine side chain by the hydrophobic S1 pocket and stabilization of the substrate by hydrogen bond between Asp97 and the terminal amine (b) coordination of the O_C to the metal ion along with hydrogen bonding between the residues Glu204, His79 and the amino group of the scissile peptide bond (c) cleavage of the scissile peptide bond followed by release of the products (d) regeneration of the active site by addition of a water molecule to the metal ion and another water molecule bridging between the first and His178.

Note that the mechanism proposed here only involves a single Fe^{2+} metal ion at the active site. ICP-AES analysis of the metal content in crude extracts of *E. coli* cells overexpressing MetAP suggested that Fe^{2+} may be the native co-factor of the enzyme [78]. Further metal analyses of MetAP by ICP-AES as well as activation of the apoenzyme by metal ions indicated that a single metal ion was required for full catalytic activity of the enzyme [77, 79]. The Asp97 residue proposed to coordinate the second metal ion in the previous mechanism (as indicated by the x-ray crystal structures) is now suggested to orient the substrate by hydrogen bonding with the terminal amino group, a role that was earlier assigned to the second metal ion.

Structural evidence for a mononuclear metal center based catalytic mechanism was obtained from the x-ray crystal structure of NleP bound at the active site of mono-Mn(II) *EcMetAP* [80]. The mono-metalated enzyme structures were produced by using limiting amounts of the metal ion during crystallization. The metal center is pentacoordinated with Asp97, His171, Glu204, Glu235 and a water molecule (Figure 1.19).

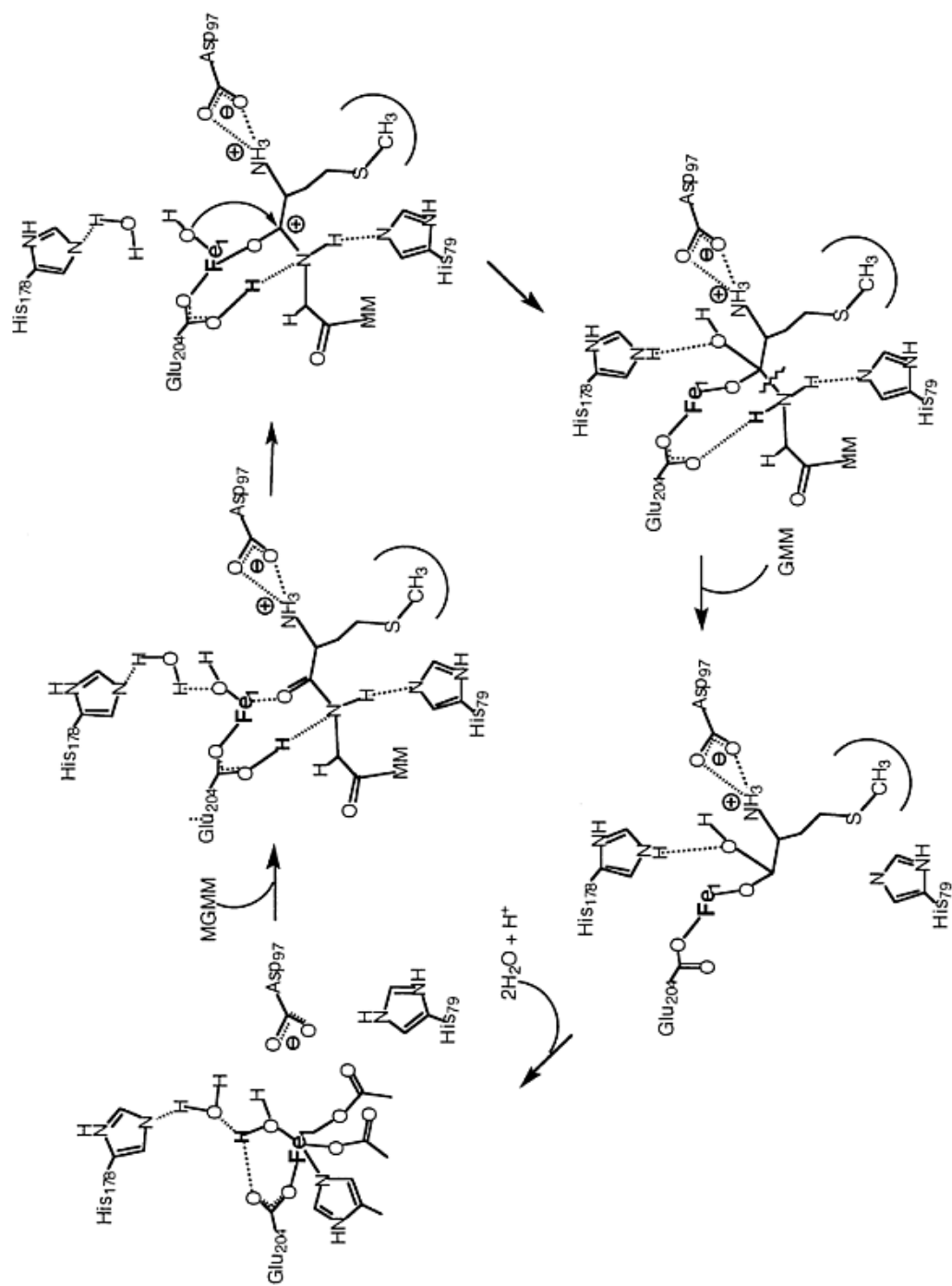


Figure 1.18. Mechanism for di-metalated MetAP based on H178A mutation.

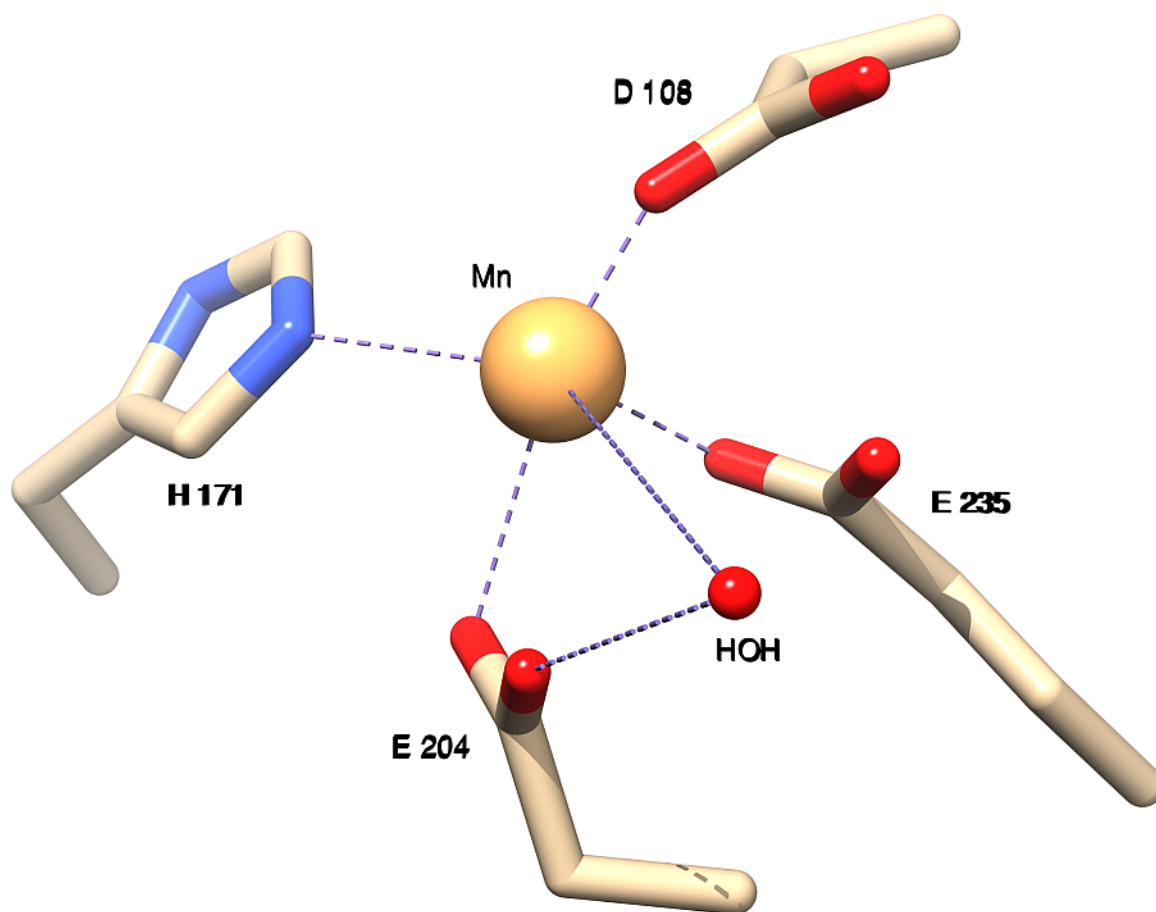


Figure 1.19. X-ray crystal structure of mono-nuclear metal center of *EcMetAP*.

The position and orientation of the active site bound substrate and transition state analogs (AHHpA-Ala-Leu and NleP respectively) were found to be superimposed in the mono and di-metalated structures. A revised catalytic mechanism for the mono-metalated enzyme was described for the tripeptide substrate Met-Ala-Leu, where the coordinates of Met were based on NleP and those of Ala and Leu were based on AHHpA-Ala-Leu (see Figure 1.20).

According to the proposed mechanism, the catalysis proceeds in the following steps: (a) the substrate approaches the metal ion in a trans configuration for the formation of a Michealis complex (b) the side chains of Asp97 and Asp108 move closer to, and form hydrogen bonds with, the amino terminus, His79 and His178 form hydrogen bonds with the nitrogen and carbonyl oxygen of the scissile peptide bond respectively, and the metal ion interacts with the O_C increasing its coordination number to six (c) with Glu204 acting as a general base, the metal coordinated water makes a nucleophilic attack on the carbonyl group to form a tetrahedral intermediate (d) His79 transfers a proton to the scissile amide nitrogen to facilitate the breakdown of the intermediate

1.4.2.3. Steady-state characterization of MetAP

Several methods are in use for the quantitative measurement of MetAP activity. These include end-point and continuous assays, the latter type including both coupled and direct assay systems. The first assay reported for MetAP involved the use of the tripeptide substrate Met-Gly-Met-Met in a combination of end-point and coupled systems [13]. The cleavage of N-terminal methionine by MetAP was terminated and the resulting free Met was quantified in a coupled assay system consisting of L-amino acid oxidase, horseradish peroxidase and ϕ -dianisidine dihydrochloride as described in

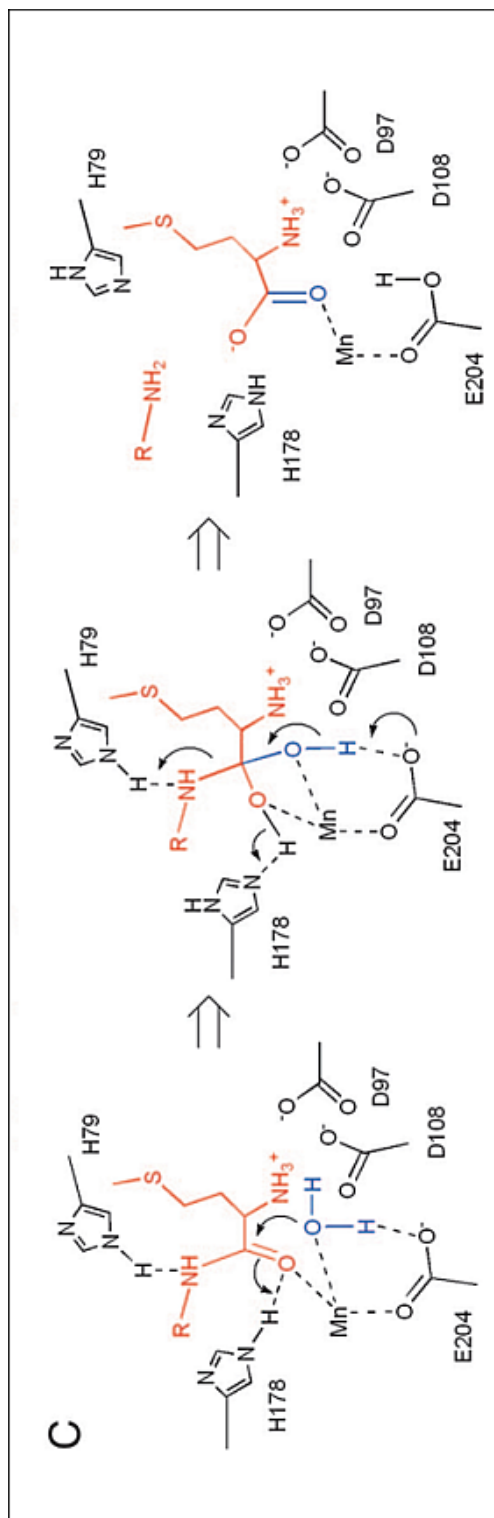


Figure 1.20. Structure based mechanism for mono-metalated *EcMetAP*.

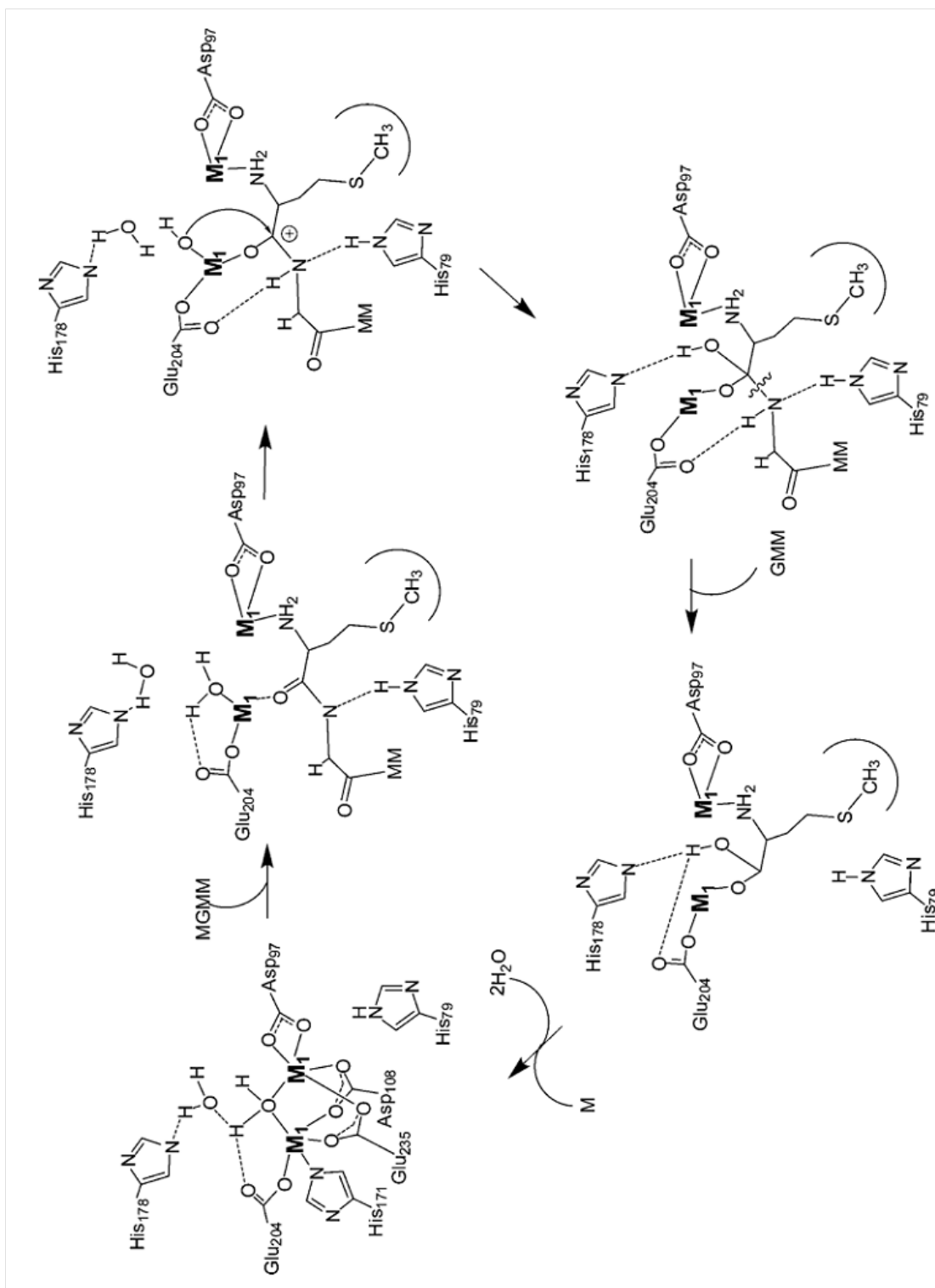
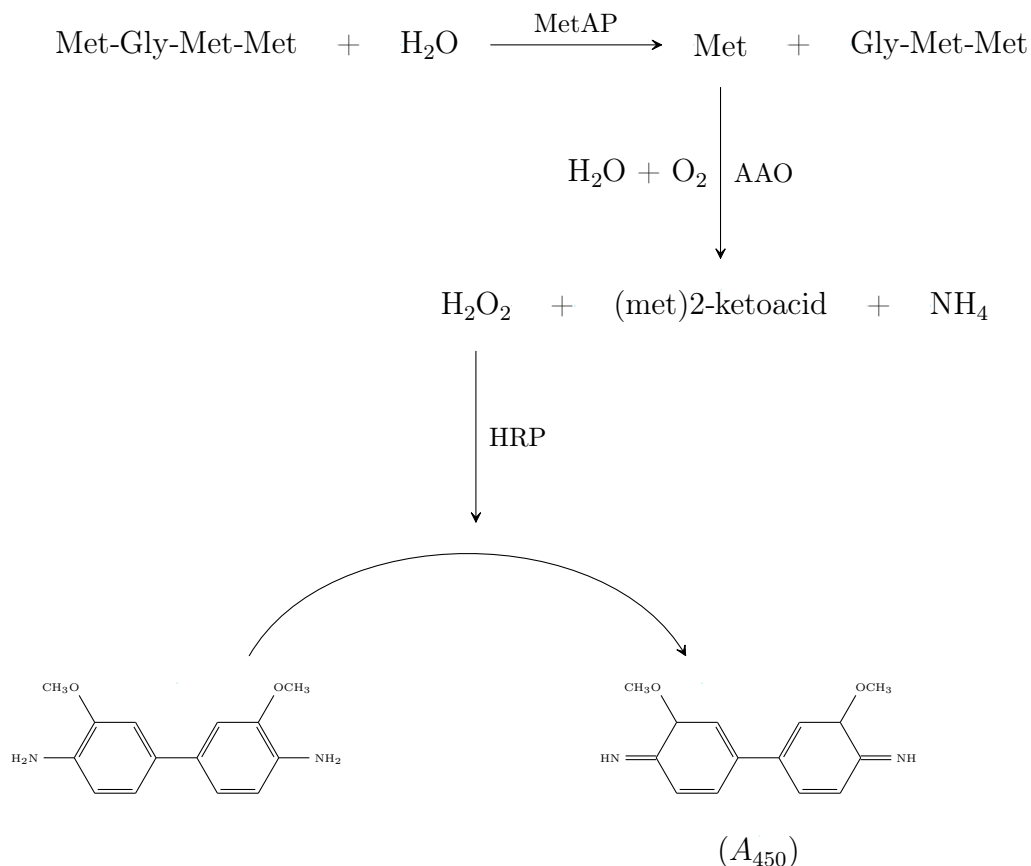


Figure 1.21. Mechanism for di-metalated MetAP based on H79A mutation.



Scheme 1.3. Coupled end-point assay for MetAP using tetrapeptide substrate.

Scheme 1.3. In a slight modification of this assay, the chromogenic dianisidine was replaced by the fluorogenic reagent Amplex[®] Red, the oxidized product of which is detected at 585 nm ($\lambda_{\text{ex}} = 570 \text{ nm}$) [81].

This assay has been used extensively and in spite of its tedious nature, continues to be used today [82]. Several related assays were developed using alternative methods of quantification of the released methionine. Typically the methionine was separated and analyzed by reversed-phase HPLC [73, 83, 84]. However, these assays remain very time consuming without providing any additional advantage. The development of continuous assays greatly simplified the measurement of catalytic activity. One of the earliest continuous assays reported by Zhou et al. [85] involved a coupled system with

the use of a thioether substrate N-[(S-methionyl)-2-mercaptoacetyl]phenylalanine, the resulting free thiol being quantified by DTNB. However the substrate was observed to be unstable resulting in significant background. Moreover the DTNB was found to slowly inactivate MetAP by reacting with a cysteine in the active site cavity, therefore this assay has seen very limited usage. The authors also reported an alternative coupled continuous assay using the chromogenic peptide substrate Met-Pro-*p*NA. The peptide product is cleaved by the coupling enzyme prolyl aminopeptidase (ProAP) and the resulting free *p*NA is measured by its absorbance at 405 nm. While this peptide substrate is relatively poor, this assay has seen widespread use due to its convenience and has led to the development of direct continuous assays using chromogenic and fluorogenic substrates, Met-*p*NA and Met-AMC respectively [81, 86, 87]. Although the substrates used in the direct assays are very poor as compared to the previous substrates, they provide a clear advantage over the coupled assays due to potential complications arising from interference with the coupling enzyme.

More recently, a new high-throughput assay has been reported wherein the cleaved methionine residue is quantified using a simultaneous coupled assay involving (a) ATP dependent conversion of free methionine to S-adenosyl-L-methionine (SAM), inorganic phosphate and pyrophosphate (PP_i), catalyzed by SAM synthase (MetK) (b) conversion of pyrophosphate to inorganic phosphate, catalyzed by inorganic pyrophosphatase and (c) spectrophotometric detection of inorganic phosphate by malachite green/molybdate reagent at 650 nm [88]. The assay is able to use any peptide substrate, such as the highly efficient tetrapeptide substrate Met-Gly-Met-Met. Moreover, although the authors have used an end-point detection technique for the quantification of the phosphate, it may be replaced with a continuous detection system allowing real time monitoring of the steady state reaction kinetics.

A cell based assay has also been recently reported for *E. coli* MetAP involving the use of a fluorogenic substrate [89]. *E. coli* cells overexpressing MetAP were permeabilized by treatment with Ca^{2+} , and hydrolysis of the substrate Met-AMC was monitored over 4 h on addition to the live cells. The authors were able to test the validity of the assay by screening known inhibitors of the enzyme. While the IC_{50} values determined by this assay were higher by as much as ten fold as compared to those determined by the standard *in vitro* assay conducted with purified enzyme and up to four fold higher than those obtained for the inhibition of cell growth, the relative potencies of the inhibitors determined by this method closely matched those observed with the traditional assays. The advantage of the cell based assay lies in the screening of inhibitors against the native form of the enzyme. This is of particular importance considering the fact that (a) the nature of the metal ion(s) at the MetAP active site remains under debate and (b) the vast majority of the metal-coordinating ligands that inhibit the enzyme under *in vitro* assays fail to show any effect on cell growth [90, 91]. The kinetic parameters of selected MetAP isoforms for some of the above substrates are listed in Table 1.2.

Table 1.2. Steady state kinetic parameters of selected MetAP isoforms

Substrate	Enzyme	Metal	k_{cat} (s^{-1})	K_{m} (μM)	Ref
MSSHRWDW	<i>E. coli</i>	Co^{2+}	70	1	[92]
	<i>P. furiosus</i>	Co^{2+}	16	2	[93]
		Fe^{2+}	22	1	
	<i>S. cerevisiae</i> 1	Co^{2+}	23	0.02	[73]
		M329A		30	0.01
	Q356A		13	0.04	

continued...

Table 1.2. Steady state kinetic parameters of selected MetAP isoforms (...continued)

Substrate	Enzyme	Metal	k_{cat} (s^{-1})	K_{m} (mM)	Ref
MGMM	<i>E. coli</i>	Co^{2+}	18	3	[78]
	H178A		39	3	[77]
	D97A		0.003	1	[94]
	H63A		5	3	[92]
	<i>E. coli</i>	Fe^{2+}	28	2	[77]
	H178A		0.6	2	
	<i>E. coli</i>	Mn^{2+}	5	1	[95]
	H79A		2	2	[94]
	<i>P. furiosus</i>	Co^{2+}	188	5	[93]
		Fe^{2+}	153	5	
	<i>H. sapiens</i>	Co^{2+}	3	0.34	[81]
Met-Pro-pNA	<i>E. coli</i>	Co^{2+}	2	0.14	[85]
	H178A		0.002	0.12	[77]
	<i>E. coli</i>	Fe^{2+}	0.01	0.13	
	<i>P. furiosus</i>	Co^{2+}	157	0.2	[93]
		Fe^{2+}	46	0.1	
	<i>H. sapiens</i> 1	Co^{2+}	0.11	0.7	[96]
Met-pNA	<i>E. coli</i>	Co^{2+}	0.006	0.44	[87]
	H63A		0.0001	0.33	[92]
	<i>H. sapiens</i> 2	Co^{2+}	0.16	0.7	[81]
Met-AMC	<i>E. coli</i>	Co^{2+}	0.011	4	[86]

continued...

Table 1.2. Steady state kinetic parameters of selected MetAP isoforms (... continued)

Substrate	Enzyme	Metal	k_{cat} (s^{-1})	K_{m} (mM)	Ref
		Mn ²⁺	0.006	6	
		Ni ²⁺	0.002	1	
	<i>H. sapiens 2</i>	Co ²⁺	0.05	0.3	[81]
		Zn ²⁺	0.011	0.2	

1.4.3. Metal binding properties of PDF

Whereas all known PDFs are reported to have a mononuclear active site, the various isoforms have been found to utilize different metal ions in their native form. While initially reported as a Zn²⁺ containing enzyme [14], the *E. coli* PDF was eventually found to use Fe²⁺ as its native cofactor [97]. The appearance of Zn²⁺ form of the PDF was later attributed to the labile nature of the Fe²⁺ form of the enzyme and the extremely high affinity of Zn²⁺ at the PDF active site. Several other PDFs have been reported or proposed to contain Fe²⁺ at the active site. In contrast, certain PDFs such as eukaryotic type IA [66], type IB from *L. pneumophila* have been identified as native Zn²⁺ enzymes. Both metalloforms of PDFs have also been reported to be active with Ni²⁺ and Co²⁺ metal ions. However the relative activity with the different metal ions is dependent on the metal ion used by the enzyme in its native state. Thus Fe²⁺ containing PDFs exhibit a decreasing activity trend in the order: Fe²⁺, Ni²⁺ > Co²⁺ >> Zn²⁺ [98], whereas Zn²⁺ containing PDFs exhibit the order: Zn²⁺ > Fe²⁺ > Ni²⁺, Co²⁺ [99].

Although the catalytic efficiency of different PDF metalloforms is known, the relative binding affinities of the metal ions to the various PDF isoforms is not yet reported. Fe^{2+} , Ni^{2+} and Co^{2+} are known to bind weakly as the activity of these metalloforms of PDFs is inhibited by metal chelating agents and the loss in activity is almost completely irreversible [9, 17]. In contrast, the Zn^{2+} form of PDF is resistant to inhibition by EDTA, dipicolinic acid and chelating resins, but inhibited by 1,10-phenanthroline (presumably via formation of a ternary complex) [100]. Moreover a stoichiometric amount of Zn^{2+} is able to replace the bound metal ion at the PDF active site [59]. These observations indicate that Zn^{2+} binds extremely tightly (possibly irreversibly [54]) to the PDF active site. However it is interesting to note that the addition of millimolar Ni^{2+} was found to enhance the activity of the Zn^{2+} form of *Ec*PDF [65]. This observation has suggested the presence of a small conformational subset of the Zn^{2+} -PDF population that binds the metal ion weakly, which can therefore be replaced by another metal ion provided sufficient mass action. Detailed thermodynamic studies conducted more recently have not only confirmed the presence of alternative conformational states in *Ec*PDF, but have suggested that the conformational states are at least partially modulated by the active site metal ion [101].

1.4.4. Metal binding properties of MetAP

The nature of the metal ion at the MetAP active site has been studied with great interest due to the relevance of the enzyme as a target for anti-cancer therapy. The initial isolation of the *E. coli* MetAP indicated that it was a metalloenzyme activated by Co^{2+} [13]. The crystal structure of the enzyme showed that the enzyme active site contained two Co^{2+} metal ions [102]. However the possibility of alternative metal ions as the native cofactor was suggested on the basis that under physiological

concentrations of reduced glutathione (GSH), the yeast MetAP I was poorly activated by Co^{2+} but highly activated by Zn^{2+} [103]. In contrast, the human and *P. furiosus* MetAP I have been shown to be inactive in the presence of Zn^{2+} [81, 93].

The native cofactor of the *EcMetAP* enzyme was suggested to be Fe^{2+} on the basis of significantly higher concentration of the metal ion observed upon whole cell ICP-AES analysis of *E. coli* with overexpression of the enzyme [78]. The authors noted that the enzyme was differentially activated by metal ions in the order $\text{Co}^{2+} > \text{Fe}^{2+} > \text{Mn}^{2+} \gg \text{Zn}^{2+}$, where as Ni^{2+} was unable to activate the enzyme. Further studies with analysis of the metal content of the purified Co^{2+} -*EcMetAP* indicated that the enzyme contained only 1 equivalent of the metal ion [79] suggesting that the enzyme may be monometalated in contrast to earlier reports. The monometalated nature was corroborated by the observation that maximal activation of the enzyme was achieved by 1 equivalent of metal ions. The binding affinity of the second Co^{2+} was determined by electronic absorption spectroscopy to be 2.5 mM as opposed to the binding affinities of the first Co^{2+} and Fe^{2+} being 0.3 and 0.2 μM respectively (determined by enzyme activation) [79]. A similar profile has been reported for Mn^{2+} (3 μM and 4.4 mM determined by ITC) [95] and for the *P. furiosus* MetAP where the binding affinities for the first metal site are 50 and 20 nM for Co^{2+} and Fe^{2+} respectively and that for the second Co^{2+} is 0.35 mM [93]. These observations suggest that the second metal ion is not required for the catalysis and is probably absent under physiological conditions.

In spite of the above studies, the features of the MetAP metal ion have been continued to be debated. Based on computational analysis of the MetAP catalytic reaction at the DF-B3LYP level of theory, the most efficient (and by extension the most probable native cofactor) metal ion for *EcMetAP* was reported to be Zn^{2+} , with the transition state energy barrier being about 6 to 8 kcal mol^{-1} lower than that for Mn^{2+} , Fe^{2+} and Co^{2+} [104]. However additional experimental evidence supporting Fe^{2+} as the

native cofactor in *EcMetAP* has since been reported based on the selective inhibition of *E. coli* cell growth by metalloform specific inhibitors specific for Fe^{2+} -*EcMetAP* [105]. In a separate study the number of activating metal ions was also reclaimed with the observation that the activation of *EcMetAP* by Co^{2+} was sigmoidal with a Hill coefficient of 2.1 [106]. It is clear that the features of the MetAP metal ion interaction remain obscure and further studies are required to clarify the metal binding properties of the enzyme.

1.4.5. Stability of PDF

It is of particular interest to note the biophysical properties of PDF with respect to the unique stability features of the enzyme. The unusually acute enzymatic instability of PDF thwarted the early attempts to isolate and study the enzyme. The cause of this inactivation was later found to be two fold: (a) displacement of the native Fe^{2+} cofactor by the weakly active but tight binding Zn^{2+} and (b) oxidation of the Fe^{2+} *in vitro* to the inactive Fe^{3+} form. The ubiquitous presence of trace amounts of zinc in laboratory glassware was enough to convert the highly active Fe^{2+} form of PDF to the poorly active Zn^{2+} form, which could not be detected by the low sensitivity assays used previously. However, by avoiding the displacement of the active site metal and protecting the oxidative damage of Fe^{2+} , the *E. coli* PDF has been shown to be highly stable [17, 59]. The identity of the metal cofactor has also been shown to play a role in the relative structural stability of PDFs. Increasing the temperature from 25 to 60 °C was shown to increase the catalytic rate of the Zn^{2+} -PDF by two orders of magnitude [100]. The enhanced stability of the Zn^{2+} form of PDF is further observed in unfolding studies using guanidinium chloride (GdmCl), which have indicated that the stability of different metalloforms of PDF decreases in the order: $\text{Zn}^{2+} > \text{Co}^{2+} > \text{Fe}^{2+}$ [54]. In fact later studies of GdmCl induced unfolding of PDF have revealed

a most curious phenomenon wherein at low to moderate concentrations ($< 2\text{ M}$) of GdmCl, the unfolding of PDF was abruptly reversed [107]. The energetic rationale proposed for this unique observation suggests that the unfolding of PDF proceeds via several intermediates and the free energy (ΔG) of one of the later intermediates varies as a function of the GdmCl concentration. At GdmCl concentrations $< 2\text{ M}$ the ΔG of this intermediate is lower than the energy barrier of the final transition state (ΔG^\ddagger) which in turn is higher than the ΔG^\ddagger of a previous transition state, thus favoring the reversal of the unfolding process. On the other hand, with increasing GdmCl concentration, the ΔG of this intermediate increases along with the ΔG^\ddagger of preceding transition state(s) so that the final energy barrier now has a lower ΔG^\ddagger , allowing the unfolding pathway to proceed to completion.

In addition to the metal ions, the stability of PDFs has been found to be greatly influenced by the C-terminal domain which forms an α -helix. While truncation of up to 21 residues from the C-terminus had no effect on the catalytic activity of *Ec*PDF, it resulted in enhanced stability of the enzyme against thermal unfolding [108]. Concentration has also been reported to affect the stability of PDFs, with dilute concentrations resulting in inactivation of the enzyme [65], which can be alleviated by the addition of BSA [64].

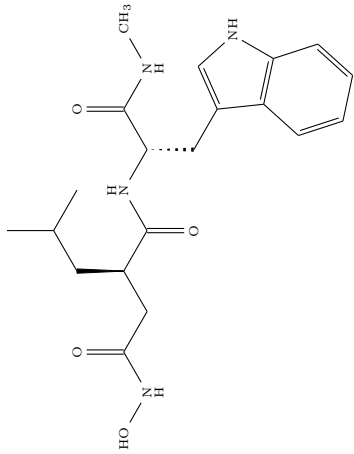
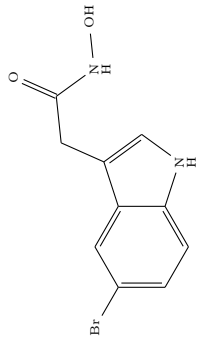
1.5. Therapeutic Potential of PDFs and MetAPs

The essential nature of the NME pathway as described in Section §1.2 has established the component enzymes, PDF and MetAP, as valuable targets for therapeutics. The discovery of PDFs generated great interest in their potential as targets for antibiotics particularly since they were only known to exist in bacteria. However PDFs have since been also found in eukaryotic organelles and inhibitors of prokaryotic

PDFs have been shown to be also active against those from eukaryotic sources. In spite of these observations, they remain highly targeted for antibiotics especially due to the emergence of multi-drug resistant strains of pathogens around the world. In fact antibiotics targeting PDF have been found to no adverse effect on human PDF at the concentrations required for antibacterial action. Moreover, due to their presence in eukaryotes, they have now also been identified as targets for treatment against pathogenic protists as well as for the development of herbicides. Similarly, the existence of distinct as well as secondary forms of MetAPs in eukaryotes led to the designation of the bacterial MetAPs (type I) as novel antibiotic targets. Like PDFs, MetAPs have also been targeted in developing therapeutics against pathogenic protists. While a plethora of compounds have been reported to inhibit the enzymes *in vitro* only a small fraction of the inhibitors have shown potential for *in vivo* use. Table(insert) lists the known inhibitors of PDFs and MetAPs with promising antibiotic activity.

In addition to being targets for antibiotics, the role of the enzymes in cancer has created a huge thrust in the development of inhibitors against them as anti-cancer drugs. Interestingly this application came to light when the target of the well known angiostatic compound fumagillin (and its derivative TNP-470) was identified as the recently discovered MetAP type II [109]. Soon after, the naturally occurring PDF inhibitor Actinonin, with known antibacterial effect, was shown to have anti-tumor activity [110]. The enhanced expression of MetAP type II in several cancers further underscored the importance of targeting the NME pathway for anti-cancer treatment [111]. Inhibitors of these enzymes with anti-cancer activity have been shown to have a range of action modes including cytotoxicity, antiproliferation and apoptosis. A selection of bio-active antibiotic and therapeutic compounds targeting PDFs and MetAPs are listed in Tables 1.3 and 1.4 respectively.

Table 1.3. PDF and MetAP as antibiotic targets

Compound	Structure	Target
		Organism Enzyme isoform
GM6001 [112]		<i>C. trachomatis</i> PDF 1B
BIHA [113]		<i>E. coli</i> PDF 1B <i>B. subtilis</i> PDF 2

continued...

Table 1.3. PDF and MetAP as antibiotic targets (... continued)

Compound	Structure	Target	
		Organism	Enzyme isoform
BB-3497 [114]		G-ve bacteria	PDF 1B
Actinonin		G+ve bacteria [115] <i>A. thaliana</i> [116]	PDFs 1 & 2 PDF 1B

continued...

Table 1.3. PDF and MetAP as antibiotic targets (... continued)

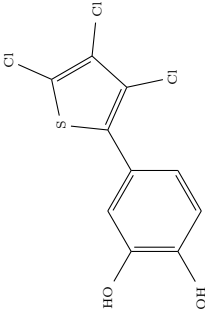
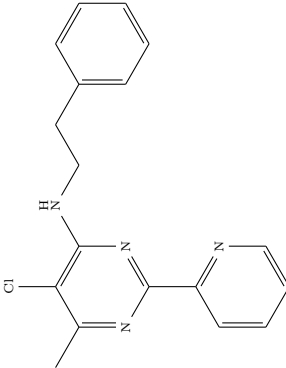
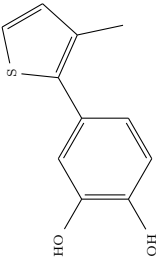
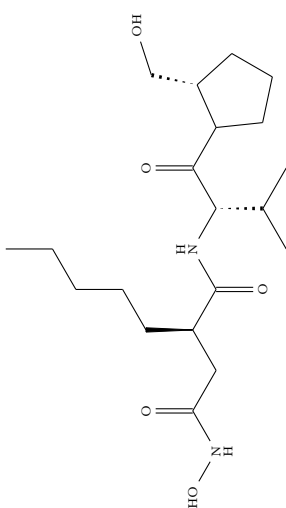
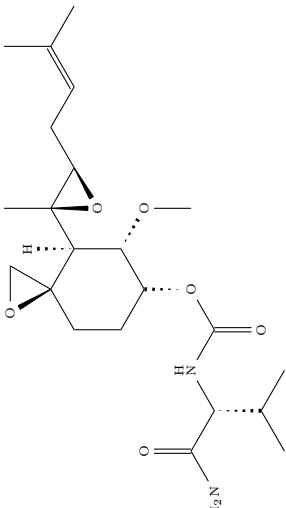
Compound	Structure	Target	
		Organism	Enzyme isoform
TCTB [117]		<i>S. aureus</i> (MRSA)	MetAP Ia
XC11 [118]		<i>P. falciparum</i>	MetAP Ib
MTB [119]		<i>M. tuberculosis</i>	MetAP Ic

Table 1.4. PDF and MetAP as therapeutic targets

Compound	Structure	Action	Target
Actinonin		anti-proliferative [120]	PDF 1D
PPI-2458		immuno-modulator [121] anti-proliferative [122, 123]	MetAP II

2. STATEMENT OF PROBLEM

MetAP plays a major role in protein synthesis in all living organisms, especially in concert with PDF in bacterial cells, by removing the N-terminal (formyl-)methionine residue (an essential step for most proteins) from new protein chains while they are being synthesized. As a result, both MetAP and PDF have attracted attention as novel targets for drug design. However, both these metalloenzymes have yet to be thoroughly characterized and understood and it is necessary to rectify this shortcoming in order to be able to exploit them in the interest of medicine. Specifically, a poor understanding of the metallo-specific properties of MetAP has been blamed for the failure to develop effective antibiotics against the enzyme. Further, PDF has been noted to have highly unusual properties and the C-terminal domain has been implicated to play a role in these features.

The goal of this dissertation is to contribute to the effort in understanding these two metalloenzymes. In particular, the investigation was carried out with the following objectives:

1. To identify potent and bacterial isozyme selective inhibitors of MetAP.
2. To characterize metallo-specific inhibition and ligand interaction of MetAP.
3. To characterize the metal-ion binding and catalytic features of MetAP.
4. To elucidate the significance of the C-terminal domain with respect to the structural-functional properties of PDF.

The studies were designed to provide new insight into the structure and function of MetAP and PDF, particularly in the role of drug targets, as well as augment the overall understanding of enzymes.

3. MATERIALS

General: Yeast extract and tryptone were from Becton Dickinson (Sparks, MD). HEPES, Tris, PMSF, TCEP and cyclodextrins were from Sigma-Aldrich (St. Louis, MO). Dimethylformamide, acetonitrile and dimethylsulfoxide were from EMD Chemicals (Billerica, MA). All other chemicals were of reagent A.C.S. grade.

Filtration and chromatography: Polycarbonate membrane filters and centrifugal filtration devices were from Millipore (Billerica, MA). Polyethanesulfone membrane filters and syringe filtration devices were from Pall Life Sciences (Ann Arbor, MI). Dialysis membranes were from Spectrum Laboratories, Inc. (Rancho Dominguez, CA). Sepharose and amylose resins were from GE Healthcare Biosciences (Pittsburg, PA) and New England Biolabs (Ipswich, MA) respectively. Iminodiacetic acid was from TCI America (Portland, OR). Butanediol diglycidyl ether was from Electron Microscopy Sciences (Hatfield, PA).

Protein estimation and enzyme assays: Bradford reagent and protein estimation kit for the BCA assay were from Bio-Rad (Hercules, CA) and Pierce Biotechnology (Rockford, IL) respectively. Met-Pro-*p*Nitroaniline was provided by Dr. Sanku Mallik. Met-7-*am*onio-4-methylcoumarin was from Enzo Life Sciences (Farmingdale, NY). *Aeromonas* aminopeptidase was from ProSpec (Ness-Ziona, Israel). 96 and 384-well microplates were from Corning Life Sciences-Axygen Inc. (Union City, CA), or Greiner Bio-One (Monroe, NC).

Cloning: The clones containing *EcMetAP*-6His and 6His-*HsMetAP* were provided by Dr. Brian Matthews at the University of Oregon (Eugene, OR). *E. coli* DH5 α and BL21-DE3 competent cells and *Pfu* DNA polymerase were from Stratagene (La Jolla, CA). Restriction enzymes and T4 DNA ligase were from New England Biolabs (Ipswich, MA). Plasmid DNA purification kit was from Qiagen (Valencia, CA). Primers were synthesized by Integrated DNA Technologies (Coralville, IA).

4. METHODS

4.1. Cloning, Expression and Purification

4.1.1. Expression and purification of His-tagged *E. coli* MetAP

Recombinant clones of *E. coli* BL21-DE3 Gold cells containing *EcMetAP-6His* were provided kindly by Dr. Anthony Adlagatta and Dr. Brian Matthews, in the form of colonies on a Kanamycin nutrient agar plate. Expression and purification of *EcMetAP-6His* was carried out as described by Lowther et al. [124], and modified as reported by Adlagatta et al. [96]. Starter cultures were prepared by inoculating a single colony into 5 ml of sterile Luria-Bertani (LB) medium containing 50 µg/ml of kanamycin. After incubation at 37 °C for 16 hours, part of the culture was used to inoculate 1 L of media containing kanamycin and the rest was stored at -20 °C in the form of glycerol stocks. The 1 L cultures were incubated at 37 °C for 4 to 6 h, and then expression of the enzyme was induced by adding 1 mM isopropyl β-D-1-thiogalactoside (IPTG). Expression was allowed to continue overnight at room temperature (RT). The cells were then pelleted out by centrifugation at 10,000 g and 4 °C for 30 min. The pellets were resuspended in lysis buffer (50 mM HEPES, pH 8 containing 0.5 M KCl, 0.1 % Triton X-100, 10 % glycerol, 5 mM imidazole and 0.1 mg/ml phenylmethylsulfonyl fluoride (PMSF)) and lysed by sonication (power level 4, 50 % duty cycle) in an ice-bath for 10 min, in 1 min steps. The lysate was centrifuged at 15,000 g and 4 °C for 30 min and the resulting supernatant was loaded onto an iminodiacetic acid (IDA) sepharose column that was charged with NiCl₂ and pre-equilibrated with lysis buffer. The IDA sepharose was prepared by cross linking IDA with oxirane activated Sepharose 6B as described by Sundberg and Porath [125]. The loaded column was washed with lysis

buffer until the absorbance at 280 nm reached the baseline, followed by washing with 3 column volumes of wash buffer (lysis buffer containing 20 mM imidazole, without Triton X-100 and glycerol). The protein was then eluted with elution buffer (wash buffer containing 100 mM imidazole) and stored with 1 mM EDTA until further processing. An Econo low pressure chromatography system (BioRad, Hercules, CA) was used for all column operations. The presence of pure *EcMetAP-6His* in the collected fractions was confirmed by SDS-PAGE and such fractions were pooled and dialyzed into storage buffer (25 mM HEPES pH 8 containing 150 mM, KCl and 5 mM methionine). The protein was then concentrated and stored in aliquots at -80°C .

4.1.2. Expression and purification of 6His-*HsMetAP*

Recombinant clones of *E. coli* BL21-DE3 Gold cells containing 6His-*HsMetAP* were provided kindly by Dr. Anthony Adlagatta and Dr. Brian Matthews, in the form of colonies on an Ampicillin nutrient agar plate. Expression and purification of 6His-*HsMetAP* was carried out as reported by Adlagatta et al. [96] with some modifications. Starter cultures were prepared by inoculating a single colony into 5 ml of sterile Luria-Bertani (LB) medium containing 50 $\mu\text{g}/\text{ml}$ of ampicillin. After incubation at 37°C for 16 hours, part of the culture was used to inoculate 1 L of media containing ampicillin and the rest was stored at -20°C in the form of glycerol stocks. The 1 L cultures were incubated at 37°C for 4 - 6 hours, and then expression of the enzyme was induced by adding 1 mM IPTG. Expression was allowed to continue overnight at room temperature (RT). The cells were then pelleted out by centrifugation at 10,000 g and 4°C for 30 min. The pellets were resuspended in lysis buffer (50 mM HEPES, pH 8 containing 0.5 M KCl, 0.1 % Triton X-100, 10 % glycerol, 5 mM imidazole and 0.1 mg/ml PMSF) and lysed by sonication (power level 4, 50 % duty cycle) in an ice-bath for 10 minute, in 1 minute steps. The lysate was centrifuged at 15,000 g

and 4 °C for 30 min and the resulting supernatant was loaded onto an iminodiacetic acid (IDA) sepharose column that was charged with NiCl₂ and pre-equilibrated with lysis buffer. The IDA sepharose was prepared by cross linking IDA with oxirane activated Sepharose 6B as described by Sundberg and Porath [125]. The loaded column was washed with lysis buffer until the absorbance at 280 nm reached the baseline, followed by washing with 5 column volumes of wash buffer (lysis buffer containing 5 mM imidazole, without Triton X-100 and glycerol). The protein was then eluted by applying a gradient of 10 to 150 mM imidazole and stored with 1 mM EDTA until further processing. The presence of pure 6His-*HsMetAP* in the collected fractions was confirmed by SDS-PAGE and such fractions were pooled and dialyzed into storage buffer (25 mM HEPES pH 8 containing 150 mM, KCl and 5 mM methionine). The protein was then stored in aliquots at -80 °C.

4.1.3. Cloning, expression and purification of *EcMetAP*

In order to remove the C-terminal 6His-tag (as well as the accompanying thrombin cleavage site) from *EcMetAP*-6His and introduce an N-terminal 6His-tag with a TEV cleavage site, the *EcMetAP*-6His gene from the pET28 expression vector (obtained from *E. coli* BL21-DE3 Gold cells as provided by Dr. Anthony Adlagatta and Dr. Brian Matthews) was subcloned into a pLIC vector provided by Dr. Stephen Bottomley. The overall process was accomplished via the ligation independent cloning method as described by Cabrita et al. [126]. Plasmid DNA from the above clone was extracted and the *EcMetAP* sequence was amplified by PCR using the oligonucleotides 5'-CCAGGGAGCAGCCTCGATGGCTATCTCAATCAAGACC-3' and 5'-GCAAAGCACCGGCCTCGTTATTCGTCGTGCGAGATTATCG-3' as the forward and reverse primers respectively. The PCR product was purified using QIAquick[®] spin columns and treated with T4 DNA Polymerase (1U/0.1 pmol) and 2.5 mM dATP at 22 °C for

30 min, followed by a 20 min heat inactivation step. The pLIC vector was similarly treated but with 2.5 mM dTTP. In the annealing step 1 μ l of treated vector was mixed with 2 μ l of treated PCR product and incubated at RT for 1 hour followed by addition of 1 μ l of 25 mM EDTA pH 8 and further incubation for 5 min. The annealed vector was then transformed into DH5 α [™] competent cells. The cells were plated on nutrient agar plates containing 0.1 mg/ml ampicillin and the resulting colonies of transformed clones were stored as glycerol stocks at -80°C . Plasmid extracted from the transformed DH5 α [™] cells was then transformed in to competent *E. coli* BL21-DE3 Gold cells. Expression and purification of 6His-*EcMetAP* was carried out as described in section §4.1.1. Purified 6His-*EcMetAP* was treated with 6His tagged TEV protease (see section §4.1.6) at 4°C for 2 days and the tag free *EcMetAP* was repurified by passing through a Ni-IDA column. Pure *EcMetAP* was eluted in the load flow through and was concentrated and stored in aliquots at -80°C .

4.1.4. Expression and purification of *EcPDF*

EcPDF was expressed and purified from *E. coli* BL21-CodonPlus[®] DE3(RIL) clones containing pT7HMT-PDF_{Ec} plasmid as described by Berg et al. [107]. 5 ml nutrient media containing 100 μ g/ml ampicillin and 30 μ g/ml chloramphenicol were inoculated with glycerol stock of the above clone and incubated at 37°C for 16 hours. The starter cultures were inoculated into 1 L of media with the above antibiotics and incubated at 37°C until the cultures reached an OD₆₀₀ of 0.5. Expression of the enzyme was induced by adding 1 mM IPTG and the cells were allowed to grow overnight at RT. The next day, the cells were harvested by centrifugation at 10,000 *g* and 4°C for 30 min. The pellets were resuspended in lysis buffer containing 50 mM HEPES pH 7.5, 20 mM NiCl₂ and 0.1 mg/ml PMSF and lysed by sonication. The lysate was centrifuged and the supernatant was dialyzed overnight at 4°C against lysis buffer

without PMSF. Precipitate formed during dialysis was removed by centrifugation. The supernatant was loaded onto a Fractogel TMAE column and washed with buffer containing 50 mM HEPES pH 7.5, 25 mM KCl and 5 mM NiCl₂. The protein was eluted using a KCl gradient from 20 to 200 mM. Fractions containing pure protein were identified by SDS-PAGE, then pooled, concentrated and dialyzed at 4 °C into storage buffer (50 mM HEPES pH 7.5 and 2 mM NiCl₂) and stored at 4 °C for immediate or at -20 °C for later use.

4.1.5. Cloning, expression and purification of *EcPDF-CΔ21*

The truncated protein *EcPDF-CΔ21* was obtained by deleting the coding region for the 21 amino acid C-terminal helix Pro149 – Ala169 and cloning the truncated gene into a pLIC vector. The truncation mutation was achieved by inserting a stop codon after Ser148 using the oligonucleotides 5'-CCAGGGAGCAGCCTCGATGTCAGTTTTGCAAGTGTTAC-3' and 5'-GCAAAGCACCGGCCTCGTTATGACAGATAATCCATAAACAGTTTG-3' as the forward and reverse primers respectively to amplify the *EcPDF* gene (from the plasmid described above) by PCR. The PCR product was purified using QIAquick[®] spin columns and treated with T4 DNA Polymerase (1U/0.1 pmol) and 2.5 mM dATP at 22 °C for 30 min, followed by a 20 min heat inactivation step. pLIC vector containing N-terminal MBP tag with TEV cleavage site was similarly treated but with 2.5 mM dTTP. In the annealing step 1 µl of treated vector was mixed with 2 µl of treated PCR product and incubated at RT for 1 hour followed by addition of 1 µl of 25 mM EDTA pH 8 and further incubation for 5 min. The annealed vector was then transformed into DH5α[™] competent cells. The cells were plated on nutrient agar plates containing 0.1 mg/ml ampicillin and the resulting

colonies of transformed clones were stored as glycerol stocks at -80°C . Plasmid extracted from the transformed DH5 α^{TM} cells was then transformed in to competent *E. coli* BL21-DE3 Gold cells.

Transformed *E. coli* BL21-DE3 Gold clones were inoculated into 5 ml of LB media containing 0.1 mg/ml ampicillin and grown at 37°C for 16 hours. The starter cultures were used to inoculate 1 L of media and incubated in a shaker at 37°C for 4 - 6 hours. Expression of the protein was induced by adding 1 mM IPTG and the cells were allowed to grow overnight at RT. The cells were then harvested by centrifugation at 10,000 *g* and 4°C for 30 min. The pellets were resuspended in lysis buffer (50 mM, HEPES pH 7.5 containing 2 mM NiCl_2 and 0.1 mg/ml PMSF) and lysed by sonication (power level 4, 50 % duty cycle) in an ice-bath for 10 minute, in 1 min steps. The lysate was centrifuged at 15,000 *g* and 4°C for 30 min and the resulting supernatant was loaded onto an amylose resin column pre-equilibrated with lysis buffer without PMSF. The column was washed with buffer containing 50 mM HEPES, pH 7.5 containing 2 mM NiCl_2 and 10 mM maltose until the absorbance of the eluent at 280 nm returned to baseline. The protein was eluted with buffer containing 100 mM maltose. The eluted protein was reloaded onto a fresh amylose resin column and the process was repeated once more to obtain pure MBP-*EcPDF-C Δ 21* which was confirmed by SDS-PAGE. The purified MBP-*EcPDF-C Δ 21* was treated with TEV protease to cleave the MBP tag and the tag was removed by running the mixture through an amylose resin column. The protein eluting with the load flow through was reloaded on to a fresh amylose resin column and pure *EcPDF-C Δ 21* was collected in the load flow through. Purity was confirmed by SDS-PAGE and the samples were stored at -80°C .

4.1.6. Expression and purification of TEV protease

TEV protease containing N-terminal 6His tag was expressed and purified from *E. coli* BL21-DE3 cells containing the pRK792 expression vector. The cells were grown in LB media containing 100 µg/ml ampicillin and expression was induced with 1 mM IPTG. After overnight growth at RT, the cells were pelleted by centrifugation at 10,000 *g* and 4 °C for 30 min. The pellets were resuspended in lysis buffer (50 mM HEPES pH 8, 100 mM NaCl and 1 mM TCEP) and lysed by sonication. The lysate was centrifuged and the supernatant was loaded onto an IDA-sepharose column charged with Ni²⁺ and pre-equilibrated with lysis buffer. The column was washed with lysis buffer containing 15 mM imidazole and the protein was eluted using a linear gradient of imidazole from 15 to 250 mM. Fractions containing pure TEV were identified by SDS-PAGE and pooled and dialyzed into buffer containing 20 mM HEPES pH 8, 100 mM NaCl, 1 mM TCEP and 0.5 mM EDTA. The protein was stored at 4 °C for immediate use.

4.1.7. Purity and yield of proteins

The level of expression of each of the above proteins and their purity during each stage of purification was qualitatively determined by SDS-PAGE (ref). A resolving gel of 12 % acrylamide (acrylamide:bisacrylamide, 1:30) prepared in 1.5 M Tris, pH 8.8 and a stacking gel of 4 % acrylamide prepared in 0.5 M Tris, pH 6.8 were used, both containing 0.1 % SDS. Samples were dissolved in loading dye (100 mM Tris, pH 6.8 containing 25 % glycerol, 10 % SDS, 5 mM β-mercaptoethanol and 0.015 % bromophenol blue) and heated in a boiling water-bath for 10 min before loading. The gels were run at 200 V in Tris-glycine buffer (25 mM Tris, 190 mM glycine and 0.1 %, pH 8.3 and then stained with 0.1 % Coomassie blue solution (10 % acetic acid and 10 % methanol) at 37 °C for 15 min. Destaining was carried out by a solution of 10 % acetic

acid and 40% methanol. Protein estimation was carried out in 96 well micro-titre plates by the Bradford method [127] with BSA as the standard. 2 - 10 μ l of protein sample was mixed with 200 μ l of 1:5 diluted Bradford reagent and the absorbance was measured at 595 nm. The sample was compared with the BSA standards in the range of 0.05 - 0.5 mg/ml and the molar concentrations were determined using the molecular masses listed below.

4.1.8. Determination of metal content of proteins

The Zn^{2+} content of *EcPDF* and *EcPDF-C Δ 21* samples was determined by inductively coupled plasma mass spectrometry at the University of Georgia Chemical Analysis Laboratory (Athen, GA). Two samples of each protein were prepared by dialyzing against 20 mM HEPES pH 7.2 containing 20 mM KCl, with and without 2.5 mM NiCl_2 . A sample of *EcPDF-C Δ 21* was also prepared by dialyzing against the above buffer containing NiCl_2 followed by a heat treatment of 60 °C for 150 min using a thermal cycler, then incubating overnight at 4 °C. Dialysate buffers were used as blanks and the protein concentrations of the samples were determined by the Bradford method prior to analysis. The concentration of Zn^{2+} in the samples was determined in units of part-per-billion which was then converted to units of μ M and mole fraction of protein.

4.2. Electronic Spectroscopic Characterization

4.2.1. Circular dichroism studies of peptide deformylases

Circular dichroic (CD) spectra of PDFs were measured on a J-710 spectropolarimeter (Jasco, Tokyo, Japan) using a 1 mm path-length quartz cuvette. 150 μ l samples of 10 - 20 μ M enzyme were prepared in 5 mM HEPES buffer, pH 7.5 containing 2 mM NiCl₂.

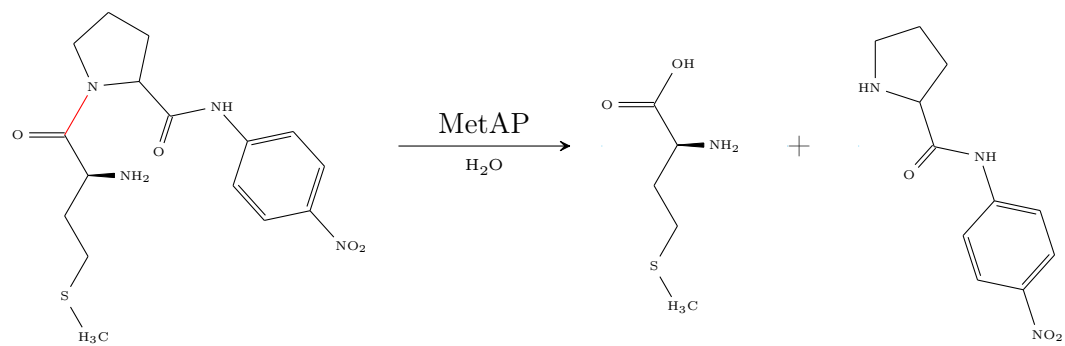
4.3. Steady State Kinetic Methods

4.3.1. The coupled assay for methionine aminopeptidase

The coupled assay for measuring the activity of methionine aminopeptidases was carried out as described by Zhou et al. [85] (see Scheme 4.1). Methionine from the substrate Met-Pro-*p*-nitroaniline was cleaved by MetAP, followed by cleavage of proline by proline aminopeptidase (ProAP). The free *p*-nitroaniline thus generated was quantified over time by its absorbance at 405 nm.

The assays were monitored either by a Lambda 3B spectrophotometer (Perkin-Elmer, Waltham, MA) using a 1 cm path-length cuvette, or a SpectraMax[®] Plus³⁸⁴ absorbance microplate reader (Molecular Devices, Sunnyvale, CA) using a flat bottom 96-well microtitre plate. A typical assay (0.1 ml in a 96-well plate or 1 ml in a cuvette) was carried out in 50 mM HEPES buffer, pH 7.5 containing 100 mM NaCl, 100 μ M CoCl₂, 400 μ M Met-Pro-*p*NA and 1U/ml ProAP. The assay was initiated by the addition of 1 μ M MetAP and monitored for up to 40 min. The initial rate of the

Primary Reaction:

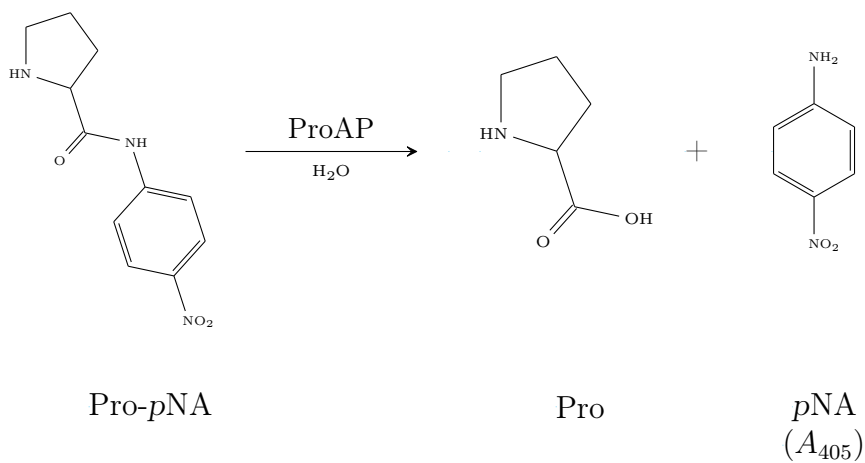


Met-PropNA

Met

Pro-pNA

Secondary Reaction:



Pro-pNA

Pro

pNA
(A_{405})

Scheme 4.1. Coupled spectrophotometric assay for MetAP.

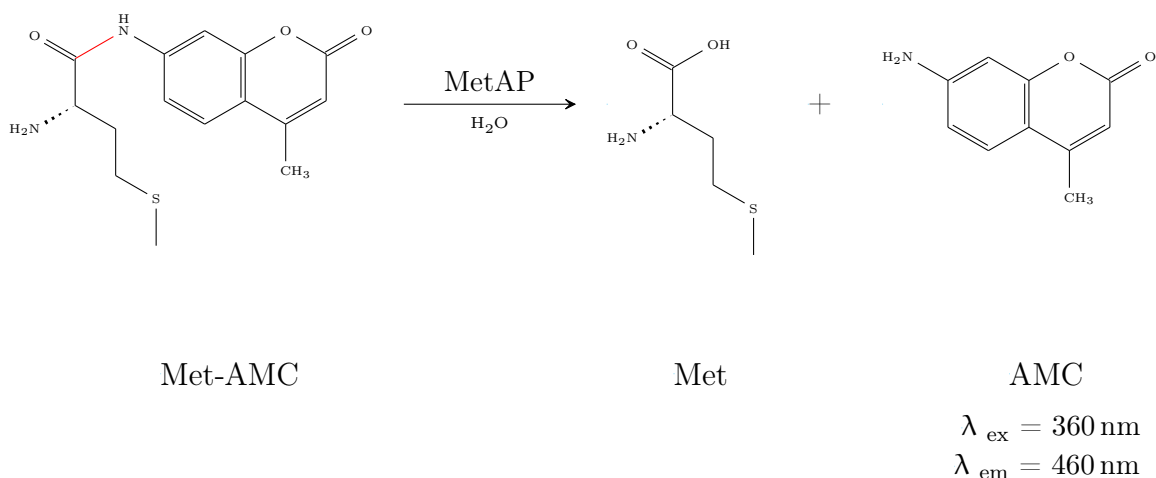
reaction was determined from the slope of the linear region of the progress curve. A standard curve plot (absorbance vs. concentration) of the product (pNA) was used to convert the units of the slope (Abs/min) into units of $\mu\text{M}/\text{min}$.

4.3.2. The direct assay for methionine aminopeptidase

The direct assay for measuring the activity of MetAP was carried out using the fluorogenic substrate Met-7-amino-4-methylcoumarin (Met-AMC) as described in Scheme 4.2. The assays were monitored at 460 nm ($\lambda_{\text{ex}} = 360 \text{ nm}$) by a Gemini[™] EM fluorescence plate reader (Molecular Devices, Sunnyvale, CA) using either 96-well or 384-well microtitre plates in a top-read configuration. A typical assay (100 μl in a 96-well plate or 75 μl in a 384-well plate) was carried out in 50 mM HEPES buffer, pH 7.5 containing 100 mM NaCl, 10 μM CoCl_2 and 100 μM Met-AMC. The assay was initiated by the addition of 1 μM MetAP and monitored for up to 40 min. The initial rate of the reaction was determined from the slope of the linear region of the progress curve. A standard curve plot (fluorescence vs. concentration) of the product (AMC) was used to convert the units of the slope (RFU/min) into units of $\mu\text{M}/\text{min}$.

4.3.3. The coupled assay for peptide deformylase

The activity of native and truncated PDFs was measured using the coupled assay reported by Wei and Pei [61] (see Scheme 4.3. The formyl group from the substrate fMet-Leu-pNA was cleaved by PDF followed by sequential removal of methionine and leucine by leucyl aminopeptidase from *Aeromonas proteolytica* (AAP). The assays were monitored at 405 nm by the SpectraMax[®] Plus³⁸⁴ absorbance plate reader using 96-well microtitre plates. A typical assay of 100 μl was carried out in 25 mM HEPES buffer, pH 7.5 containing 100 mM KCl, 2 mM NiCl_2 , 0.1 mg/ml BSA, 10U/ml AAP and 100 μM fMet-Leu-pNA. The assay was initiated by addition of PDF and



Scheme 4.2. Direct fluorometric assay for MetAP.

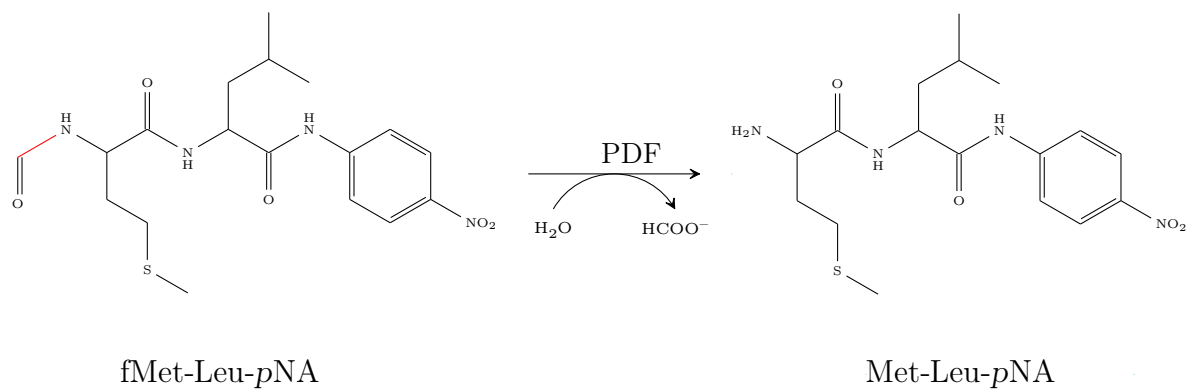
monitored for upto 20 min. The initial rate of the reaction was determined from the slope of the linear region of the progress curve. A standard curve plot (absorbance vs. concentration) of the product (*p*NA) was used to convert the units of the slope (Abs/min) into units of $\mu\text{M}/\text{min}$.

4.3.4. Determination of the kinetic parameters

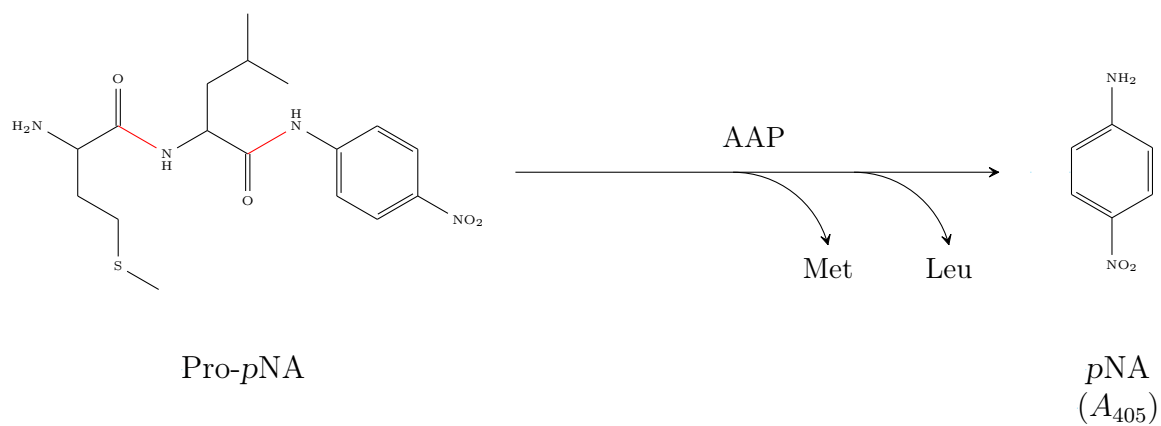
The kinetic parameters K_m and k_{cat} of the above enzyme catalyzed reactions were determined by measuring the reaction rate with varying substrate concentrations. The initial rates were plotted as a function of substrate concentration and the data were analyzed either by the standard Michealis-Menten equation

$$v = \frac{V_{\text{max}}[S]}{K_m + [S]} \quad (1)$$

Primary Reaction:



Secondary Reaction:



Scheme 4.3. Coupled spectrophotometric assay for PDF.

where V_{\max} is the maximum steady-state rate, $[S]$ is the substrate concentration, K_m is the apparent binding constant of the substrate to the enzyme and v is the initial rate at the substrate concentration $[S]$, or by the modified equation incorporating substrate inhibition

$$v = \frac{V_{\max}[S]}{K_m + [S] \left(1 + \frac{[S]}{K_{mi}}\right)} \quad (2)$$

where K_{mi} is the apparent binding constant of the substrate to the enzyme other than at the active site. The data analysis was performed by non-linear regression using either GraFit 4.12 (Erithacus Software, London, UK) or Origin 7.5 (OriginLab, Northampton, MA) softwares. The value of k_{cat} was obtained from the relationship

$$k_{\text{cat}} = \frac{V_{\max}}{[E]_t}$$

where $[E]_t$ is the enzyme concentration in the assay.

4.3.5. Steady state experiments to study the inhibition of methionine aminopeptidases

Screening of inhibitors for MetAPs was carried out using the coupled assay described in section §4.3.1. The assays were conducted in 96-well plates in the presence of 10 μM inhibitors with a control assay without any inhibitor. The reactions were initiated (simultaneously in each plate column) by addition of the enzyme using a multi-channel pipette. The inhibitors that reduced the activity by 50% or more (as compared to the control) were retested as potential inhibitors of the enzymes.

The inhibition constant (K_i) of the potential inhibitors was determined by measuring the activity of the enzyme in the presence of a range of concentrations of the inhibitor. The data were analyzed by non-linear regression using the equation described by Banerjee et al. [128]

$$v = \frac{V_0 K_i}{K_i + [I]_t - \frac{1}{2} \left(([I]_t + [E]_t + K_i) - \sqrt{([I]_t + [E]_t + K_i)^2 - 4[I]_t[E]_t} \right)} \quad (3)$$

where V_0 is the steady-state rate in the absence of inhibitor, $[I]_t$ and $[E]_t$ are the total inhibitor and enzyme concentrations, K_m and K_i are the apparent binding constants of the substrate and inhibitor to the enzyme and v is the initial rate at the inhibitor concentration $[I]_t$.

4.4. Characterization of *EcMetAP* Inhibition by Cyclodextrin

4.4.1. Steady-state experiments to determine the inhibition model

For inhibition studies, the enzyme activity was measured using the direct assay in the presence of varying concentrations of the substrate (10 – 800 μ M) and CD (0 to 12 mM). The mode of inhibition was determined by assaying the enzyme activity as a function of inhibitor as well as substrate concentrations. The data were analyzed by non-linear regression using Dynafit 3 (BioKin Ltd., Watertown, MA) software [129] which also utilized model discrimination analysis on the basis of Akaike weight [130] to delineate the most probable mechanism of inhibition.

4.4.2. Determination of the CD-MetAMC complex crystal structure

For crystallization of CD-MetAMC complex, 1 mmol solutions of β -cyclodextrin (β -CD) and MetAMC were prepared in water and ethanol, respectively. The solutions were slowly mixed and heated to 60 °C and maintained the temperature for 2 hours. This was followed by slowly cooling the reaction mixture which resulted in the formation of the β -CD-MetAMC crystal. Single crystal X-ray diffraction data set was collected on a Bruker Apex Duo diffractometer (I μ S microfocus Cu-radiation) with an Apex 2 CCD area detector. The structure was solved by direct methods and refined on F2 using Apex 2 v2010.9-1 software package, after integration with SAINT v7.68A and multi-scan absorption correction.

4.4.3. Molecular modelling studies

The docking studies of CD bound Met-AMC to EcMetAP were carried out using the software Autodock Vina 1.1.1 [131]. EcMetAP crystal structure from PDB (2GTX) [80] was used as the model for the enzyme. MetAMC structure was produced in GaussView 5.0 [132] or used from the data obtained above. β -cyclodextrin crystal structure from PDB (1Z0N) [133] or from the crystallography data described above was used as the model for CD as is. Alternatively, 2-hydroxypropyl- β -cyclodextrin was generated by adding hydroxypropyl chains to the CD crystal structure. The docking input files were prepared using AutoDock Tools 1.5.6rc1 [134]. Solvent molecules from the crystal structure were deleted along with additional macromolecule chains (chain B). Hydrogens and Gastieger charges were added to the protein molecule which was saved in the PDBQT file format. The search space for the docking was set with a grid box of 28x28x26 Å centered over the enzyme active site, for docking the CD-MetAMC complex to EcMetAP. The docking was run with an exhaustiveness parameter of 50. Molecular dynamics simulations were conducted with the all-atom CHARMM22

force field [135] in NAMD 2.8 [136]. Input files for the MD simulations were prepared using VMD 1.9.1 [137]. The topology and parameter files for CD and MetAMC were generated using SWISS-PARAM [138]. In a typical setup the protein backbone atoms were set as fixed, the molecules were solvated in a water sphere with a padding of 15 Å using the TIP3P water model, and ions (Na^+ and Cl^-) were added at a concentration of 100 mM NaCl. The simulation was run with spherical boundary conditions at 300 K (with Langevin dynamics) for up to 250 ps, with 1 fs time steps. Non-bonded interactions were cut-off at 12 Å using a switching function at 10 Å and the bond-lengths and bond-angles of water molecules were constrained using the SHAKE algorithm. The equilibration of the systems was confirmed by RMSD analysis [139] and calculation of internal as well as interaction energies.

4.5. Metal-ion Binding Studies of *EcMetAP*

4.5.1. Luminescence spectra of lanthanides

The luminescence experiments involving Eu^{3+} were carried out on a Quantamaster life-time spectrofluorometer (PTI, Birmingham, NJ), configured with both pulsed Xenon and LED as excitation sources. The Eu^{3+} luminescence spectra were acquired using the pulsed Xenon as the excitation source with $\lambda_{\text{ex}} = 295$ nm, $\lambda_{\text{em}} = 525$ to 625 nm, and a high bandpass cutoff filter of 340 nm. To eliminate the fluorescence signal of the protein, a "gate time" of 150 μs was applied. The signal quality was improved by integrating over 2150 μs and averaging 10 spectra. All experiments were carried out in the assay buffer containing 3.6 μM *EcMetAP*. The binding affinity of Eu^{3+} to the enzyme was measured by titrating EuCl_3 into apo-*EcMetAP* and plotting the increase in luminescence intensity ($\lambda_{\text{ex}} = 295$ nm, $\lambda_{\text{em}} = 614$ nm) as a function

of the metal ion concentration. A control experiment was performed in the absence of MetAP, and the data were subtracted from the binding experiment to correct for background luminescence of free europium. The binding data were analyzed by a complete solution of the underlying quadratic equation (Eq. (4)) as described by Wang et al. [140]:

$$L = C * \frac{\left(([M] + K_d + n[E]_t) - \sqrt{([M] + K_d + n[E]_t)^2 - 4n[E]_t} \right)}{2} \quad (4)$$

Where L , C , $[M]$, n and $[E]_t$ represent the luminescence signal, total change in signal, metal ion (Eu^{3+}) concentration, stoichiometry of the enzyme- Eu^{3+} complex and total enzyme concentration, respectively.

4.5.2. Determination of metal-ion binding affinity by displacement of europium from MetAP

The binding affinities of various metal ions to *Ec*MetAP were determined by titrating the enzyme- Eu^{3+} complex ($3.6 \mu\text{M}$ *Ec*MetAP and $50 \mu\text{M}$ EuCl_3) with different metal ions and measuring the decrease in the luminescence intensity (due to competitive displacement of Eu^{3+} from the enzyme's active site) as a function of the metal ion concentration. The data were analyzed by a modified form of the competitive binding model (Eq. (5)) as described by Banerjee et al. [128]

$$L = \frac{L_c}{[E]_t} ([E]_t - [EM]) + \text{offset}$$

where $[EM] = [E]_t + [M]_t + K_d + (K_d/K'_d) [\text{Eu}^{3+}]$

$$- \frac{\sqrt{([E]_t + [M]_t + K_d + (K_d/K'_d) [\text{Eu}^{3+}])^2 - 4[E]_t[M]_t}}{2} \quad (5)$$

Where L_c is the total change in luminescence signal (L) upon complete displacement of Eu^{3+} from the active site, $[E]_t$, $[M]_t$ and $[\text{Eu}^{3+}]$ are the concentrations of the enzyme, the displacing metal ion, and Eu^{3+} respectively, while K_d and K'_d are the dissociation constants of displacing metal ion and Eu^{3+} respectively.

4.5.3. Determination of metal-ion activation constant

The activity of various metalloforms of *EcMetAP* was measured using the direct assay system described in section §4.3.2. The enzyme assay was performed at RT in 50 mM HEPES buffer, pH 7.5, containing 100 mM NaCl, 400 μM substrate, and varying concentrations of metal salts (total volume = 200 μl) in 96 well plates. The enzymatic reaction was initiated by addition of appropriately diluted *EcMetAP*, and the reaction progress was monitored for 30 min at 460 nm ($\lambda_{\text{ex}} = 360$ nm). The slope of the linear region of the reaction trace was taken as the measure of the initial rate of the enzyme catalyzed reaction. The activation constants (K_a 's) of metal ions for the enzyme were determined from the plots of the initial rates of the enzyme catalysis as a function of metal concentrations, and the data were analyzed by applying the quadratic equation Eq. (4) described earlier, as follows:

$$v = C * \frac{\left(([M] + K_a + n[E]_t) - \sqrt{([M] + K_a + n[E]_t)^2 - 4n[E]_t} \right)}{2} \quad (6)$$

Where v , C , M , n and $[E]_t$ represent the signal (initial rate), change in signal (maximal increase in rate at saturating concentration of the metal ions), metal ion concentration, stoichiometry of the enzyme-metal complex and total enzyme concentration respectively.

4.6. PDF Stability Studies

4.6.1. Heat inactivation of peptide deformylase

Aliquots of PDF prepared in assay buffer (25 mM HEPES buffer, pH 7.5 containing 100 mM KCl and 2 mM NiCl₂) were divided in 0.5 ml microcentrifuge tubes and incubated at 60 °C in a water bath or thermal cycler. The different aliquots were incubated for varying periods of time, ranging from approximately 1 min to 3.5 h, after which they were incubated at 4 °C overnight. The aliquots were then added to a 96-well plate and the activity of the enzyme was assayed by adding 100 μM substrate (fMet-Leu-pNA) in the presence of 0.1 mg/ml BSA and 10U/ml AAP. An untreated aliquot maintained at 4 °C was used as the control. The initial velocities, observed in a plate reader as an increase in absorbance at 405 nm, were recorded and plotted as a function of the period of heat treatment.

4.6.2. Thermal unfolding of peptide deformylase

The temperature dependent unfolding of the PDF secondary structure was measured on a Jasco-715 CD spectropolarimeter equipped with a peltier temperature control. The ellipticity (θ) of 15 to 25 μM PDF was measured at 223 nm in 5 mM HEPES buffer, pH 7.5 containing 2 mM NiCl₂ using a 1 mm path-length quartz cuvette. The temperature was ramped from 25 to 90 °C at a rate of 1 °C min⁻¹ and the change in θ_{223} was plotted as a function of temperature. The data were analyzed by a modified sigmoidal (Boltzmann) function

$$\theta_{223} = \frac{A_0 - A_1}{1 + e^{x-p/dx_1}} + \frac{A_1 - A_2}{1 + e^{x-q/dx_2}} + A_2 \quad (7)$$

where A_0 and A_1 are the baseline ellipticity for each phase, p and q are the temperature at unfolding transition (T_m) for each phase, dx_1 and dx_2 are the rates of unfolding at each transition, and A_2 is the final ellipticity after completion of unfolding.

Kinetic unfolding studies were conducted by incubating the enzyme solution at 60°C for up to 2.5 h, with an equilibration time of 30 s. Ellipticity measurements were made as above and plotted as a function of time. The data were analyzed by a double exponential function

$$\theta_{223} = 1 - \left(A_1 e^{-k_1 t} + A_1 e^{-k_2 t} \right) + offset \quad (8)$$

where the rate of unfolding of each phase is given by k_1 and k_2 .

5. RESULTS

5.1. Cloning, Expression and Purification of Methionine Aminopeptidases and Peptide Deformylases

5.1.1. Expression and purification of 6His-tagged methionine aminopeptidases

The 6His-tagged methionine aminopeptidases (MetAPs) were expressed and purified from clones of *E. coli* BL21-Gold (DE3) cells. The clones producing the *E. coli* and human forms of MetAP, contained the genes for kanamycin and ampicillin resistance respectively. The cells were grown in LB media in a batch of 4L, and the cultures reached the recommended OD₆₀₀ of 1.5 in 4 to 6 h. The expression of the enzymes was induced by IPTG and the cells were allowed to grow overnight at room temperature, prior to harvesting by centrifugation. The harvested cells were freeze-thawed to aid in lysis prior to sonication. The cell lysate was loaded onto a freshly prepared 30 ml Ni-IDA column and the purification of the 6His-tagged MetAP was carried out as described in sections §4.1.1 and §4.1.2. Most of the MetAP enzyme was retained on the column as determined by measuring the enzyme activity and SDS-PAGE analysis of the load flow-through fractions. A gradient of 5 to 150 mM imidazole was initially applied to elute both the enzymes. On optimization, it was noted that *Ec*MetAP-6His was eluted by 100 mM imidazole after washing the column with 10 column volumes of wash buffer (50 mM HEPES pH 8, containing 0.5 M KCl, and 5 mM imidazole). On the other hand, the concentration of imidazole at which 6His-*Hs*MetAP eluted varied from batch to batch and the overall process could not be optimized. Therefore a gradient (5 to 100 mM) was used for the elution of 6His-*Hs*MetAP each

time. The eluted enzymes were converted to their apo forms by adding EDTA and dialysing against the storage buffer (25 mM HEPES pH 8, containing 150 mM KCl and 5 mM methionine), then stored at -70°C . However, during the dialysis process, it was observed that a considerable amount of 6His-*HsMetAP* was lost due to precipitation.

The purity of the enzyme preparations was confirmed by SDS-PAGE analysis (Figure 5.1). The *EcMetAP* and *HsMetAP* bands corresponded to the molecular mass of 29 kDa and 43 kDa respectively, as expected.

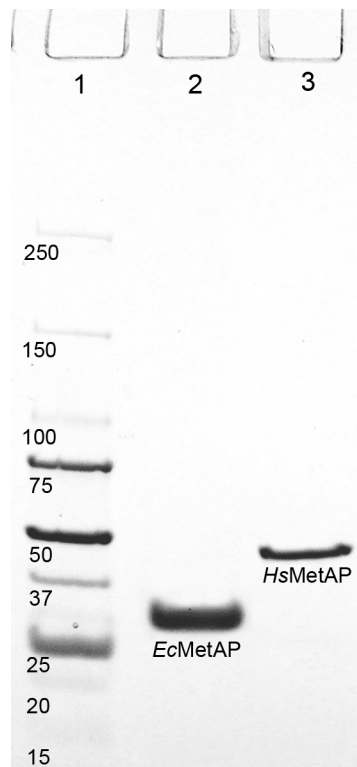


Figure 5.1. SDS-PAGE analysis of purified MetAPs. The bands in lane 1 represent the protein standard with the molecular sizes given in kDa. The bands in lanes 2 and 3 represent the purified 6His-tagged *EcMetAP* and *HsMetAP* respectively.

Protein estimation of the purified enzymes was carried out by the Bradford method using BSA as the standard (see Figure 5.2). An initial comparison of protein estimation results for *EcMetAP*-6His from the Bradford (with BSA and IgG standards)

and BCA (with BSA standard) methods indicated that both methods yielded similar results. On the other hand it was found that the estimation of 6His-*HsMetAP* by the Bradford method using BSA as the standard was two times higher than that obtained either by using IgG as the standard, or by estimating using the BCA method. Therefore the protein estimation results of 6His-*HsMetAP* obtained by the Bradford method (with BSA standards) were modified by a factor of 0.5. Yields of up to 90 mg of *EcMetAP*-6His and up to 10 mg of 6His-*HsMetAP* were obtained per liter of their respective *E. coli* culture.

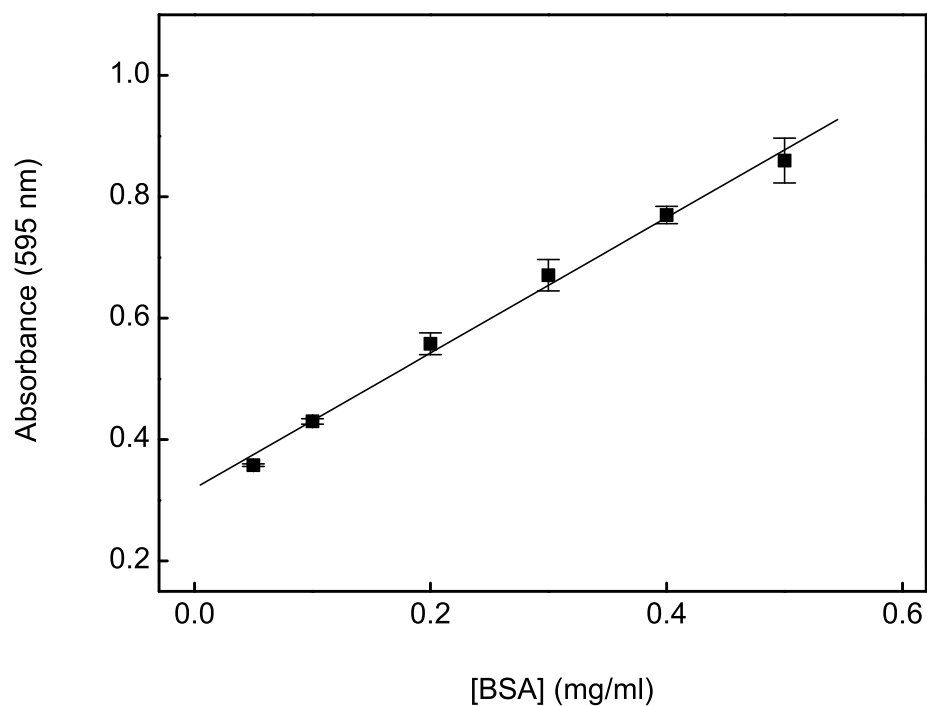


Figure 5.2. BSA standard plot for the Bradford assay. The estimation was carried out using the 'standard procedure for microplate assay' with BSA concentrations of 0.05, 0.1, 0.2, 0.3, 0.4 and 0.5 mg/ml. The data were averaged over four sets and the linear fit represents an R^2 value of 0.997.

5.1.2. Cloning, expression and purification of native *EcMetAP*

The plasmid vector containing the *EcMetAP* coding sequence with a C-terminal 6His tag and thrombin cleavage site was extracted from the *E. coli* clone as described in section §4.1.3. The vector was then used as a template for the PCR amplification of the *EcMetAP* coding sequence with modification to contain a TEV cleavage site. The existing thrombin cleavage site (and the following 6His tag) was removed by introducing a stop codon in the reverse primer. The N-terminal 6His tag and TEV cleavage site were included in the receiving vector (pLIC) cloning site and thus were incorporated at the N-terminal of the amplified *EcMetAP* coding sequence. The plasmid was transformed into competent DH5 α [™] cells, amplified by growing the transformed cells and finally extracted. The purified plasmid was sent for sequencing to confirm the presence of the 6His-*EcMetAP* coding region.

The purified pLIC plasmid containing the 6His-*EcMetAP* coding sequence was transformed into competent *E. coli* BL21-DE3 Gold cells and the transformed cells were grown in LB media containing ampicillin. Expression of 6His-*EcMetAP* was induced by IPTG and purification of the enzyme was carried out on a Ni-IDA column as described in section §4.1.1. The 6His tag was cleaved by treatment with 6His-TEV, and the His-tag free *EcMetAP* was purified by running through a second Ni-IDA column. Estimation of the purified enzyme, as described in section §5.1.1, indicated a net yield of 20 mg of His-tag free *EcMetAP* from one liter of the *E. coli* culture.

5.1.3. Cloning, expression and purification of truncated *EcPDF*

The coding sequence of native *EcPDF* was obtained from the pET20b(+) vector that was previously generated in our lab [64]. The plasmid was expressed and purified from DH5 α [™] clones and used as the template to produce the truncated form of the

coding sequence. Truncation was achieved by introducing a stop codon via the reverse primer at cytosine 445 of the sense strand (the position equivalent to the amino acid Pro149 of the *EcPDF* polypeptide). The forward and reverse primers (section §4.1.5) were designed with overlaps for the pLIC vector containing an N-terminal MBP tag and TEV cleavage site. The truncated sequence obtained from PCR amplification was introduced into the MBP-TEV-pLIC vector which was then transformed into chemically competent DH5 α [™] cells. The transformed cells were grown on LB agar containing ampicillin. The plasmid from the transformed cells was purified and sent for sequencing with the forward and reverse primers to confirm the presence of the MBP-TEV-*EcPDF*-C Δ 21 sequence. Analysis of the sequencing data (Figure 5.4) by BLAST [141] revealed 95% identity with the *E. coli* maltose transporter subunit and 100% identity with the *E. coli* peptide deformylase enzyme.

The plasmid was then transformed into competent *E. coli* BL21-DE3 Gold cells. The transformed cells were grown in LB media containing ampicillin, and expression of *EcPDF*-C Δ 21 was induced by IPTG, in the presence of 2 mM NiCl₂. Purification of the MBP-tagged enzyme was carried out on an amylose resin column as described in section §4.1.5. The MBP tag was cleaved by overnight treatment with TEV and separated from *EcPDF*-C Δ 21 by running the mixture through a second amylose resin column. The purity of the *EcPDF*-C Δ 21 was confirmed by running the sample on SDS-PAGE (see Figure 5.3) which revealed a single band at 17 kDa as expected. The protein content was estimated by the Bradford assay indicating a yield of about 10 mg of MBP-*EcPDF*-C Δ 21 and finally 1 mg of *EcPDF*-C Δ 21 per liter of the *E. coli* culture.

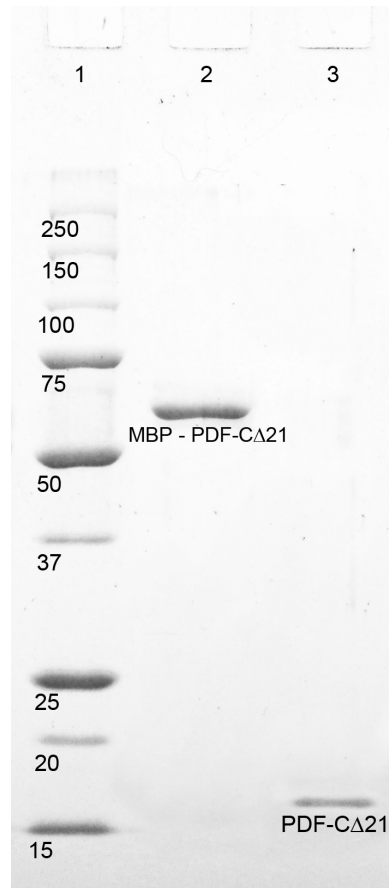


Figure 5.3. SDS-PAGE analysis of purified *EcPDF-CΔ21*. The bands in lane 1 represent the protein standard with the molecular sizes given in kDa. The bands in lanes 2 and 3 represent the purified MBP-tagged *EcPDF-CΔ21* and the purified *EcPDF-CΔ21* after TEV cleavage respectively.

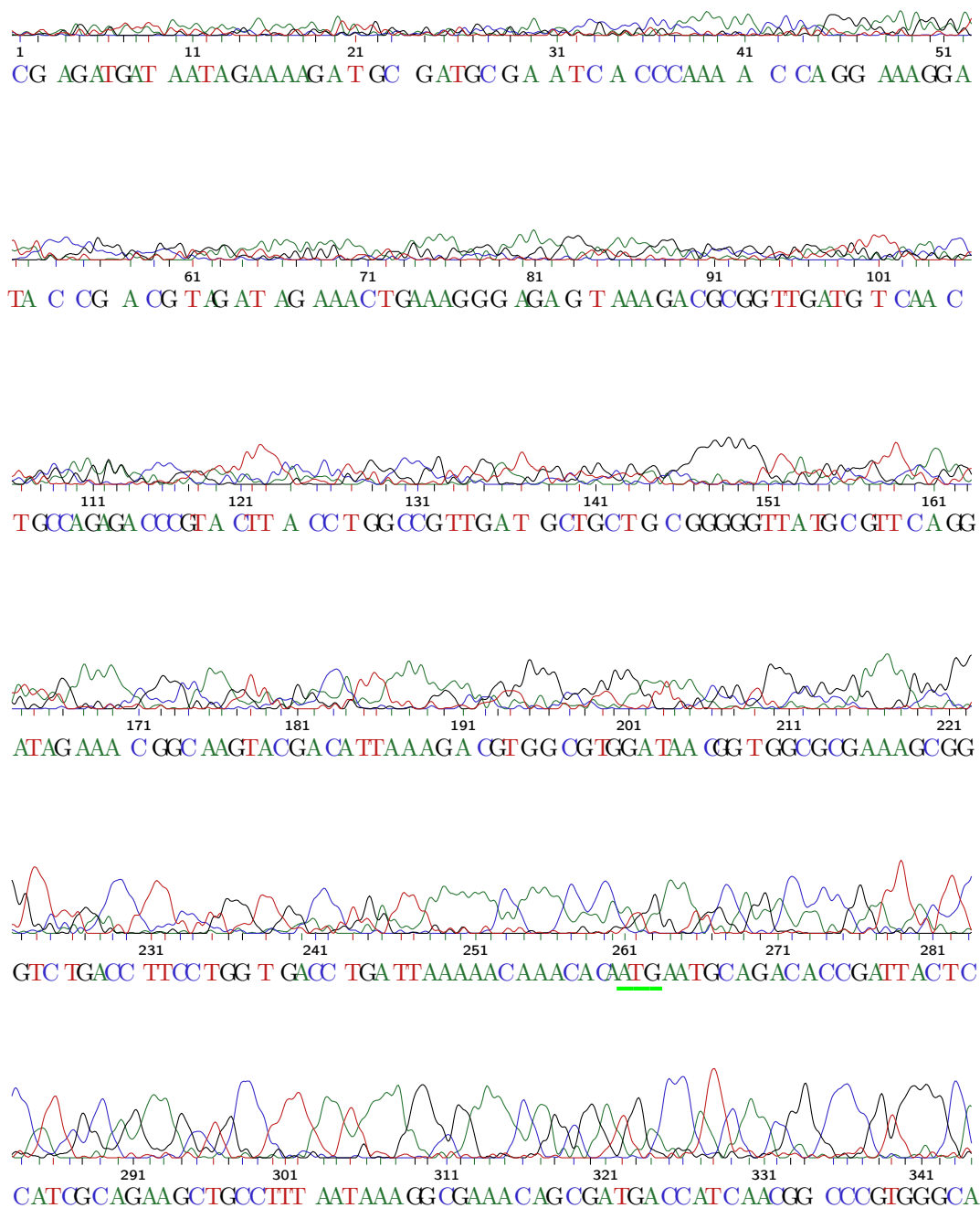


Figure 5.4. DNA sequence of the MBP-TEV-*EcPDF*-C Δ 21 construct. The chromatogram was generated by combining the sequencing data from the forward and reverse primers. The green bar indicates the initiating codon equivalent to Met220 of maltose binding protein (MBP).

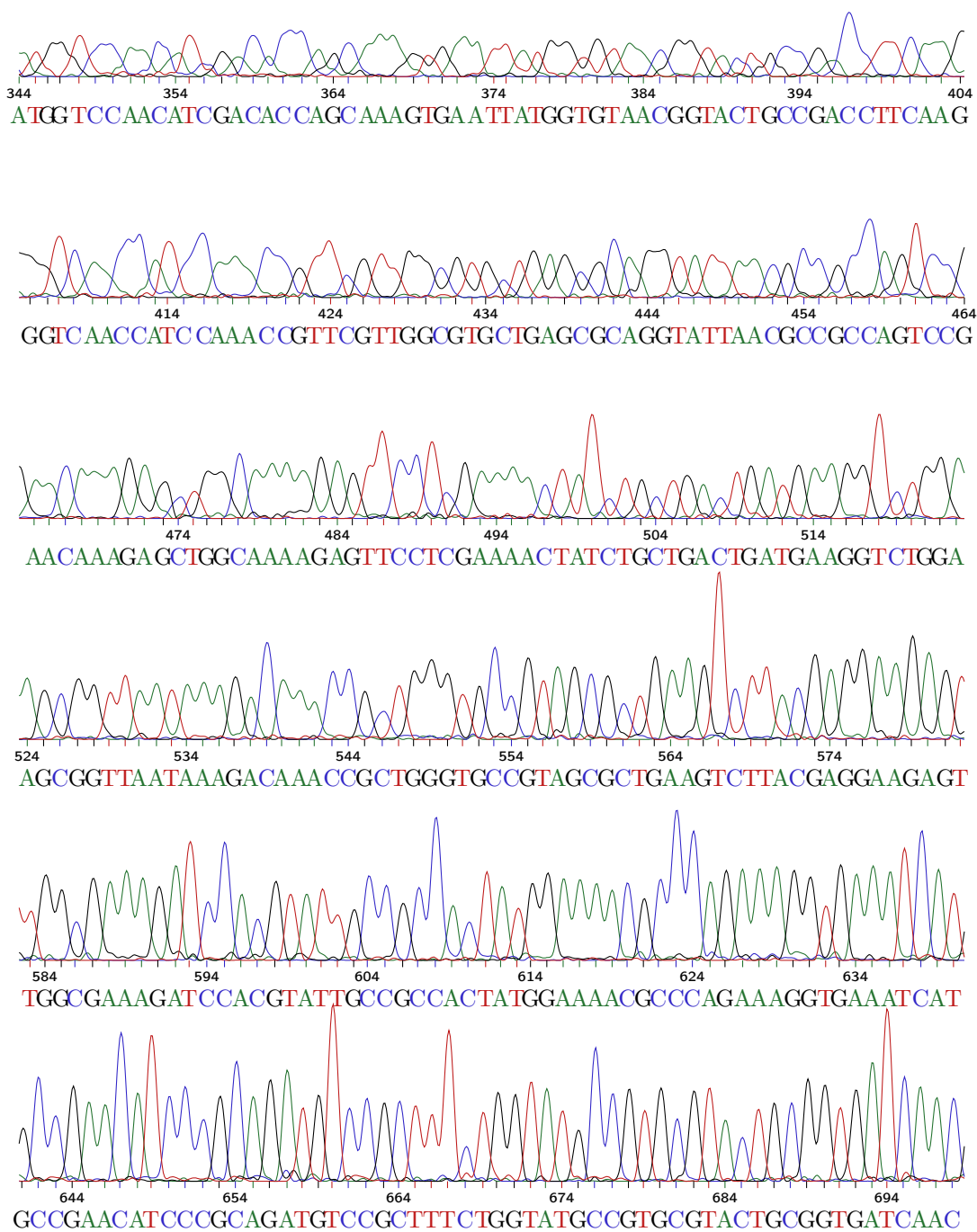


Figure 5.4. (...cont.) DNA sequence of the MBP-TEV-*EcPDF-CΔ21* construct.

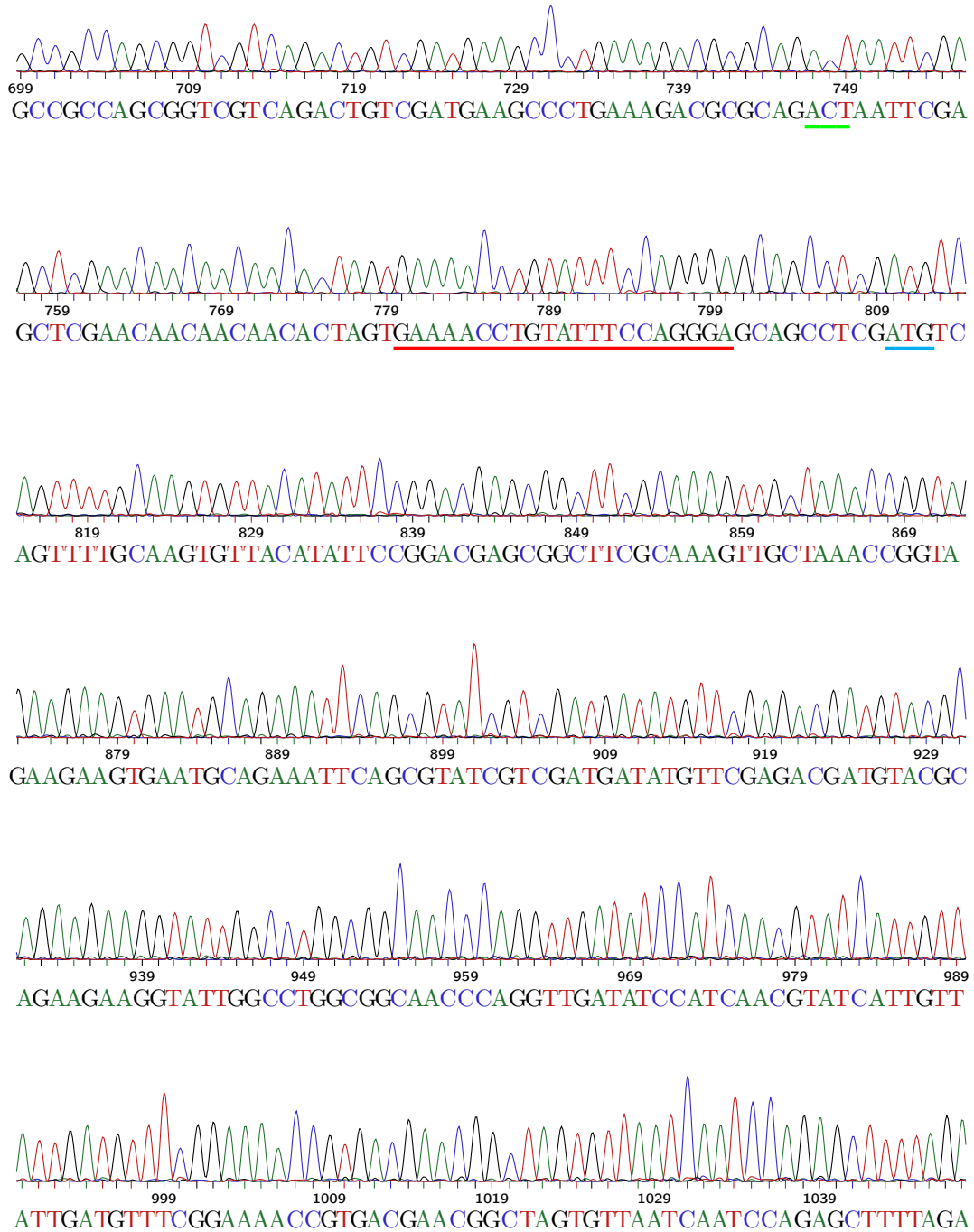


Figure 5.4. (... cont.) DNA sequence of the MBP-TEV-*Ec*PDF-CΔ21 construct. The green bar indicates the last codon of MBP (residue Thr393). The red bar indicates the TEV cleavage site (ENLYFQG). The blue bar indicates the initiating codon for PDF (Met1).

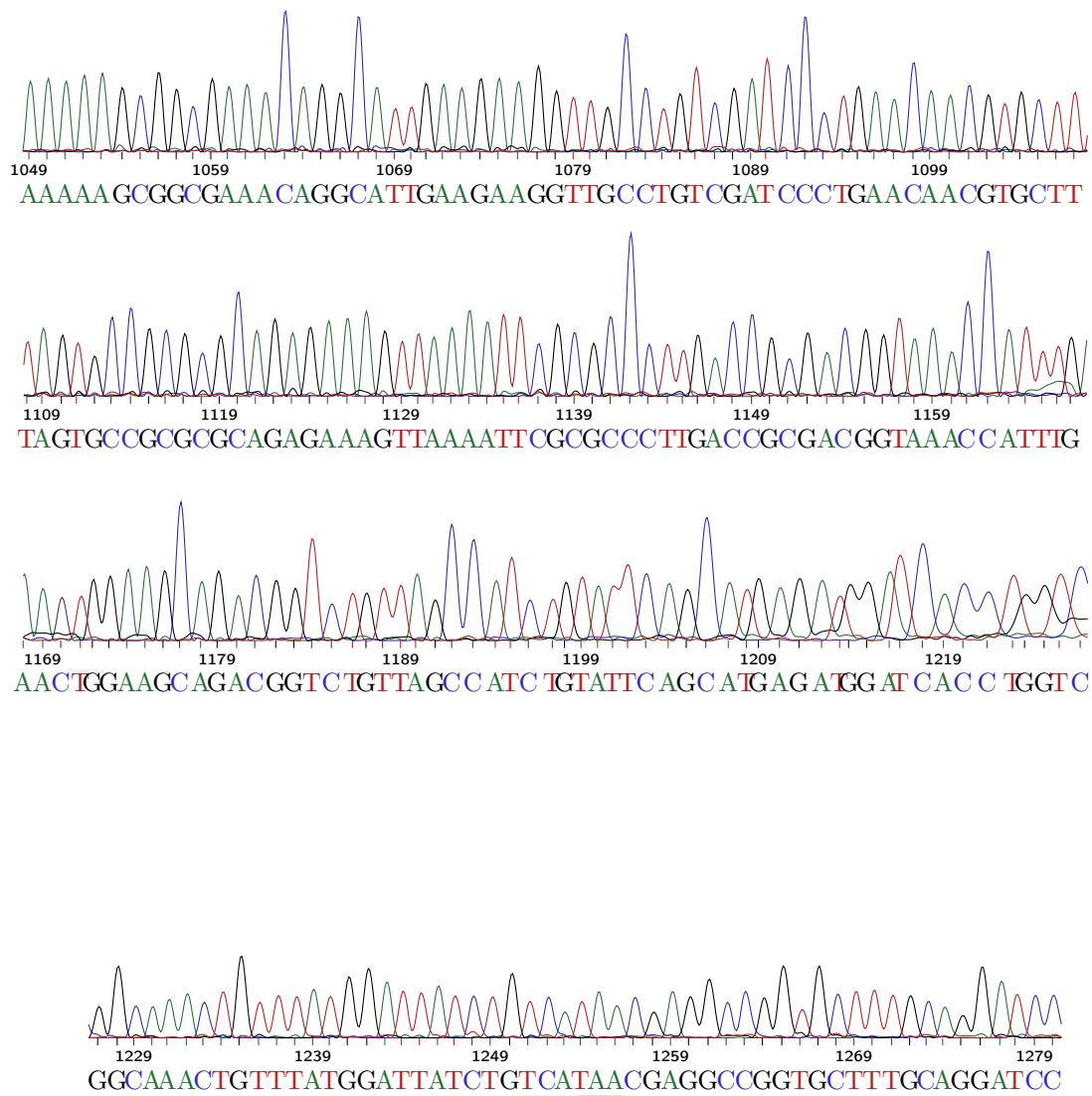


Figure 5.4. (... cont.) DNA sequence of the MBP-TEV-*Ec*PDF-C Δ 21 construct. The blue bar indicates the last codon for the truncated PDF (Ser148). The black bar indicates the termination codon.

5.1.4. Determination of metal content of proteins

The studies with the truncated form of PDF were undertaken to unravel the role of the C-terminal helix in the catalytic activity and stability of the enzyme. However, it is known that the active site metal ion also affects these properties in PDF. Therefore it was necessary to quantify the relative fractions of different metal ions in the purified preparations of the native as well as the truncated form of the enzyme.

Samples of native and truncated PDF prepared in buffer containing NiCl_2 were dialyzed against 5 mM HEPES pH 7.5 with or without 1 mM NiCl_2 . The Ni^{2+} free buffer was prepared by treating with Chelex[®] 100 to remove all contaminating trace metals. The dialysate buffers were used as blanks. The metal content of the samples were determined by the Chemical Analysis Laboratory at the University of Georgia, using ICP-AES analysis.

The results of the analysis are shown in Table 5.1. The Zn^{2+} content in the PDF preparations was found to be surprisingly consistent across the samples. It is interesting to note that the dialysis of both forms of PDF resulted in some loss of bound Zn^{2+} . The Zn^{2+} -bound fraction of PDF appears to exist in two distinct populations characterized by the lability of the metal ion. Thus approximately 60 % of the bound Zn^{2+} was found to be labile while 40 % remained tightly bound to the enzyme. While the analysis also determined the Ni^{2+} content, this was found to be artificially higher than the molar content of enzyme present in the sample, possibly due to an incomplete removal of the Ni^{2+} during dialysis.

Table 5.1. Metal content of PDFs. ¹

Sample	% Zn
<i>Ec</i>PDF	
with 1 mM NiCl ₂	33
dialyzed	13
<i>Ec</i>PDF-CΔ21	
with 1 mM NiCl ₂	33
dialyzed	13

¹ Samples of *Ec*PDF and *Ec*PDF-CΔ21 were either dialyzed against metal free buffer or incubated in buffer containing 1 mM NiCl₂. The Zn content of variously treated samples was analyzed by ICP-AES.

5.2. Electronic Spectroscopic Properties of MetAPs, PDFs and ligands

5.2.1. Absorbance spectra of PDF

From the metal analysis data (Table 5.1), it was clear that some fraction of the purified PDFs contained tightly bound Zn²⁺. However due to the presence of excessive Ni²⁺ in the buffers used, the Ni²⁺ content of the enzymes could not be determined by ICP-AES analysis. The active site Ni²⁺ is known to exhibit a characteristic charge-transfer band at 355 nm due to charge transfer between the active site Cys90 residue and Ni²⁺. This property was exploited by recording the absorbance spectra of the enzymes in an attempt to determine the Ni²⁺ content of the native and truncated PDFs.

The absorbance spectra of 50 μM PDF were measured in 5 mM HEPES buffer pH 7.5 containing 2 mM NiCl₂ and 100 mM KCl. Both native and truncated forms showed the same spectral profile (Figure 5.5). The absorption by aromatic amino acids can be seen by the peak at 280 nm. Note that the Cys90–Ni²⁺ charge-transfer

peak expected to be seen at 355 nm is absent. The absence of the charge-transfer band in spite of maintaining the enzymes in 2 mM NiCl₂ suggests that the enzymes do not contain any Ni²⁺ bound at the active site.

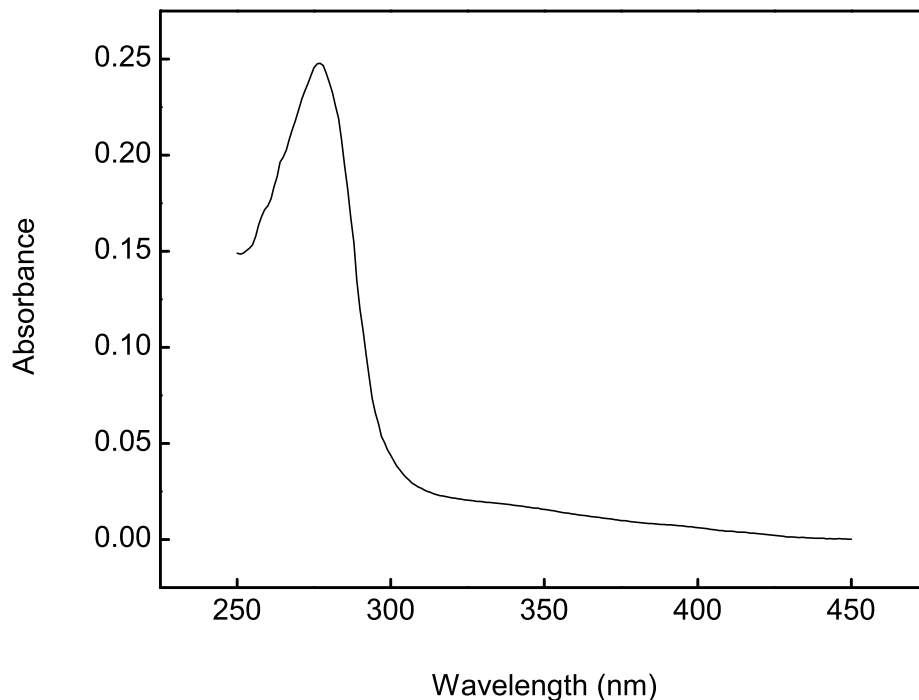


Figure 5.5. *EcPDF* absorbance spectrum. The absorbance spectra of 50 μ M *EcPDF* were measured in 5 mM HEPES buffer pH 7.5 containing 2 mM NiCl₂ and 100 mM KCl. The absorbance of the buffer was subtracted as blank.

5.2.2. Fluorescence spectra of ligands

5.2.2.1. Fluorescence spectra of Met-AMC and AMC

The catalytic activity of MetAPs is customarily measured using either oligopeptide substrates in an end point assay system, or using chromogenic dipeptide substrates in a coupled, continuous assay system [13, 81–83]. In order to avoid the drawbacks of these assay methods as described earlier in section §1.4.2.3, a direct assay using the

fluorogenic substrate methionyl-7-amino-4-methylcoumarin (Met-AMC) was employed. The rate of release of the fluorophore (AMC), upon cleavage by MetAP, is an unequivocal measure of the catalytic reaction of the enzyme. The excitation and emission spectra of Met-AMC and AMC (the substrate and product, respectively, of the MetAP direct assay) were measured to determine the optimum wavelengths for monitoring the release of AMC. Figure 5.6 shows the normalized fluorescence absorption and emission spectra of Met-AMC and AMC. It can be discerned from the spectral data that the excitation and emission wavelengths of in the region of 350 to 370 nm and 430 to 470 nm, respectively, would result in the most optimal signal, based on the comparative ratio of fluorescence intensities of the product (AMC) and substrate (Met-AMC) in these wavelength regions. Test assays with varying wavelengths in the above ranges confirmed that an excitation wavelength of 360 nm and an emission wavelength of 460 nm provided the best signal for the enzyme assay.

The data in Figure 5.7 shows that although the fluorescence intensity was higher by an order of magnitude at 430 nm ($\lambda_{\text{ex}} = 350 \text{ nm}$), the measurement obtained at 460 nm ($\lambda_{\text{ex}} = 360 \text{ nm}$) had much better signal to noise ratio as well as an increased slope, allowing the assays to be conducted with accuracy using a much lower amount of enzyme.

5.2.2.2. Fluorescence spectra of dansylamide-5-(2-chlorophenyl)furanic acid

As discussed in sections §1.4.4 and §1.5, the metal dependent properties of MetAP have not been extensively characterized, and an understanding of the metal and metal-ligand interactions in MetAPs is critical to the development of effective inhibitors of the enzyme. It has been known that 5-(2-chlorophenyl)furanic acid serves as a potent selective inhibitor for the Mn^{2+} form of *Ec*MetAP [142]. The metallo-specific property

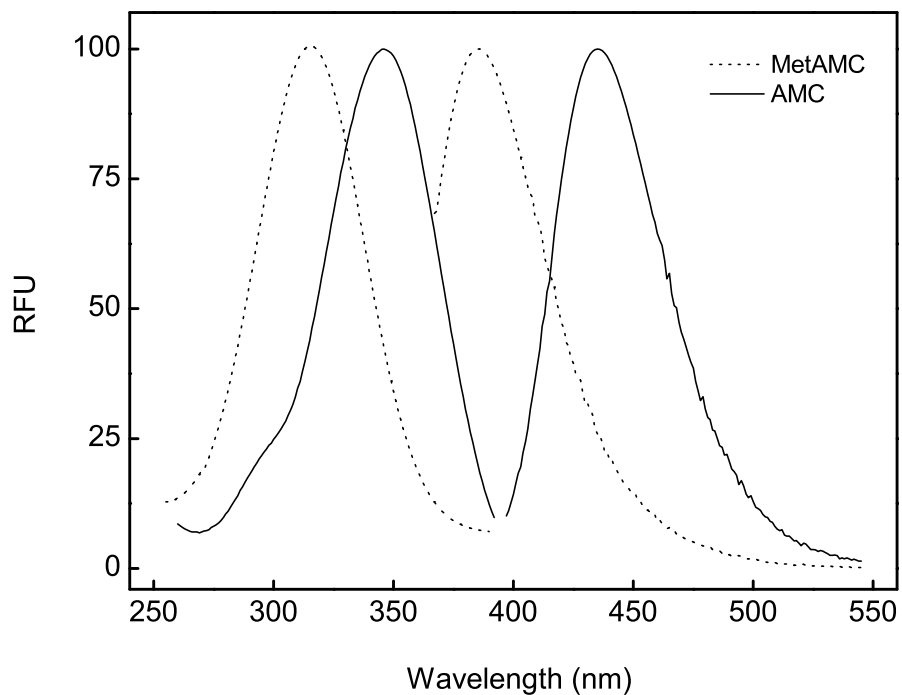


Figure 5.6. Spectral features of Met-AMC and AMC. Absorption and emission spectra of 10 μM Met-AMC and 1 μM AMC were measured in 25 mM HEPES pH 7.5 containing 100 mM NaCl and 10 μM CoCl_2 and normalized for the plot. The absorption and emission maxima of the substrate are 315 and 385 nm and those of the product are 345 and 435 nm, respectively.

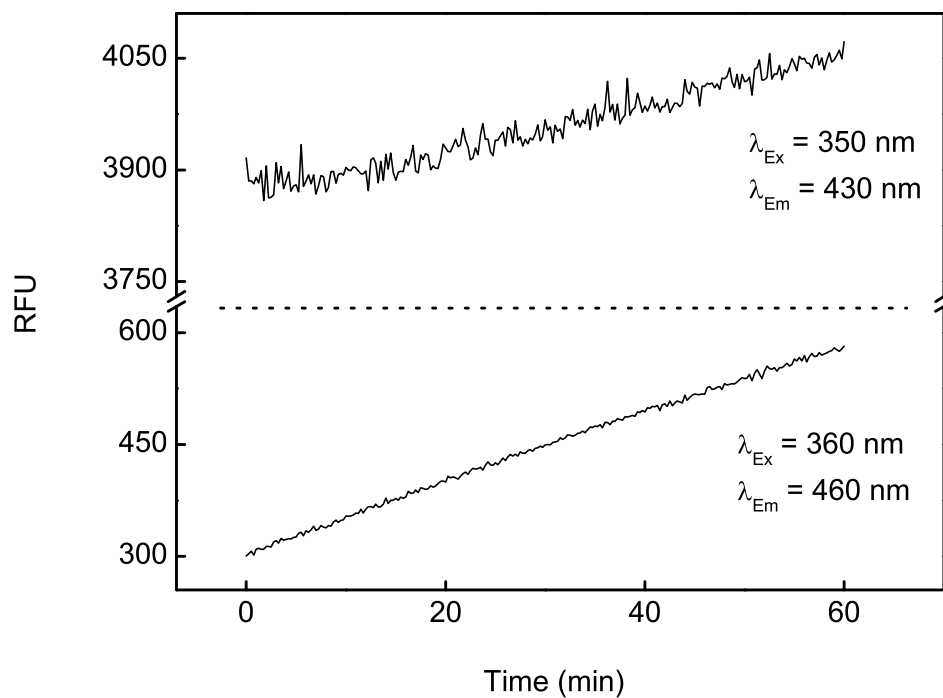


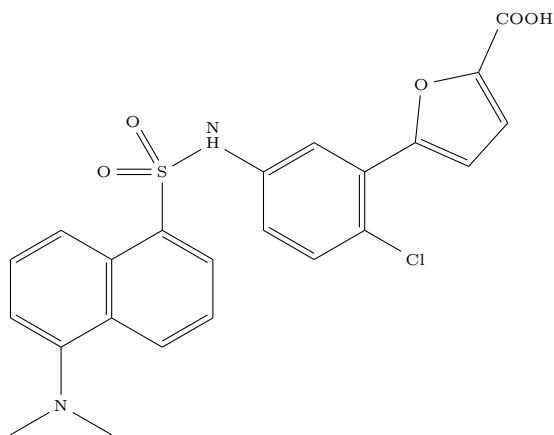
Figure 5.7. Fluorescence parameters for the direct MetAP assay. The activity of *EcMetAP* was measured in a 96 well plate using the substrate Met-AMC. The release of AMC was monitored at two wavelength settings. The top curve was obtained by exciting at 350 nm and monitoring the emission at 430 nm (cutoff filter at 420 nm). The bottom curve was obtained simultaneously by $\lambda_{\text{ex}} = 360$ nm and $\lambda_{\text{em}} = 460$ nm (cutoff filter at 455 nm).

of this inhibitor was deemed to be an excellent tool to study the nature of metallo-specific ligand interactions in *EcMetAP*. The inhibitor was derivatized (by the CPR Core Synthesis Lab at the Department of Chemistry & Biochemistry, North Dakota State University) with the dansylamide group to provide a new fluorescent signal, to probe the micro-environment of the enzyme's active site pocket. Figure 5.8 shows the structure and fluorescence spectra of Dansylamide-5-(2-ChloroPhenyl)Furanoic acid (DCPF). Note that the excitation and emission peaks are at 300 and 550 nm respectively. Further characterization of DCPF and its interaction with different metalloforms of *EcMetAP* was carried out and is detailed in section §5.6.

5.2.3. Circular dichroic spectropolarimetric studies of PDFs

In order to ascertain the possible structural difference between the native and truncated forms of PDF, it was necessary to determine the secondary structural contents of the enzymes. This was particularly so since the C-terminal region of the native (full length) enzyme is known to form either an α -helix or an unstructured loop under different conditions. The circular dichroic spectra of the native and truncated forms of PDF were recorded to measure the secondary structural content of the enzymes. The far-UV CD spectra shown in Figure 5.9 indicate two minima at 223 and 208 nm, which is consistent with the α -helix and β -sheet content (34 and 29%, respectively) determined from the crystal structure.

The above figure shows that the CD spectra of both, the native and truncated PDF, are very similar. It is interesting to note that the secondary structural content of the truncated form of PDF is in very close agreement with that of the native PDF. In the form of an α -helix, the C-terminal region would contribute approximately 30% to the total α -helical content of the protein. Since the native and truncated forms



Dansylamide-5-(2-Chlorophenyl)Furanoic acid (DCPF)

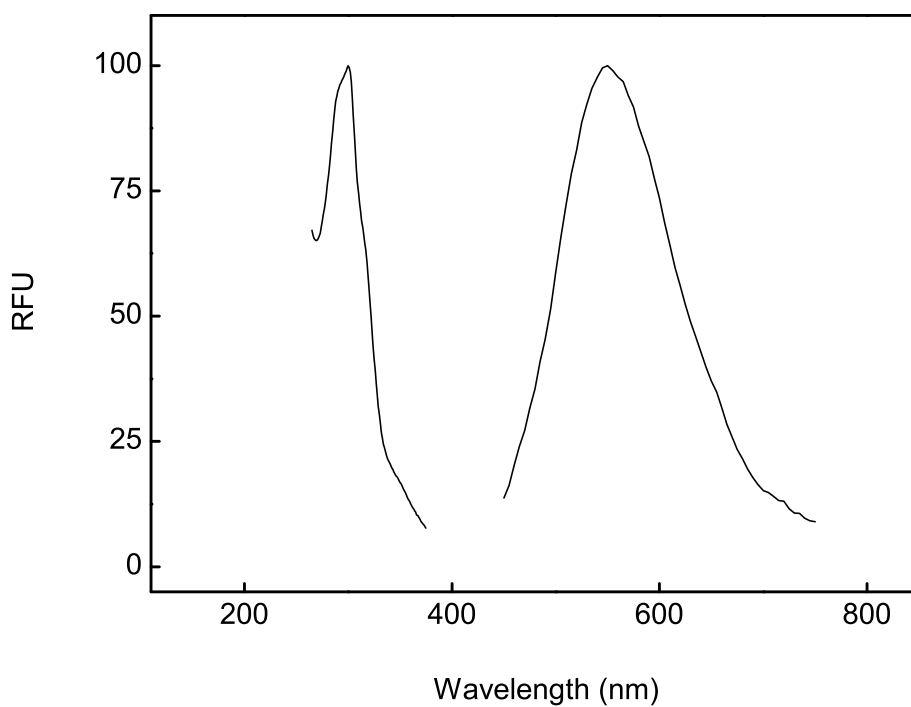


Figure 5.8. Fluorescence spectra of DCPF. The normalized excitation and emission spectra of 10 μM DCPF in 25 mM HEPES pH 7.5 containing 100 mM NaCl. The excitation and emission peaks correspond to 300 and 550 nm.

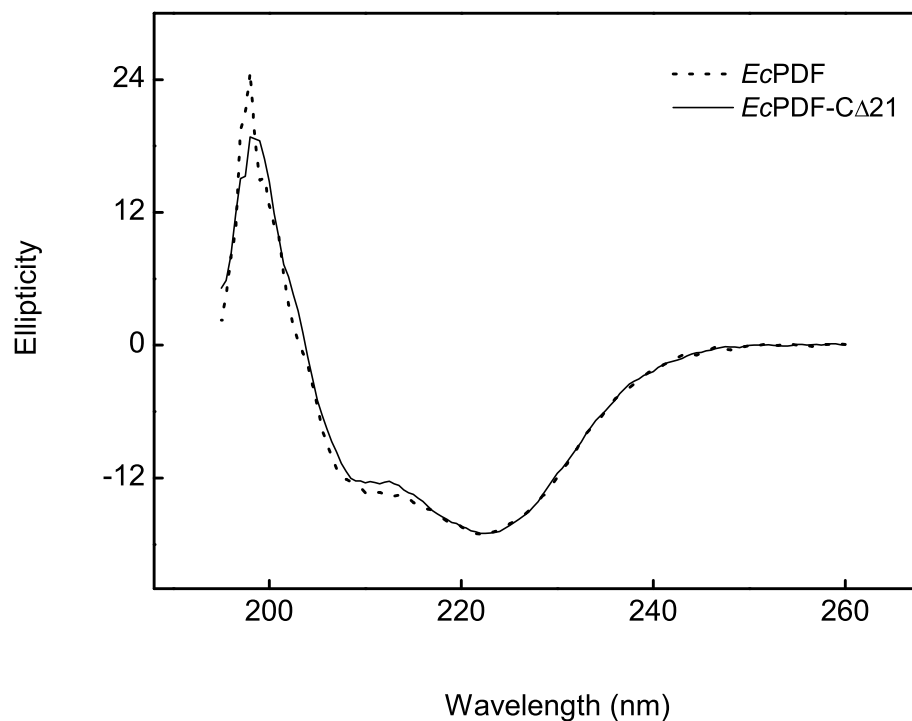


Figure 5.9. CD spectra of native (dotted) and truncated (solid) PDFs. The spectra of 15 μM PDF were measured in 5 mM HEPES buffer pH 7.5 using a quartz cuvette of 1 mm path length. The data were collected with a response time of 8 s and averaged over three scans.

close resemble each other in their α -helix content, this data supports the notion that the C-terminal region of the enzyme remains mostly unfolded or disordered, thus contributing very little to the observed secondary structure.

5.3. Steady State Kinetics of MetAP and PDF Catalyzed Reactions

5.3.1. Steady-state kinetics of MetAP catalyzed reactions

5.3.1.1. Coupled assay for MetAP catalysis

The coupled assay for the catalytic activity of MetAP involved the cleavage of N-terminal methionine from the chromogenic substrate Met-Pro-*p*NA, followed by the release of the *p*NA group by the subsequent action of proline aminopeptidase on the intermediary reaction product Pro-*p*NA (see Scheme 4.1 on page 69). The time dependent generation of free *p*NA was monitored at 405 nm as a measure of the reaction velocity. By maintaining a large excess of ProAP in the assay, the release of *p*NA served as an indicator of the rate limiting release of the methionine residue from the MetAP catalyzed reaction. To determine the minimum concentration of ProAP required to satisfy the above criteria in the assay, the catalytic parameters of the purified coupling enzyme were determined using Pro-*p*NA as the substrate, under the conditions used for the MetAP assay. Figure 5.10 shows the initial reaction rate of the purified ProAP as a function of substrate (Pro-*p*NA) concentration. With increasing substrate concentration the enzyme reaction rate increases and attains a plateau which is characteristic of the hyperbolic profile of the Michealis-Menten model of enzyme kinetics. The non-linear regression analysis of the data using the Michealis-Menten model gave the values of k_{cat} and K_m as $100 \pm 10 \text{ s}^{-1}$ and $116 \pm 49 \mu\text{M}$, respectively. These values are similar to those reported (95 s^{-1} and $130 \mu\text{M}$, respectively) by Zhou et al. [85]. Based on these values, a concentration of 1 to 2 μM of ProAP per μM of MetAP was deemed sufficient for the coupled assay system.

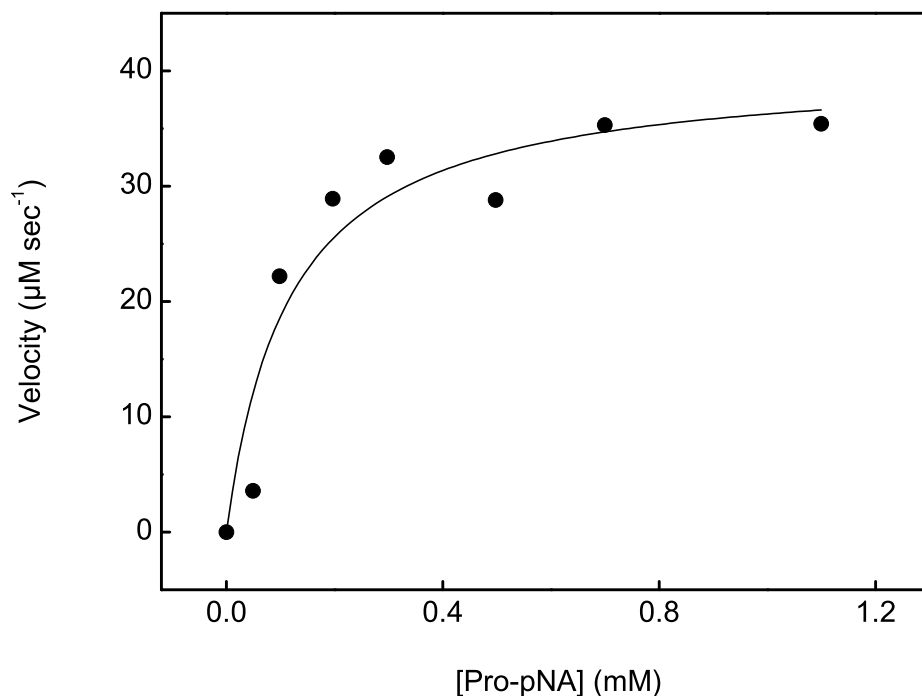


Figure 5.10. Steady state parameters of ProAP. The activity of $0.4\ \mu\text{M}$ ProAP was assayed in $25\ \text{mM}$ HEPES pH 7.5 containing $100\ \text{mM}$ NaCl and $100\ \mu\text{M}$ CoCl_2 in the presence of increasing concentrations of the substrate Pro-pNA. The reaction rate was monitored at $405\ \text{nm}$. The solid line represents the best fit of the data for K_m and V_{max} values of $116 \pm 49\ \mu\text{M}$ and $40 \pm 4\ \text{s}^{-1}$, respectively.

The steady-state data for *EcMetAP* and *HsMetAP* conformed to the above hyperbolic dependence and are shown in Figure 5.11. The k_{cat} and K_m values for *EcMetAP* were determined to be $2.4 \pm 0.1\ \text{s}^{-1}$ and $138 \pm 32\ \mu\text{M}$, respectively. The values for *HsMetAP* were determined to be $2.38 \pm 0.06\ \text{s}^{-1}$ and $647 \pm 48\ \mu\text{M}$, respectively. These steady-state parameters are in close agreement with the values reported in the literature [85].

In some of the coupled assay systems, the initial rate of the MetAP reaction was found to be non-linear, resulting from an apparent lag phase. This is presumably due to the build up of the intermediate, for the coupling enzyme to convert to the reaction product. Under such situations, the steady state rates were accurately measured after 4

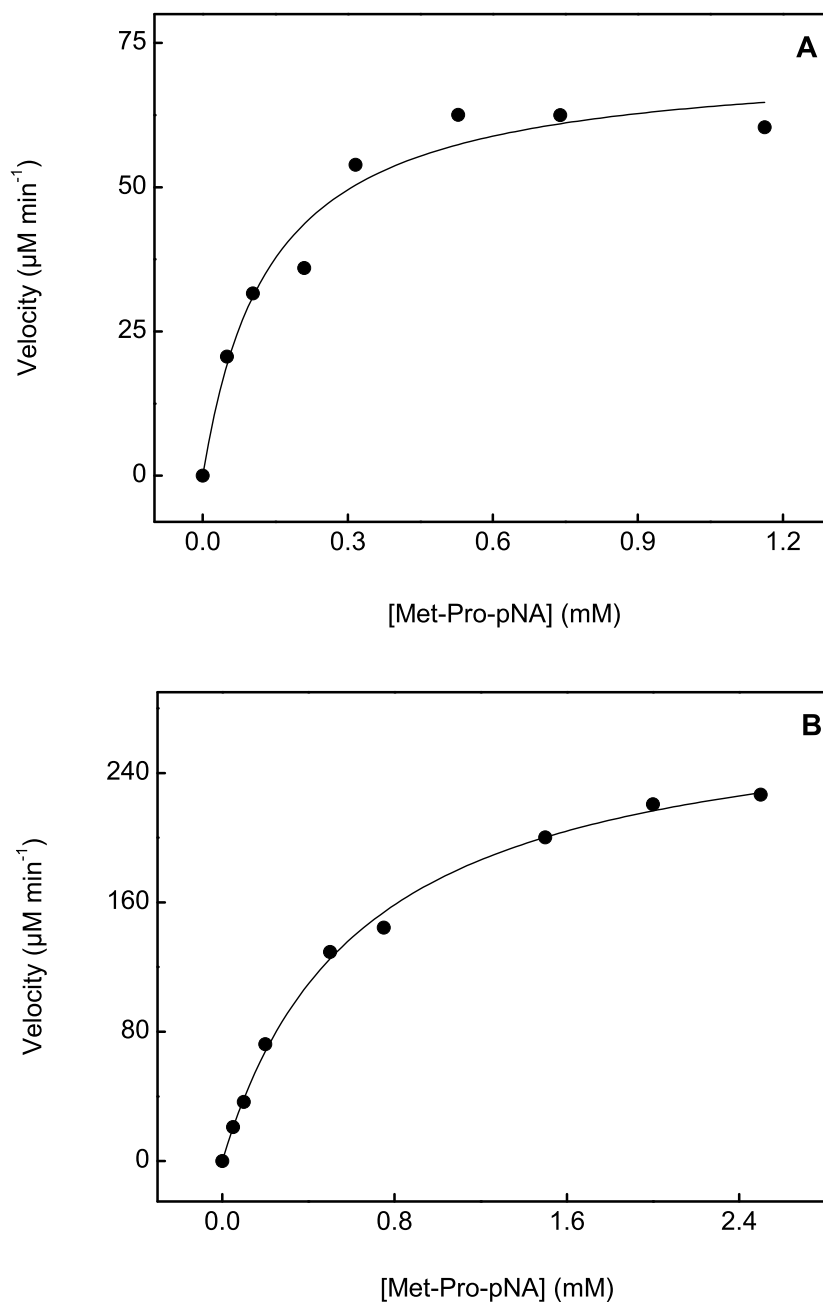


Figure 5.11. MetAP steady-state parameters with substrate Met-Pro-pNA. The activity of 0.5 μM *EcMetAP* (**A**) and 2 μM *HsMetAP* (**B**) was measured using the coupled assay with ProAP as the coupling enzyme. The solid lines represent the best fit of the data for the values of K_m being 138 ± 32 and $647 \pm 48 \mu\text{M}$, and the values of V_{\max} being 72 ± 4 and $286 \pm 7 \text{ min}^{-1}$ for *EcMetAP* and *HsMetAP* respectively.

to 5 min of the reaction progress, after which the rate was found to be linear for 20 min (see Figure 5.12). The appearance of the lag phase could not be completely abolished by tweaking the enzyme concentrations in the assay system, suggesting that the coupling enzyme (ProAP) may be inhibited by the MetAP substrate (Met-Pro-pNA). In order to test this hypothesis, the activity of ProAP was assayed in the presence of a fixed concentration of its own substrate (Pro-pNA) and increasing concentrations of the MetAP substrate Met-Pro-pNA. Figure 5.13 shows that the ProAP enzyme is indeed inhibited by the MetAP substrate Met-Pro-pNA, with an inhibition constant of 0.6 mM. In order to minimize this inhibitory effect, all further coupled assays for MetAP were conducted with 0.4 mM of the Met-Pro-pNA substrate.

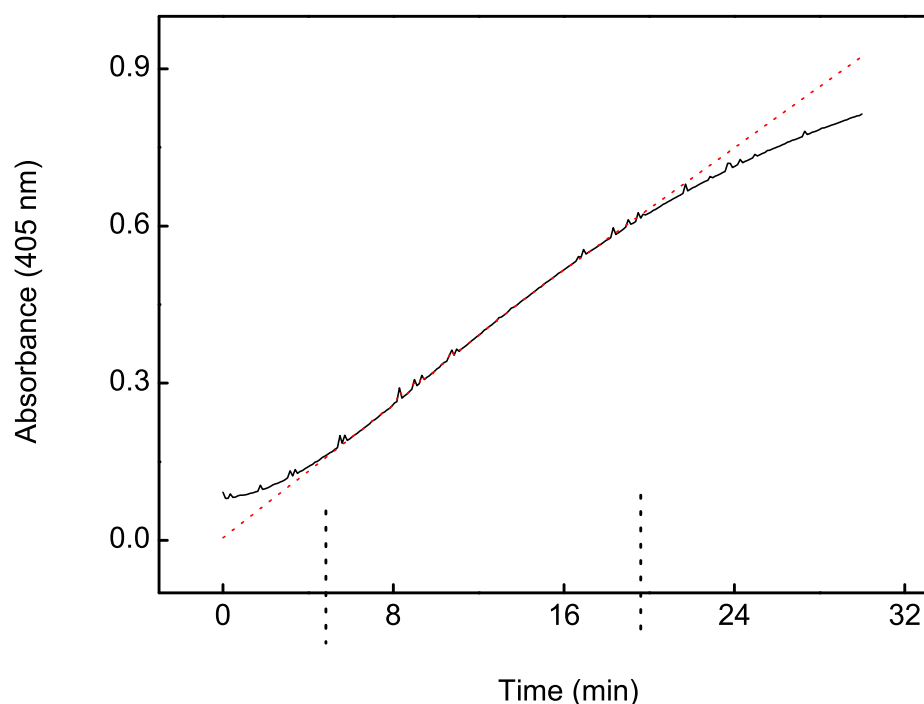


Figure 5.12. MetAP activity measured by the coupled assay. The solid black curve represents the the release of pNA from Met-Pro-pNA upon the sequential action of MetAP and ProAP, as measured by the change in absorbance at 405 nm. The dashed red line indicates the fit for the linear region of the data, shown by the the markers on the X axis at 6 and 20 min

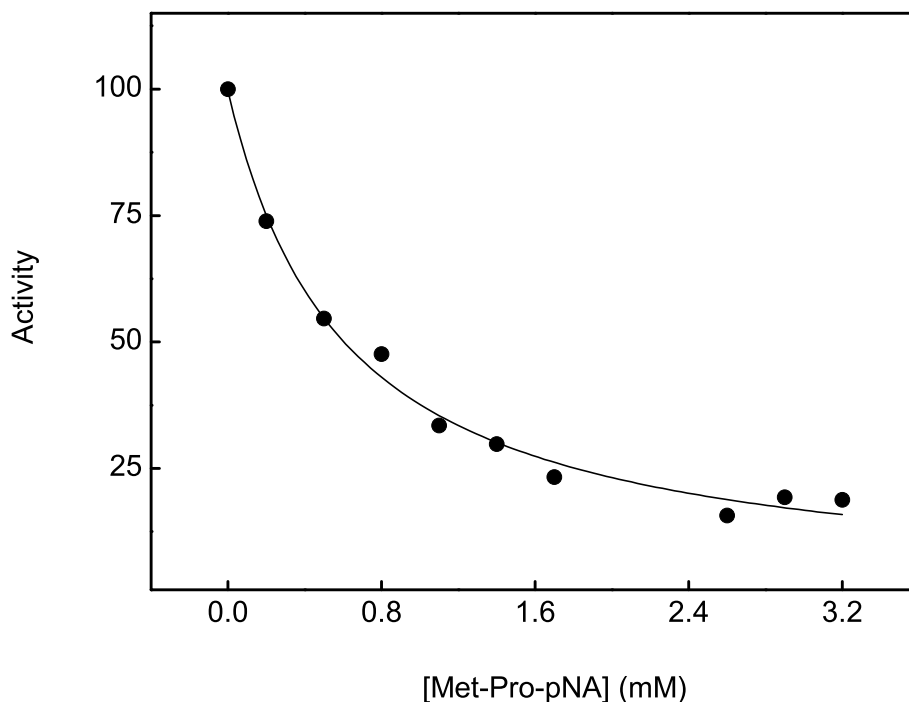


Figure 5.13. ProAP inhibition by Met-Pro-*p*NA. The activity of 0.4 μM ProAP was assayed in 25 mM HEPES pH 7.5 containing 100 mM NaCl and 100 μM CoCl_2 in the presence of 100 μM substrate (Pro-*p*NA) and increasing concentrations of the MetAP substrate Met-Pro-*p*NA. The reaction rate was monitored at 405 nm. The solid line represents the best fit of the data for the value of K_i being equal to $607 \pm 74 \mu\text{M}$.

5.3.1.2. Direct assay of MetAP catalysis

The catalytic activity of MetAP was measured directly by using the fluorogenic substrate Met-AMC as described in Scheme 4.2 on page 71. During this assay, the cleavage of the methionine residue released the fluorophore 7-amino-4-methylcoumarin (AMC), resulting in enhanced fluorescence at 460 nm ($\lambda_{\text{ex}} = 360 \text{ nm}$).

Since the fluorescence signal is measured in random units, the observed change in signal could not be directly used as a measure of the change in fluorophore concentration, for the calculation of the enzyme reaction rate. In order to convert the observed slope (RFU/min) in the enzyme assay to the standard units of enzyme activity ($\mu\text{M min}^{-1}$) the “molar fluorescence coefficient” of AMC was determined under

the same conditions as those used for the assay. 1 to 5 μM AMC was prepared in assay buffer and the fluorescence intensity was measured in a plate reader ($\lambda_{\text{ex}} = 360 \text{ nm}$, $\lambda_{\text{em}} = 460 \text{ nm}$) using a volume of 200 μl in a 96-well microplate or 75 μl in a 384-well microplate. The standard plot of the RFU as a function of AMC concentration (Figure 5.14) resulted in an excellent linear fit indicating that no inner-filter effect occurred up to 1 mM AMC. The molar fluorescence coefficient of 4.04×10^9 obtained from this data was used to calculate the concentration of AMC produced during the direct MetAP assay.

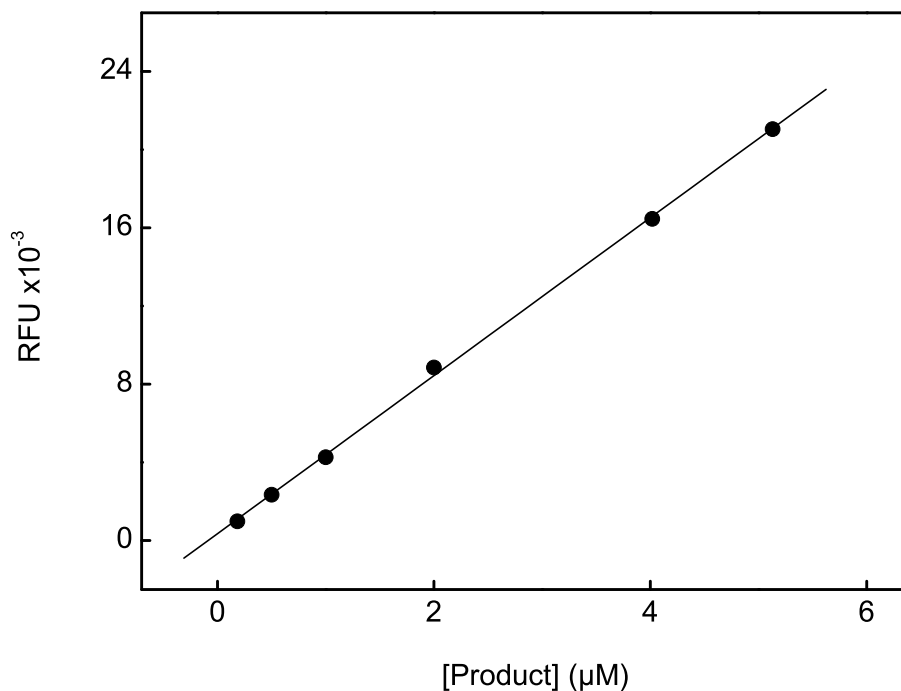


Figure 5.14. AMC standard plot. The fluorescence of AMC was measured in a 96-well microplate under the direct assay conditions. The “molar fluorescence coefficient” was determined from the linear fit of the data as being equal to $(4.04 \pm 0.05) \times 10^9$

The steady state kinetic data from the direct assay of *EcMetAP* activity exhibited a hyperbolic profile characteristic of the Michealis-Menten model of enzyme kinetics (Figure 5.15). The k_{cat} and K_{m} values for the Met-AMC substrate were determined

to be $0.066 \pm 0.002 \text{ s}^{-1}$ and $76 \pm 6 \mu\text{M}$, respectively. The catalytic efficiency ($k_{\text{cat}}/K_{\text{m}}$) reported here is two orders of magnitude higher than that reported in literature (Table 1.2 on page 46). It is surmised that the difference is due to the superior quality of enzyme preparation obtained in this investigation.

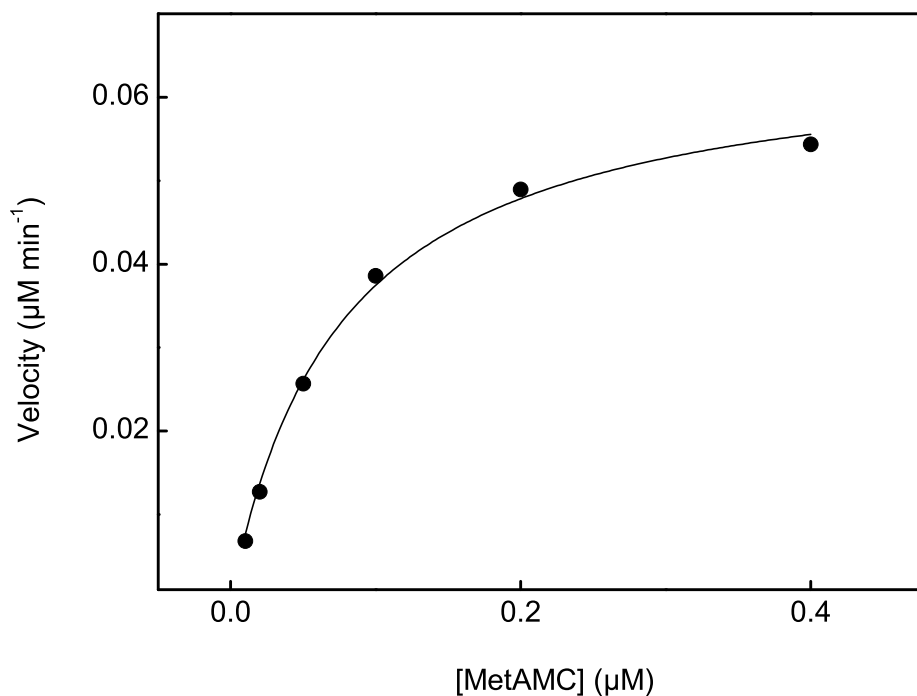


Figure 5.15. Catalytic features of MetAP with fluorogenic substrate MetAMC. The activity of $0.75 \mu\text{M}$ *EcMetAP* was assayed in the presence of 10 to $400 \mu\text{M}$ substrate in a 96 well micro-titre plate, in 25 mM HEPES pH 7.5 containing 100 mM NaCl and $10 \mu\text{M}$ CoCl_2 . The reaction was monitored using a plate reader ($\lambda_{\text{ex}} = 360 \text{ nm}$, $\lambda_{\text{em}} = 460 \text{ nm}$) and the slope of the linear portion of the reaction trace was used to calculate the initial velocity. The smooth line represents the best fit of the data for the values of K_{m} and V_{max} as being equal to $76 \pm 6 \mu\text{M}$ and $0.050 \pm 0.001 \text{ s}^{-1}$, respectively.

5.3.2. Steady-state kinetic parameters of PDF catalysis

The activity of PDF was measured using a coupled assay with fMet-Leu-pNA as the substrate and *Aeromonas* aminopeptidase (AAP) as the coupling enzyme, according to the protocol optimized by Berg [64]. The assays were conducted with

1 Unit of AAP in 5 mM HEPES buffer pH 7.5 containing 2 mM NiCl₂ and 100 mM KCl. 0.1 mg/ml BSA was added to the assay to stabilize the PDF enzyme and the reactions were monitored at 405 nm for 5 min. Figure 5.16 shows the enzyme reaction rates of native and truncated PDFs as a function of substrate concentration. The data reflect hyperbolic profiles of the Michealis-Menten model and the k_{cat} and K_m values were determined to be $0.39 \pm 0.01 \text{ s}^{-1}$ and $35 \pm 6 \mu\text{M}$, respectively for *Ec*PDF; $0.94 \pm 0.01 \text{ s}^{-1}$ and $4.8 \pm 0.4 \mu\text{M}$, respectively for *Ec*PDF-C Δ 21.

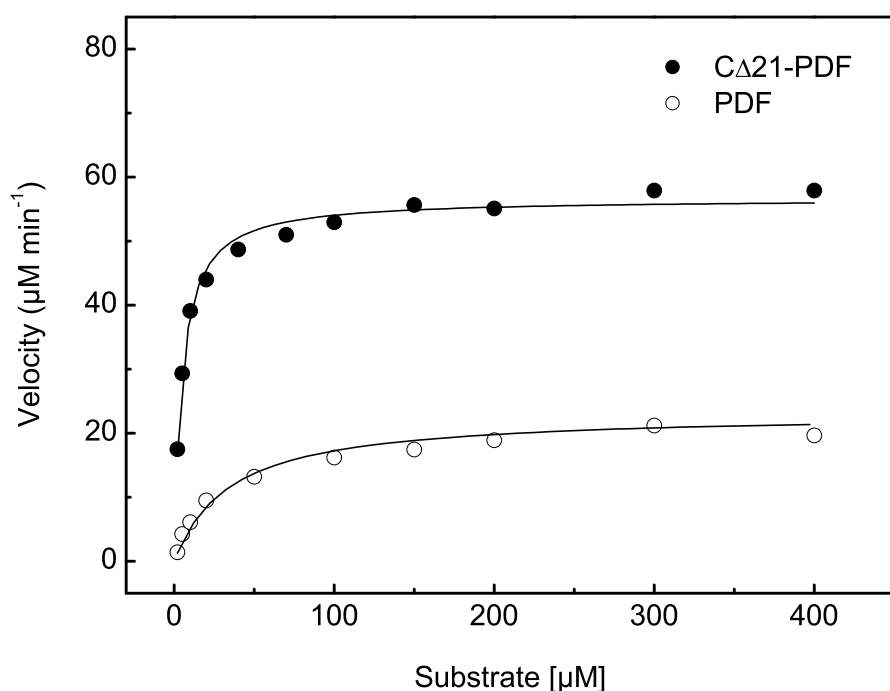


Figure 5.16. Comparison of catalytic features of native and truncated PDFs. Activity of $0.03 \mu\text{M}$ native and $0.025 \mu\text{M}$ truncated PDF was measured at varying substrate (fMet-Leu-pNA) concentrations (2 to $400 \mu\text{M}$) in 5 mM HEPES buffer pH 7.5 containing 2 mM NiCl₂, 100 mM KCl and 0.1 mg/ml BSA using AAP as a coupling enzyme. The data were normalized to $1 \mu\text{M}$ enzyme. Formation of product was monitored over time at 405 nm in a plate reader and the initial rate was used as a measure of the enzyme activity. The concentration of product formed was determined using a product standard curve. The solid smooth lines represent the best fit of the data for the K_m values of 35 ± 6 and $4.8 \pm 0.4 \mu\text{M}$ and V_{max} values of 23.2 ± 0.9 and $56.6 \pm 0.7 \mu\text{M min}^{-1}$ for *Ec*PDF and *Ec*PDF-C Δ 21 respectively.

It is clear from the data that the truncated PDF (*Ec*PDF-C Δ 21) is significantly more active than the native enzyme, with the $k_{\text{cat}}/K_{\text{m}}$ value being almost 18 fold higher. However, the steady-state parameters of the native enzyme determined in this study were disparate in comparison to those reported for the enzyme by others. A likely explanation for this difference was suggested by the possibility that the enzyme preparation contained Zn²⁺ form of the enzyme. Support of this hypothesis emerges from the observation that the Ni²⁺-PDF charge transfer peak was absent from the absorbance spectra of the enzymes (section §5.2.1). In order to further confirm this hypothesis, the steady-state characterization of the Zn²⁺ form of PDFs was undertaken. The Zn²⁺ forms of *Ec*PDF and *Ec*PDF-C Δ 21 were specifically prepared by incubating the enzymes overnight in the presence of 2 mM ZnCl₂. The activity of the enzymes was assayed as before, in the assay buffer containing ZnCl₂ instead of NiCl₂. The steady-state data are shown in Figure 5.17. The k_{cat} and K_{m} values for *Ec*PDF were determined to be $0.28 \pm 0.01 \text{ s}^{-1}$ and $28 \pm 3 \text{ }\mu\text{M}$, respectively. These values are very similar to those determined earlier (Figure 5.16) indicating that the *Ec*PDF preparation is indeed mostly in the Zn²⁺ form. The k_{cat} and K_{m} values for *Ec*PDF-C Δ 21 ($0.96 \pm 0.05 \text{ s}^{-1}$ and $11 \pm 2 \text{ }\mu\text{M}$) are also similar to those determined earlier, indicating the Zn²⁺ nature of the enzyme.

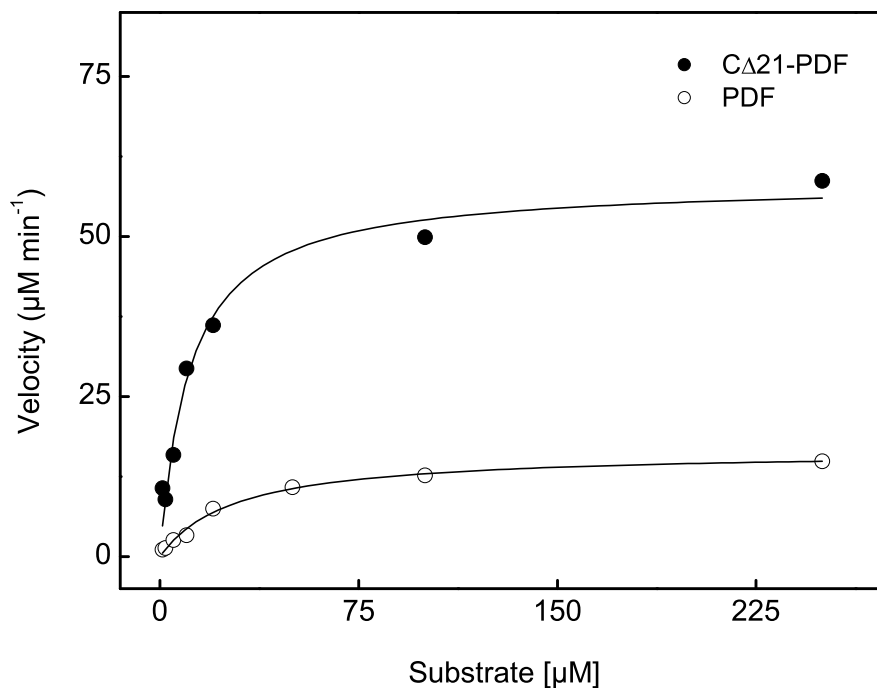


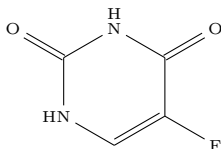
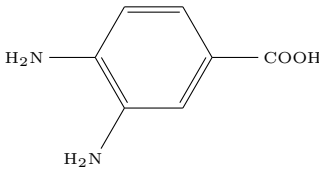
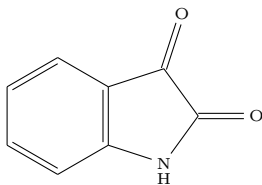
Figure 5.17. Catalytic features of the Zn^{2+} forms of native and truncated PDFs. Activity of $0.05 \mu\text{M}$ native and $0.165 \mu\text{M}$ truncated PDF was measured with varying concentrations (1 to $250 \mu\text{M}$) of substrate (*fMet-Leu-pNA*) after incubating with 2 mM ZnCl_2 overnight. The assay was carried out in 5 mM HEPES pH 7.5 containing 100 mM KCl, 0.1 mg/ml BSA and AAP as coupling enzyme and the activity was normalized to $1 \mu\text{M}$ enzyme. The formation of product was monitored over time at 405 nm in a plate reader and the initial rate was used as a measure of the enzyme activity. The smooth solid lines represent best fits of the data for the K_m values of 28 ± 3 and $11 \pm 2 \mu\text{M}$ and V_{max} values of 16.6 ± 0.6 and $58 \pm 3 \mu\text{M}/\text{min}$ for *EcPDF* and *EcPDF-CΔ21* respectively.

5.4. Inhibitors of MetAPs

5.4.1. Screening of inhibitors for MetAPs

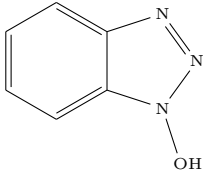
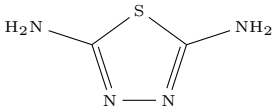
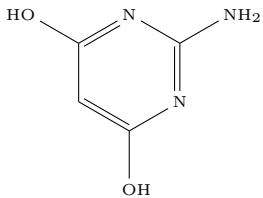
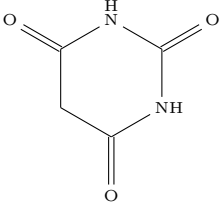
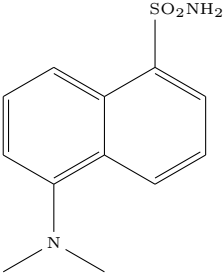
As discussed in section §1.5, bacterial MetAPs are considered as a novel and potent target for antibiotic drug design. In a preliminary attempt to identify compounds with such pharmaceutical potential, various small organic compounds (listed in Table 5.2) were tested for their inhibitory potencies against the *E. coli* and human type I MetAPs. These included known pharmacologically active compounds with and without associated spectroscopic signals. In particular, barbituric acid was found to inhibit the activity of both the isoforms by about 50%.

Table 5.2. Lead inhibitor compounds

Compound	Name/ID	Inhibition (%) ¹
	5-fluorouracil	—
	3,4-diaminobenzoic acid	x
	Isatin	—

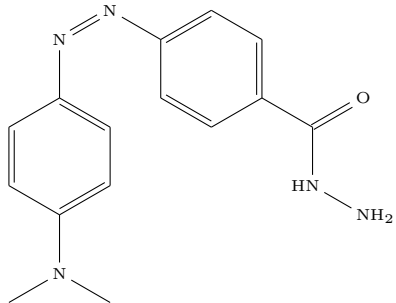
continued...

Table 5.2. Lead inhibitor compounds (... continued)

Compound	Name/ID	Inhibition (%)
	Hydroxybenzotriazole	10
	1,3,4-thiadiazole-2,5-diamine	–
	2-aminopyrimidine-4,6-diol	–
	Barbituric acid	52
	Dansylamide	31

continued...

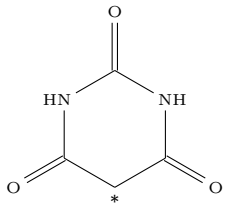
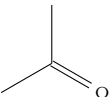
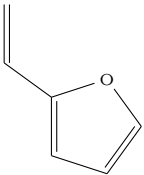
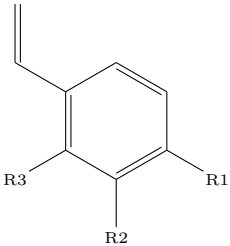
Table 5.2. Lead inhibitor compounds (...continued)

Compound	Name/ID	Inhibition (%)
	RS-V-19	–

¹ *EcMetAP* and *HsMetAP* activity was assayed in 25 mM HEPES pH 7.5 containing 100 mM NaCl and 100 μ M CoCl₂ in the presence of 400 μ M substrate (Met-Pro-*p*NA) and 400 μ M inhibitor and the reduction in activity was compared to control assays in the absence of inhibitor. The % inhibition of *EcMetAP* is shown in the table.

Using barbituric acid as the lead compound, numerous barbiturate derivatives (synthesized by Dr. Sanku Mallik's group at NDSU) were screened for inhibitory activity against the *E. coli* and human type I MetAPs (Table 5.3). Typically compounds with a phenyl group at C5 were tested, where the phenyl ring was derivatized at the *ortho*, *meta* or *para* positions. Additionally, compounds with varying linker length (1 to 3 carbons) between barbiturate and phenyl were tested. The compounds which exhibited an inhibition of either MetAP isoform greater than 45% at a concentration of 10 μ M were selected for further enzymological studies with the MetAP isoforms.

Table 5.3. Oxobarbiturate derivatives

Compound		ID	% inhibition ¹		
			<i>EcMetAP</i>	<i>HsMetAP</i>	
					
		RS-IV-46	43		
		MDS-1-11	-	-	
					
—R1	—R2	—R3			
-	-	-	MH-5-50	-	6
—NO ₂	-	-	MH-5-51b	9	54
—N-(CH ₃) ₂	-	-	MH-5-53	42	48

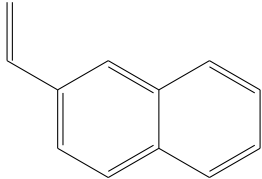
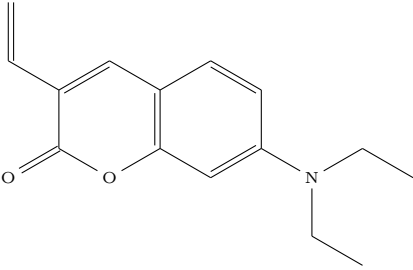
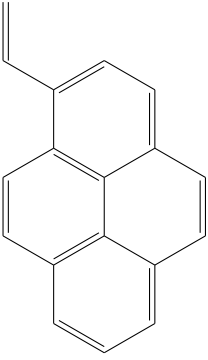
continued ...

Table 5.3. Oxobarbiturate derivatives (... continued)

Compound			ID	% inhibition	
				<i>EcMetAP</i>	<i>HsMetAP</i>
—COOH	-	-	MH-5-54	-	67
—OH	-	-	MH-5-68	70	49
—CF ₃	-	-	MDS-1-7	-	-
—OCH ₃	-	-	MDS-1-8	28	81
—COO—CH ₃	-	-	MDS-1-13	-	-
—OCO—CH ₃	-	-	MDS-1-14	57	-
—F	-	-	MDS-1-20	10	82
—Cl	-	-	MDS-1-21	-	-
—OH	—OCH ₃	-	MDS-1-6	42	91
-	—OH	-	MDS-1-3	-	-
-	—OCH ₃	-	MDS-1-4	27	12
-	—OH	—OH	MDS-1-17	8	57
-	-	—NO ₂	MDS-1-5	88	-
-	-	—CH ₃	MDS-1-16	-	-
-	-	—Cl	MDS-1-22	-	-
—OCH ₃	-	—OH	MDS-1-10	29	9
—OCH ₃	—OCH ₃	—OCH ₃	MDS-2-7	39	6
—5-methyl barbiturate	-	-	MDS-4-6	-	-

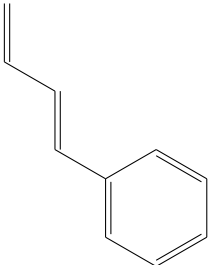
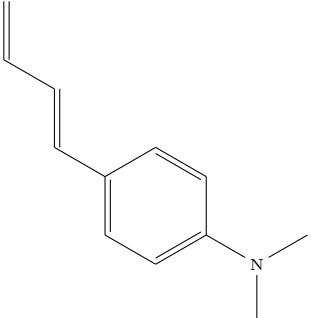
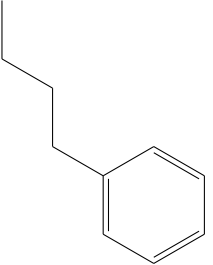
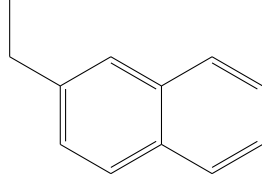
continued ...

Table 5.3. Oxobarbiturate derivatives (... continued)

Compound	ID	% inhibition	
		<i>EcMetAP</i>	<i>HsMetAP</i>
	MH-5-52	8	49
	MH-5-75	74	39
	MH-5-76	-	46

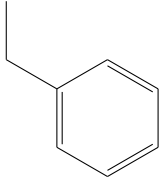
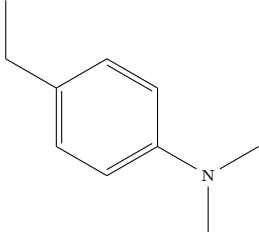
continued ...

Table 5.3. Oxobarbiturate derivatives (... continued)

Compound	ID	% inhibition	
		<i>EcMetAP</i>	<i>HsMetAP</i>
	MH-5-69	45	52
	MH-5-74	80 ²	90 ²
	RS-V-48	-	-
	RS-V-50	-	-

continued ...

Table 5.3. Oxobarbiturate derivatives (... continued)

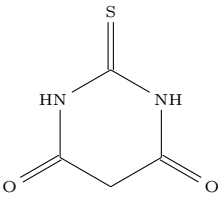
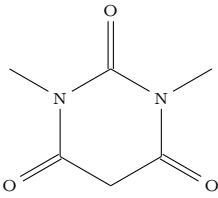
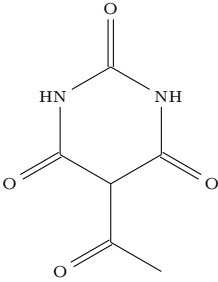
Compound	ID	% inhibition	
		<i>EcMetAP</i>	<i>HsMetAP</i>
	RS-V-53	-	-
	RS-V-75	8	-

¹ MetAP activity was assayed in 25 mM HEPES pH 7.5 containing 100 mM NaCl and 100 μ M CoCl₂ in the presence of varying inhibitor concentrations and the activity was determined from the linear region of the reaction progress curve. The % inhibition was calculated by comparing with a control assay in the absence of any inhibitor.

² MH 5-74 was screened at a concentration of 1 μ M due to poor solubility of the compound.

As seen from the data in Table 5.3, most inhibitors preferentially inhibited *HsMetAP* over *EcMetAP*. This was the opposite of the desired result since potential antibiotic compounds would be expected to selectively inhibit *EcMetAP*. In order to identify more appropriately selective inhibitors, the barbiturate based compounds, thiobarbituric acid, 1,3-dimethylbarbituric acid and 5-acetylbarbituric acid were tested as lead compounds against the *E. coli* and human type I MetAPs (Table 5.4).

Table 5.4. Barbiturate based lead compounds.

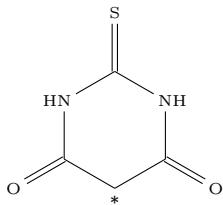

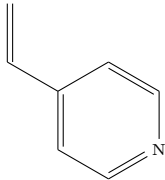
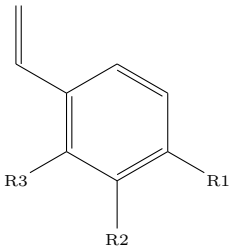
Compound	Name	% inhibition ¹	
		<i>EcMetAP</i>	<i>HsMetAP</i>
	2-Thiobarbituric acid	65	55
	1,3-Dimethylbarbituric acid	45	50
	5-acetylbarbituric acid	–	–

¹ MetAP activity was assayed in 25 mM HEPES pH 7.5 containing 100 mM NaCl and 100 μ M CoCl₂ in the presence of 400 μ M substrate (Met-Pro-*p*NA) and 400 μ M inhibitor and the reduction in activity was compared to a control assay in the absence of inhibitor.

Whereas 5-acetylbarbituric acid had no effect on MetAP activity, both 1,3-dimethylbarbituric acid and 5-acetylbarbituric acid showed similar inhibitory potency as barbituric acid. Derivatives of 1,3-dimethylbarbituric acid and 5-acetylbarbituric acid were

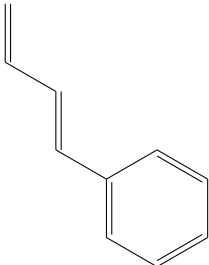
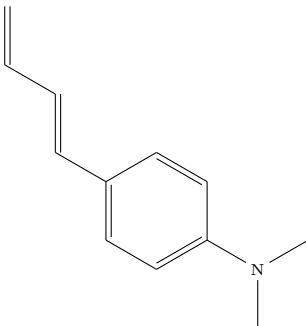
further screened to identify compounds inhibiting *EcMetAP* by more than 45% at 10 μ M concentration of the inhibitor (Tables 5.5 and 5.6). Since compounds selectively or preferentially inhibiting *HsMetAP* were not of interest, the enzyme was not used in the primary screening step. Compounds inhibiting *EcMetAP* by more than 45% were further studied for inhibition against both *EcMetAP* and *HsMetAP*.

Table 5.5. Thiobarbiturate derivatives

			ID	% inhibition ¹
Compound			ID	% inhibition ¹
			RS-IV-49	25
			MDS-2-5	11
				
—R1	—R2	—R3		
—N-(CH ₃) ₂	-	-	MDS-1-25	-
—F	-	-	MDS-1-27	6

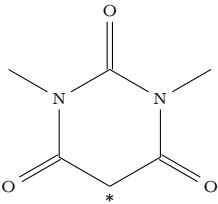
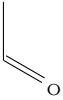
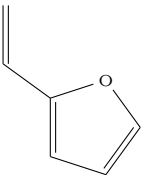
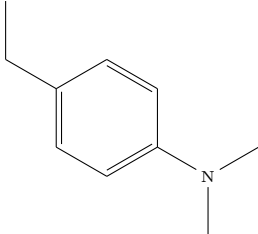
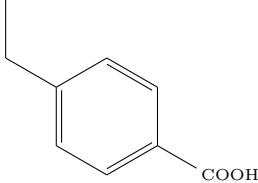
continued ...

Table 5.5. Thiobarbiturate derivatives (...continued)

Compound			ID	% inhibition
—COOH	-	-	MDS-2-14	-
—OCO—CH ₃	-	-	MDS-2-17	5
—OH	-	-	MDS-2-25	37
—OH	—OCH ₃	-	MDS-2-22	45
-	—OCH ₃	-	MDS-3-2	15
-	-	—CH ₃	MDS-2-9	16
-	-	—NO ₂	MDS-2-18	46
—OCH ₃	—OCH ₃	—OCH ₃	MDS-2-19	18
			MDS-1-24	23
			MDS-1-23	36

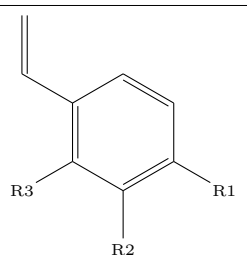
¹ *EcMetAP* activity was assayed in 25 mM HEPES pH 7.5 containing 100 mM NaCl and 100 μ M CoCl₂ in the presence of varying inhibitor concentrations and the activity was determined from the linear region of the reaction progress curve. The % inhibition was calculated by comparing with a control assay in the absence of any inhibitor.

Table 5.6. Dimethylbarbiturate derivatives

Compound	ID	% inhibition ¹
		
	RS-IV-44	21
	MDS-1-11	-
	RS-V-39	-
	RS-V-55	-

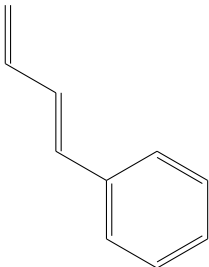
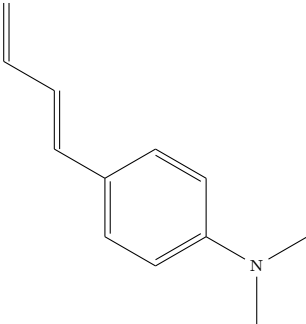
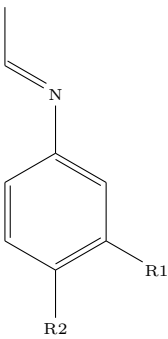
continued ...

Table 5.6. Dimethylbarbiturate derivatives (... continued)

Compound			ID	% inhibition
				
—R1	—R2	—R3		
-	-	-	MDS-3-25	-
—N—(CH ₃) ₂	-	-	MDS-2-2	42
—F	-	-	MDS-1-27	6
—COO—CH ₃	-	-	MDS-3-12	17
—Cl	-	-	MDS-3-18	-
—NO ₂	-	-	MDS-3-20	-
—COOH	-	-	MDS-3-22	12
—OCO—CH ₃	-	-	MDS-3-27	6
—OCH ₃	-	-	MDS-3-38	11
-	—OH	-	MDS-3-11	29
-	—OCH ₃	-	MDS-3-21	-
-	—OH	—OH	MDS-3-29	-
-	—OH	—OCH ₃	MDS-6-5	6
-	-	—NO ₂	MDS-3-19	17
-	-	—CH ₃	MDS-6-12	-

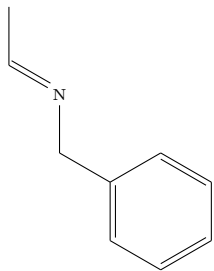
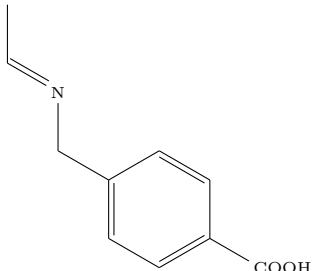
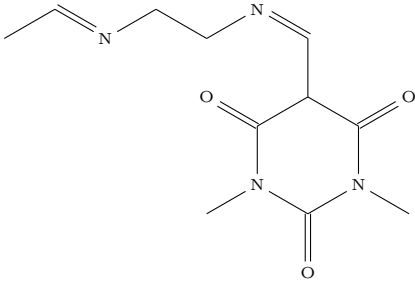
continued ...

Table 5.6. Dimethylbarbiturate derivatives (... continued)

Compound			ID	% inhibition
—OCH ₃	—OCH ₃	—OCH ₃	MDS-2-6	-
			MDS-3-36	20
			MDS-2-1	34
				
—R1	—R2			
—NO ₂	-		RS-IV-82	27
—COOH	—OH		RS-IV-99	20

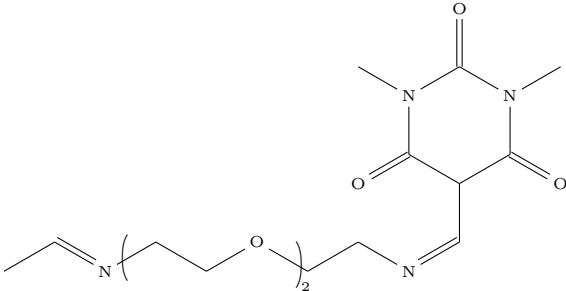
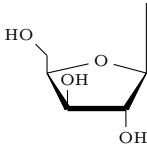
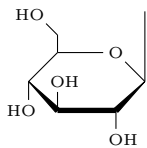
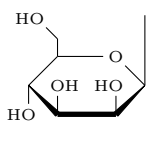
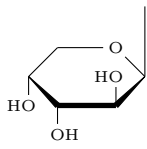
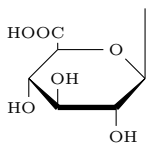
continued ...

Table 5.6. Dimethylbarbiturate derivatives (... continued)

	Compound	ID	% inhibition
-	—OH	RS-IV-85	21
		RS-IV-65	10
		RS-IV-67	14
		RS-IV-90	15

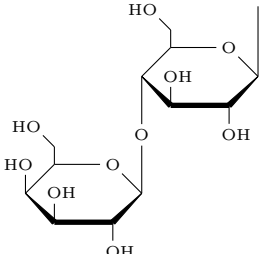
continued ...

Table 5.6. Dimethylbarbiturate derivatives (... continued)

Compound	ID	% inhibition
	RS-IV-94	-
	MDS-4-8	-
	MDS-4-9	-
	MDS-4-12	-
	MDS-4-23	-
	MDS-5-7	-

continued ...

Table 5.6. Dimethylbarbiturate derivatives (... continued)

Compound	ID	% inhibition
	MDS-5-6	9

¹ *EcMetAP* activity was assayed in 25 mM HEPES pH 7.5 containing 100 mM NaCl and 100 μ M CoCl₂ in the presence of varying inhibitor concentrations and the activity was determined from the linear region of the reaction progress curve. The % inhibition was calculated by comparing with a control assay in the absence of any inhibitor.

5.4.2. Determination of inhibition constants

The inhibition constants (K_i) of the compounds, selected from the screening in the previous section, were determined for both *EcMetAP* and *HsMetAP*. The activity of each enzyme was assayed in the presence of 400 μ M substrate and varying concentrations of inhibitors, and the data were analyzed according to the quadratic function for competitive inhibition (Eq. (3) described in section §4.3.5). The inhibition profiles of some of the inhibitors (for both MetAP isozymes) are shown in Figure 5.18. Note that the human isozyme is consistently inhibited to a greater extent than the bacterial isozyme.

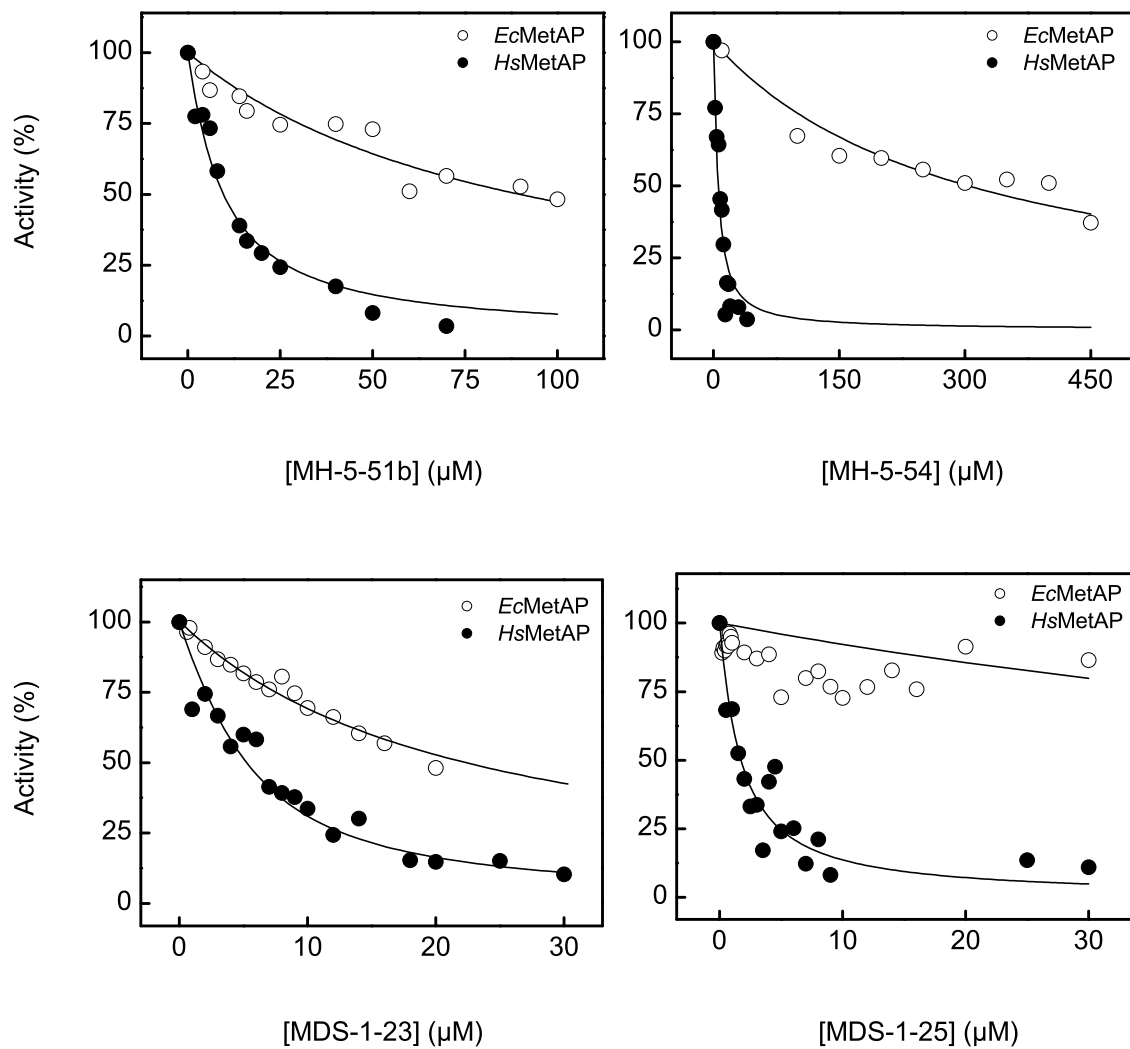


Figure 5.18. Determination of K_i for MetAP inhibitors. The K_i values of MH-5-51b (top left), MH-5-54 (top right), MDS-1-23 (bottom left) and MDS-1-25 (bottom right) for *EcMetAP* (○) and *HsMetAP* (●) are listed in Table 5.7.

The K_i values determined in the study are listed in Table 5.7. As expected from the earlier screening results, most of the inhibitors showed greater potency against the human MetAP isoform, with the exception of MH-5-68 and MH-5-75. In fact, although the latter two inhibitors had lower K_i values against *Ec*MetAP, the relative inhibition potency against the two MetAPs was not sufficiently different to be considered as isoform selective towards *Ec*MetAP.

Table 5.7. Inhibition constants of selected MetAP inhibitors.¹

Ligand	Inhibition constant (μM)	
	<i>Ec</i> MetAP	<i>Hs</i> MetAP
MH-5-76	– ²	11 ± 2
MH-5-50	517 ± 63	162 ± 13
MH-5-54	335 ± 47	5 ± 1
MDS-1-25	156 ± 15	1.7 ± 0.3
MDS-1-27	144 ± 25	5.9 ± 0.6
MH-5-52	113 ± 14	10 ± 1
MDS-1-17	108 ± 12	7.2 ± 1.3
MH-5-51b	106 ± 18	8.2 ± 1.4
MDS-1-20	89 ± 12	1.9 ± 0.2
MH-5-71	35 ± 9	28 ± 6
MDS-1-9	29 ± 2	1.9 ± 0.3
MDS-1-8	26 ± 2	2.2 ± 0.4
MDS-1-23	17 ± 1	1.0 ± 0.1
MH-5-53	13 ± 1	10 ± 2

continued...

Table 5.7. Inhibition constants of MetAP inhibitors(... continued)

Ligand	Inhibition constant (μM)	
	<i>Ec</i> MetAP	<i>Hs</i> MetAP
MDS-1-6	13 ± 1	0.94 ± 0.14
MH-5-69	12 ± 3	9 ± 2
MH-5-68	3.9 ± 0.9	10 ± 2
MH-5-75	3.2 ± 0.7	15 ± 2
MH-5-74	0.050 ± 0.031	0.014 ± 0.003

¹ The enzyme activity was measured using the coupled assay with ProAP in 25 mM HEPES pH 7.5 containing 100 mM NaCl and 100 μM CoCl_2 with 100 μM substrate (Met-Pro-*p*NA) and increasing concentrations of the ligand. The data were analyzed using the quadratic function for competitive inhibition described in section §4.3.5. The ligands are arranged in increasing order of inhibition efficiency against *Ec*MetAP.

² No inhibition of *Ec*MetAP was observed by MH-5-75 up to a concentration of 400 μM .

5.4.3. (4-dimethylamino)phenyl based barbiturate derivatives as MetAP inhibitors

The screening of barbiturate derivative compounds revealed that the derivatives with (4-dimethylamino)phenyl moiety were typically good inhibitors of both *E. coli* and human type I MetAPs. The inhibitor 5-[-3-[4-(dimethylamino)phenyl]prop-2-en-1-ylidene]-barbituric acid (MH-5-74) was particularly potent with nanomolar inhibition constants for both *Ec*MetAP and *Hs*MetAP (Figure 5.19). However, due to the extremely poor solubility of this compound (0.56 g L^{-1} in DMF, and much lower in

aqueous media), it could not be used for further experiments such as transient kinetics or micro-calorimetry to analyze the enzyme-inhibitor interaction. On the other hand, in addition to being good inhibitors of MetAPs, these compounds also exhibited unique spectrophotometric properties making them potentially useful as probes for studying the physico-chemical properties of the MetAP isoforms. The spectral properties of these inhibitors were investigated in the absence and presence of each MetAP isoform in order to ascertain their viability for use as reporter probes.

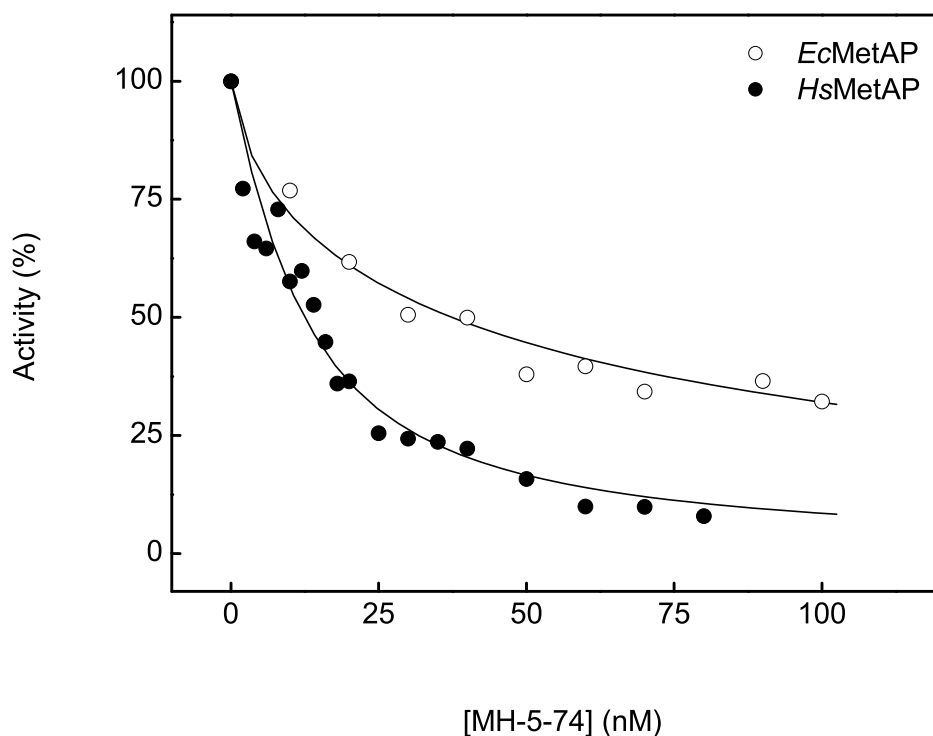


Figure 5.19. MH-5-74 inhibition constants for *EcMetAP* and *hmap*. The activity of 1 μM *EcMetAP* and 4 μM *HsMetAP* was measured in 25 mM HEPES pH 7.5 containing 100 mM NaCl and 100 μM CoCl_2 with 100 μM substrate (Met-Pro-*p*NA) and increasing concentrations of the inhibitor MH-5-74. The data were analyzed for competitive inhibition using Eq. (3). The solid lines represent the best fit of the data with the K_i values being equal to 44 ± 5 and 11 ± 1 nM for *EcMetAP* and *HsMetAP* respectively.

The inhibitor 5-[4-(dimethylamino)phenyl]methylidene-barbituric acid (MH-5-53) showed particularly interesting spectral properties, wherein the two isoforms of MetAP caused significantly different changes in the absorbance spectra of the compound. Figure 5.20 shows the absorbance spectra of the inhibitor in 25 mM HEPES *pH* 7.5 containing 100 mM NaCl in the absence and presence of MetAP. The absorbance spectrum of MH-5-53 has two peaks at 355 and 485 nm. As seen from the data in Figure 5.20, the absorbance spectra are affected on the addition of both *Ec*MetAP and *Hs*MetAP such that the two peaks are differently affected. Whereas the absorbance of MH-5-53 at 355 nm remains unchanged upon addition of enzyme, the absorbance at 485 nm is decreased. However, the extent of change at 485 nm is different with *Ec*MetAP and *Hs*MetAP and this difference is illustrated by the ratio of the two peaks (355:485 nm) in the presence of each isozyme, as shown in Table 5.8 on page 136.

In order to identify the factors affecting the above changes in the spectral properties of MH-5-53, the effect of various conditions on the absorbance spectra of the inhibitor were studied. The effects of solvent polarity and *pH* on the absorbance spectra of MH-5-53 are shown in Figure 5.21 (panels A and B respectively). It is apparent that both factors, non-polar environment (dimethylformamide) and acidic *pH* (phosphate buffer *pH* 4.8), selectively enhanced the absorption at the second (485 nm) peak (see Table 5.8). In addition, the peaks were blue-shifted by 15 nm in case of DMF.

Since the *pH* of the solution was able to change the absorbance spectra of MH-5-53, the reversibility of the change was studied by repeatedly alternating the *pH* of the inhibitor solution between acidic and basic conditions, by the addition of HCl or NaOH. Figure 5.22 shows the change in absorbance at the 485 nm peak as a function of *pH* of the MH-5-53 solution. It is clear that the *pH* dependent change in spectra of MH-5-53 is almost completely reversible, with a small loss in signal apparent

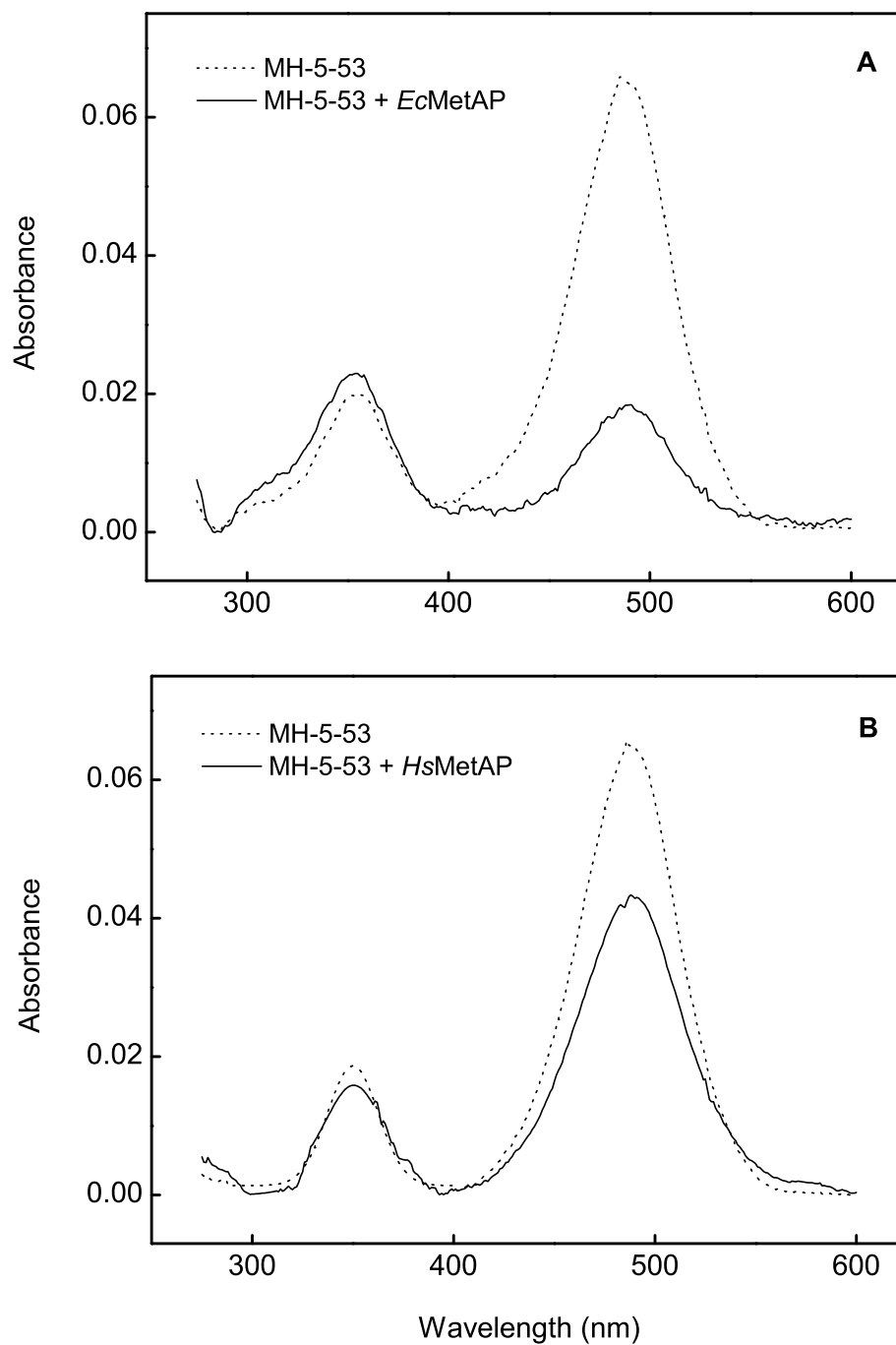


Figure 5.20. Spectral changes in MH-5-53 upon binding to *EcMetAP* and *HsMetAP*. The absorption spectra of 1 μM MH-5-53 were measured in 25 mM HEPES pH 7.5 containing 100 mM NaCl and 100 μM CoCl_2 in the absence (dotted line) and presence (solid line) of *EcMetAP* (A) or *HsMetAP* (B).

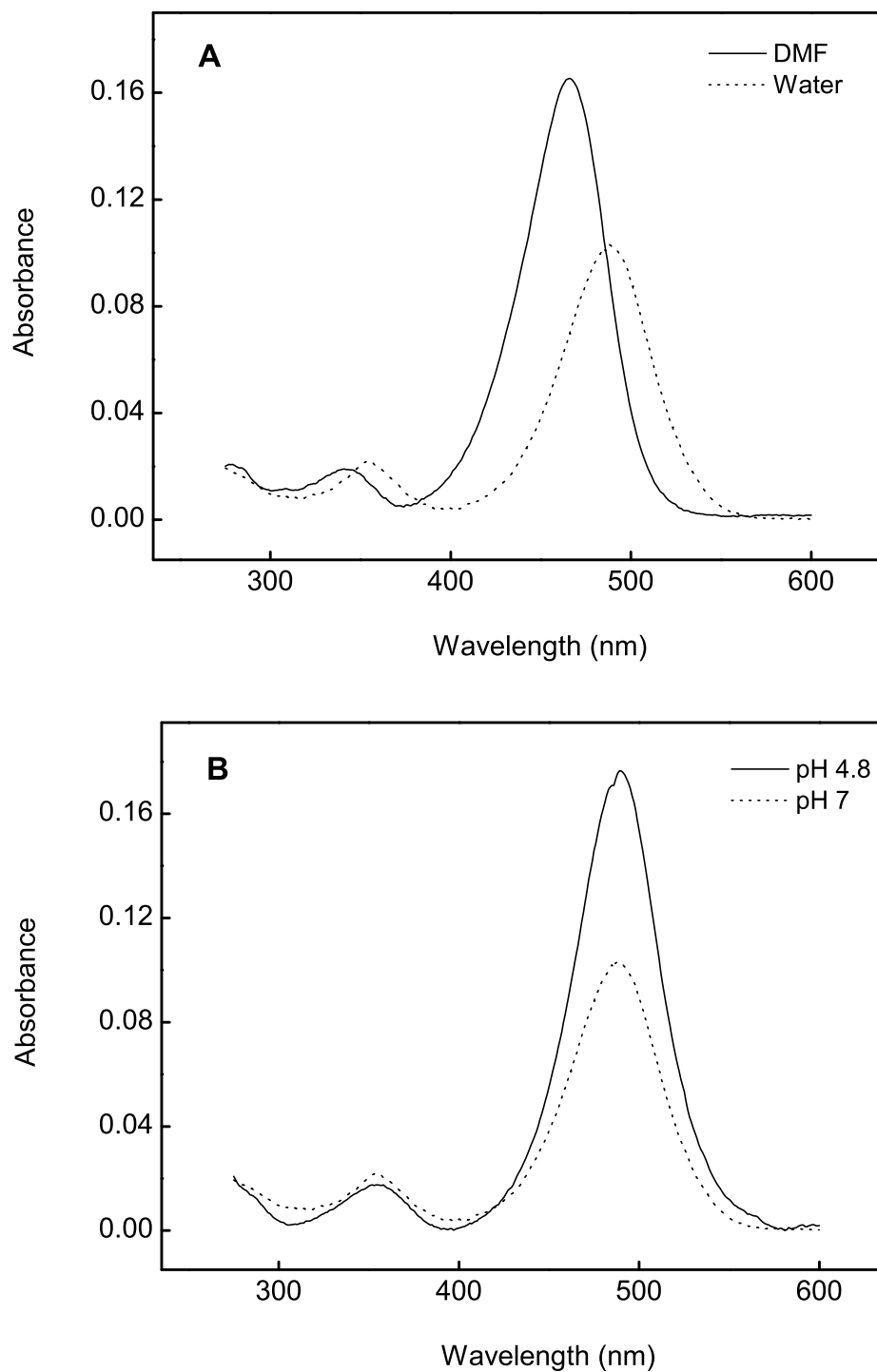


Figure 5.21. Effect of solvent and pH on the spectral properties of MH-5-53. The absorption spectra of MH-5-53 were measured in different solvents (DMF and water, **A**) as well as in phosphate buffers of varying pH (pH 4.8 and pH 7, **B**).

over time. In order to ascertain the reason for the small loss in reversibility of the spectra, a solution of the inhibitor was incubated in HEPES pH 7.5 and the spectra were recorded over time. Figure 5.23 shows the change in spectra over time in HEPES buffer pH 7.5 (panel A).

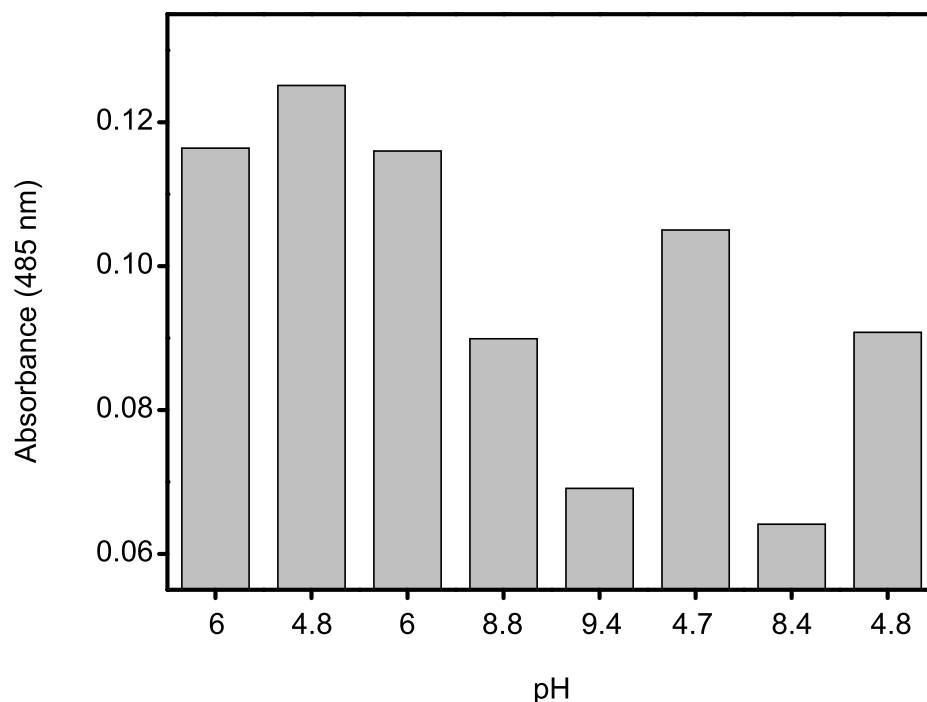


Figure 5.22. pH dependent reversibility of MH-5-53 spectra. The absorbance (A_{485}) of 4 μ M MH-5-53 (prepared in water) was measured at pH 6. Further measurements (left to right) were made immediately after changing the pH of the solution by adding acid (HCl) or base (NaOH).

Note that while the absorbance at 485 nm decreases, the absorbance at 355 nm concomitantly increases. It is evident from the data that the ratio of the two peaks changes as a function of time. Figure 5.23B shows the time dependent change in absorbance at 485 nm under various conditions. The solution of MH-5-53 was thus found to be stable in DMF and at pH 4.8. Under other conditions, the decrease in absorbance at the 485 nm peak was accompanied by an increase in the absorbance at the 355 nm peak as seen in panel A, except in the case of EDTA where the absorbance

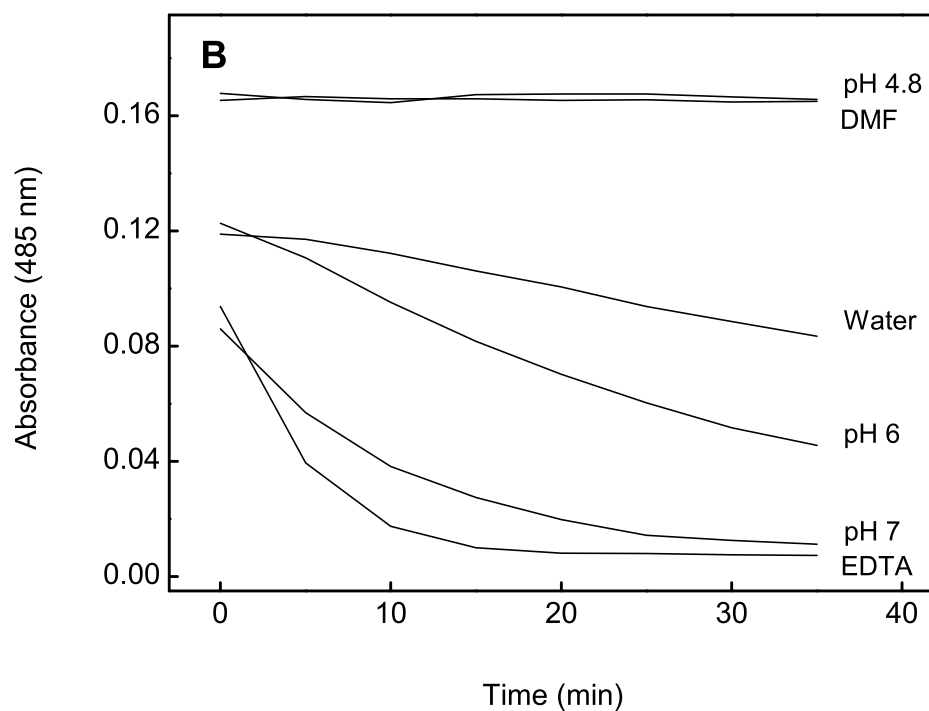
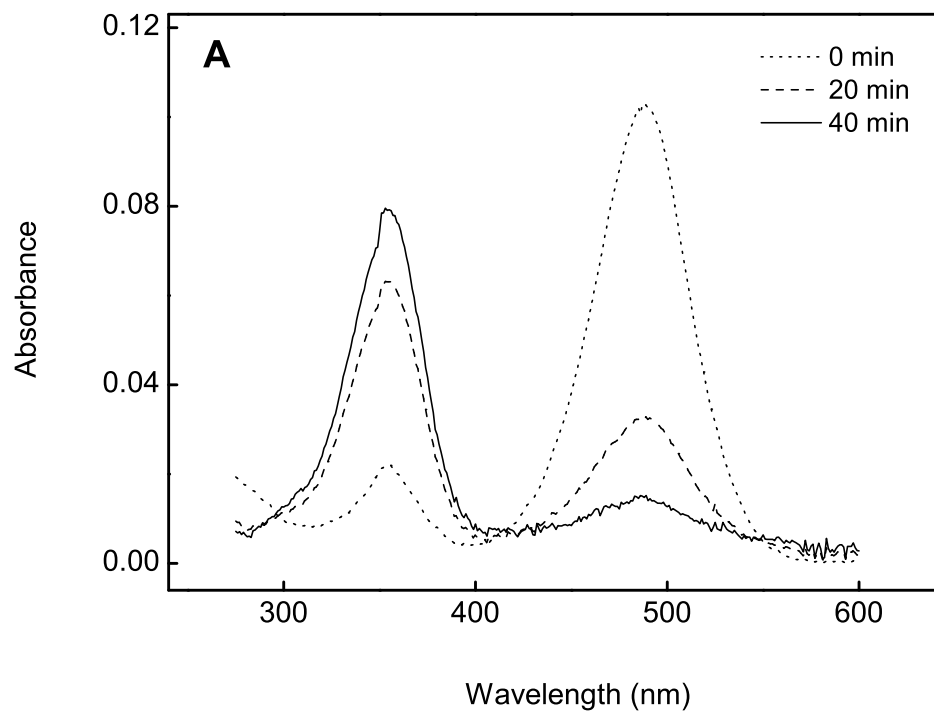


Figure 5.23. Change in MH-5-53 spectra over time. The absorbance spectra of MH-5-53 were recorded over time. Panel **A** shows the change in the spectra after 20 and 40 min. The change in absorbance at 485 nm was plotted as a function of time in panel **B**.

Table 5.8. Changes in MH-5-53 spectra.¹

Effector	A_{485}/A_{355} ratio
Control	4
<i>EcMetAP</i>	0.78
<i>HsMetAP</i>	2.6
DMF ²	8.7
pH 4.8	19
60 min ³	0.12

¹ Absorbance spectra of MH-5-53, prepared in DMF and diluted in either buffer (phosphate buffer pH 4.8 or 7) or DMF, were measured. Alternatively, the spectra were measured in HEPES pH 7.5 in the absence and presence of MetAPs.

² The absorbance ratio in DMF was taken at the blue-shifted peaks (465/340).

³ The incubation for 60 min was carried out at pH 7.

at 355 nm remained constant despite the decrease at 485 nm. It must be noted that the spectral changes reported in the presence of MetAP isoforms (Figure 5.20 on page 132) were immediate and remained stable over time. A possible explanation of the above features of MH-5-53 and its interaction with the MetAP isozymes is presented in section §6.1.1.

5.5. Inhibition of *EcMetAP* by Cyclodextrin

5.5.1. Effect of HP- β -CD on *EcMetAP* activity

As described in section §5.4, although the inhibitor MH-5-75 had a strong inhibitory effect on both *E. coli* and human MetAP type 1, its extremely poor solubility prevented further characterization of the enzyme-inhibitor interaction. A preparation

of the inhibitor in complex with the solubilizing agent 2-hydroxypropyl- β -cyclodextrin (HP- β -CD) was therefore considered as a ‘solution’ to this problem, and an attempt was made to test the efficacy of the inhibitor-HP- β -CD complex against *EcMetAP* activity.

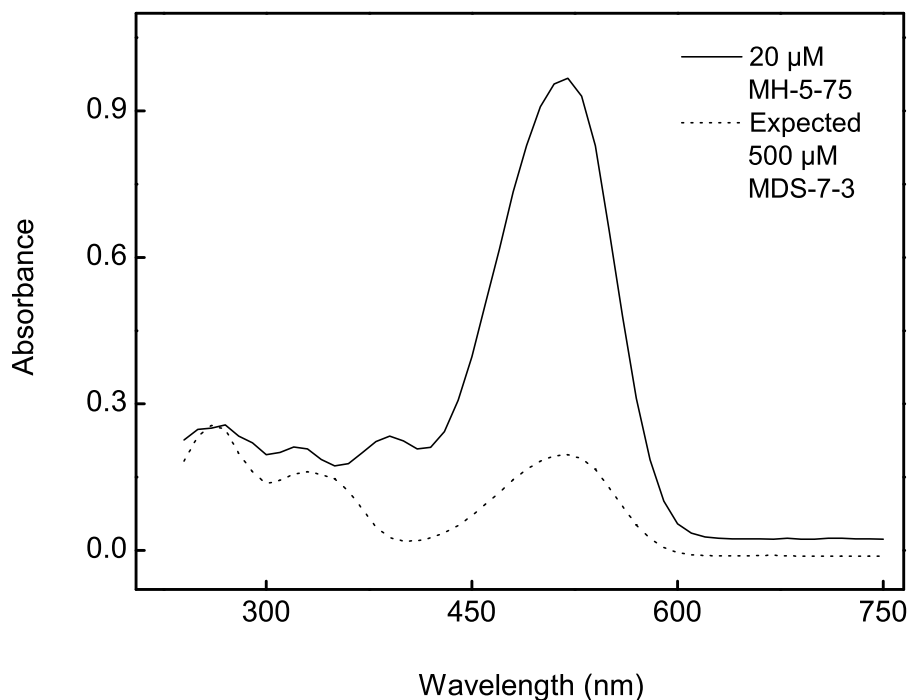


Figure 5.24. Absorbance spectra of free and encapsulated MH-5-75. The absorbance spectra of 20 μ M MH-5-75 and 500 μ M MDS-7-3 (encapsulated MH-5-75) were measured in DMF.

The MH-5-75-HP- β -CD complex was kindly provided by Dr. Sanku Mallik as a compound (henceforth referred to as MDS-7-3) containing 19 mg of MH-5-75 encapsulated in a total of 247 mg of the preparation. However while studying the inhibitory properties of MDS-7-3, it was observed that its potency against *EcMetAP* was greatly reduced as compared to the free inhibitor MH-5-75 (see Figure 5.25 on the following page). It was deemed probable that the fractional yield of MH-5-75 in the preparation was much lower than expected. In order to test this hypothesis, the absorbance spectra of MH-5-75 and MDS-7-3 solutions (prepared in DMF, at the same

concentration based on the expectation that 19 mg of MH-5-75 was encapsulated in a total 247 mg of MDS-7-3 preparation, i.e. 7.7%) were compared (Figure 5.24). It is apparent that the absorbance of MH-5-75 in the MDS-7-3 preparation is greatly reduced. These data suggested that the content of MH-5-75 in the complex preparation (MDS-7-3) was much lower than that expected from a 7.7% yield. The difference in the absorbance of the two solutions indicate a 100 fold lower concentration of MH-5-75 in the complex than expected. A comparison of the absorbance of the MDS-7-3 preparation with a standard curve of MDS-5-75 revealed that the actual inhibitor (MH-5-75) content in the encapsulated preparation (MDS-7-3) was 0.065%.

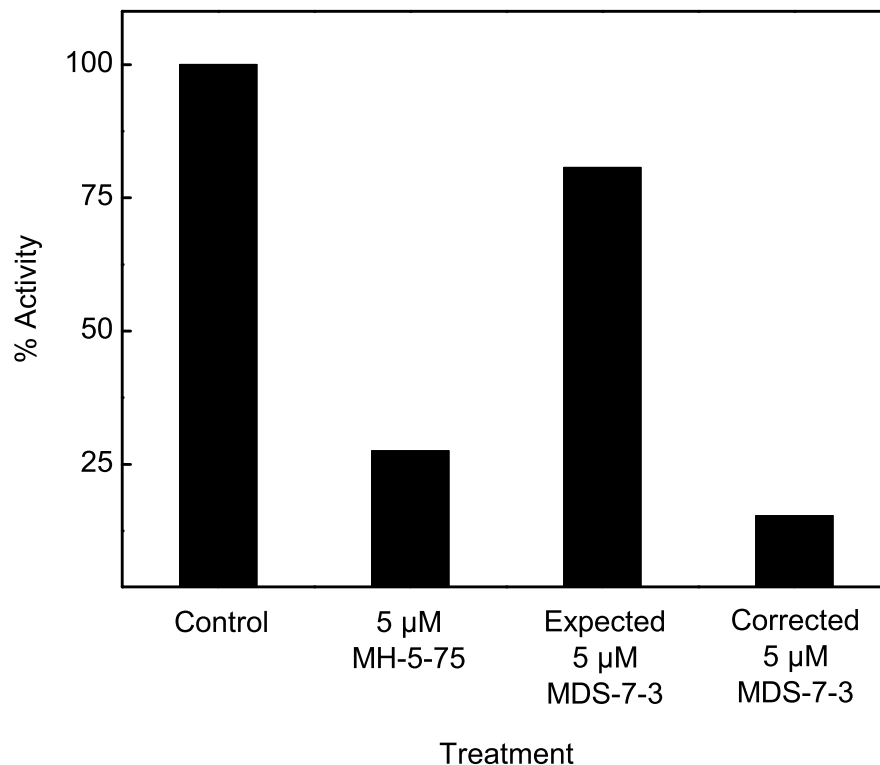


Figure 5.25. Comparison of *EcMetAP* inhibition by free and encapsulated MH-5-75. The activity of *EcMetAP* was measured by the direct assay in the absence (control) and presence of 5 μM MH-5-75 or MDS-7-3. The expected and corrected 5 μM solutions were prepared based on the given encapsulation yield and the experimentally determined concentration respectively.

In order to compensate for the low MH-5-75 content in the preparation, the inhibitory effect of the complex was re-examined at an appropriately higher concentration of MDS-7-3. Figure 5.25 shows the relative inhibitory effects of 5 μM MH-5-75, 5 μM MDS-7-3 prepared based on the known yield (7.7%), and 5 μM MDS-7-3 prepared based on the experimentally determined yield (0.065%). It is clear from the data that the solution of MDS-7-3 prepared according to the experimentally determined yield of inhibitor was much more potent than what was observed earlier. In fact it seemed that the effect of encapsulated inhibitor was greater than that of the free ligand. However due to the nature of the preparation, upon increasing the concentration to achieve true 5 μM MH-5-75 in the MDS-7-3 compound, the concentration of HP- β -CD was equally increased, resulting in a concentration of 3 mM HP- β -CD in the assay. Hence it was necessary to discount the interference of the solubilizing agent in the enzyme assay, due its unusually high concentration. A quick test revealed that pure HP- β -CD itself had an inhibitory effect on the activity of *EcMetAP* (Figure 5.26).

As is evident from the data of Figure 5.26, increasing concentrations of free HP- β -CD showed an increasing inhibitory effect on *EcMetAP* activity. The inhibition of enzyme activity by cyclodextrins has been reported to occur via occlusion of the substrate within the cyclodextrin cavity. In order to confirm this scenario, the interaction of HP- β -CD with the *EcMetAP* substrate Met-AMC was studied using the fluorescence signal of the substrate.

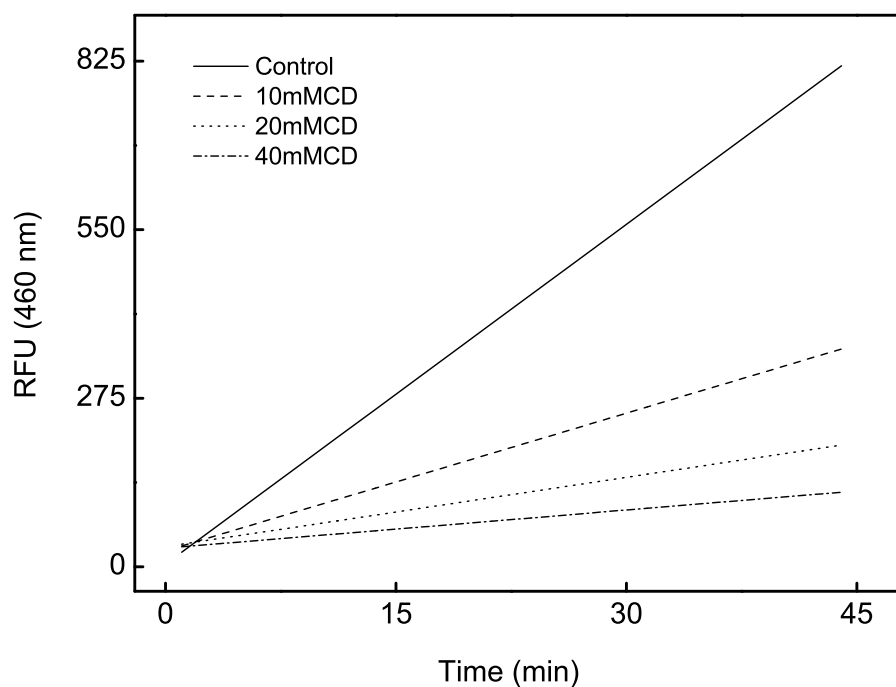


Figure 5.26. The catalytic activity of $1\ \mu\text{M}$ *EcMetAP* was measured in a 96 well micro-titer plate in assay buffer (25 mM HEPES pH 7.5 containing 100 mM NaCl and $10\ \mu\text{M}$ CoCl_2) with $400\ \mu\text{M}$ of substrate Met-AMC in the absence (Control) and presence of 10, 20 and 40 mM HP- β -CD, by monitoring the release of AMC ($\lambda_{\text{ex}} = 360\ \text{nm}$, $\lambda_{\text{em}} = 460\ \text{nm}$) over time using a plate reader.

5.5.2. Interaction of Met-AMC with HP- β -CD

Cyclodextrins are known to affect the spectral properties of their guest molecules and this effect is commonly attributed to the exclusion of solvent molecules from the surface of the entrapped guest molecules. In order to probe the potential formation of a host-guest complex between HP- β -CD and Met-AMC, changes in the fluorescence spectra of Met-AMC were studied in the absence and presence of HP- β -CD.

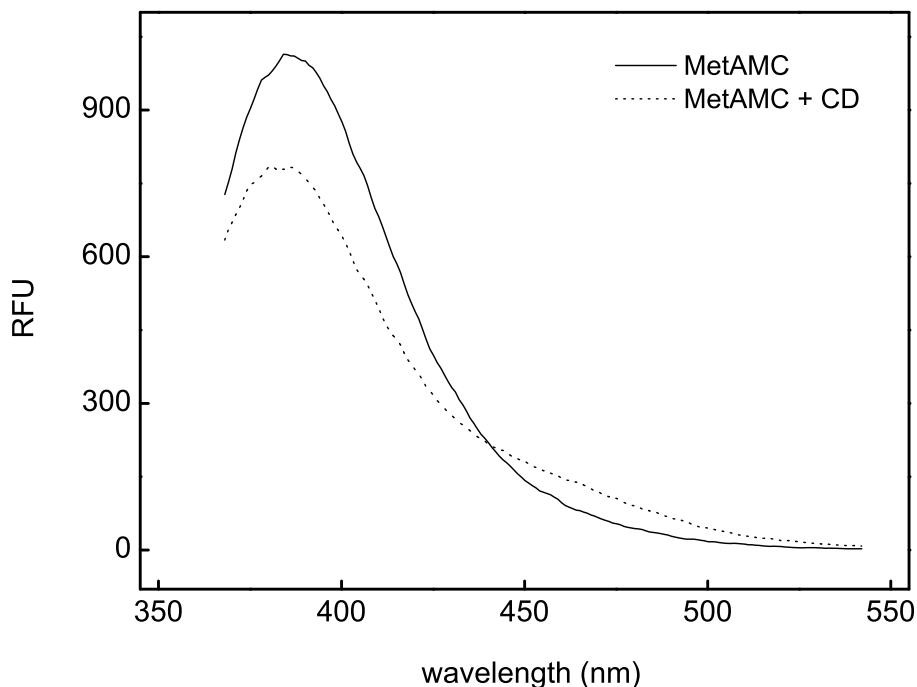


Figure 5.27. Effect of CD on Met-AMC fluorescence spectra. The emission spectra ($\lambda_{\text{ex}} = 315 \text{ nm}$) of $10 \mu\text{M}$ Met-AMC in the absence (solid) and presence (dotted) of 20 mM CD were taken in 25 mM HEPES pH 7.5 containing 100 mM NaCl and $10 \mu\text{M}$ CoCl_2

Figure 5.27 shows the effect of HP- β -CD on the fluorescence spectrum of Met-AMC. The spectra of $10 \mu\text{M}$ Met-AMC were measured ($\lambda_{\text{ex}} = 315 \text{ nm}$) in the absence and presence of 20 mM HP- β -CD. The addition of HP- β -CD clearly altered the fluorescence spectrum resulting in a decrease in intensity at the 380 nm peak and an increase at 460 nm , indicating an interaction between HP- β -CD and Met-AMC.

The above change in fluorescence was used to determine the binding affinity of the HP- β -CD–Met-AMC complex. A fixed concentration of Met-AMC was titrated with increasing concentrations of HP- β -CD and the increase in fluorescence intensity at 460 nm was measured. The data, shown in Figure 5.28, conformed to the hyperbolic profile typical of weak, non-cooperative binding. Analysis with the complete quadratic function (Eq. (4) described in section §4.5.1) gave the best fit of the data with a single binding site and the dissociation constant of the complex being 3.50 ± 0.25 mM.

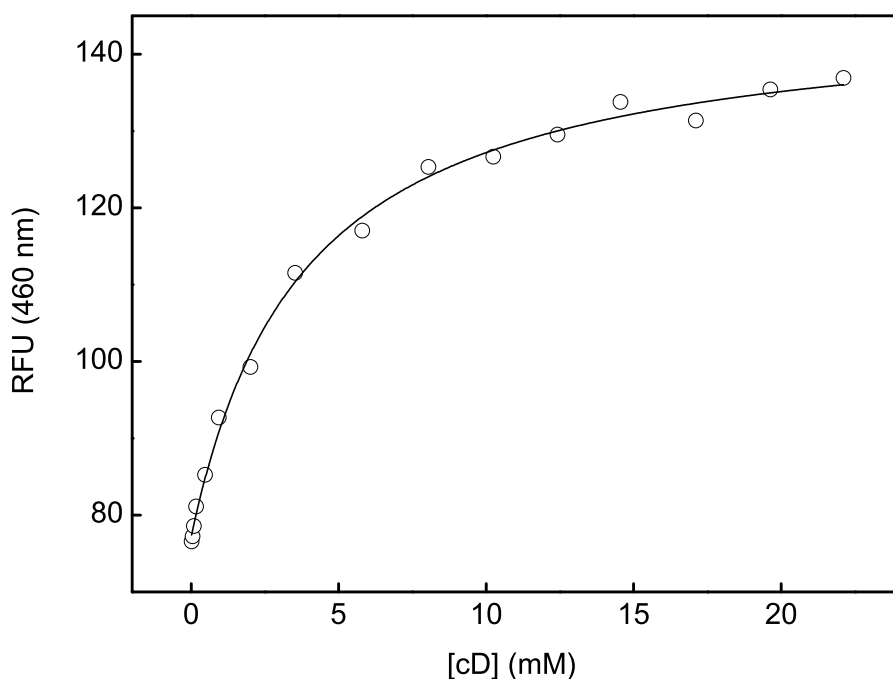


Figure 5.28. Binding affinity of the Met-AMC– CD complex. The increase in intensity at 460 nm on titration of CD into 10 μ M Met-AMC is plotted as a function of CD concentration. The smooth line is the best fit of the data for the K_d value of the CD–Met-AMC complex being equal to 3.50 ± 0.25 mM.

5.5.3. Mechanism of *EcMetAP* inhibition by HP- β -CD

A study of the HP- β -CD inhibition of *EcMetAP* activity was undertaken to confirm the mode of action of the solubilizing agent on the enzyme. The activity of *EcMetAP* was measured in the presence of varying concentrations of both substrate

(Met-AMC) and HP- β -CD (see Figure 5.32 on page 149). Upon inspection of the data in Figure 5.32, it was observed that *EcMetAP* was apparently inhibited at higher concentrations of substrate even in the absence of cyclodextrin. In order to rule out the possibility of inner-filter effect due to high concentration of the substrate (Met-AMC), the fluorescence intensity of Met-AMC was measured as a function of concentration (up to 1 mM Met-AMC). The standard plot of the RFU as a function of Met-AMC concentration (Figure 5.29) resulted in an excellent linear fit indicating that no inner-filter effect occurred up to 1 mM Met-AMC.

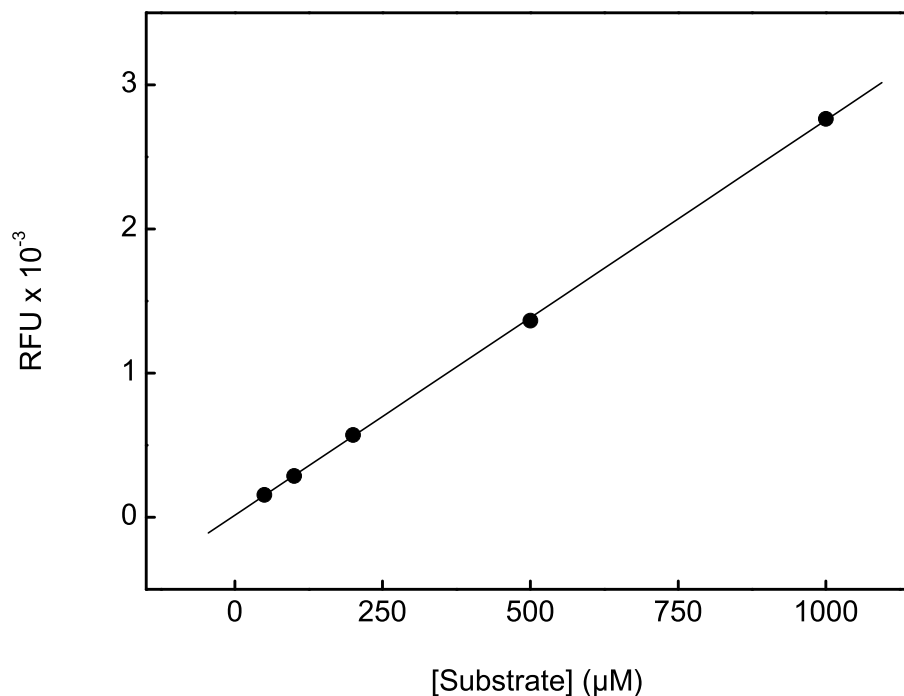


Figure 5.29. MetAMC standard plot. The fluorescence of MetAMC was measured in a 96-well microplate under the direct assay conditions. The data conformed to a linear fit with $R^2 = 0.9999$.

In the absence of inner-filter effect, the decrease in activity of *EcMetAP* could be explained by substrate inhibition caused by the binding of the substrate at a non-specific secondary site. In order to account for this inhibition at higher Met-AMC concentrations, the steady-state parameters of *EcMetAP* were investigated using an

extended range of the substrate. Figure 5.30 shows the data for *EcMetAP* activity with up to 800 μM Met-AMC. Note that the enzyme activity is clearly reduced at substrate concentrations above 400 μM , which is typical of inhibition caused by the binding of the substrate at an alternative, non-specific site on the enzyme. Analysis of the data with an alternative Michealis-Menten equation, modified to include substrate inhibition (Eq. (2) described in section §4.3.4), revealed the values of K_m , K_{mi} and k_{cat} to be $123 \pm 6 \mu\text{M}$, 1.1 mM and $0.034 \pm 0.002 \text{ s}^{-1}$, respectively.

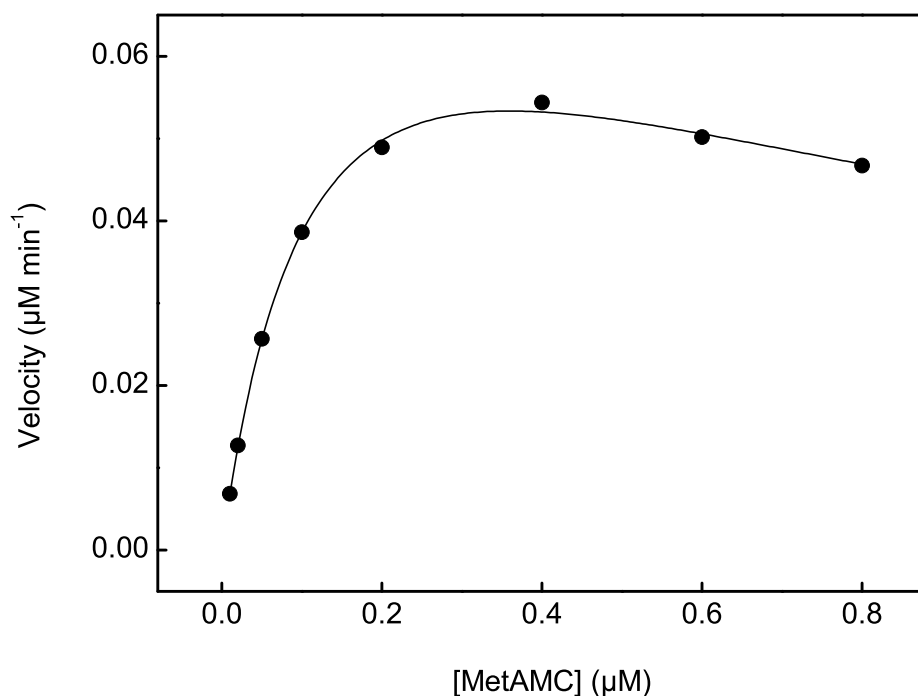
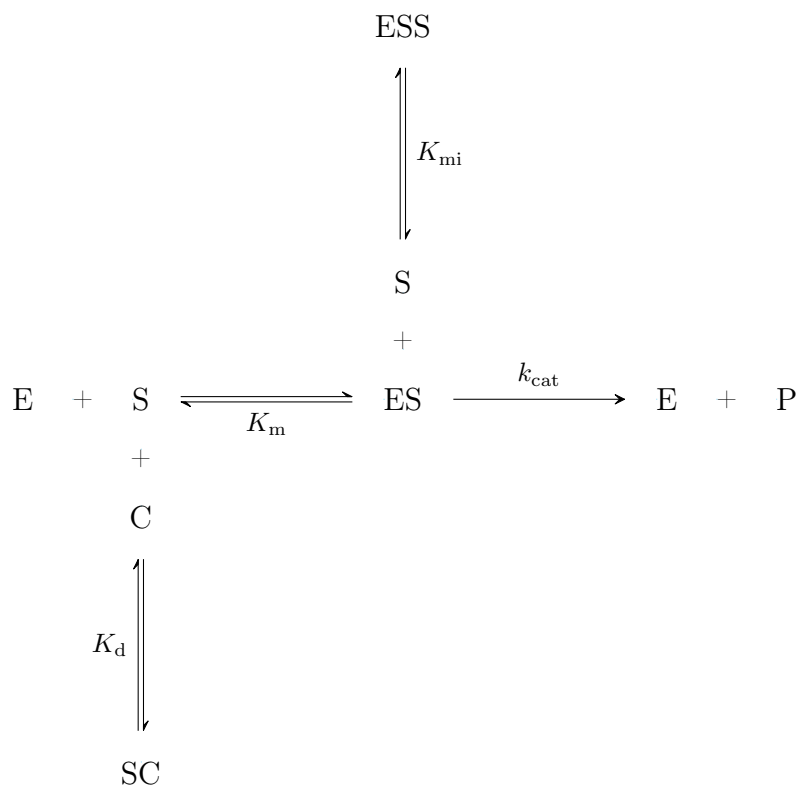


Figure 5.30. Catalytic features of *EcMetAP* with fluorogenic substrate Met-AMC. The activity of 0.75 μM *EcMetAP* was assayed in the presence of 10 to 800 μM substrate in a 96 well micro-titre plate, in 25 mM HEPES pH 7.5 containing 100 mM NaCl and 10 μM CoCl_2 . The reaction was monitored using a plate reader ($\lambda_{\text{ex}} = 360 \text{ nm}$, $\lambda_{\text{em}} = 460 \text{ nm}$) and the slope of the linear portion of the reaction trace was used to calculate the initial velocity. The smooth line represents the best fit of the data for the values of K_m , K_{mi} and k_{cat} as being equal to $123 \pm 6 \mu\text{M}$, 1.1 mM and $0.034 \pm 0.002 \text{ s}^{-1}$, respectively.

With the catalytic parameters of *EcMetAP* for substrate inhibition determined above, and based on the mode of cyclodextrin inhibition reported in literature as well as the evidence for the formation of HP- β -CD–Met-AMC complex, the *EcMetAP* inhibition data in Figure 5.32 were analyzed for the model described in Scheme 5.1, using the K_m , K_{mi} , k_{cat} and K_d values determined in this study.



Scheme 5.1. Mechanism of inhibition by cyclodextrin

According to this model, the data were fit to a ‘modified’ substrate-inhibition function (described by Eq. (2)) in which $[S]$ is substituted by $([S_0] - [SC])$, where $[SC]$ is the concentration of substrate-cyclodextrin complex formed in the assay, given by the equation

$$[SC] = \frac{[S] + K_d + [C] - \sqrt{([S] + K_d + [C])^2 - 4[S][C]}}{2} \quad (9)$$

However, the non-linear regression analysis of the data in Figure 5.32 using this model, failed to arrive at a reasonable fit. A comparison of the experimental data with simulated data (based on the mechanism of Scheme 5.1 and the steady-state parameter values listed above) is shown in Figure 5.31. Note that the observed activity of *EcMetAP*, as a function of HP- β -CD concentration, is much lower than that predicted by the model in Scheme 5.1. The discrepancy between the two indicates additional or alternative mechanisms involved in the inhibition of *EcMetAP* activity.

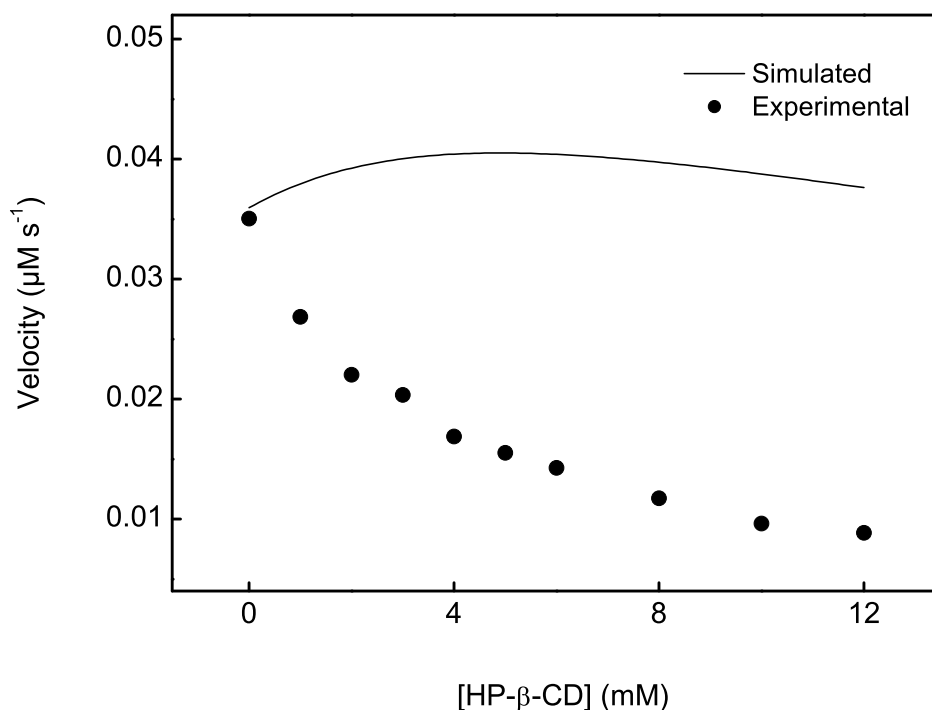
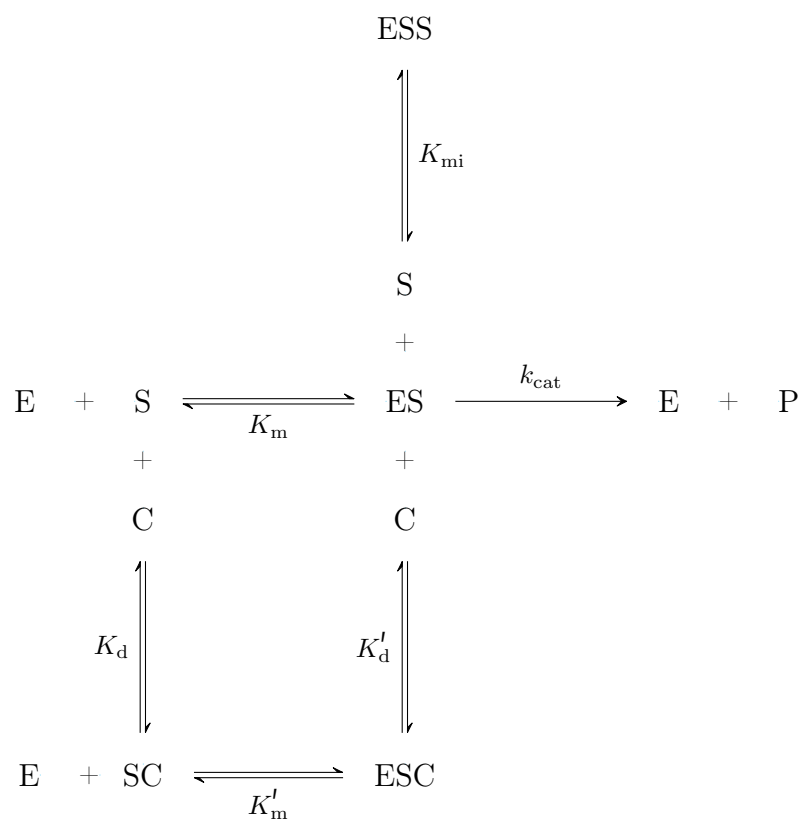


Figure 5.31. Experimental vs. simulated data for *EcMetAP* the inhibition of *EcMetAP* by HP- β -CD. The experimental data are for *EcMetAP* activity with 800 μM substrate (Met-AMC) and varying concentrations of HP- β -CD. The simulated data were obtained by calculating the concentration of free substrate in the assay as $([S_0] - [SC])$ (where $[SC]$ is given by Eq. (9)) and applying that to the substrate-inhibition model described by Eq. (2).

In order to identify the mechanism of *EcMetAP* inhibition by HP- β -CD, the data were then analyzed by the various possible interaction models. Due to the algebraic complexity introduced by the multiplex of probable interactions, the analysis was



Scheme 5.2. Mechanism of MetAP inhibition by cyclodextrin via substrate

conducted using the symbolic reactions based numerical methods via DynaFit software. Model discrimination analysis of the resulting fits from the different models, was also carried out through DynaFit (see Table 5.9), wherein the Akaike weight predicts the validity of a given model. Note that most of the models tested gave a Delta value > 10 and an Akaike weight of 0, indicating that these mechanisms of inhibition were highly improbable. The data in Table 5.9 revealed that the ‘mixed model’ (Scheme 5.2) was the most probable mechanism (Akaike weight ~ 1).

The complete data of *EcMetAP* inhibition by HP- β -CD, as analyzed by the mixed-model described in Scheme 5.2, is shown in Figure 5.32. The smooth lines indicate the best fit of the data for the K'_m and K'_d values of $55 \pm 5 \mu\text{M}$ and $1.2 \pm 0.1 \text{ mM}$, respectively. All other steady-state parameter values were calculated to be in close agreement with those determined previously.

Table 5.9. Model discrimination analysis for *EcMetAP* inhibition by HP- β -CD.¹

Model ²	AICc	Delta	weight
competitive (i)	20.9	462.6	0
competitive (ii)	20.9	462.6	0
uncompetitive	20.9	462.6	0
noncompetitive (i)	-462.3	15.4	0.000 45
noncompetitive (ii)	-365.7	76.0	0
noncompetitive (iii)	-323.5	118.2	0
mixed (i)	-441.7	0	0.999 55
mixed(ii)	-379.8	61.9	0
mixed (iii)	-423	42.3	0

¹ A delta value between 0 and 2 indicates “substantial” support for the model, where as a value greater than 10 indicates “essentially no” support. The most plausible model is identified by the highest Akaike weight.

² The various ‘competitive’, ‘uncompetitive’, ‘noncompetitive’ and ‘mixed’ models are described in the appendix.

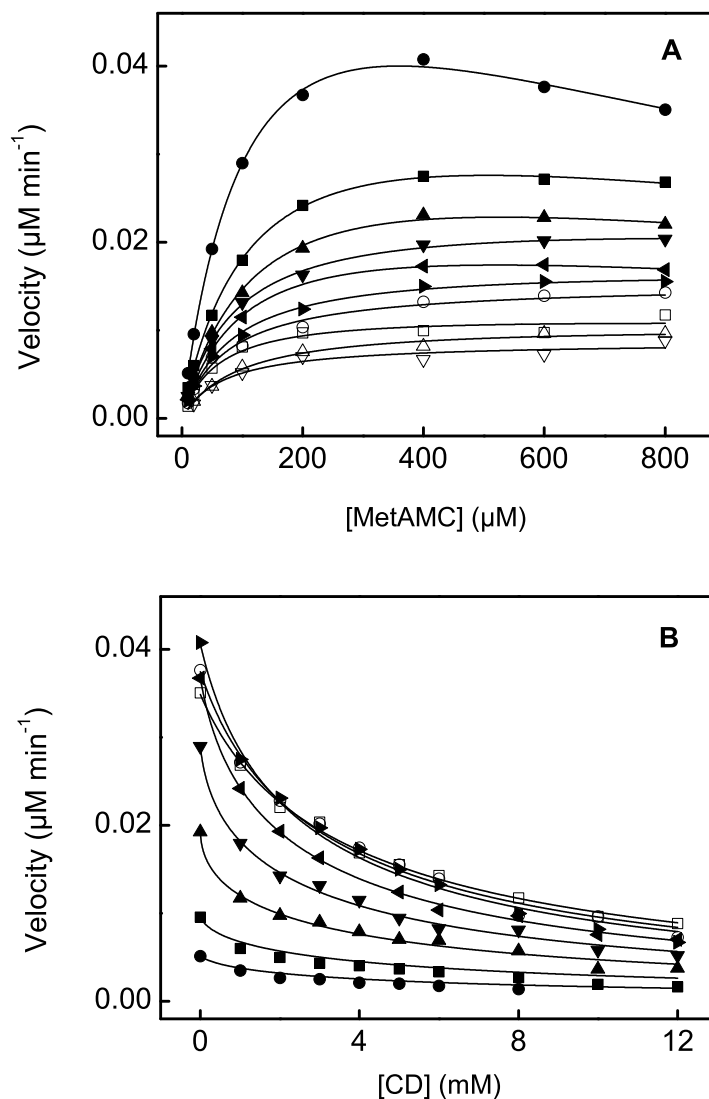


Figure 5.32. CD dependent inhibition profile of *EcMetAP*. The activity of $0.75 \mu\text{M}$ *EcMetAP* was measured in a 96 well micro-titer plate in assay buffer (25 mM HEPES pH 7.5, 100 mM NaCl, $10 \mu\text{M}$ CoCl_2) with 10 to $1000 \mu\text{M}$ substrate (MetAMC) in the presence of 0 to 12 mM CD. (A) The rates of the enzyme catalyzed reaction as a function of substrate (MetAMC) concentration in the presence of 0 (\bullet), 1 (\blacksquare), 2 (\blacktriangle), 3 (\blacktriangledown), 4 (\blacktriangleleft), 5 (\blacktriangleright), 6 (\circ), 8 (\square), 10 (\triangle) and 12 (∇) mM CD. (B) Replot of the data of (A) as a function of CD concentration at 10 (\bullet), 20 (\blacksquare), 50 (\blacktriangle), 100 (\blacktriangledown), 200 (\blacktriangleleft), 400 (\blacktriangleright), 600 (\circ) and 800 (\square) μM substrate (MetAMC). The smooth lines represent the best fit of the data using the model depicted in scheme 5.2, for the values of K_m , k_{cat} , K_{mi} , K_m^I , K_d and K_d^I being equal to $143 \pm 17 \mu\text{M}$, $0.090 \pm 0.006 \text{ min}^{-1}$, $894 \pm 148 \mu\text{M}$, $55 \pm 5 \mu\text{M}$, $3.3 \pm 0.4 \text{ mM}$ and $1.2 \pm 0.1 \text{ mM}$, respectively.

5.5.4. Crystal structure of the HP- β -CD–Met-AMC complex

According to the model describing the mechanism of substrate dependent inhibition of *EcMetAP* by cyclodextrin (Schmrefsd.final), the cyclodextrin-substrate complex (HP- β -CD–Met-AMC) binds reversibly to the enzyme active site forming a non-functional ternary complex. In order to gain support for the formation of this ternary complex as suggested by the steady-state kinetic data, the structure of the HP- β -CD–Met-AMC complex was studied.

The cyclodextrin cavity is relatively hydrophobic, which allows the molecule to act as an ideal guest for poorly soluble compounds. Of the two moieties in the *EcMetAP* substrate, methionine and 7-amino-4-methylcoumarin, it is conceivable that the coumarin moiety will be preferentially enclosed within the cyclodextrin cavity. In this scenario, the methionine residue remains exposed allowing the amino acid to interact and bind to the *EcMetAP* active site pocket.

A molecular docking of HP- β -CD and Met-AMC was carried out to test the conformation of the complex hypothesized above. An X-ray crystal structure of β -cyclodextrin (β -CD) from the RCSB protein databank was used to dock a molecule of Met-AMC built *in silico*. Figure 5.33 shows the output of the analysis, with the AMC moiety enclosed in the cyclodextrin cavity, and the methionine side chain projecting out of the β -CD cavity as envisioned.

In order to further prove the existence of the HP- β -CD–Met-AMC complex in the conformation described above, the complex was crystallized and the crystal structure was resolved by data from X-ray diffraction. Due to the inability of HP- β -CD to form a crystalline lattice, β -cyclodextrin was used as a substitute. Colorless plate-like crystals were obtained by slow cooling a heated mixture of 1 mmol β -cyclodextrin in water and 1 mmol Met-AMC in ethanol. X-ray diffraction data collection and structure resolution and refinement were carried out by Dr. Angel Ugrinov at the

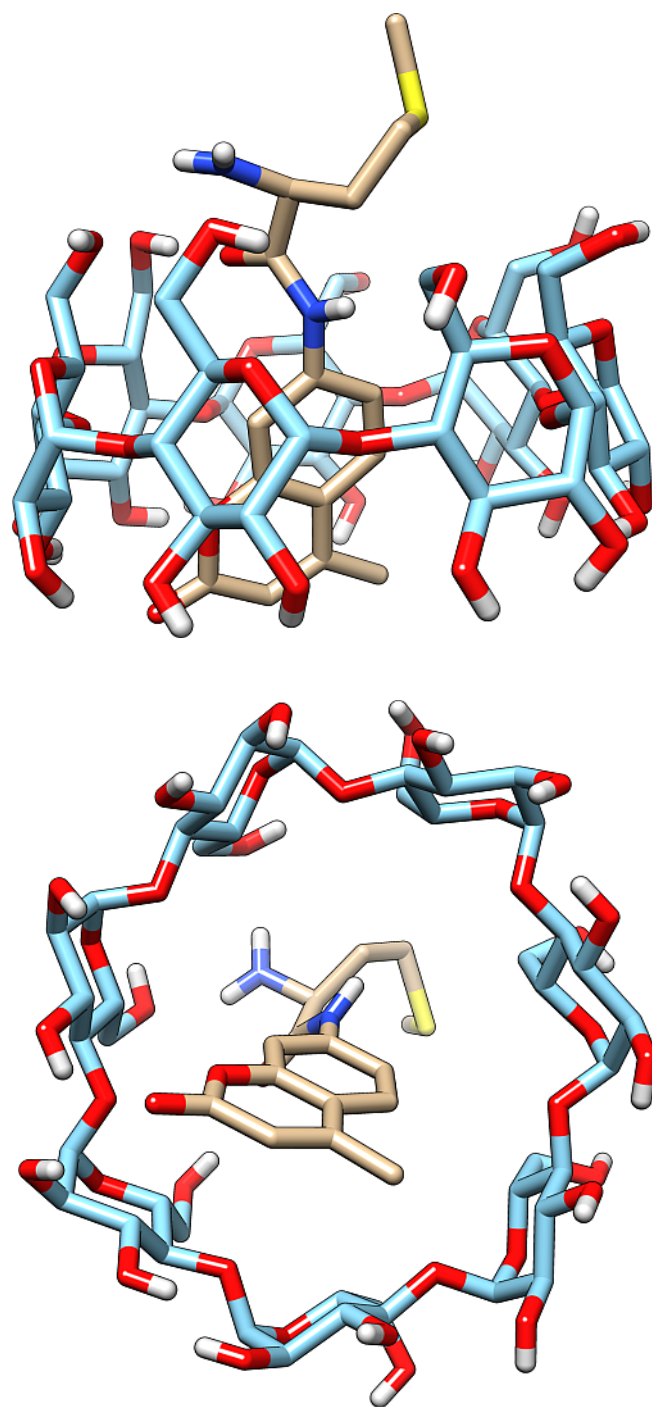


Figure 5.33. Molecular docking of HP- β -CD and Met-AMC. Met-AMC was docked with the crystal structure of β -cyclodextrin (from 2ZYN) using AutoDock Vina.

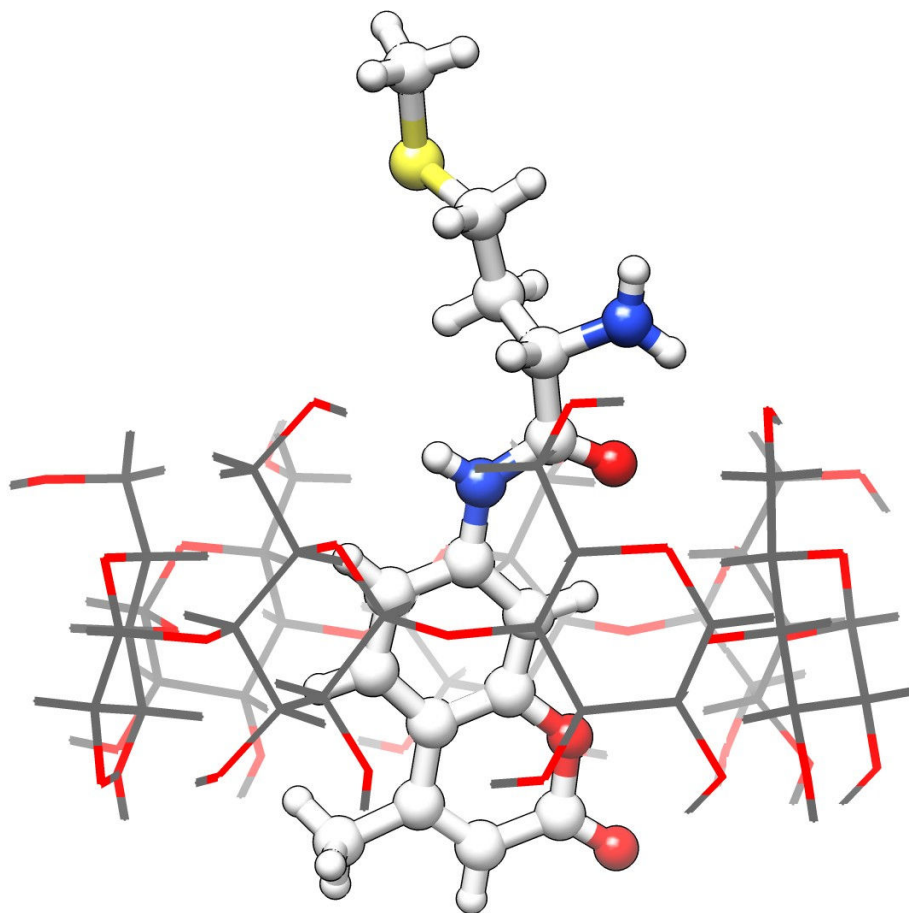


Figure 5.34. X-ray crystal structure of the Met-AMC- β -CD complex. The structures of Met-AMC and β -cyclodextrin are represented by ball-and-stick and wire models respectively. Note that the methionine residue of Met-AMC is protruding out of the β -cyclodextrin cavity

Department of Chemistry & Biochemistry, North Dakota State University (Fargo, ND). A representation of the crystal structure is shown in Figure 5.34. As hypothesized earlier, and supported by the docking results, the coumarin moiety of the substrate is seen trapped within the cyclodextrin cavity, while the methionine side chain extends outside. The X-ray crystal structural data reveals that the methionine side chain extends about 6.5 Å from the cyclodextrin surface.

5.5.5. Molecular modeling studies

In the previous sections, the formation of a HP- β -CD–Met-AMC complex was shown to occur, with the specific conformation wherein the methionine side chain of the substrate projects out of the cyclodextrin cavity. Additionally, steady-state kinetic data suggested that this complex interacted with the *Ec*MetAP active site pocket, resulting in inhibition of enzyme activity. In order to prove the formation of such a *Ec*MetAP–HP- β -CD–Met-AMC ternary complex, attempts were made to probe the binding via isothermal titration calorimetry. However these attempts were unsuccessful due to the extremely high heat of dilution of HP- β -CD [143]. Moreover no suitable spectroscopic signal could be detected for the interaction of the HP- β -CD–Met-AMC complex with *Ec*MetAP. Therefore the feasibility of this interaction was studied via molecular dynamics simulations.

The structures of each interacting species (*Ec*MetAP, Met-AMC and HP- β -CD) were minimized in a solvent sphere prior to MD simulations. For each simulation, the interacting species were placed at a distance of $< 10 \text{ \AA}$ from each other, within a solvent sphere. Simulations were run for the following interacting complexes (a) Met-AMC and HP- β -CD (S + C), (b) *Ec*MetAP and Met-AMC (E + S), and (c) *Ec*MetAP, Met-AMC and HP- β -CD (E + S + C). The equilibration of the above systems was confirmed by RMSD analysis of the trajectories. Figure 5.35 shows the RMSD data for the substrate (Met-AMC) for the initial 50 ps of the equilibration (total run time of upto 250 ps). The initial increase represents the translocation of the molecule to its interaction partner (the cavity of cyclodextrin, or the active site pocket of the enzyme). The following plateau indicates the equilibration of the system in its energetically stable state. The interaction energies for the species were calculated for

the equilibrated systems and compared to affirm the relative stability of each complex as suggested by the model in Scheme 5.2. The total interaction energies for each system are listed in Table 5.10.

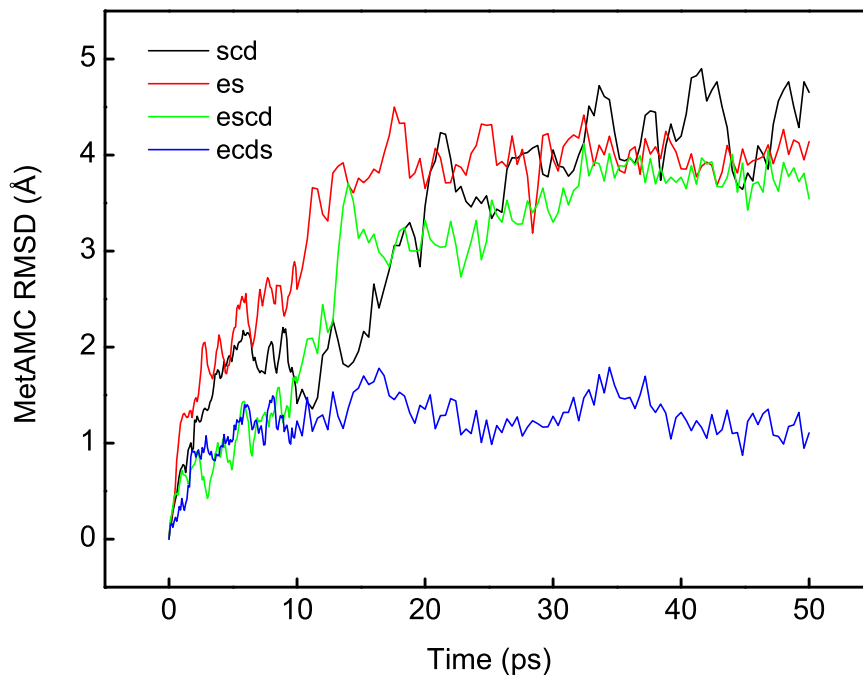


Figure 5.35. Met-AMC RMSD over the course of MD trajectories. The molecules in each system were positioned to mimic the pathway of complex formation described in scheme 5.2 on page 147 (except for E + CD + S which is not described by the scheme). The large value of RMSD of Met-AMC for the S + CD, E + S, and E + S + CD simulations (4 Å) indicates the translocation of the substrate to within the cavity of cyclodextrin, enzyme active-site or both, resulting in the formation of the respective complexes. The low RMSD for the E + CD + S simulation (1 Å) indicates that the substrate remained in solution and the ternary complex did not form.

The relatively lower energy for the ternary complex of *Ec*MetAP–Met-AMC–HP- β -CD (E + S + C) suggests that this species is the most energetically stable among all interaction species, thus driving the equilibrium towards the formation of this complex. The contributions of each interaction in the ternary complex (E + S + C) were calculated to be (a) $-259 \text{ kcal mol}^{-1}$ for the methionine residue within

Table 5.10. Total interaction energies of systems from MD simulations.¹

System	Energy (kcal mol ⁻¹)
E + S	-330
S + C	-42
E + S + C	-340

¹ The interaction energies of the species in the equilibrated system were calculated using the NAMDEnergy module in VMD.

the *EcMetAP* active site pocket, (b) $-30 \text{ kcal mol}^{-1}$ for the AMC moiety within the HP- β -CD cavity, and (c) $-39 \text{ kcal mol}^{-1}$ for the interaction between *EcMetAP* and HP- β -CD.

The result of the MD simulation with *EcMetAP*, Met-AMC and HP- β -CD is shown in Figure 5.36. The clipped view reveals the interaction of the methionine residue of the substrate (magenta stick) with the active site pocket of the enzyme (gray) while the coumarin moiety of the substrate resides within the cyclodextrin cavity (blue). As indicated earlier, the methionine residue projects 6.5 \AA out from the CD cavity. Thus in the ternary (MetAP–Met-AMC–CD) complex, it is long enough to enter into the active site pocket. However within the above complex, the scissile bond of Met-AMC does not reach in the vicinity of the active site resident metal ion. Hence the enzyme catalyzed cleavage of the bridged Met-AMC (between CD and MetAP) is precluded, resulting in the inhibition of the enzyme catalyzed reaction as per the model mechanism of Scheme 5.2.

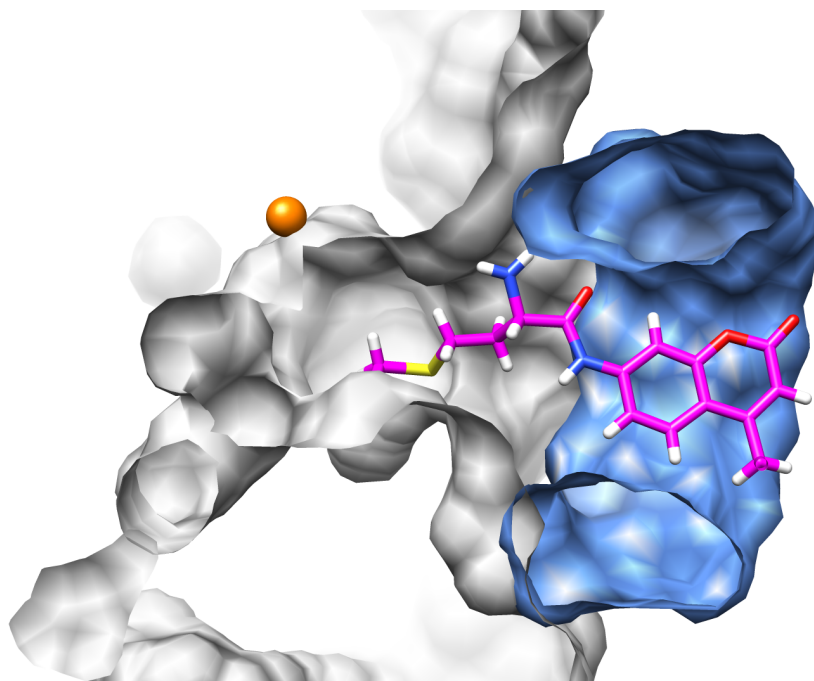


Figure 5.36. MD simulation of the *EcMetAP*–Met-AMC–HP- β -CD complex. Met-AMC is represented as magenta stick form and the molecular surfaces of *EcMetAP* and HP- β -CD are represented by gray and blue respectively. The active site metal ion (Mn^{2+}) is represented by the orange ball model.

5.6. Dansylamide-5-(2-ChloroPhenyl)Furanoic acid (DCPF) as a Metallo-specific Probe of *EcMetAP*

5.6.1. Metallo-specific inhibition of *EcMetAP* by DCPF

It has been noted that many potent inhibitors of MetAP are ineffective *in vivo* as a result of being specific for certain metal ions at the enzyme active site. In order to examine the nature of metallospecific binding of ligands to MetAP, the dansylamide derivatized metallo-specific inhibitor of *EcMetAP*, 5-(2-chlorophenyl)furanoic acid, was used as a probe, and its interactions with different metalloforms of *EcMetAP* were characterized. Since 5-(2-chlorophenyl)furanoic acid is known to be selective for the Mn^{2+} form of *EcMetAP*, the inhibition constant of DCPF for Mn^{2+} -*EcMetAP* was first determined by measuring the activity of Mn^{2+} -*EcMetAP* using the direct assay with 100 μM substrate (Met-AMC) and increasing concentrations of the inhibitor (DCPF).

Figure 5.37 shows the inhibition of Mn^{2+} -*EcMetAP* by DCPF. Analysis of the data by the quadratic function for competitive inhibition (Eq. (3)) gave the inhibition constant (K_i) of $0.56 \pm 0.24 \mu\text{M}$. Similar inhibition experiments were conducted with other metalloforms of *EcMetAP* to study the metal selective inhibition by DCPF (Figure 5.38). The inhibition constants for the various metalloforms of *EcMetAP* determined in this study are summarized in Table 5.11.

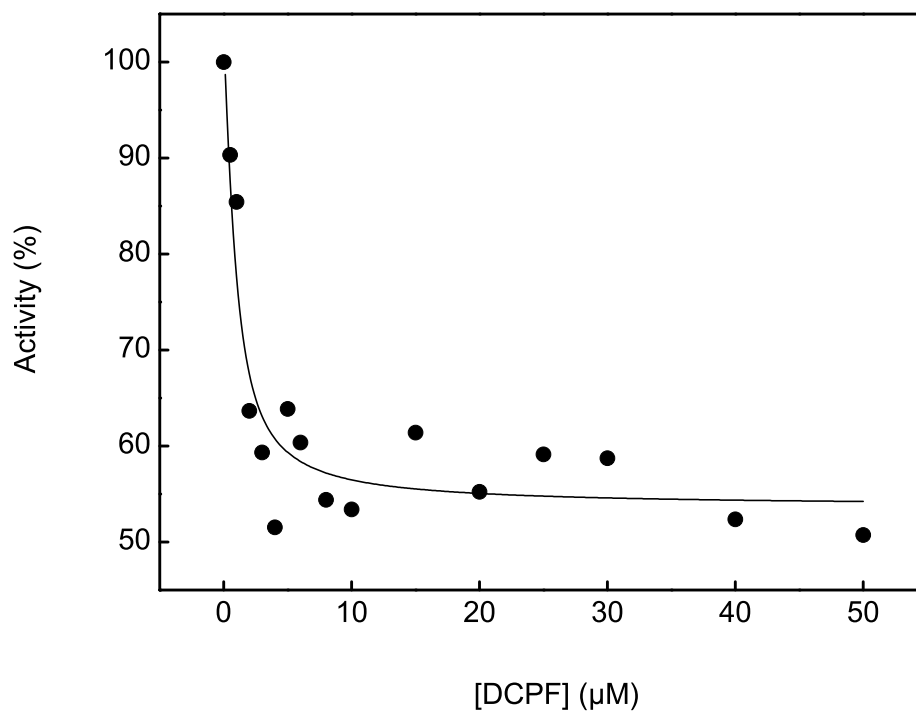


Figure 5.37. Inhibition of Mn^{2+} -*EcMetAP* by DCPF. The inhibition constant of DCPF was determined for the Mn^{2+} form of *EcMetAP* by measuring the activity of the enzyme in the presence of increasing concentrations of the inhibitor. The solid line represents the best fit of the data for the value of K_i being equal to $0.56 \pm 0.24 \mu\text{M}$.

Table 5.11. Metallospecific inhibition of *EcMetAP* by DCPF.¹

Metalloform	Inhibition constant (μM)
Mn^{2+}	0.56 ± 0.24
Co^{2+}	24 ± 4
Ni^{2+}	15 ± 3

¹ *EcMetAP* activity was measured in 25 mM HEPES pH 7.5 containing 100 mM NaCl and 10 μM of MnCl_2 , CoCl_2 or NiCl_2 and varying concentrations of DCPF, using the direct assay described in section §4.3.2.

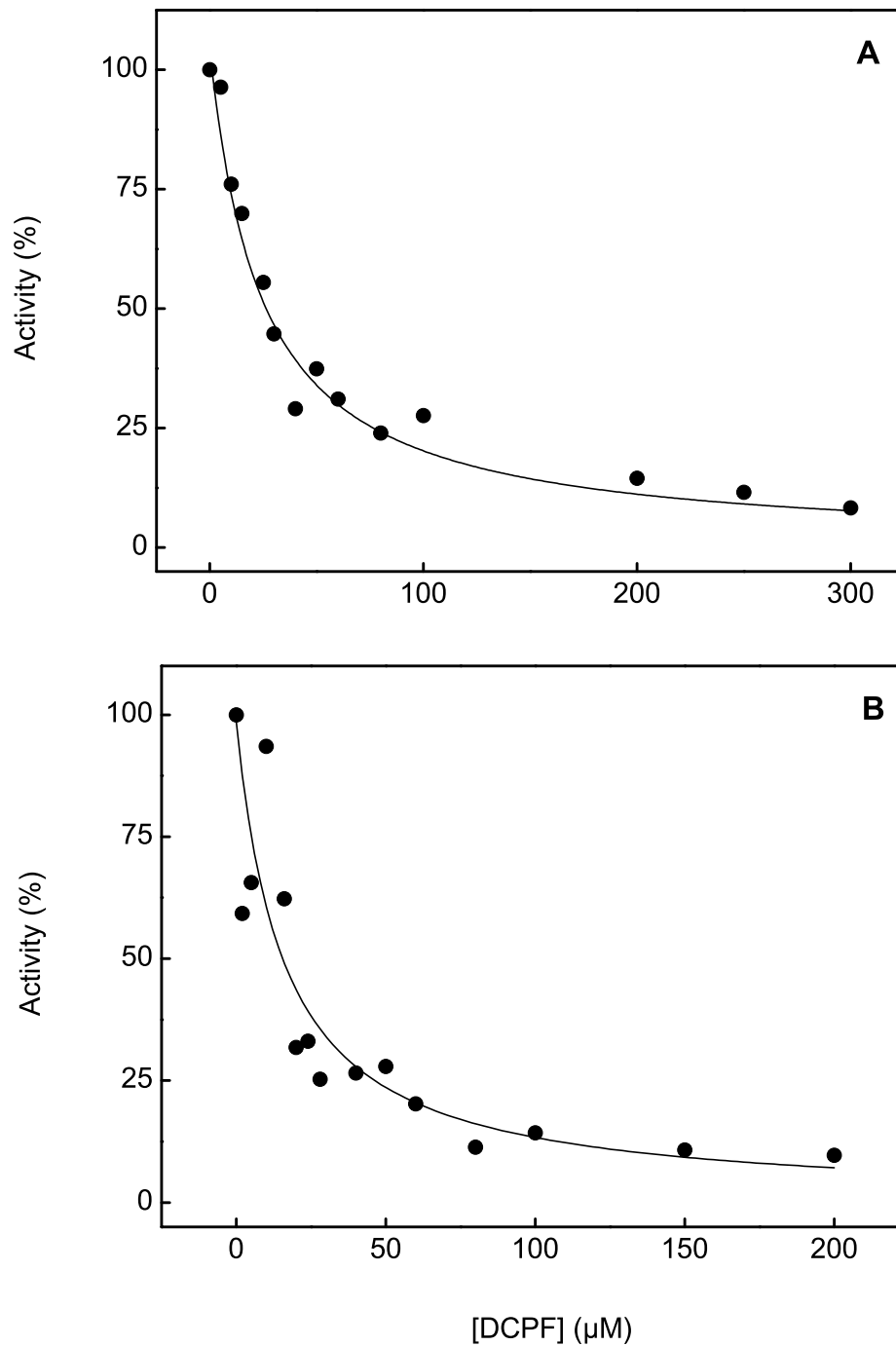


Figure 5.38. Inhibition of different metalloforms of *EcMetAP* by DCPF. The inhibition constant of DCPF was determined for the Co^{2+} and Ni^{2+} forms of *EcMetAP* (panel **A** and **B** respectively) by measuring the activity of the enzyme in the presence of increasing concentrations of the inhibitor. The solid line represents the best fit of the data for the value of K_i being equal to 24 ± 4 and $15 \pm 3 \mu\text{M}$ for the Co^{2+} and Ni^{2+} forms respectively.

5.6.2. Metallo-specific spectral properties of DCPF

The spectral properties of DCPF (as seen in Figure 5.8 on page 98) were ideal to study the interaction of the ligand with *EcMetAP*. The fluorescence emission spectra of DCPF (350 to 600 nm) were measured by exciting at 315 nm and were found to be significantly altered upon addition of apo-*EcMetAP* as shown in Figure 5.39, indicating the formation of DCPF-*EcMetAP* complex. Note that the emission peak of DCPF (525 nm) is enhanced, as well as blue shifted to 500 nm, on interaction with the enzyme.

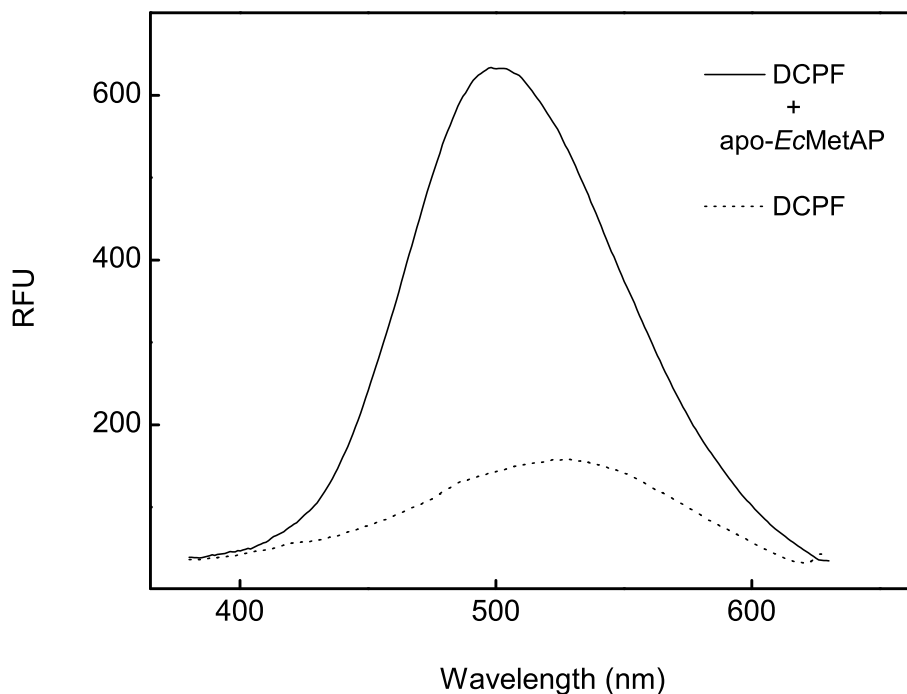


Figure 5.39. Effect of *EcMetAP* on DCPF fluorescence. The fluorescence spectra of 1 μM DCPF were measured ($\lambda_{\text{ex}} = 315 \text{ nm}$) in the absence (dotted line) and presence (solid line) of 10 μM apo-*EcMetAP*.

Upon establishing the metal dependent interaction of DCPF with *EcMetAP* as indicated by the inhibition of different metalloforms of the enzyme in the previous section, it was of interest to study the spectral properties of the inhibitor with respect to the various metalloforms of *EcMetAP*. The addition of various metalloforms of

EcMetAP to DCPF resulted in distinct changes in the fluorescence spectra of the inhibitor. Figure 5.40 shows the difference spectra of DCPF–*EcMetAP* obtained by subtracting the fluorescence spectra of DCPF from that of the DCPF–*EcMetAP* complex.

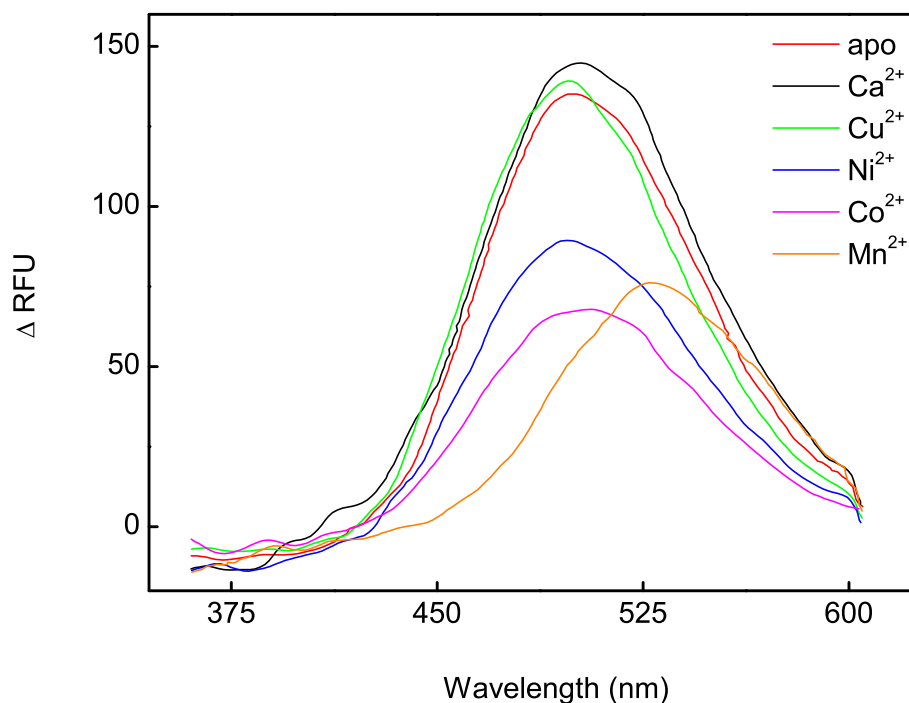


Figure 5.40. *EcMetAP* metalloform dependent spectra of DCPF. The fluorescence spectra of DCPF were measured ($\lambda_{\text{ex}} = 315 \text{ nm}$) in the absence and presence of various metalloforms of *EcMetAP* and the difference spectra were plotted. The maximal spectral change for DCPF– Mn^{2+} –*EcMetAP* is 530 nm, whereas that for all other DCPF–*EcMetAP* complexes is 495 nm.

It is evident from the data in Figure 5.40 that the fluorescence spectral properties of DCPF are distinctly affected by the different metalloforms of *EcMetAP*. The data also indicates that the inhibitor not only bound to inactive metalloforms of *EcMetAP* (such as Cu^{2+} and Ca^{2+}), but also interacted with the apo enzyme. A maximal change in the spectra was observed at 530 nm on interaction with Mn^{2+} –*EcMetAP* whereas interaction with other metalloforms of the enzyme, including apo–*EcMetAP*, resulted in a maximal fluorescence increase at 495 nm.

The metallo-specific spectral changes were found to be easily reversible between the different metalloforms of *EcMetAP* (Figure 5.41). Thus addition of EDTA to DCPF–Mn²⁺-*EcMetAP* resulted in the DCPF–apo-*EcMetAP* specific spectra, and the addition of sufficient Co²⁺ to this mixture resulted in the DCPF–Co²⁺-*EcMetAP* specific spectra. Further addition of EDTA resulted in the spectra of the DCPF–apo-*EcMetAP* form again, and finally, addition of Mn²⁺ returned the spectra similar to the original state specific to DCPF–Mn²⁺-*EcMetAP*.

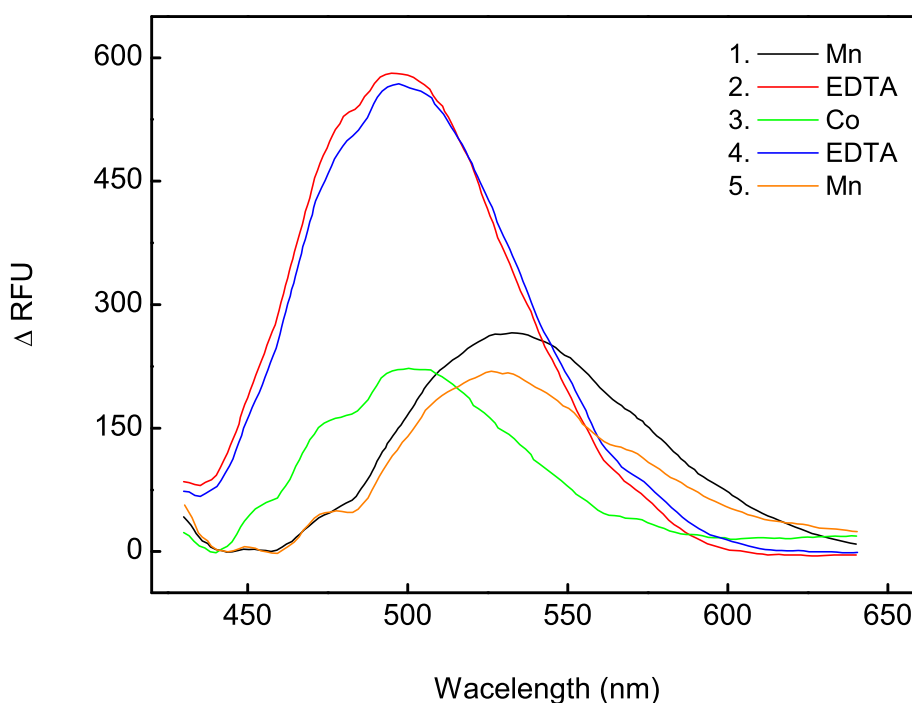


Figure 5.41. Reversibility of DCPF metallo-specific spectral properties. The fluorescence spectra of DCPF–Mn²⁺-*EcMetAP* were recorded (1) after removing the active site metal-ion (by adding EDTA) (2) and replacing with Co²⁺ (3). The Co²⁺ was in turn removed again by adding EDTA (4) and replaced with Mn²⁺ (5).

The above observations suggest that the different spectral changes with various metalloforms of *EcMetAP* arose from the varying electronic changes upon interaction of DCPF with different metals at the active site. In addition, the position of the dansylamide moiety within the active site pocket could be supposed to encounter a

varying micro-environment due to the orientation and/or conformations of DCPF within the active site of different *EcMetAP* metalloforms. The contribution of polar/nonpolar environments on the change in fluorescence spectra of DCPF was characterized by measuring the fluorescence of inhibitor in various solvents. Figure 5.42 shows the normalized fluorescence spectra of DCPF in dioxane (dielectric constant (ϵ_r)= 2.3), DMF ($\epsilon_r = 38$) and water ($\epsilon_r = 80$). The emission peak in each solvent was 495, 515 and 550 nm, respectively. The change in spectra as a function of solvent polarity is indicative of positive solvatochromic shift, similar to that seen with the DCPF–*EcMetAP* complex in Figure 5.39. The significance of these observations is discussed later in section §6.1.2.

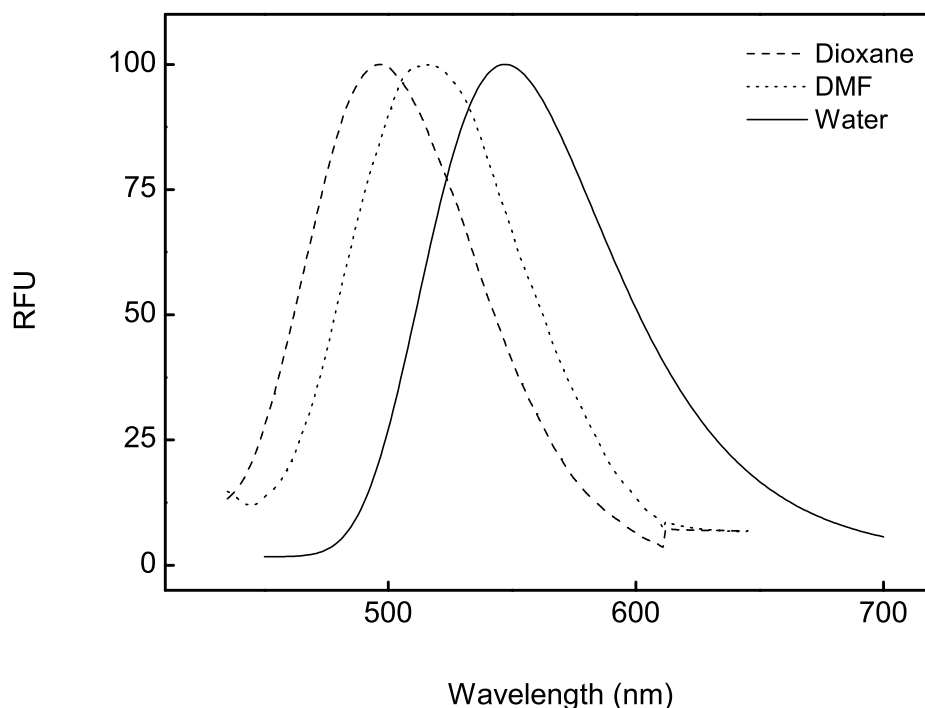


Figure 5.42. Effect of solvent polarity on the fluorescence spectra of DCPF. The fluorescence spectra of DCPF were measured in HEPES pH 7.5 buffer (solid line), dioxane (dashed line) and DMF (dotted line) and normalized. The emission maxima for the three solvents are 495, 515 and 550 nm, respectively.

5.6.3. DCPF-*EcMetAP* binding kinetics

Transient kinetic studies for the association of DCPF with various metalloforms of *EcMetAP* were conducted by mixing the inhibitor and enzyme using a stopped-flow device and monitoring the change in fluorescence signal. A representative kinetic trace for the association of DCPF with Mn^{2+} -*EcMetAP* is shown in Figure 5.43. Since the data did not fit the single exponential profile, they were analyzed by multiphasic functions. Panel A of Figure 5.43 shows the double exponential fit of the data (top), which clearly resulted in non-random residuals (bottom). Analysis by triple exponential function (Panel B) resulted in a much improved fit (top) as confirmed by the residuals (bottom).

The association kinetics were studied with varying concentrations of DCPF, while maintaining pseudo first-order conditions by using excess DCPF. The resulting data were analyzed by the triple exponential function and the observed rates were plotted as a function of DCPF concentration in Figure 5.44. All three observed rate constants followed a linear relationship with the concentration of DCPF. However, due to the complexity of the multiphasic process, no attempt was made to determine the individual rate constants from the data.

In spite of the observed complexity of the DCPF-*EcMetAP* binding process, it was of interest to compare the kinetics of binding with other metalloforms of the enzyme. Representative kinetic traces of DCPF binding to Co^{2+} & Ca^{2+} *EcMetAP* are shown in Figure 5.45 and Figure 5.46 shows a representative trace for the association of DCPF-*apo-EcMetAP*. Panel A of Figure 5.46 shows the kinetic data for DCPF-*apo-EcMetAP* binding for a duration of 2 seconds which is similar to the duration used for the acquisition of kinetic data with other metalloforms of *EcMetAP*. The data was analysed by the triple exponential function and the observed rates were plotted as a function of DCPF concentration in Figure 5.46 panel B. However, when the binding

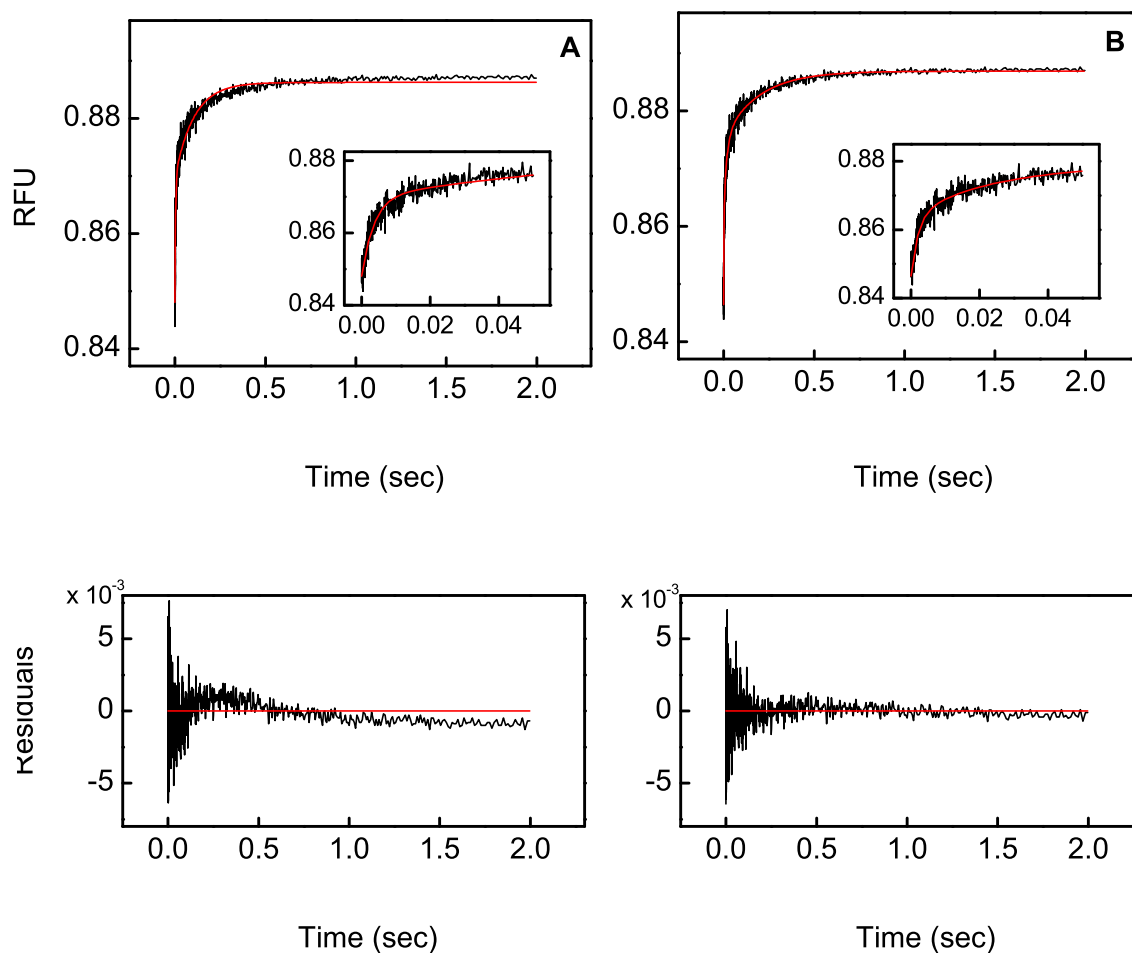


Figure 5.43. DCPF-Mn²⁺-*EcMetAP* association kinetics. 1 μM *EcMetAP* with 10 μM Mn²⁺ was mixed with 20 μM DCPF and the change in fluorescence were measured over time. Panel **A** shows the analysis of the data by a double exponential function (top) and the residuals from the resulting fit (bottom). Panel **B** shows the analysis of the data by a triple exponential function (top) and the residuals from the resulting fit (bottom).

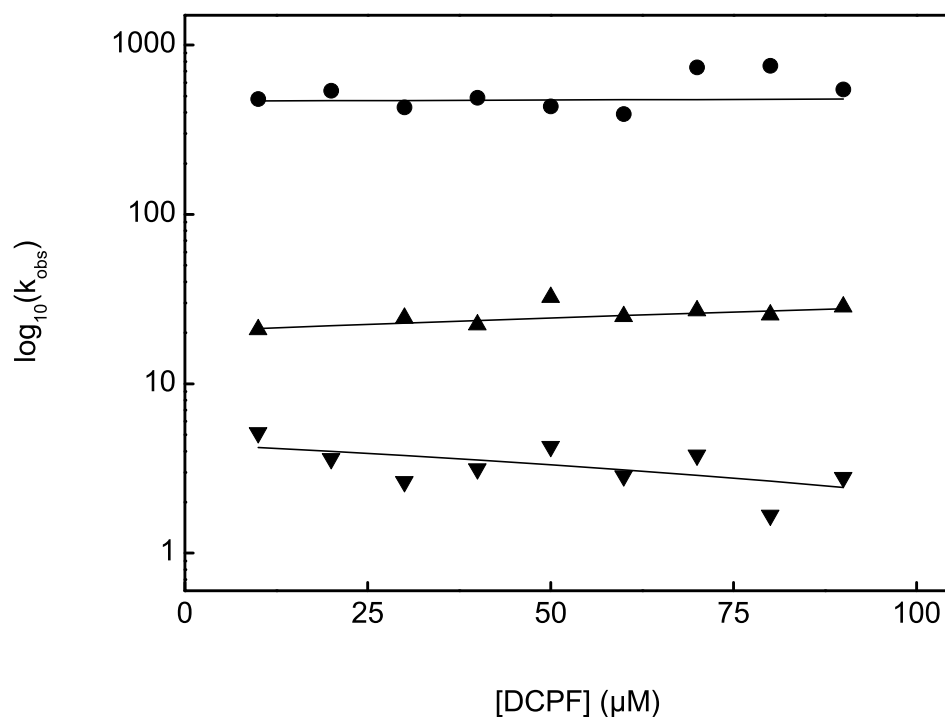


Figure 5.44. Concentration dependence of DCPF–Mn²⁺–*EcMetAP* binding phases. The observed rates determined from the kinetic traces of DCPF–Mn²⁺–*EcMetAP* association were plotted as a function of DCPF concentration. The *EcMetAP* concentration was 1 μM.

kinetics of DCPF–apo-*EcMetAP* were monitored for longer durations, it was apparent that additional phases existed in the already complex association process. Figure 5.47 shows the kinetic trace for DCPF–apo-*EcMetAP* binding extended up to 10 seconds, with the extrapolated triple exponential fit overlaid in red. Complete analysis of the extended kinetic data could not be achieved due to complexity of the data and the multiplicity of variables involved in the non-linear regression, although the analysis of partial data suggests the presence of five exponential phases.

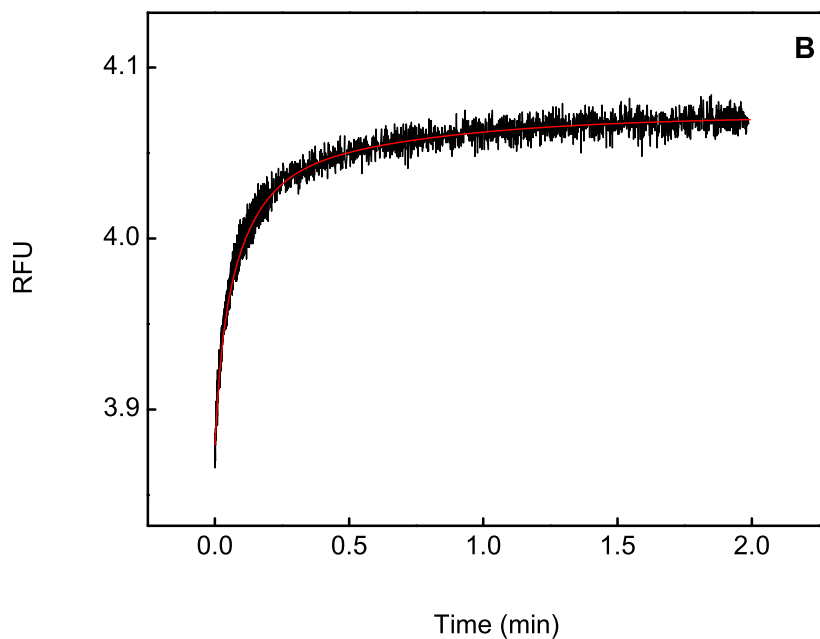
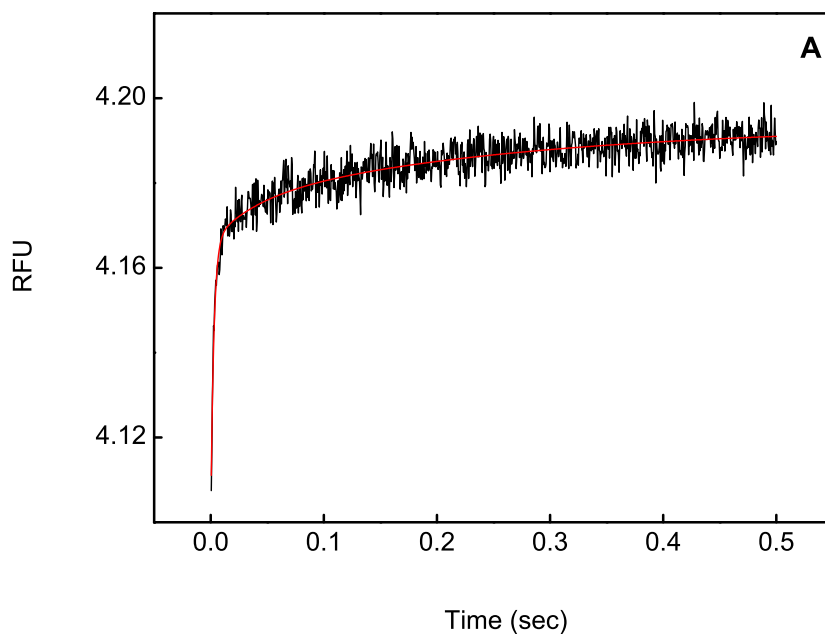


Figure 5.45. DCFP association kinetics with Co^{2+} & Ca^{2+} *EcMetAP*. $1\ \mu\text{M}$ *EcMetAP* with $10\ \mu\text{M}$ Co^{2+} or $100\ \mu\text{M}$ Ca^{2+} was mixed with DCFP (20 and $80\ \mu\text{M}$ respectively) and the change in fluorescence were measured over time. The DCFP- Co^{2+} -*EcMetAP* binding data were best fit by double exponential function for the rates of 377 ± 36 and $3.9 \pm 1.3\ \text{s}^{-1}$. The DCFP- Ca^{2+} -*EcMetAP* binding data were best fit by triple exponential function for the rates of 42 ± 3 , 9.2 ± 0.5 and $1.5 \pm 0.1\ \text{s}^{-1}$.

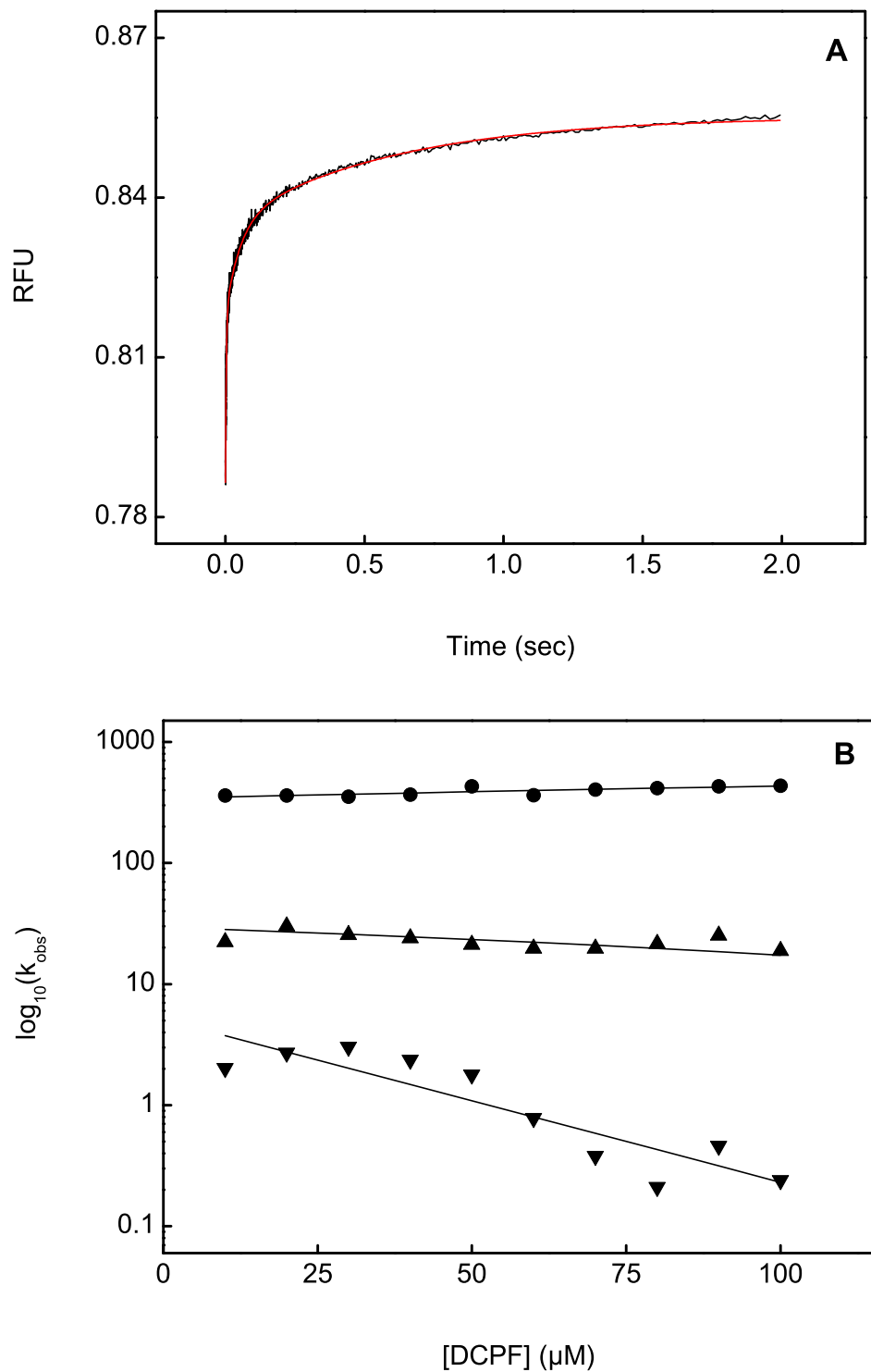


Figure 5.46. DCPF–apo-*EcMetAP* association kinetics. **A** Representative kinetic trace for DCPF–apo-*EcMetAP* association analyzed with triple exponential function. **B** Concentration dependence of the DCPF–apo-*EcMetAP* binding phases.

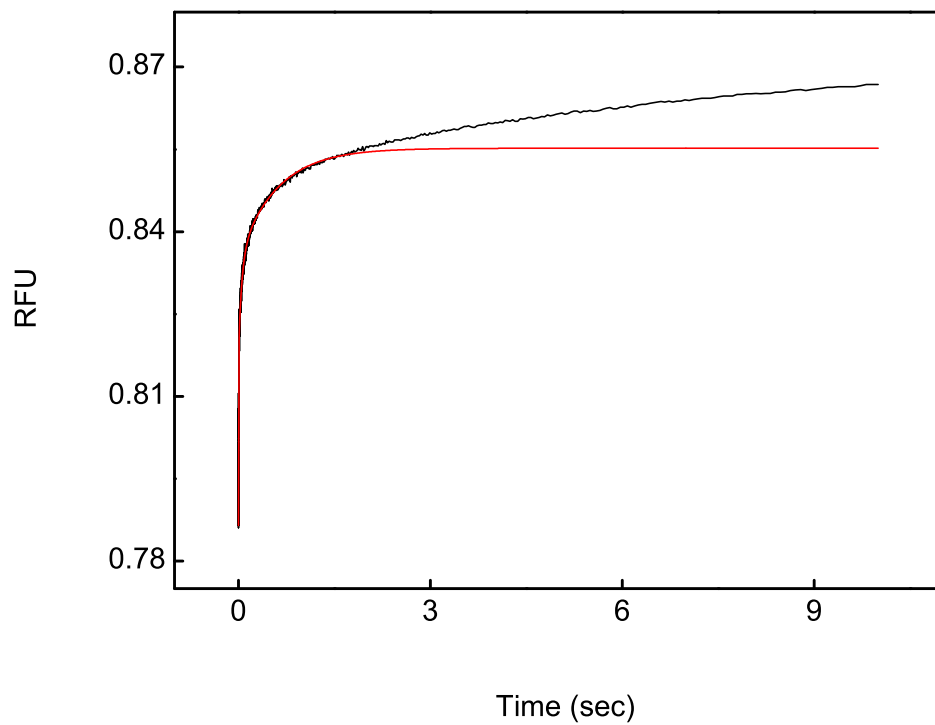


Figure 5.47. Extended DCPF-apo-*EcMetAP* association kinetics. Representative kinetic trace for DCPF-apo-*EcMetAP* association monitored for 10 s with the triple exponential fit shown in red.

5.7. Metal Ion Binding and Selectivity of *EcMetAP*

5.7.1. Identification of europium as a spectrometric probe for MetAP

As discussed in section §1.4.4, the metal binding properties of MetAPs have been under considerable debate. The weak binding affinity of metal ions to the MetAP active site has presented a hurdle in identifying the physiological metal ion, which in turn has prevented the development of biologically active inhibitors of the enzyme. The elucidation of metal binding features of MetAP has therefore been of significant interest. With this purpose in mind, the binding and activation constants of various metal ions to *EcMetAP* were determined in this study.

Based on several reports of lanthanide interactions with proteins, the luminescence properties of the lanthanides Tb^{3+} and Eu^{3+} in the presence of MetAP were investigated in the search for a viable and reliable signal for the binding of metal ions to the active site of MetAP. Whereas the fluorescence lifetimes of proteins are typically < 10 nanoseconds [144], the luminescence lifetimes of lanthanides are in the order of a few milliseconds. Using this large (about six orders of magnitude) difference in lifetimes, the contribution of intrinsic protein fluorescence to the lanthanide luminescence spectra was eliminated by applying a gate time of $150 \mu\text{s}$. The signal to noise ratio was enhanced by integrating the luminescence signal over $1250 \mu\text{s}$ and averaging ten spectra.

Both Tb^{3+} and Eu^{3+} were found to bind to *EcMetAP* resulting in enhancement of their luminescence spectra. In particular, Eu^{3+} not only showed significant enhancement of its luminescence on binding to *EcMetAP*, it was also found to catalytically activate the enzyme albeit with low efficiency. Figure 5.48 shows the luminescence spectra of $15 \mu\text{M}$ Eu^{3+} in the absence and presence of $15 \mu\text{M}$ apo-*EcMetAP*. As seen from the data, binding to *EcMetAP* enhanced the intensity of

Eu^{3+} luminescence by 300 % with no apparent change in the emission peaks or shape of the spectrum. The increase in luminescence intensity is possibly due to the decrease in the oscillator strength of the solvated Eu^{3+} upon exchange of the coordinated water molecules by the residues of the enzyme active site.

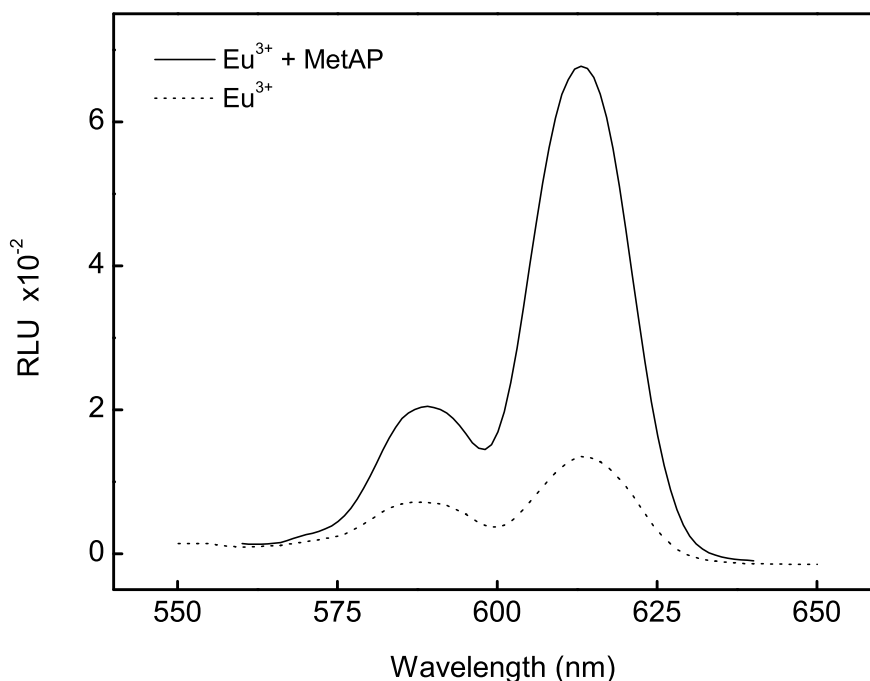


Figure 5.48. Change in Eu^{3+} luminescence spectra on binding to *EcMetAP*. The luminescence spectra of $15 \mu\text{M}$ Eu^{3+} were measured in 25 mM HEPES pH 7.5 containing 100 mM NaCl in the absence (dotted) and presence (solid) of $15 \mu\text{M}$ *EcMetAP*. The excitation wavelength and gate time were set at 295 nm and 2150 μs respectively.

By using the change in luminescence signal of Eu^{3+} upon binding to *EcMetAP*, the binding affinity of the metal ion to the enzyme could be determined. The increase in Eu^{3+} luminescence at 614 nm ($\lambda_{\text{ex}} = 295 \text{ nm}$) was measured as a fixed concentration of the apo form of *EcMetAP* was titrated with increasing concentrations of Eu^{3+} . In trial experiments it was observed that the luminescence signal of free Eu^{3+} gradually decreased over time. This was attributed to the unavoidable tendency of Eu^{3+} to bind to the walls of the cuvette. In comparison, the signal of Eu^{3+} in the presence of

EcMetAP was found to be stable over several hours, suggesting that the affinity of the metal to the enzyme was relatively stronger than that to the quartz glass of the cuvette. In order to correct for the observed decrease in free Eu^{3+} signal, the intensity values obtained from a titration of Eu^{3+} into buffer were subtracted from the values obtained by titrating the metal into apo-*EcMetAP*.

Figure 5.49 shows the increase in *EcMetAP*-bound Eu^{3+} luminescence intensity (adjusted as described above) as a function of Eu^{3+} concentration. The solid smooth line represents the best fit of the data for the dissociation constant of the Eu^{3+} -*EcMetAP* complex being equal to $25 \pm 5 \mu\text{M}$. While the affinity of the MetAP active site to metal ions is known to be weak, the binding affinity of Eu^{3+} to *EcMetAP* as determined in this study is weaker by an order of magnitude than that of other metal ions reported in literature. This difference provided a convenient opportunity to study the binding properties of the enzyme with various other metal ions, particular those with no spectroscopic or catalytic signal.

5.7.2. Determination of *EcMetAP* metal binding affinity

The displacement of Eu^{3+} from the *EcMetAP* active site upon binding of a competing metal ion was observed as a decrease in the intensity of the *EcMetAP*-bound Eu^{3+} luminescence signal in response to the addition of Co^{2+} in a preliminary experiment. The change in luminescence signal, as a result of competitive displacement of the enzyme bound Eu^{3+} ion by titration of a secondary metal ion, was used to determine the binding affinities of several metal ions.

A solution with fixed concentrations of *EcMetAP* and Eu^{3+} ($3.6 \mu\text{M}$ and $50 \mu\text{M}$ respectively) was titrated with increasing concentrations of competing metal ions. The resulting decrease in Eu^{3+} luminescence (upon displacement from the enzyme active site) was plotted as a function of the competing metal ion concentration and the data

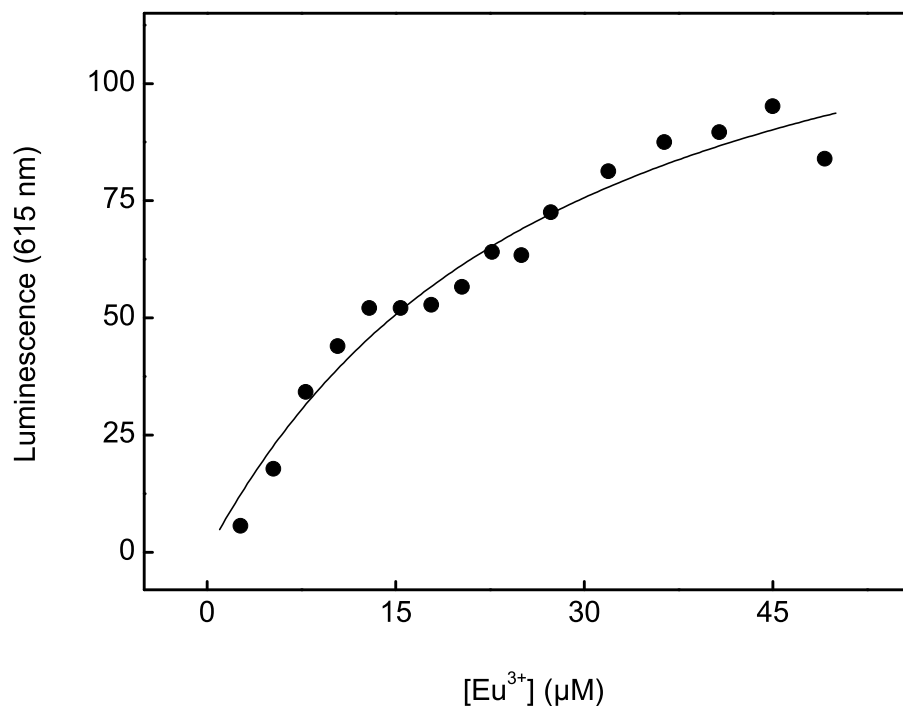


Figure 5.49. Binding affinity of the Eu^{3+} -MetAP complex. The increase in luminescence intensity of Eu^{3+} ($\lambda_{\text{ex}} = 295 \text{ nm}$, $\lambda_{\text{em}} = 615 \text{ nm}$) upon binding to *EcMetAP* was plotted as a function of the lanthanide ion concentration. The solid smooth line is the best fit of the data for the K_d value of the complex being equal to $25 \pm 5 \mu\text{M}$.

were analyzed by Eq. (5) on page 77. Figure 5.50 shows the data for the metal ions used in the study, including the common transition and alkaline earth metals as well as Zn^{2+} and Cd^{2+} . The dissociation constants for the metal-enzyme complex determined from the data are listed in Table 5.12.

While attempting to study the displacement of Eu^{3+} from *EcMetAP* by the trivalent ferric ion prepared as an aqueous solution of FeCl_3 , the formation of a significant amount of precipitation was observed in the metal chloride stock solution over time. The cloudy brown precipitate was a result of the near instantaneous hydrolysis of FeCl_3 to form primarily $\text{Fe}(\text{OH})_3$ among other hydroxides and oxides, followed by the gradual polymerization and precipitation of the species. Although

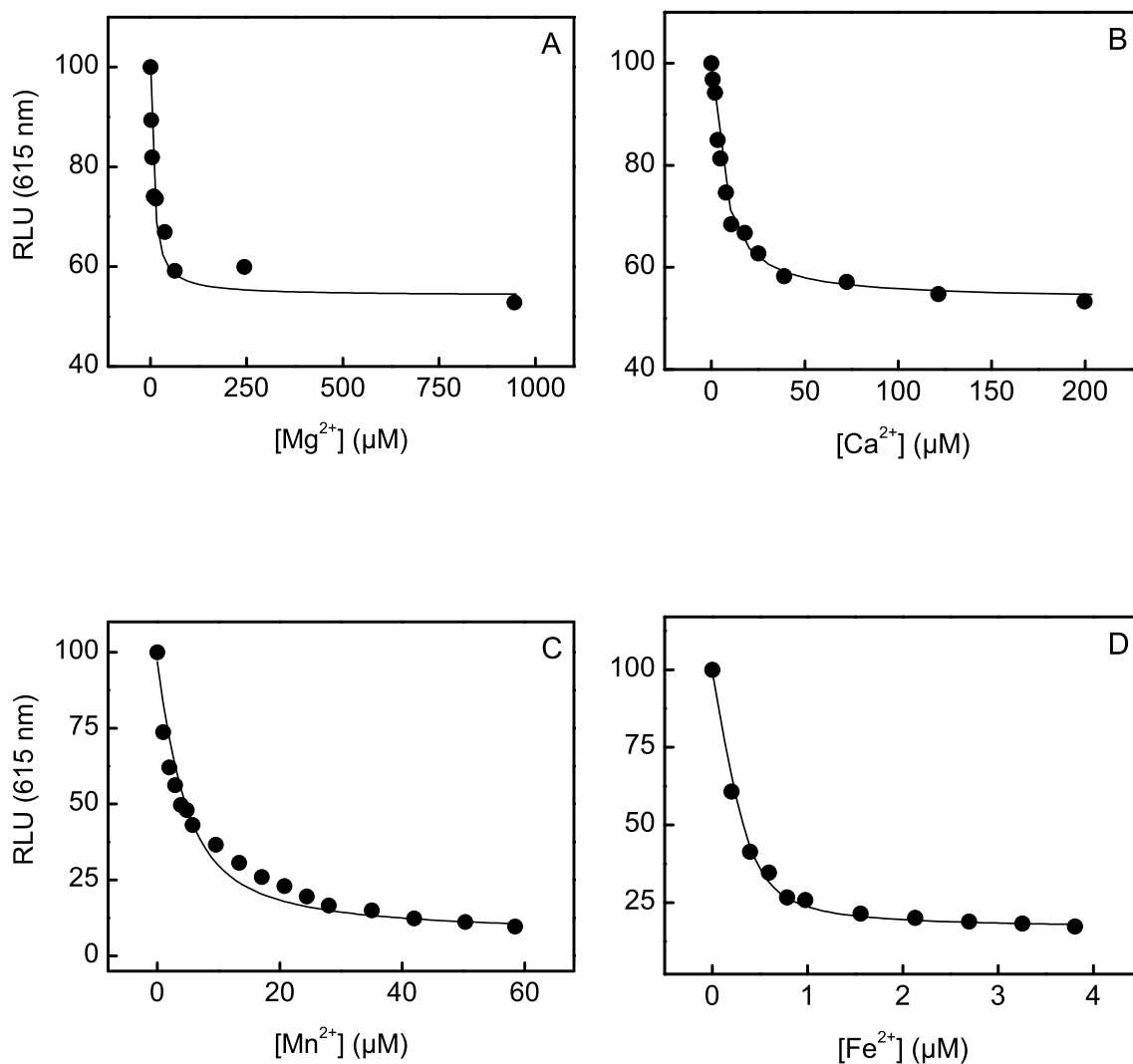


Figure 5.50. Determination of metal binding affinity by Eu^{3+} displacement. A fixed concentration of *EcMetAP* and Eu^{3+} ($3.65 \mu\text{M}$ and $50 \mu\text{M}$ respectively) were titrated with increasing concentrations of metal ions, and the decrease in Eu^{3+} luminescence ($\lambda_{\text{ex}} = 295 \text{ nm}$, $\lambda_{\text{em}} = 615 \text{ nm}$) was plotted as a function of the competing metal ion concentration. The smooth lines represent the best fit of the data for K_d values of Mg^{2+} (A), Ca^{2+} (B), Mn^{2+} (C) and Fe^{2+} (D) being equal to 2.0 ± 0.7 , 1.6 ± 0.2 , 0.7 ± 0.1 and $0.020 \pm 0.004 \mu\text{M}$ respectively as described by Eq. (5).

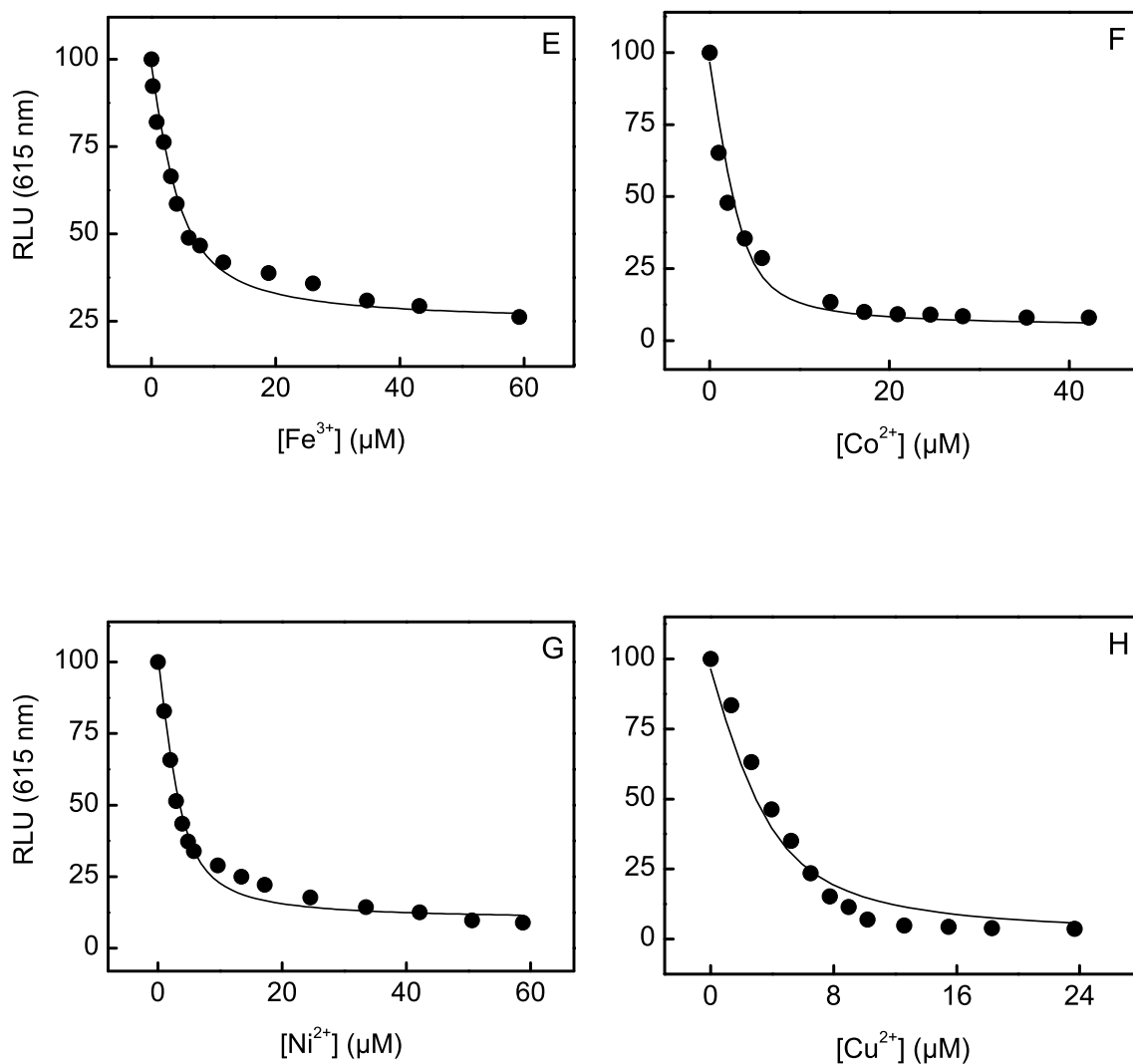


Figure 5.50. (... cont.) Determination of metal binding affinity by Eu^{3+} displacement. A fixed concentration of *EcMetAP* and Eu^{3+} ($3.65 \mu\text{M}$ and $50 \mu\text{M}$ respectively) were titrated with increasing concentrations of metal ions, and the decrease in Eu^{3+} luminescence ($\lambda_{\text{ex}} = 295 \text{ nm}$, $\lambda_{\text{em}} = 615 \text{ nm}$) was plotted as a function of the competing metal ion concentration. The smooth lines represent the best fit of the data for K_{d} values of Fe^{3+} (E), Co^{2+} (F), Ni^{2+} (G) and Cu^{2+} (H) being equal to 0.12 ± 0.10 , 0.2 ± 0.1 , 0.30 ± 0.06 and $0.4 \pm 0.2 \mu\text{M}$ respectively as described by Eq. (5).

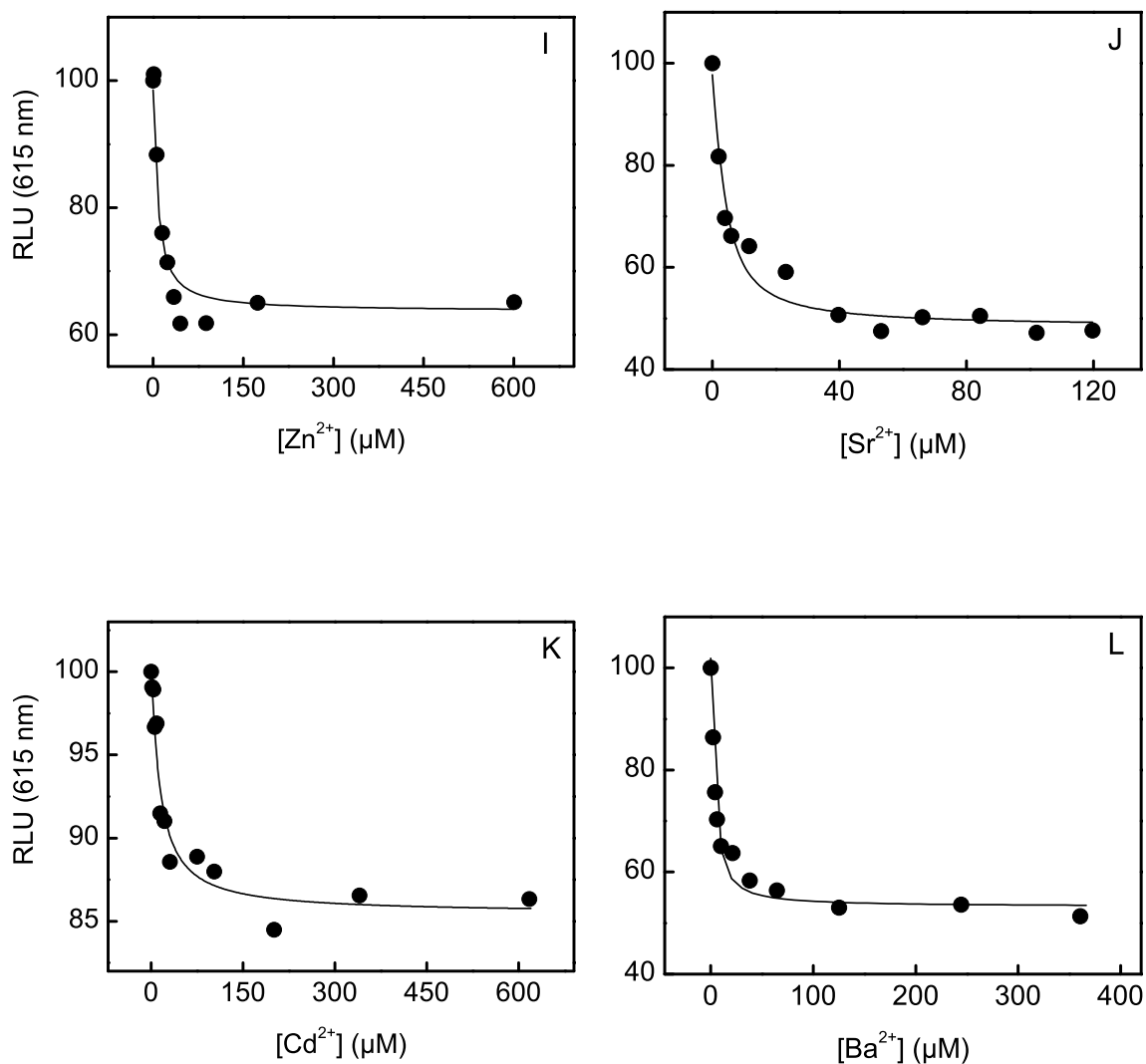


Figure 5.50. (... cont.) Determination of metal binding affinity by Eu^{3+} displacement. A fixed concentration of *EcMetAP* and Eu^{3+} ($3.65 \mu\text{M}$ and $50 \mu\text{M}$ respectively) were titrated with increasing concentrations of metal ions, and the decrease in Eu^{3+} luminescence ($\lambda_{\text{ex}} = 295 \text{ nm}$, $\lambda_{\text{em}} = 615 \text{ nm}$) was plotted as a function of the competing metal ion concentration. The smooth lines represent the best fit of the data for K_{d} values of Zn^{2+} (I), Sr^{2+} (J), Cd^{2+} (K) and Ba^{2+} (L) being equal to 1.9 ± 0.8 , 1.0 ± 0.2 , 4.1 ± 1.2 and $1.0 \pm 0.1 \mu\text{M}$ respectively as described by Eq. (5).

the formation of the precipitate occurred over an extended period of time, it was noted that the formation of insoluble $\text{Fe}(\text{OH})_3$, while visibly unnoticeable, affected the concentration of available Fe^{3+} in the experimental solution.

Since it was practically impossible to avoid the hydrolytic reactions under experimental conditions, the true concentration of Fe^{3+} in the solution was experimentally determined. The extent of hydrolysis was determined on the basis of spectrophotometric measurements of the unhydrolyzed and completely hydrolyzed solutions of varying FeCl_3 concentrations. Since the hydrolysis of Fe^{3+} is pH dependent, a solution of FeCl_3 was prepared in concentrated HCl to maintain the unhydrolyzed metal ion. Alternatively, complete hydrolysis was achieved by preparing the solution in NaOH. Figure 5.51 shows the absorbance spectra of the unhydrolyzed and completely hydrolyzed solutions in comparison to the partially hydrolyzed aqueous solution of FeCl_3 .

It is apparent from Figure 5.51 that the absorbance of the FeCl_3 solution decreases on hydrolysis of the ferric ion. The absorbance of unhydrolyzed (acidic) FeCl_3 solutions of known concentrations was used to determine the molar extinction coefficient. However, it is clear from the data that the spectra are a composite of multiple hidden peaks. The change in the absorbance spectrum upon partial hydrolysis suggests a differential decrease in the component peaks of the spectrum. Therefore the spectra of the FeCl_3 solutions were deconvoluted as shown in Figure 5.52 (top). The dotted line represents the best fit of the data for five Lorentzian peaks. The absorbance at the 385 nm peak was plotted as a function of FeCl_3 concentration (Figure 5.52, bottom) and the linear fit indicates a directly proportional relationship.

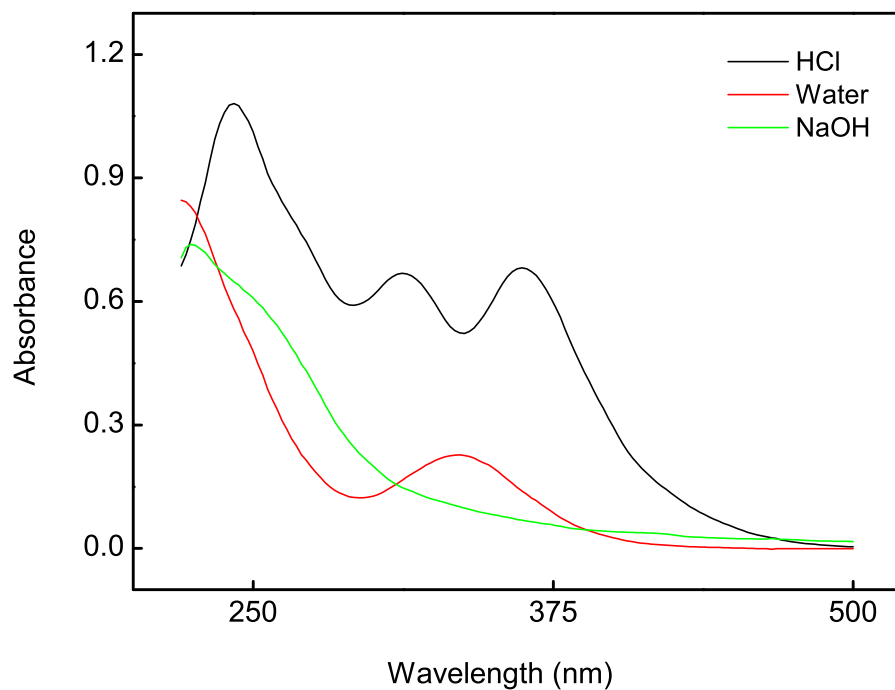


Figure 5.51. Absorption spectra of FeCl_3 species in solution. 0.1 mM solutions of FeCl_3 were prepared in concentrated HCl, water and NaOH to obtain unhydrolyzed, partially hydrolyzed and completely hydrolyzed forms of the salt. The absorption spectra of each solution was measured immediately in a quartz cuvette.

In a similar experiment, the absorbance spectra of partially hydrolyzed (aqueous) FeCl_3 solutions were recorded at varying concentrations. Figure 5.53 (top) shows the absorbance spectrum of 0.1 mM aqueous FeCl_3 . The dotted line represents the best fit of the data for four Lorentzian peaks. The absorbance at the 388 nm peak was plotted as a function of FeCl_3 concentration (Figure 5.53, bottom).

While the hydrolysis of Fe^{3+} is known to be concentration dependent, the linear fit indicates that the extent of hydrolysis at experimentally relevant concentrations of FeCl_3 has a linear relationship. Thus a comparison of the absorbance data from the unhydrolyzed and partially hydrolyzed solutions provided a direct estimate of the true Fe^{3+} concentration in the aqueous FeCl_3 solution. The concentration of Fe^{3+} was found to be reduced by 80% across all the concentrations tested (0.01 to 0.5 mM).

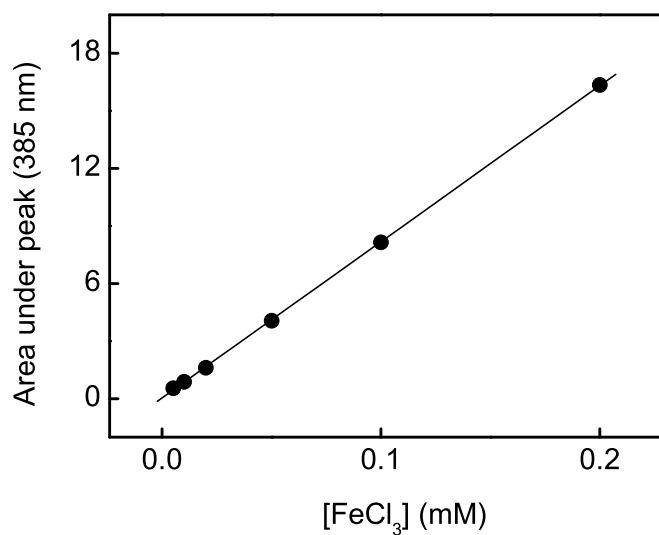
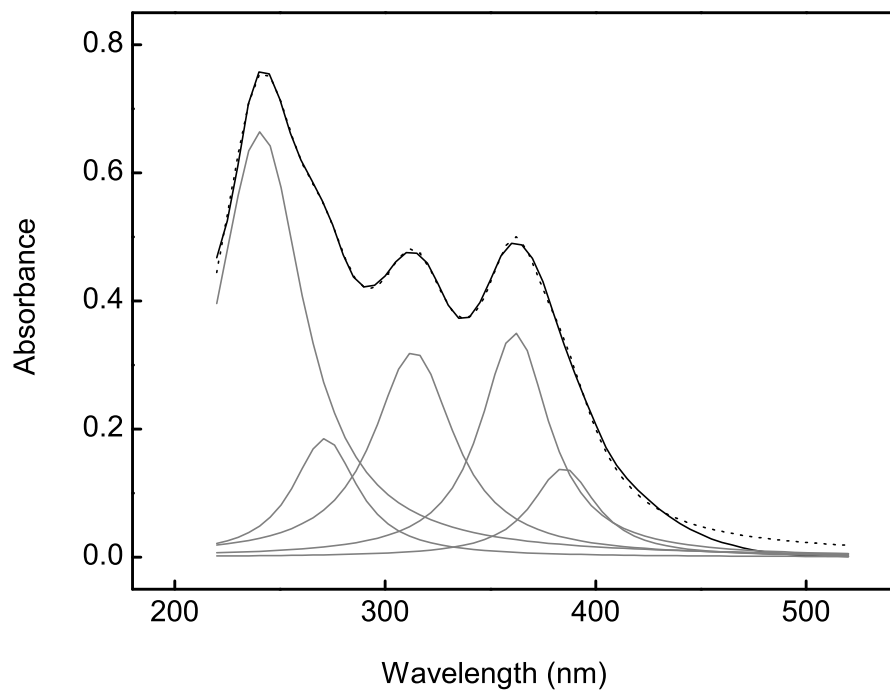


Figure 5.52. Spectrophotometric determination of FeCl₃ in solution. The absorption spectra of 0.1 mM FeCl₃ prepared in concentrated HCl was measured in a quartz cuvette. The spectral data were deconvoluted to fit 5 lorentzian peaks at 240, 265, 313, 361 and 385 nm.

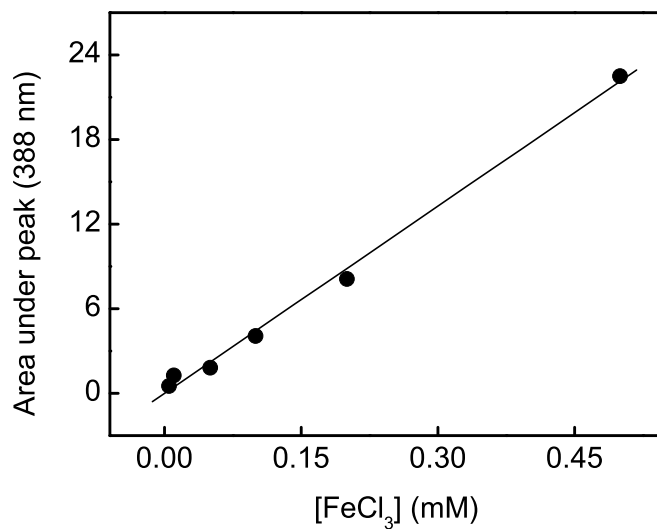
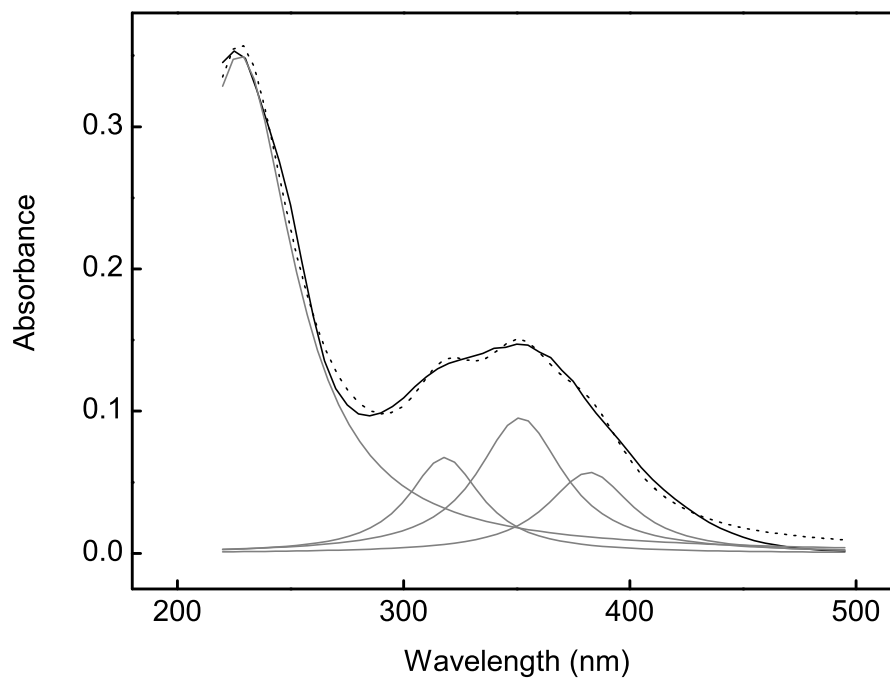


Figure 5.53. The absorption spectra of 0.1 mM FeCl₃ prepared in water was measured in a quartz cuvette. The spectral data were deconvoluted to fit 4 Lorentzian peaks at 230, 317, 358 and 388 nm. The area under the deconvoluted peak at 388 nm was plotted as a function of FeCl₃ concentration.

Therefore the concentrations of Fe^{3+} used in the experiment for displacement of Eu^{3+} was adjusted by this value to obtain the correct dissociation constant for the metal ion from the *EcMetAP* active site.

From the results listed in Table 5.12, the binding affinity of the metal ions to *EcMetAP* is revealed to be $\text{Fe}^{2+} > \text{Co}^{2+}$, $\text{Fe}^{3+} > \text{Ni}^{2+} > \text{Cu}^{2+} > \text{Mn}^{2+} \gg \text{Ca}^{2+} > \text{Mg}^{2+} > \text{Cd}^{2+}$. As suggested in the table, the metal ions appear to form two classes based on their affinity to *EcMetAP*. The metal ions of class I have $K_d < 1 \mu\text{M}$, where as those of class II have $K_d > 1 \mu\text{M}$. Additionally, all the transition metals tested in this study occupy class I where as all other metals such as Zn^{2+} , Cd^{2+} and alkaline earth metals occupy class II.

5.7.3. Determination of metal ion activation constants for *EcMetAP*

On determining the direct binding affinity of the various metal ions to the *EcMetAP* active site, it was of interest to ascertain the activation constant of the metal ions for the catalytic activity of the enzyme. As mentioned in section §1.4.4, Co^{2+} , Fe^{2+} , Mn^{2+} , Ni^{2+} and Zn^{2+} have been found to activate the various MetAPs. However, the activation constants of only Fe^{2+} and Co^{2+} have been reported for the *EcMetAP* enzyme. The determination of the activation constants of all the known activating metal ions of *EcMetAP* was therefore undertaken in this study. Additionally the activation constant of Eu^{3+} , a previously unknown activator of *EcMetAP*, was also determined.

Figure 5.54 shows the relative efficiencies of the various metal ions in the catalytic activation of *EcMetAP*. The activity of apo-*EcMetAP* was assayed in the presence of $10 \mu\text{M}$ metal ion ($50 \mu\text{M}$ in case of Eu^{3+}) using the Met-AMC substrate. In accordance with the literature data, the efficiency decreased in the order $\text{Co}^{2+} > \text{Fe}^{2+} > \text{Mn}^{2+} > \text{Ni}^{2+}$. In addition, Eu^{3+} was able to activate the enzyme up to 20% as compared

to the maximal activation by Co^{2+} . Zn^{2+} , Fe^{3+} and Sr^{2+} appeared to impart $< 2\%$ activity and all other metals were unable to produce any measurable activity in the enzyme.

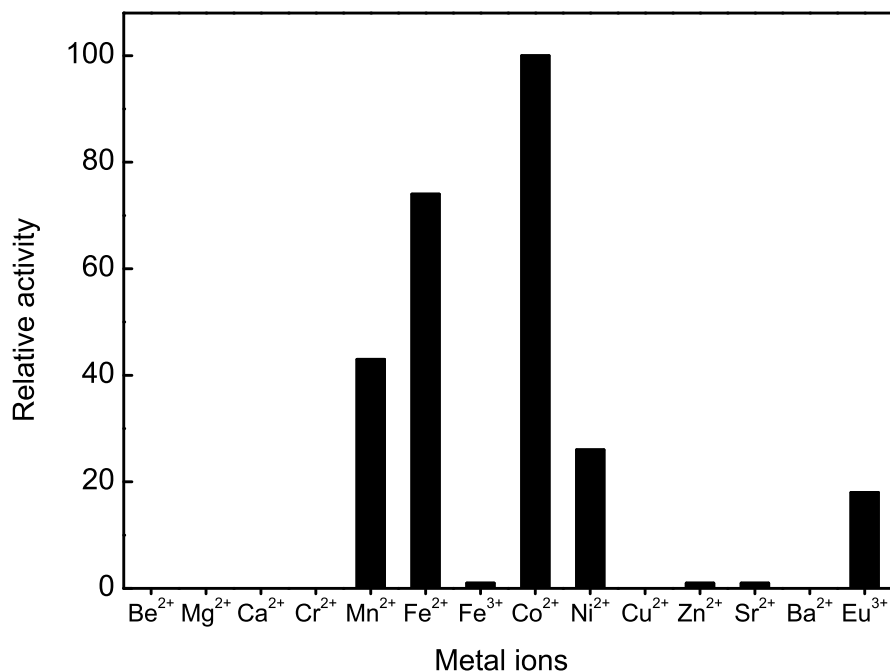


Figure 5.54. The activity of $1\ \mu\text{M}$ *EcMetAP* (determined by the time-dependent cleavage of Met-AMC) was measured in the presence of $10\ \mu\text{M}$ metal-ion over a 30 min time period, and normalized with respect to the enzyme's activity containing Co^{2+} as the cofactor

On the basis of this data, the activation constants of the above catalytically active metals Mn^{2+} , Fe^{2+} , Co^{2+} , Ni^{2+} and Eu^{3+} were determined. The activity of apo-*EcMetAP* was assayed in the presence of increasing concentration of each metal ion. Where as most assays were conducted in 96 well micro-titer plates, the facile oxidation of Fe^{2+} in such a setup prevented the reliable measurement of Fe^{2+} -*EcMetAP* activity. In order to assay the activity of the Fe^{2+} form of the enzyme, all buffers were treated to repeated cycles of deaeration and purging with nitrogen gas. 2 mM TCEP

was used as a reducing agent to stabilize the Fe^{2+} in the assay. The enzyme reactions were conducted in a cuvette whose mouth was sealed using a teflon cap during the assay.

Figure 5.55 shows the activation profile of Eu^{3+} -*EcMetAP* as a function of Eu^{3+} concentration. The smooth line represents the best fit of the data for the K_a value of $15 \pm 5 \mu\text{M}$. This value is in close agreement with the direct binding affinity of the metal ion for the enzyme reported in Figure 5.49.

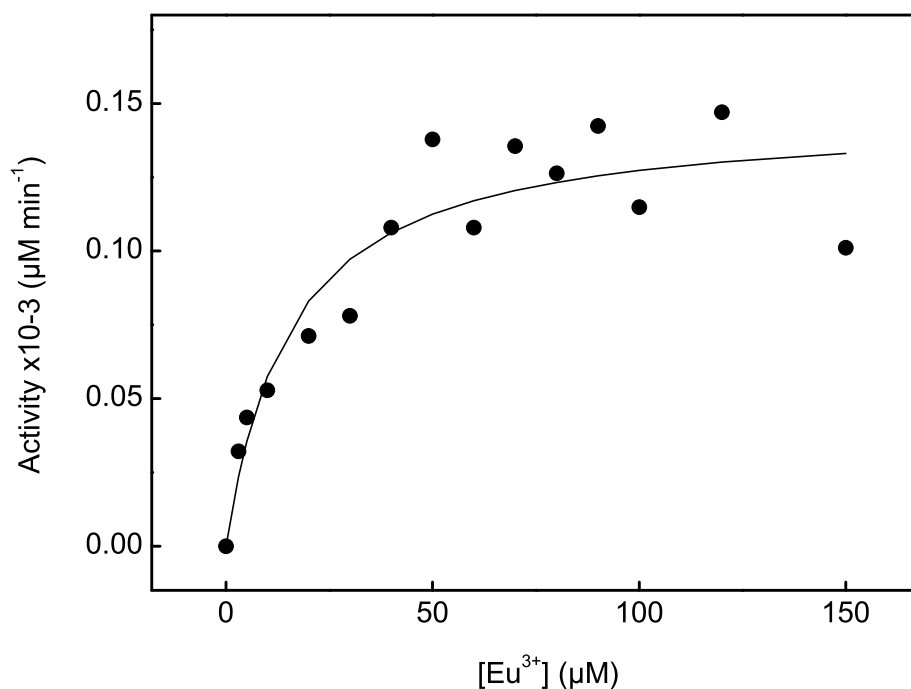


Figure 5.55. Determination of the activation constant of Eu^{3+} for *EcMetAP*. The activity of $1 \mu\text{M}$ *EcMetAP* was measured in the presence of $300 \mu\text{M}$ substrate and increasing concentrations of EuCl_3 , and plotted as a function of the lanthanide concentration. The smooth line represents the best fit of the data for the K_a value being equal to $15 \pm 5 \mu\text{M}$.

The activation data for the metal ions Co^{2+} , Mn^{2+} , Ni^{2+} and Fe^{2+} are shown in Figure 5.56. The activation constants of the metal ions for *EcMetAP* are listed in Table 5.12. A comparison of the direct binding affinities and activation constants of metal ions in the table shows that the two values are in good agreement with each other.

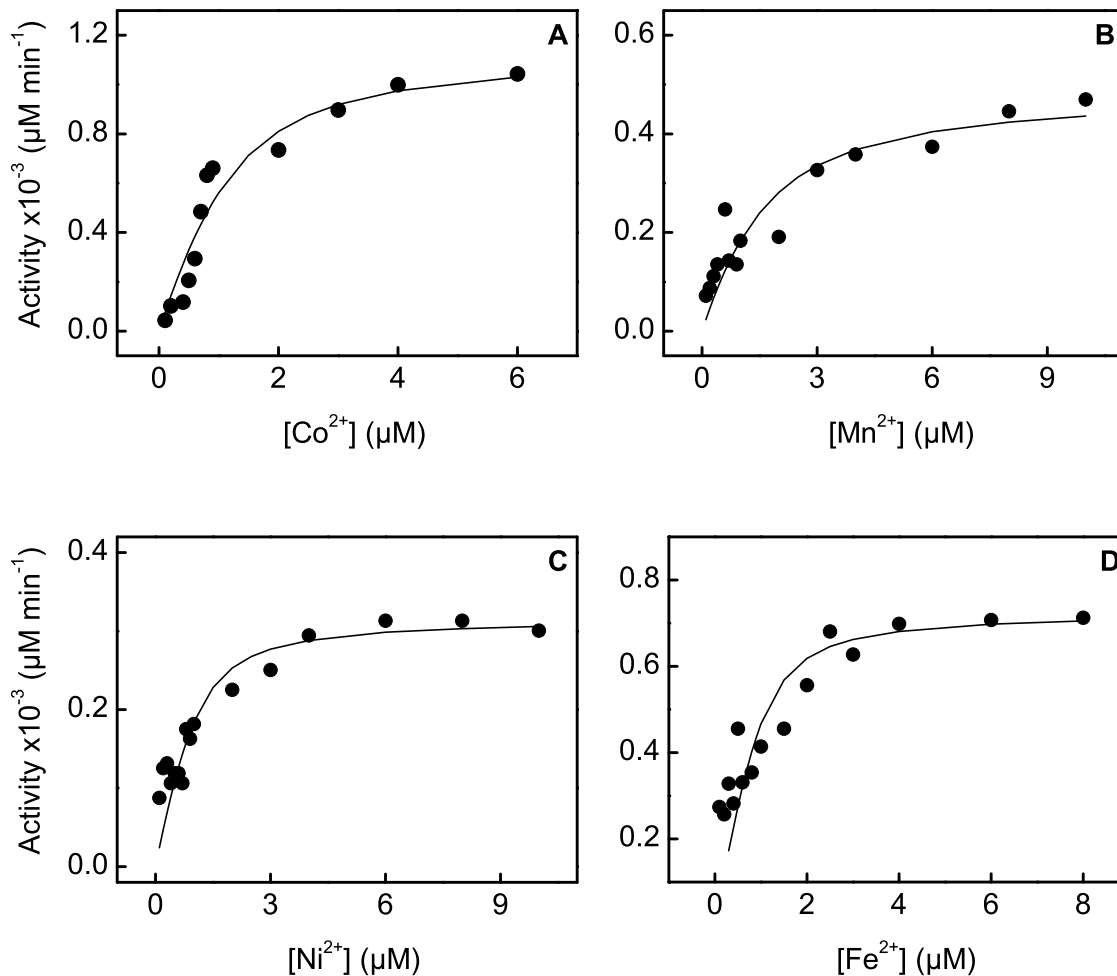


Figure 5.56. Determination of *EcMetAP* activation constants for various metal ions. The activity of 1 μM apo-*EcMetAP* was measured with 300 μM substrate in the presence of varying concentrations of Co²⁺ (A), Mn²⁺ (B), Ni²⁺ (C) and Fe²⁺ (D) metal ions. The smooth lines represent the best fits of the data for the K_a values of Co²⁺, Mn²⁺, Ni²⁺ and Fe²⁺ being equal to $0.50 \pm 0.25 \mu\text{M}$, $0.6 \pm 0.4 \mu\text{M}$, $0.300 \pm 0.004 \mu\text{M}$ and $0.4 \pm 0.2 \mu\text{M}$, respectively.

Table 5.12. Binding affinity (K_d) and activation constants (K_a) of various metals for *EcMetAP*

Metal	K_d (μM) ²	K_a (μM) ²
Class I		
Mn ²⁺	0.7 ± 0.1	0.6 ± 0.4
Fe ²⁺	0.020 ± 0.004	0.4 ± 0.2
Fe ³⁺	0.12 ± 0.10	inactive
Co ²⁺	0.2 ± 0.1	0.50 ± 0.25
Ni ²⁺	0.30 ± 0.06	0.30 ± 0.04
Cu ²⁺	0.4 ± 0.2	inactive
Class II		
Mg ²⁺	2.0 ± 0.7	inactive
Ca ²⁺	1.6 ± 0.2	inactive
Zn ²⁺	1.9 ± 0.8	inactive
Sr ²⁺	1.0 ± 0.2	inactive
Cd ²⁺	3.5 ± 0.4	inactive
Ba ²⁺	1.0 ± 0.1	inactive

¹ Metal binding affinity to *EcMetAP* was determined by Eu³⁺ displacement from Eu³⁺-*EcMetAP* as described in section §4.5.2.

² Activation constants of metal ions was determined by assaying apo-*EcMetAP* activity in the presence of varying metal ion concentrations as described in section §4.5.3.

5.7.4. Determination of metal dependent *EcMetAP* steady-state parameters

In addition, the effect of the different activating metal ions on the steady-state kinetic parameters of the enzyme was further studied for the cleavage of the Met-AMC substrate. The K_m and k_{cat} values of the different metalloforms of the *EcMetAP* enzyme were determined by assaying the enzyme activity in the presence of each metal ion, with increasing concentrations of substrate. Figure 5.57 shows the data for Co^{2+} , Mn^{2+} , Ni^{2+} and Eu^{3+} form of *EcMetAP*.

The steady-state kinetic parameters of the above *EcMetAP* metalloforms for Met-AMC cleavage are listed in Table 5.13. The specificity constant (k_{cat}/K_m) for the *EcMetAP* metalloforms decreases in the order $\text{Co}^{2+} > \text{Ni}^{2+} > \text{Eu}^{3+} > \text{Mn}^{2+}$.

Table 5.13. Steady-state kinetic parameters of various metalloforms of *EcMetAP*.¹

Metal	K_m (μM)	k_{cat} ($\times 10^{-11} \text{s}^{-1}$)
Co^{2+}	196 ± 39	6.87 ± 0.58
Mn^{2+}	193 ± 39	3.45 ± 0.40
Ni^{2+}	131 ± 40	3.18 ± 0.27
Eu^{3+}	91 ± 21	1.72 ± 0.12

¹ The activity of apo-*EcMetAP* was assayed with $10 \mu\text{M}$ metal ion ($40 \mu\text{M}$ in case of Eu^{3+}) in the presence of increasing concentrations of substrate (5 to $600 \mu\text{M}$ Met-AMC) as described in section §4.5.3.

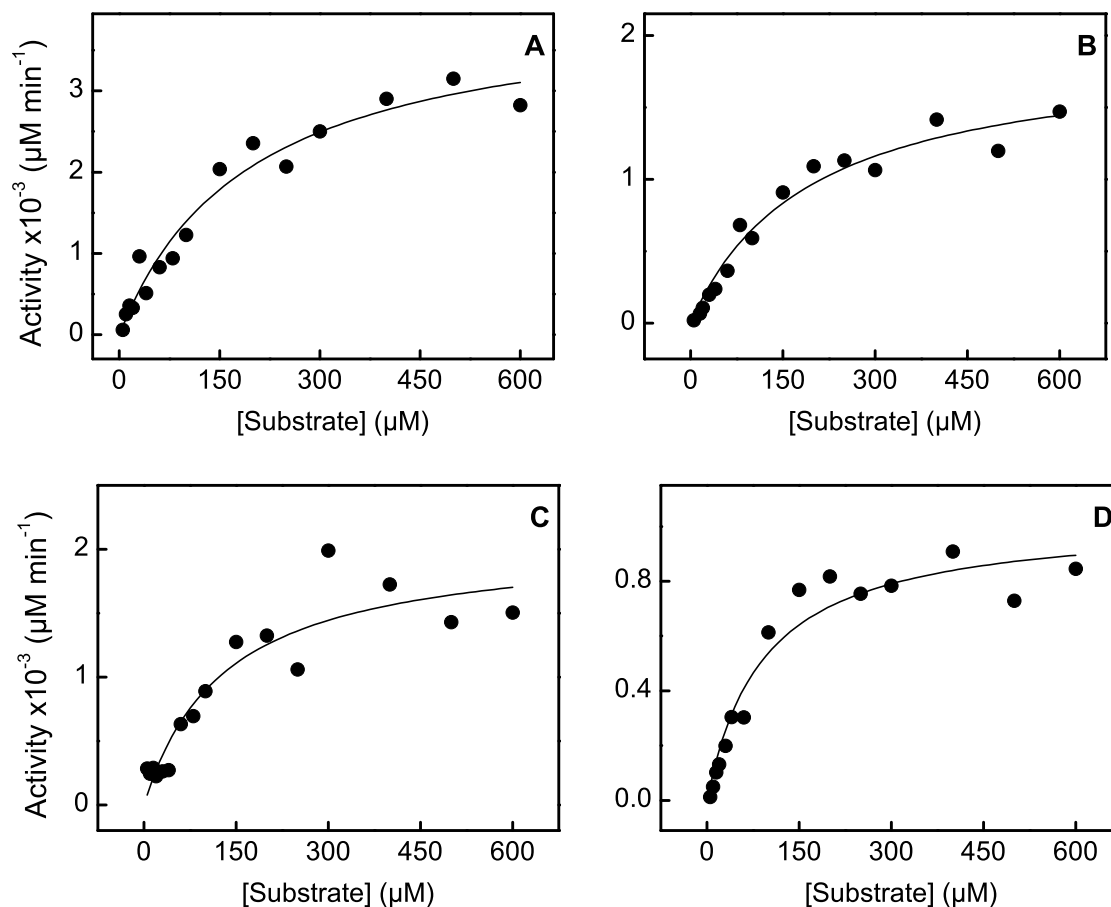


Figure 5.57. Determination of steady-state kinetic parameters of various *EcMetAP* metalloforms. The activity of 1 μM apo-*EcMetAP* was measured with 10 μM metal ion (40 μM in case of Eu^{3+}) in the presence of increasing concentrations of substrate (5 to 600 μM Met-AMC). The smooth lines represent the best fits of the data for the K_m values of Co^{2+} , Mn^{2+} , Ni^{2+} and Eu^{3+} being equal to 196 ± 39 , 193 ± 39 , 131 ± 40 and 91 ± 21 μM , respectively; and for the V_{max} values being equal to 4.12 ± 0.35 , 2.07 ± 0.24 , 1.91 ± 0.16 and 1.03 ± 0.07 nM min^{-1} , respectively.

5.8. MetAP and PDF interaction

The PDF and MetAP enzymes are known to function in close succession at the ribosome exit site, with evidence that both may interact with the ribosome. The consecutive formyl and methionine group cleavage from the growing polypeptide chain suggests a close proximity between the two enzymes. A quick binding study was performed in order to study the potential interaction between *Ec*PDF and *Ec*MetAP. *Ec*PDF was incubated with *Ec*MetAP-6His for 30 min at 4 °C in solution, then loaded onto a Ni-IDA column. Alternatively, *Ec*PDF was loaded onto a column previously loaded with *Ec*MetAP-6His and the column was incubated for 30 min at 4 °C. Each enzyme was separately loaded onto different columns as controls. The columns were washed to remove unbound protein, followed by elution with 100 mM imidazole. The absorbance of the eluate fractions was measured at 280 nm to monitor the presence of protein.

Figure 5.58 shows the elution profiles for the controls and the co-incubated samples. The two distinct peaks appearing in the co-incubated samples indicate that *Ec*PDF and *Ec*MetAP-6His eluted separately, during the wash and elution steps respectively. Both enzymes were found to elute independently, regardless of the method of co-incubation (in solution or on the column). These results indicate that *Ec*PDF and *Ec*MetAP do not have a strong interaction with each other. However, when the enzymes were co-incubated on the column (panel D), the second peak (representative of *Ec*PDF), appeared later as opposed to when the enzymes were co-incubated in solution. Thus the movement of *Ec*PDF appears to have been impeded when incubated with *Ec*MetAP-6His on the Ni-IDA column, suggesting weak but significant interaction between *Ec*PDF and *Ec*MetAP.

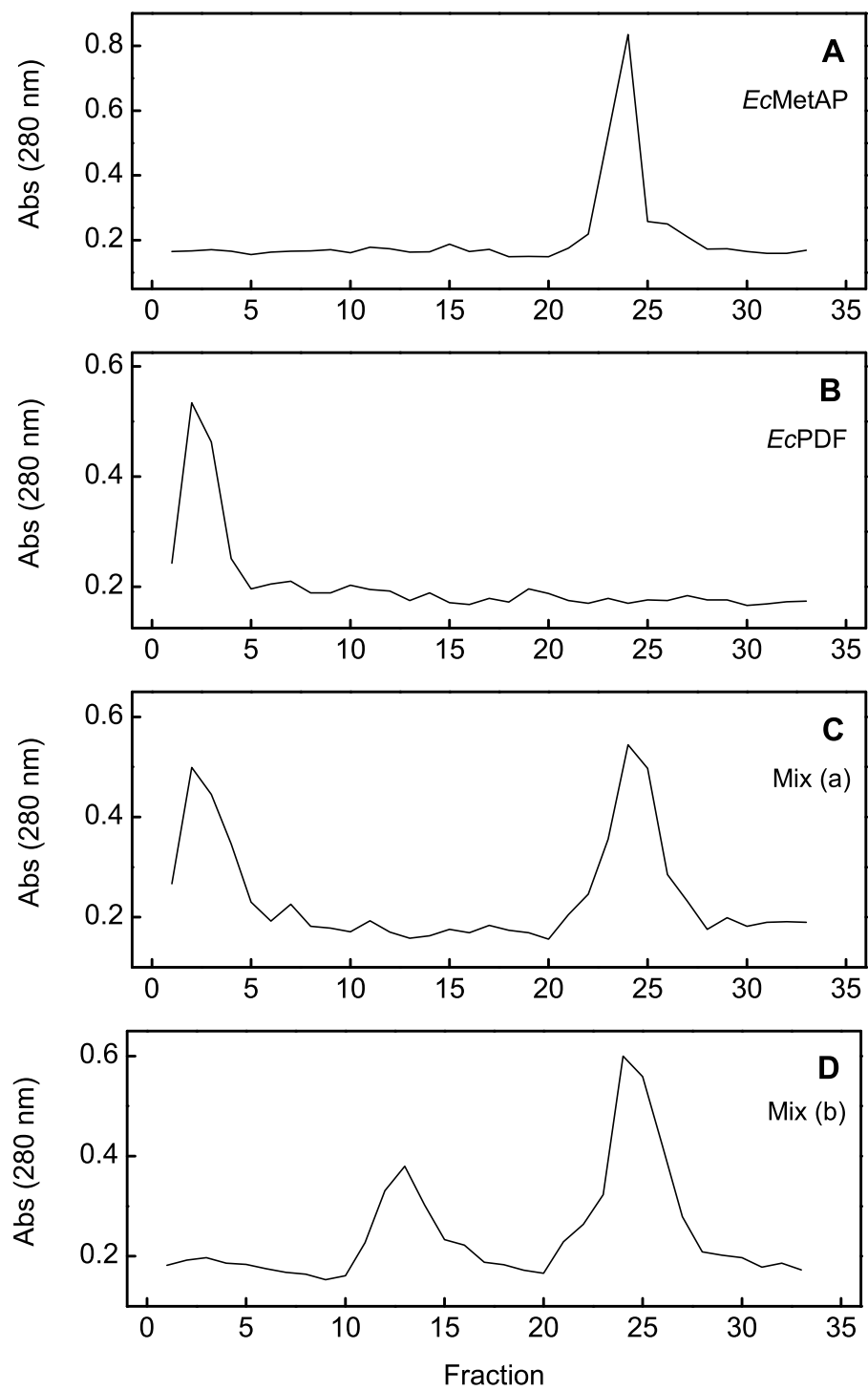


Figure 5.58. Interaction of *EcPDF* with *EcMetAP*. The above profiles indicate the elution of protein from Ni-IDA columns loaded with *EcMetAP*-6His (**A**), *EcPDF* (**B**), both mixed together(**C**) or both added sequentially (**D**).

5.9. Thermal Stability of PDFs

5.9.1. Thermal unfolding of PDFs

The contribution of the C-terminal helix to the stability of *Ec*PDF was probed by conducting thermodynamic studies comparing the native and truncated forms of the enzyme. The thermal unfolding of native and truncated forms of *Ec*PDF was studied by measuring the loss of secondary structure (monitored by the ellipticity at 223 nm) as a function of temperature. A solution of 15 to 25 μM of enzyme was heated from 25 to 95 $^{\circ}\text{C}$ at a rate of 0.5 $^{\circ}\text{C min}^{-1}$ in 5 mM HEPES pH 7.5 containing 1 mM NiCl_2 .

Figure 5.59 shows the unfolding data for native *Ec*PDF. The loss of secondary structure appears biphasic with each phase accounting for half of the total unfolding process, and the two unfolding transitions are at 51 and 75 $^{\circ}\text{C}$. These results are consistent with previously reported data for native *Ec*PDF [64]. The unfolding data of the truncated *Ec*PDF (*Ec*PDF-C Δ 21) is shown in Figure 5.60. Note that the unfolding data of the truncated PDF is also biphasic, but appears significantly different from that of the native enzyme. Whereas the unfolding transitions for *Ec*PDF-C Δ 21 remain the same as seen for the full length enzyme (51 and 75 $^{\circ}\text{C}$), the two unfolding phases account for 10 and 90 % of the total unfolding process. This is clearly a marked departure from the characteristics of the native enzyme, and suggests either a shift in the low and high thermally stable populations of *Ec*PDF at equilibrium or a dynamic change in the stability as a function of temperature.

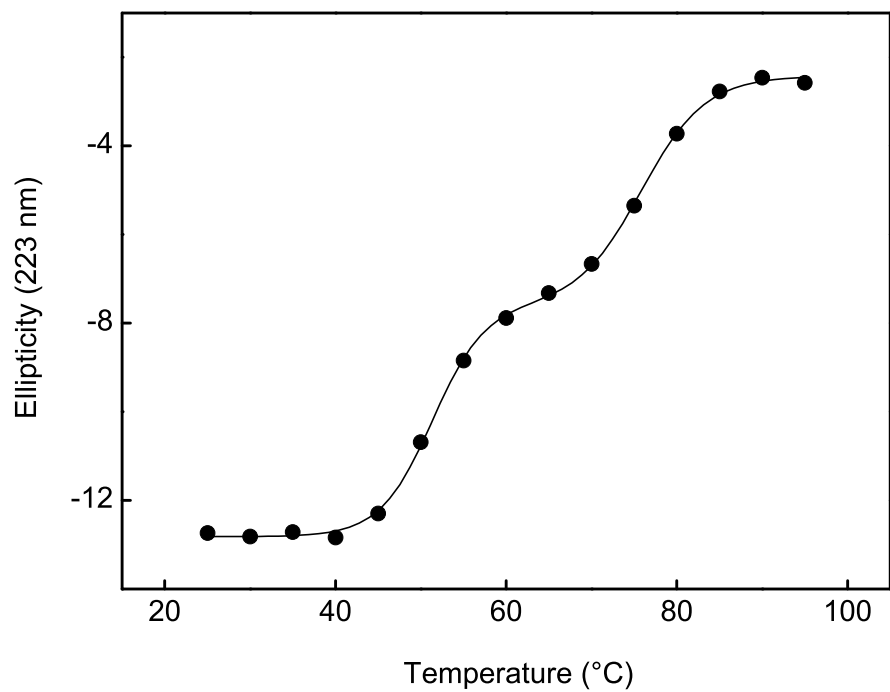


Figure 5.59. Temperature dependent unfolding of native PDF. The ellipticity of native PDF was measured at 223 nm as a function of temperature. The temperature was ramped from 25 to 95 °C at a rate of 0.5 °C min⁻¹ using a Peltier temperature controller. The solid smooth lines represent the best fit of the data for T_m values of 51 and 75 °C, with the slope at each T_m being equal to 3.1 and 3.8, and the fraction amplitude of the two unfolding phases being 0.5 each.

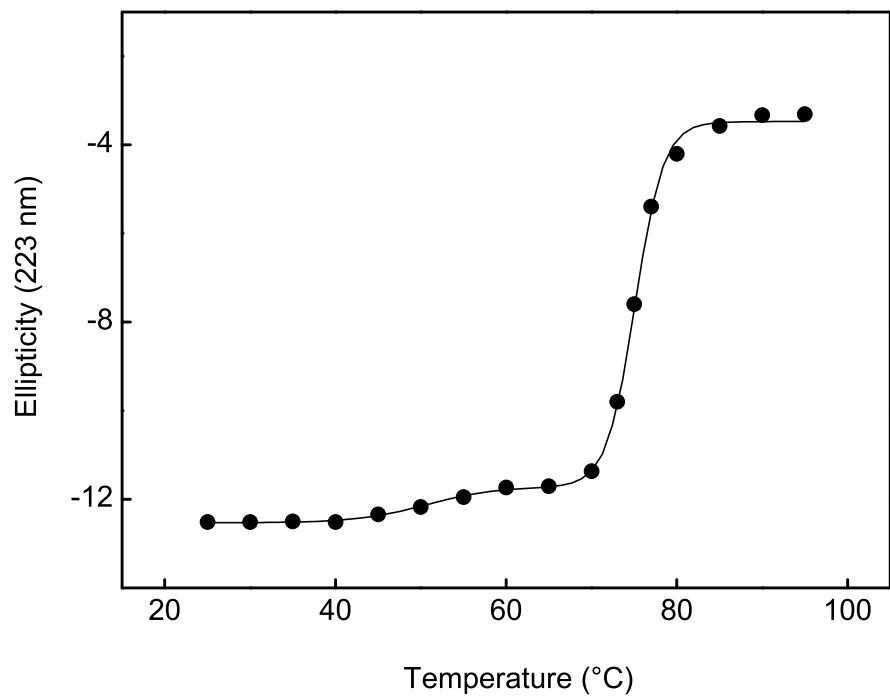


Figure 5.60. Temperature dependent unfolding of *EcPDF-CΔ21*. The ellipticity of *EcPDF-CΔ21* was measured at 223 nm as a function of temperature. The temperature was ramped from 25 to 95 °C at a rate of 0.5 °C min⁻¹ using a Peltier temperature controller. The solid smooth lines represent the best fit of the data for T_m values of 51 and 75 °C, with the slope at each T_m being equal to 4.1 and 3.8, and the fraction amplitude of the two unfolding phases being 0.1 and 0.9 respectively.

5.9.2. Unfolding kinetics of PDFs

The time dependent thermal unfolding of the native and truncated forms of PDF was studied by measuring the ellipticity ($\theta_{223\text{nm}}$) of the enzyme solution incubated at 60°C as a function of time. Figure 5.61 shows the data for the thermal unfolding kinetics of native *Ec*PDF. The data reveals a biphasic process which was analyzed by a double exponential function (Eq. (8) described in section §4.6.2) to yield the rate constants of $(7.12 \pm 0.47) \times 10^{-2}$ and $(8.87 \pm 0.25) \times 10^{-3} \text{ min}^{-1}$, with the fraction amplitude each phase being 0.36 and 0.67, respectively. In comparison, the unfolding kinetics of *Ec*PDF-C Δ 21 (shown in Figure 5.62) also appear biphasic, but gave the significantly lower rate constants of $(7.12 \pm 0.47) \times 10^{-2}$ and $(8.87 \pm 0.25) \times 10^{-3} \text{ min}^{-1}$, with the fraction amplitudes of each phase being 0.12 and 0.88, respectively.

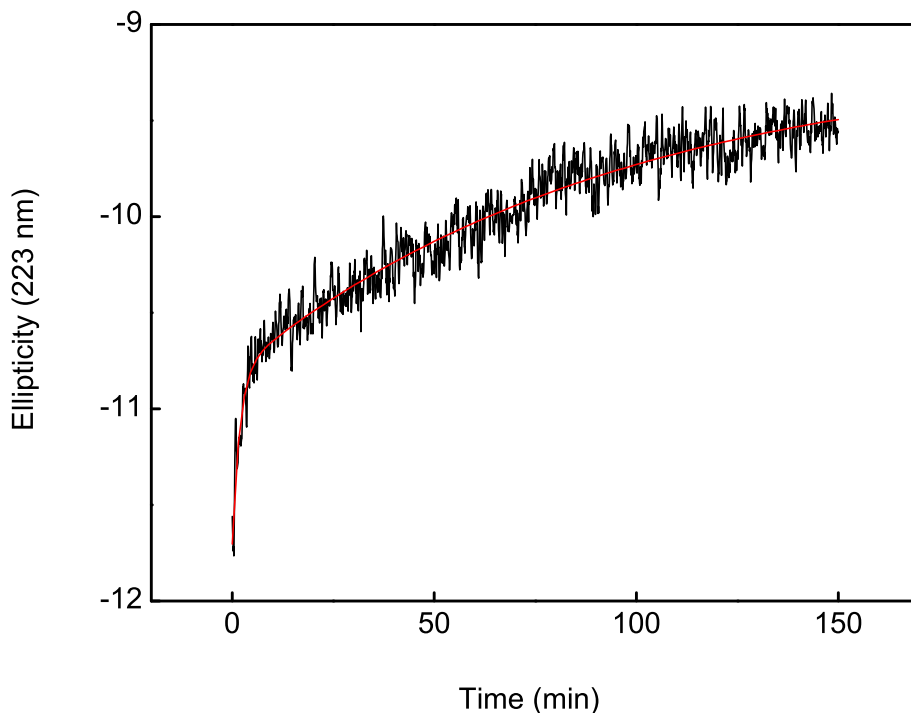


Figure 5.61. Unfolding kinetics of native *Ec*PDF. The ellipticity of native *Ec*PDF was measured at 223 nm while incubating the enzyme at 60°C . The smooth red line represents the best fit of the data for the rate constants being equal to $(5.40 \pm 0.39) \times 10^{-1}$ and $(1.07 \pm 0.04) \times 10^{-2} \text{ min}^{-1}$.

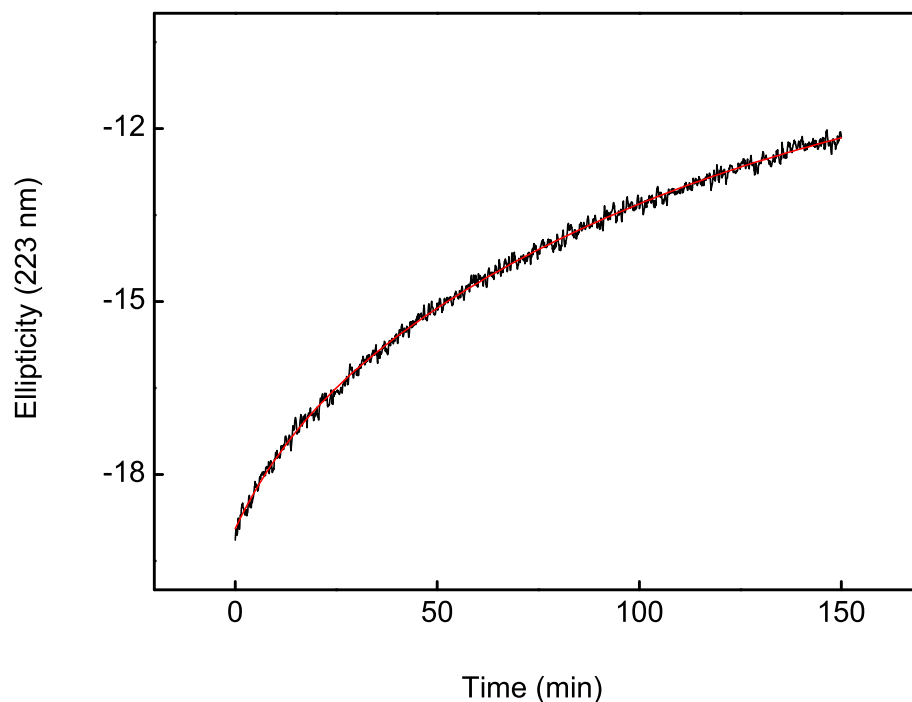


Figure 5.62. Unfolding kinetics of *EcPDF-CΔ21*. The ellipticity of native *EcPDF-CΔ21* was measured at 223 nm while incubating the enzyme at 60 °C. The smooth red line represents the best fit of the data for the rate constants being equal to $(7.12 \pm 0.47) \times 10^{-2}$ and $(8.87 \pm 0.25) \times 10^{-3} \text{ min}^{-1}$.

5.9.3. Thermal inactivation of PDFs

The time dependent loss of PDF activity as a result of high temperature was studied by measuring the activity of the native and truncated forms of PDF upon incubation of the enzyme at 60 °C for increasing periods of time. Since the introduction of the heated enzyme sample into assay buffer would result in some reversal of the unfolding process during the assay, any potential refolding was allowed to complete by incubating the samples at 4 °C overnight prior to measuring the activity. Figure 5.63 shows the time dependent inactivation of native *EcPDF* when incubated at 60 °C. Analysis of the data reveals two exponential decreases in activity where each phase has an equal amplitude, with the rate constants of 3.26 ± 1.05 and $0.12 \pm 0.04 \text{ min}^{-1}$. On the other hand, the thermal inactivation data of *EcPDF-CΔ21* (see Figure 5.64)

reveal a markedly different profile in the loss of activity. Whereas the data for the truncated PDF also appeared biphasic, the two rate constants were determined to be 0.95 ± 0.75 and $0.12 \pm 0.04 \text{ min}^{-1}$, with the fraction amplitudes being 0.12 and 0.88, respectively. These results indicate the presence of a significantly heat-stable fraction in the *EcPDF*-C Δ 21 population.

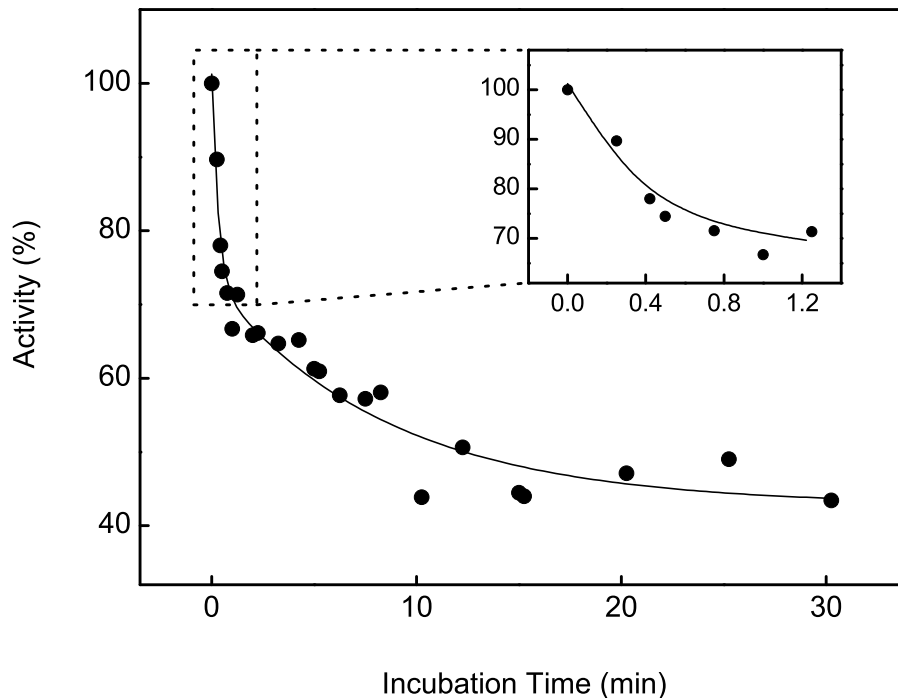


Figure 5.63. Temperature dependent inactivation of native *EcPDF*. Aliquots of *EcPDF* were incubated at 60°C for increasing periods of time, followed by incubation at 4°C . The activity of the heat treated enzyme was then measured and plotted as a function of incubation period at 60°C . The smooth line represents the best fit of the data with a bi-exponential decay function for the rate constants being equal to 3.26 ± 1.05 and $0.12 \pm 0.04 \text{ min}^{-1}$, with the fraction amplitudes being 0.52 and 0.48, respectively.

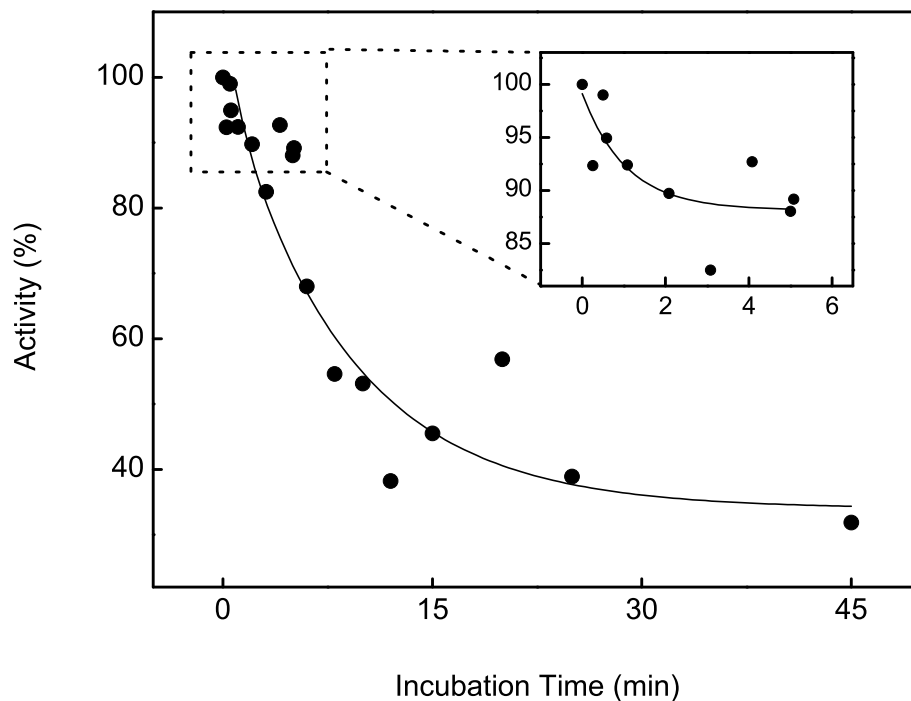


Figure 5.64. Temperature dependent inactivation of native *EcPDF-C Δ 21*. Aliquots of *EcPDF-C Δ 21* were incubated at 60 °C for increasing periods of time, followed by incubation at 4 °C. The activity of the heat treated enzyme was then measured and plotted as a function of incubation period at 60 °C. The smooth line represents the best fit of the data with a bi-exponential decay function for the rate constants being equal to 0.95 ± 0.75 and $0.12 \pm 0.04 \text{ min}^{-1}$ with the fraction amplitudes being 0.12 and 0.88, respectively.

5.9.4. Steady-state properties of heat stable *Ec*PDF-C Δ 21

The heat stable fraction of *Ec*PDF-C Δ 21 was prepared by incubating the enzyme at 60 °C for 2.5 h, followed by an overnight incubation at 4 °C. CD spectra of the heat treated *Ec*PDF-C Δ 21 revealed that the unfolded enzyme fraction did not recover any significant secondary structure upon cooling. The steady-state parameters of the heat stable enzyme were then determined as described previously in section §4.3. Figure 5.65 shows the steady-state properties of *Ec*PDF-C Δ 21. The data conforms to the Michealis-Menten model and was analyzed by Eq. (1) to obtain the k_{cat} and K_m values for the heat stable enzyme (5.8 s^{-1} and $13\text{ }\mu\text{M}$, respectively). Note that these values are similar to those of the Zn^{2+} form of the enzyme.

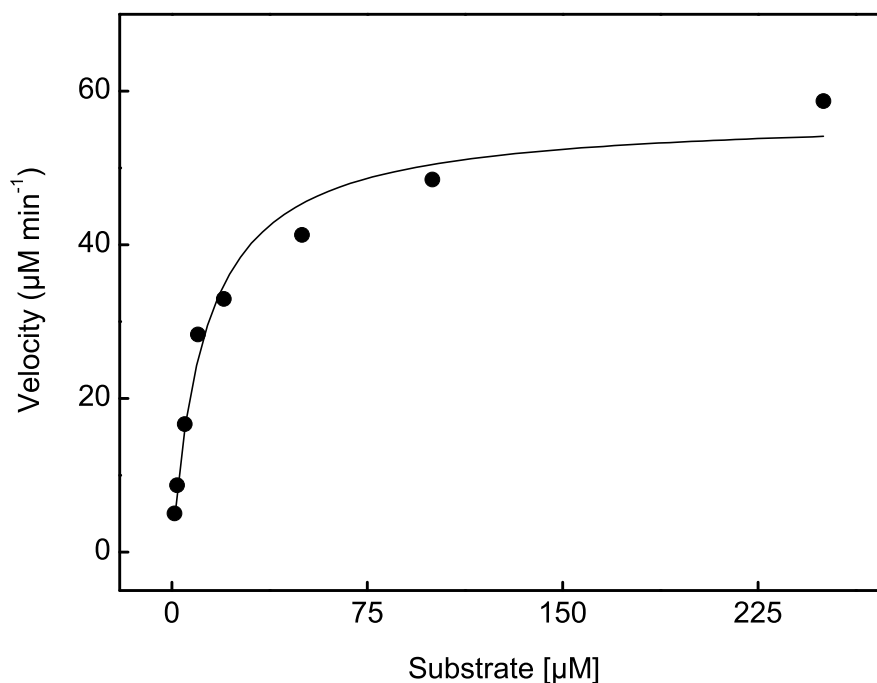


Figure 5.65. Steady-state parameters of heat stable *Ec*PDF-C Δ 21. The activity of $0.165\text{ }\mu\text{M}$ *Ec*PDF-C Δ 21 was measured after heat treatment at 60 °C for 2.5 h followed by overnight incubation at 4 °C. The solid smooth line represents the best fit of the data for the K_m and V_{max} values of $13 \pm 2\text{ }\mu\text{M}$ and $57 \pm 3\text{ }\mu\text{M/min}$, respectively.

6. DISCUSSION

6.1. Selective Inhibition of Type I MetAPs

Realizing the importance of the bacterial MetAP as an untapped target for antibiotic development, a focused library of small organic compounds was tested for efficacy as potential inhibitors of the type I MetAP. As noted in Chapter 1, an ideal antibiotic would not only (a) selectively inhibit the bacterial (*E. coli*) MetAP isoform while having little or no effect on the human homologue, it would also (b) be active against the native metalloform of the bacterial enzyme. With such primary criteria in mind, a two pronged approach was undertaken. The sections below discuss the results obtained from the experiments conducted to identify inhibitors selective for the *E. coli* MetAP isoform (section §6.1.1) and to study their selectivity for specific metalloforms of *EcMetAP* (section §6.1.2).

6.1.1. Isoform selective inhibition of MetAPs

Through an initial screening, barbituric acid based compounds (barbituric acid, thiobarbituric acid and dimethyl barbituric acid) were found to inhibit the catalytic activity of the *EcMetAP* enzyme (Tables 5.2 and 5.4, pages 110 and 118). The barbituric acid moiety functions as a Lewis base which is a common feature of previously reported inhibitors of MetAP. The barbiturate derivatives are therefore expected to coordinate with the active site metal ion via the carbonyl oxygen or the ring nitrogen (or both) of the barbiturate moiety. Support for this feature is derived from the docking results of one of the highly potent inhibitors identified in this study. This can be seen in Figure 6.1 depicting the inhibitor MH-5-74 docked within the

EcMetAP active site cavity. The carbonyl oxygen of the MH-5-74 barbiturate moiety is at 2.7 Å from the active site metal ion, suggesting its strong interaction with the enzyme.

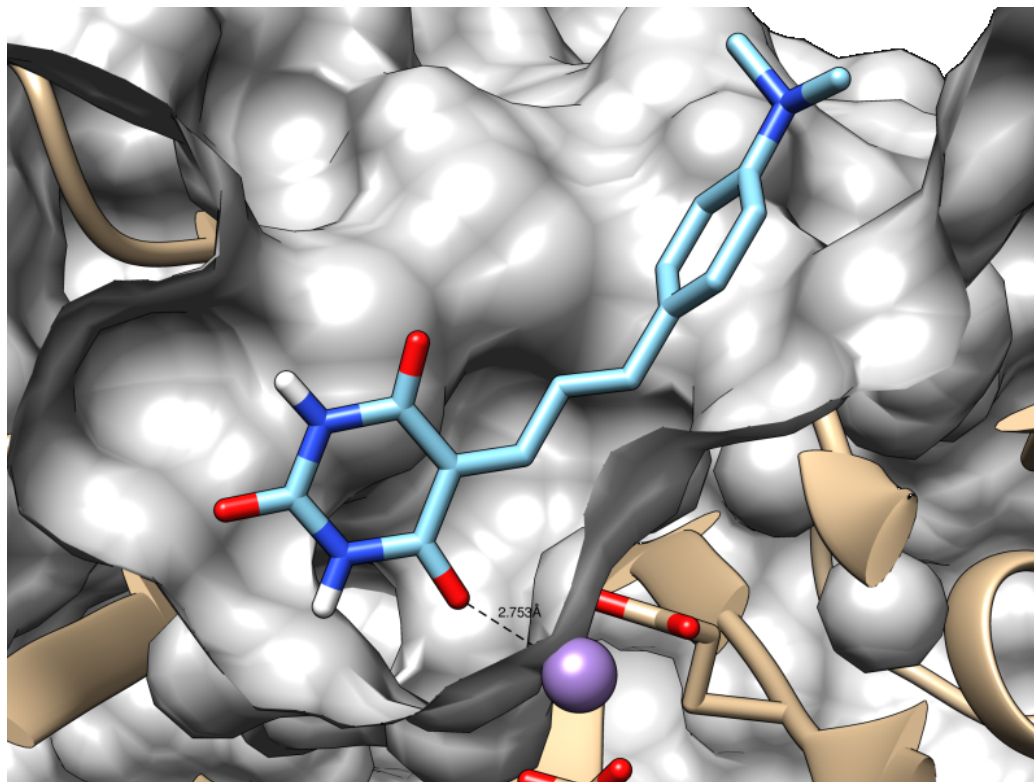
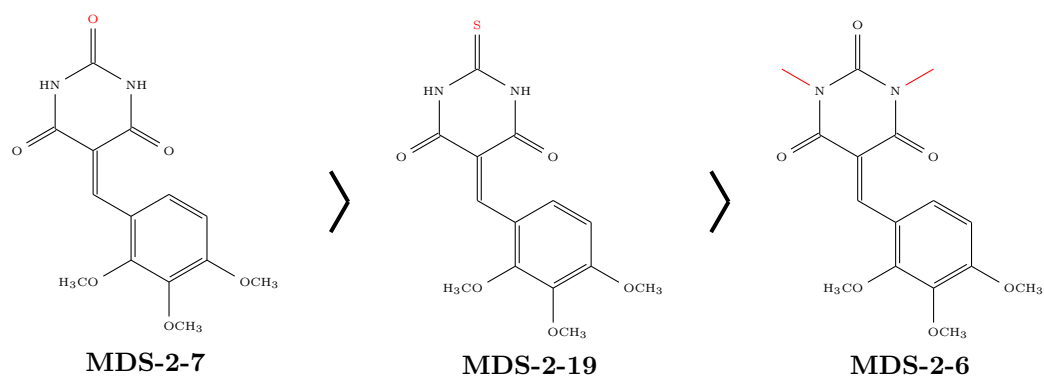


Figure 6.1. MH-5-74 docked within *EcMetAP* active site. The clipped molecular surface of *EcMetAP* reveals the interaction of the active site metal ion with the barbiturate moiety of the inhibitor. The inhibitor structure was docked with the X-ray crystal structure of mononuclear *EcMetAP* (2GTX) using AutoDock Vina.

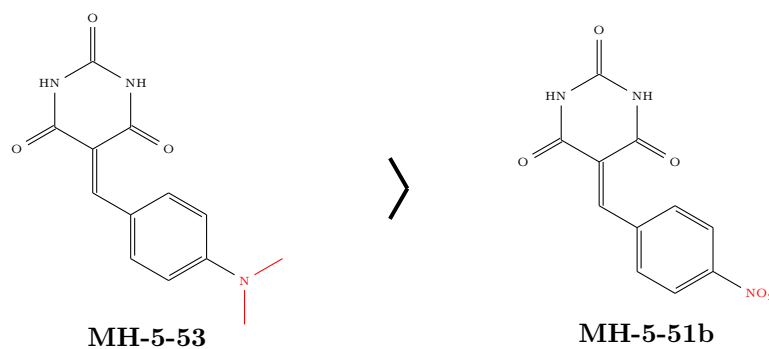
In the search for a potent and isoform selective inhibitor for *EcMetAP*, a series of derivatives of the above barbiturate based compounds were screened and the results of these screenings are listed in Tables 5.2, 5.3, 5.4, 5.5 and 5.6. The typical barbiturate derivative consisted of a variously substituted phenyl moiety attached via a conjugated linker of either one or three carbons in length. The screening of this series of barbiturate derivatives allowed the qualitative determination of the effect of each physico-chemical variable upon the inhibitory potency of the compounds. For example, the compounds

with substituents on the barbiturate moiety (2-thio and 1,3-dimethyl) were significantly less effective at inhibiting *EcMetAP*. The only exceptions to this observation were MDS-2-2 and MDS-2-22. The least effective inhibitors belonged to the 1,3-dimethyl substituted group, and this may be due to steric hindrance caused by the methyl moieties within the active site sub-pocket containing the metal ion. Inhibition was also affected by the length of the conjugated linker. An increase in the length of the linker resulted in a clear enhancement of the inhibitory effect (with the exception of MDS-2-1). A possible explanation for this is presented by the observation that the phenyl moiety of the inhibitor can form $\pi - \pi$ interaction with one of the several aromatic residues present at the mouth of the active site pocket. This interaction is prevented when the linker is too short (methyl vs. propyl) to allow the inhibitor's phenyl moiety to extend to the entrance of the enzyme active site. Additionally, the substituents on the phenyl group exhibited a marked effect on the potency of the compounds. The presence of electron donating groups resulted in good inhibition whereas electron withdrawing groups showed poor or no inhibition of *EcMetAP*. This observation agrees with the expected role of the barbiturate moiety as a Lewis base in coordinating with the active site metal ion. The presence of electron donating groups on the phenyl ring increases the strength of the Lewis base by resonance effect through the conjugated linker. Thus the carbonyl oxygen of the barbiturate moiety becomes a stronger nucleophile for interaction with the metal ion of the enzyme. This is further supported by the observation that compounds with unconjugated linkers showed no inhibition even in the presence of electron donating groups on the phenyl ring. A summary of these observations is depicted with selected inhibitors in Figure 6.2.

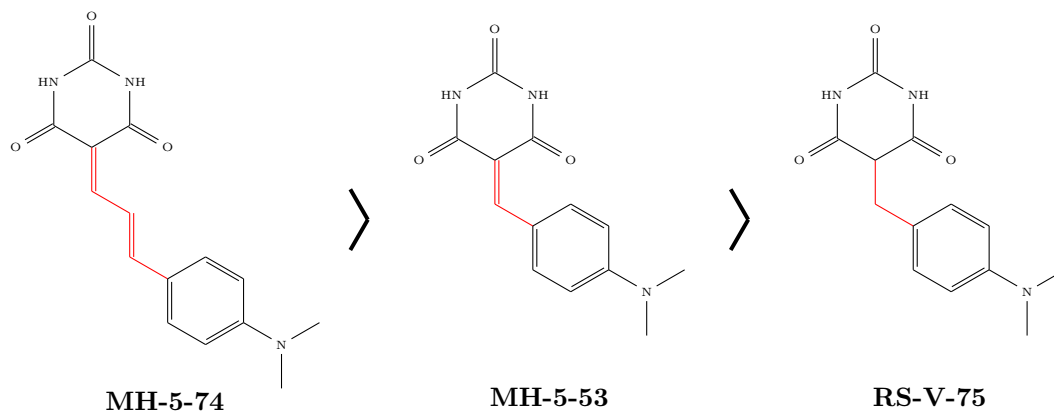
From the data presented in Tables 5.3 to 5.6, one particular class of barbiturate derivatives was identified as being of particular interest. The barbituric acid derivatives with the (4-dimethylamino)phenyl moiety (MH-5-53, MH-5-74, RS-V-39, RS-V-75,



(a) 2-oxo-barbiturates were more effective than 2-thio substituted derivatives while 1,3-dimethyl substituted derivatives were least effective.



(b) Electron donating groups on the phenyl ring were more effective than electron withdrawing groups.



(c) Three carbon conjugated linkers were more effective than once carbon conjugated linkers, while unconjugated linkers were least effective.

Figure 6.2. Selected examples of compounds showing the effect of various molecular properties on their inhibitory potency against *EcMetAP*.

MDS-1-23, MDS-1-25, MDS-2-1, MDS-2-2) displayed a potent inhibitory effect on the type I MetAPs (both *E. coli* and human forms). In particular, these compounds were marked with unique spectroscopic properties which changed upon interaction with the enzymes. Although many of these derivatives were potent inhibitors, they showed no isozyme selectivity towards the human and *E. coli* type I MetAPs. For example, the highly potent inhibitor MH-5-74 had nanomolar inhibition constants for both isozymes (Figure 5.19, page 130). The inhibitor MDS-1-25 did display selectivity in inhibiting the two isozymes, however in contradiction to the requirement, it preferentially inhibited the human isozyme (Figure 5.18, page figure 5.18). On the other hand, while the inhibitor MH-5-53 inhibited both isozymes with nearly equal potencies, it showed distinctive spectral changes upon binding with the two MetAP isozymes (Figure 5.20, page 132).

The distinct interaction of MH-5-53 with the MetAP isozymes is marked by the ratio of the two absorbance peaks (A_{355}/A_{485}) for the ligand complexed with *Ec*MetAP and *Hs*MetAP (being equal to 0.78 and 2.6 respectively, Table 5.8, page 136). A study of the spectral features of this inhibitor revealed that the absorbance peak at 485 nm was affected by the polarity as well as the *pH* of the solvent. As shown in Figure 5.21, page 133, whereas the absorbance intensity of MH-5-53 at 485 nm was enhanced by acidic *pH*, it was enhanced as well as blue shifted (by 20 nm) in the presence of solvents of low polarity (such as DMF). Since there is no evidence for a change in the absorbance maximum of MH-5-53 upon interaction with either MetAP isozyme it is apparent that the polarity of the enzyme's micro-environment is not significantly different than that of the solvent. However the increased absorption intensity of the ligand upon binding with either isozyme (but *Ec*MetAP in particular), suggests its altered protonation state at the enzymes's active site pocket. In fact, the reversibility of the change in absorbance at 485 nm as a function of *pH* (Figure 5.22, page 134) indicates that the

observed isozyme-selective spectral feature is a property of the protonation state of the ligand at the enzyme active site. The pK_a calculation data obtained from the Calculator Plugin for Marvin 5.10.3 (ChemAxon, <http://www.chemaxon.com>) shown in Figure 6.3 illustrate the distribution of different microspecies of MH-5-53 as a function of pH . These data suggest that one or both of the barbiturate ring nitrogens of MH-5-53 are deprotonated in the enzyme bound state. This can be explained by the expected coordination of the inhibitor via the barbiturate ring nitrogen to either the metal ion or one of the carboxylate moieties at the MetAP active site. From the differential spectral response of MH-5-53 to the *Ec*MetAP and *Hs*MetAP isozymes (as evidenced by the ratio of absorbance at 485/355 nm), it is conjectured that the inhibitor coordinates through both ring nitrogens in case of the bacterial isozyme but with only one in case of the human isozyme.

Further studies, however, revealed that the MH-5-53 compound was unstable in aqueous solutions at experimentally relevant pH (Figure 5.23, page 135). The slow decrease in absorbance of the 485 nm peak with the concomitant increase in absorbance of the 355 nm peak suggests that the inhibitor may be undergoing a hydrolytic breakdown giving rise to a new subspecies with enhanced absorption at 355 nm. Note that neither pH nor solvent polarity had any effect on the 355 nm absorption peak, implying that the observed spectral change over time was due to the potential generation of lysis products of MH-5-53. Due to the perceived instability of MH-5-53, further detailed biochemical characterization of its interaction with the MetAP isozyme was not undertaken. However, it is conceivable that with an understanding of the nature of MH-5-53, a suitably modified derivative may provide an excellent probe as well as potent and selective inhibitor of MetAP isozymes.

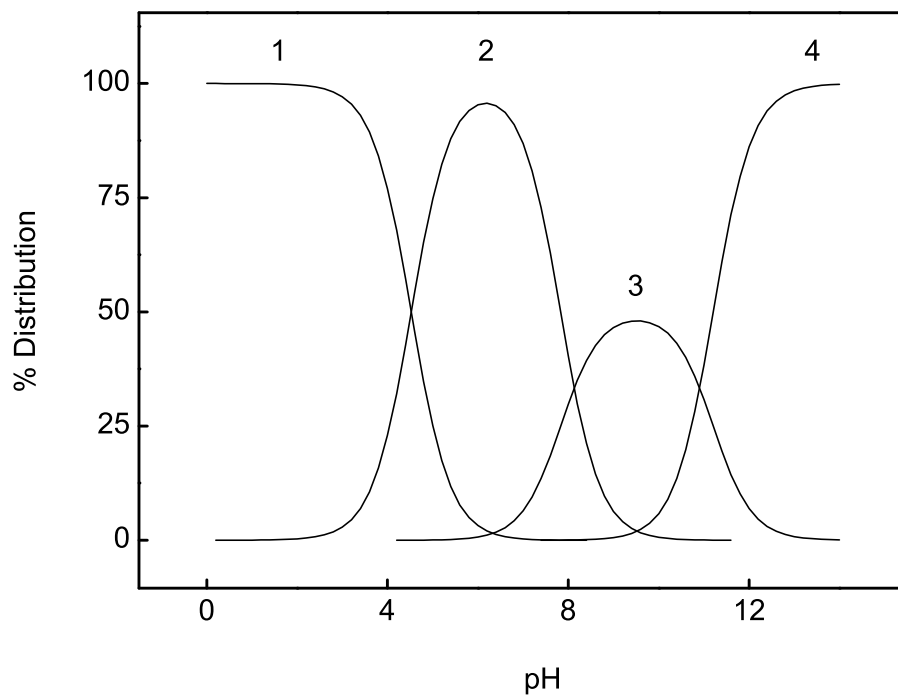
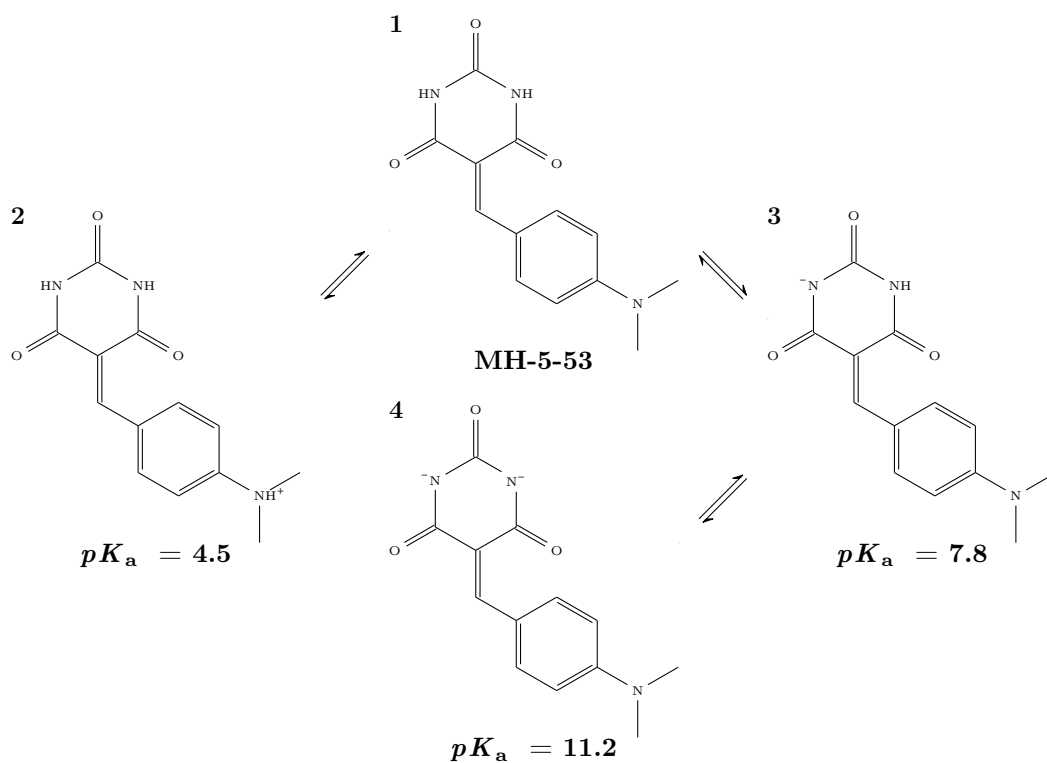


Figure 6.3. Protonation states of MH-5-53. The percent distribution of different microspecies is plotted as a function of pH . The data were obtained using the pK_a Calculator Plugin for Marvin 5.10.3 (ChemAxon).

In addition to the above class of inhibitors, several other inhibitors also displayed selectivity towards the human MetAP isozyme. These include 5-51b, 5-52, 5-54, 1-8, 1-17, 1-20 and 1-27, with inhibition constants for *Hs*MetAP ranging from 10 fold to over 60 fold lower than those for *Ec*MetAP. In summary, although this study did not reveal any potent inhibitors selective for *Ec*MetAP, several inhibitors were identified which (a) were highly potent inhibitors of both *Ec*MetAP and *Hs*MetAP, or (b) were selective inhibitors of *Hs*MetAP. The results of the inhibition studies obtained for the library of compounds in the study, in combination with the molecular predictors of the compounds (obtainable through computational methods) are a good source of data for conducting QSAR (Quantitative Structure Activity Relationship) analysis. Such analysis would provide valuable information that could be used to design new inhibitors that are highly potent as well as selective for a specific MetAP isozyme.

6.1.2. Metalloform selective inhibition

One of the primary reasons for the failure in designing or identifying *in vitro* *Ec*MetAP inhibitors that serve as antibiotics has been the inability in ascribing the physiological metal ion for the enzyme, particularly with respect to the metal ion used in conventional enzyme assays of *Ec*MetAP activity [86, 90]. This has been evident from the fact that several potent inhibitors of MetAPs display selectivity towards specific metalloforms of the enzyme. Moreover, metal ion coordinating inhibitors have been found to recruit extraneous metal ions from the solution under *in vitro* conditions resulting in spurious interactions between such ligands and the enzyme. A two fold approach was used to examine the nature of metal dependent interactions in MetAP: (a) a study of the metalloform selective inhibition in *Ec*MetAP (discussed below) and (b) a study of the metal ion binding and selectivity in *Ec*MetAP (discussed in the following section). The dansylamide derivative of the metallospecific Mn^{2+} -*Ec*MetAP

inhibitor 5-(2-chlorophenyl)furanoic acid was used as a spectroscopic probe to study the metal dependent interaction of the ligand with the *EcMetAP* active site in the presence of different bound metal ions.

Prior to such detailed studies, it was affirmed that the derivatized compound (DCPF) retained the metallospecific properties of its parent compound (5-(2-chlorophenyl) furanoic acid). The data summarized in Table 5.11, page 158 shows that while DCPF inhibited the activity of different *EcMetAP* metalloforms, the inhibitory potency against Mn^{2+} -*EcMetAP* was over 25 fold greater than the other metalloforms of the enzyme. Additionally, it was found that the fluorescent spectral feature of DCPF (Figure 5.8, page 98) is not only altered upon interaction with *EcMetAP* (Figure 5.39, page 160), but the spectral change is dependent on the specific metal ion present at the active site of the enzyme (Figure 5.40, page 161). In fact, in a seemingly curious coincidence, it is evident from Figure 5.40 that the spectral changes observed in the presence of catalytically active metalloforms of *EcMetAP* (Co^{2+} , Mn^{2+} and Ni^{2+} containing enzyme) are distinct from those occurring upon interaction with catalytically inactive forms of the enzyme (apo-enzyme and Ca^{2+} , Cu^{2+} metalloforms). Whereas the fluorescence intensity of DCPF is enhanced by approximately 75 RFU in the presence of catalytically active *EcMetAP*, it is enhanced by about 150 RFU in the presence of catalytically inactive forms. Note that in addition to this difference, the maximal change in fluorescence intensity appears at 495 nm for all metalloforms of *EcMetAP* (including the apo-enzyme) except for the Mn^{2+} form where the maximum change is seen at 530 nm. Additionally, the distinct changes in DCPF in spectra observed upon interaction with different metalloforms of *EcMetAP* were found to be reversible by changing the metal ion bound at the active site of the enzyme

(Figure 5.41, page 162). These characteristics suggest that the conformation and electronic configuration of DCPF bound within the enzyme active site cavity are affected to varying degrees by Co^{2+} , Ni^{2+} and Mn^{2+} metal ions.

Since the binding of DCPF to apo-*EcMetAP* led to a significant enhancement and blue shift in the fluorescence spectra of DCPF, it is clear that in addition to the active site metal ion, the micro-environment of the enzyme active site pocket was also a contributing factor. The effect of solvent polarity on the fluorescence spectra of DCPF (Figure 5.42, page 163) illustrates the potential for the moieties in the enzyme active site affecting DCPF fluorescence. An increasing blue shift ($\lambda_{\text{max}} = 550, 515$ and 495 nm) is seen with decreasing solvent polarity (water > dimethylformamide > dioxane) demonstrating typical positive solvatochromism. Thus the spectral features of DCPF observed upon binding to the apo enzyme (as well as certain metalloforms like Ca^{2+} - and Cu^{2+} -*EcMetAP*) may be attributed to the nonpolar amino acids lining the enzyme cavity, such as Cys59, Tyr62, Tyr65, Cys70, Cys78, Cys169, Phe177, Met206 and Trp221.

In an attempt to explicate the mechanistic process leading to the observed metalloform-selective features of the DCPF-*EcMetAP* interaction, transient kinetic studies of association of the ligand and enzyme were undertaken. The data reported in Section §5.6.3 suggest that the binding of DCPF to *EcMetAP* is a highly complex process consisting of several steps presumably involving multiple conformational changes of DCPF following the initial binding of the ligand to the active site. The change in fluorescence signal of the DCPF-*EcMetAP* complex over a period of two seconds revealed a tri-exponential association in case of Mn^{2+} -*EcMetAP*, with rate constants in the range of 3, 20 and 450 s^{-1} (Figure 5.43, page 165). On the other hand, although the association kinetics in case of apo-*EcMetAP* were tri-exponential for the same period (Figure 5.46, page 168), extended data revealed that the binding reaction

was completed on a much longer time scale with equilibrium not being established even at the end of 10 s (Figure 5.47, page 169). Note that the change in fluorescence signal in case of the DCPF–apo-*EcMetAP* complex is about two fold that in case of DCPF–Mn²⁺-*EcMetAP*. The ability to observe several additional phases in case of apo-*EcMetAP* may therefore be attributed to this feature, as the small amplitude of longer phases (appearing beyond two seconds) in case of Mn²⁺-*EcMetAP* could preclude their accurate measurement and subsequent resolution. On the other hand, it is possible that whereas the DCPF–Mn²⁺-*EcMetAP* complex attains equilibrium on a shorter time scale, the DCPF–apo-*EcMetAP* complex is unable to do so due to the absence of a metal ion to anchor and potentially stabilize the ligand within the active site pocket. Due to the complexity of the association kinetics data, no analytical conclusion could be obtained regarding the mechanisms involved in the interaction of DCPF with different metalloforms of *EcMetAP*. In this situation, the use of a hybrid quantum mechanics/molecular mechanics (QM/MM) method in the computational simulation of the DCPF–*EcMetAP* complex may reveal insights into the metalloform selective ligand interaction.

6.2. Metal Ion Binding and Selectivity of MetAP

Due to weaker binding of metal ions to different MetAPs, the identity of their physiological metal ion has been the subject of considerable debate in recent years [13, 78, 93, 103, 104, 145, 146]. Identifying the native metal ion has been particularly important since the binding affinities of inhibitors (as putative antibiotics) to the enzyme have been shown to be dependent on the nature of the metal ion present at the active site pocket of the enzyme [86, 90, 142]. In addition, there has also been a long standing controversy over the number of metal ions involved in the catalytic

activity of MetAP, with reports supporting one [79, 80, 147], two [94, 106, 148] and even three [106] metal ions at the active site pocket of the enzyme. In cognizance of these contrasting positions, there is compelling evidence for a mononuclear MetAP active site. While the identity of the native metal ion in various isoforms of MetAP remains irresolute, evidence from *in vivo* effects of Fe²⁺-selective MetAP inhibitors has suggested that Fe²⁺ serves as the physiological metal ion of the enzyme in *E. coli* [105, 149].

With the interest of determining the direct binding affinities of different metal ions for MetAP, attempts were made to identify the metal ions which would catalytically activate the enzyme as well as provide spectroscopic signatures upon binding to the enzyme active site. In a fortuitous discovery, Eu³⁺ was identified as a cofactor of *EcMetAP* (Figure 5.54, page 182) and its luminescence emission spectrum was found to be significantly enhanced upon binding to the enzyme (Figure 5.48, page 171). The determination of the binding affinity of Eu³⁺ to *EcMetAP* from both these properties (activation of enzyme and enhancement of luminescence) revealed closely similar activation/dissociation constants of about 20 μM (Figures 5.49 and 5.55, pages 173 and 183).

From preliminary experiments, it was confirmed that the binding affinities of various metal ions for *EcMetAP* could be investigated by competitively displacing the enzyme bound Eu³⁺ with other metal ions. The results described in section §5.7.2 and summarized in Table 5.12, page 186 present the most exhaustive determination and comparative account of metal ion binding affinities for the *E. coli* MetAP enzyme. The enhancement of Eu³⁺ luminescence upon binding to *EcMetAP* is presumably due to the decrease in the oscillator strength of the solvated lanthanide ion upon exchange of the coordinated water molecules by the cognate groups/residues of the enzyme within the active site pocket [150]. The analysis of the experimental data for metal

ion binding (via competitive displacement of enzyme-bound Eu^{3+}) was facilitated by the use of the complete solution of a quadratic (rather than cubic) function (Eq. (5), page 77) as previously described by Banerjee et al. [128]. This was possible due to the fact that Eu^{3+} exhibits a fairly weak affinity for *EcMetAP* as compared to most other metal ions.

Of different metal ions utilized herein, Fe^{3+} presented a particular hurdle in the accurate determination of its binding affinity to *EcMetAP*. Fe^{3+} has been known to exhibit unusual properties in aqueous solution as its salts undergo hydrolysis in a biphasic manner. The first (fast) phase involves the conversion of Fe^{3+} salts to insoluble $\text{Fe}(\text{OH})_3$, which complexes with its parent salt (in this case FeCl_3), and the latter undergo further hydrolysis during the second (slow) phase. The rate and extent of such hydrolysis are dependent on the salt type, concentration, temperature, *pH*, and other anionic components of the mixture [151–153]. As a result of this process, a significant fraction of the aqueous Fe^{3+} ion in the experiment was expected to be converted near-instantaneously to its insoluble hydroxide form and therefore be unavailable for the competitive displacement of the *EcMetAP* bound Eu^{3+} . To circumvent such a problem, typical biochemical experiments involving Fe^{3+} are performed in the presence of chelating agents, such as citrate or NTA [154, 155]. While this approach is suitable for proteins/enzymes that bind Fe^{3+} with very high affinity, it was not applicable to *EcMetAP* due to its relatively weak binding affinity for metal ions. Moreover, the interaction of such chelating agents with Eu^{3+} was found to significantly perturb the luminescence spectra of the lanthanide ion, further complicating the experimental set up and data analysis. Hence, the recourse was made to determine the effective concentration of Fe^{3+} , i.e., the metal ion which remained unhydrolyzed (during the fast phase) upon dilution of acidic FeCl_3 in the buffer solution, by monitoring the time dependent changes in the absorption spectra of Fe^{3+} . The experimental data

(Figures 5.51 to 5.53) revealed that 20 % of FeCl_3 remained unhydrolyzed during the course of the experiment, which is in agreement with the literature value [151]. With this information, the corrected binding affinity of Fe^{3+} to *EcMetAP* was calculated.

Prior to this study, the direct binding affinities of Mn^{2+} and Co^{2+} to *EcMetAP* were determined by Holz and his collaborators [77, 94, 95] via isothermal titration calorimetry. The magnitudes of the dissociation constants were $3.0\ \mu\text{M}$ [95] and $5.3\ \mu\text{M}$ [94] for Mn^{2+} , and $6.4\ \mu\text{M}$ [77] and $1.4\ \mu\text{M}$ [94] for Co^{2+} . However, it should be noted that these results were obtained using a three independent site model since the data could not be analyzed with either one or two site models, as claimed by the authors. On the other hand, as discussed below, the binding affinities reported by Holz et al. using steady-state kinetic data are consistent with those determined in this study. Moreover, under the experimental conditions of this study, the activation constants (K_a value of Table 1; determined via the steady-state kinetic method) of Mn^{2+} ($0.6\ \mu\text{M}$) and Co^{2+} ($0.5\ \mu\text{M}$) are similar to their corresponding K_d values determined via the Eu^{3+} displacement method.

As noted earlier, Eu^{3+} not only served as a luminescent probe, but also as a metal cofactor in activating apo-*EcMetAP* during the overall catalysis. The activation of certain metalloenzymes by Eu^{3+} has indeed been noted previously [150]. The activation constant of Eu^{3+} for *EcMetAP* derived from the steady state experiment $15 \pm 5\ \mu\text{M}$ being comparable to the dissociation constant determined from direct binding $25 \pm 5\ \mu\text{M}$ suggests that the binding of Eu^{3+} to the enzyme and its activating role conform to a common macroscopic pathway. The data in Table 5.12, page 186 reveals a comprehensive comparison of the relative effectiveness of the various metal ions in activating *EcMetAP*, with the order being: $\text{Co}^{2+} > \text{Fe}^{2+} > \text{Mn}^{2+} > \text{Ni}^{2+} > \text{Eu}^{3+}$. The trend in relative activation of *EcMetAP* reported by D'souza and Holz [78] ($\text{Co}^{2+} > \text{Fe}^{2+} > \text{Mn}^{2+}$) is in agreement with that reported in this study. In fact the

magnitudes of the metal ion binding affinities determined in this study by activation of *EcMetAP* are not only comparable with those reported by the Holz group using similar methods, but also comparable with those determined by direct binding (via Eu^{3+} displacement) in this study (see Table 6.1, page 213). It is thus reasonable to conclude that the method of competitive Eu^{3+} displacement has provided a very accurate means of determining the direct binding affinities of a wide range of metal ions.

Table 6.1. Comparison of the binding affinities of Mn^{2+} and Co^{2+} for *EcMetAP* determined in this study with those reported in literature.

Metal Ion	Dissociation Constants (μM) from			
	Literature[94]		This Study	
	Direct Binding ¹	Steady-State	Direct Binding ²	Steady State
Mn^{2+}	5.3	0.4	0.7	0.6
Co^{2+}	1.4	0.5	0.2	0.5

1 K_d determined by direct binding using ITC.

2 K_d determined by direct binding via Eu^{3+} displacement

It is interesting to note that while Zn^{2+} (under reducing conditions) has been reported to activate *EcMetAP* [78], the Zn^{2+} -*EcMetAP* enzyme showed practically no activity (Figure 5.54, page 182). This apparent discrepancy may however be explained by the fact that the studies involving Zn^{2+} -*EcMetAP* activity were carried out using the tetrapeptide substrate Met-Gly-Met-Met in contrast to the substrate used in this study (Met-AMC). This is supported by the observations of Yang et al. [81], Li et al. [86] where Met-AMC could not be cleaved by the Zn^{2+} form of *EcMetAP*. Conversely, Ni^{2+} was reported to be unable to activate *EcMetAP* (for cleaving the tetrapeptide

substrate Met-Gly-Met-Met) [78], but the Ni²⁺-*EcMetAP* enzyme is clearly able to cleave Met-AMC. Several other metal ions do not activate *EcMetAP* at all despite their avidity for the enzyme. On the other hand, Eu³⁺ binds to *EcMetAP* very weakly (approximately an order of magnitude weaker than all other metal ions tested), yet is able to activate *EcMetAP* to as much as 20 % of its most active form (Co²⁺-*EcMetAP*) even at sub-saturating conditions. In order to gain additional insight into the nature of selectivity of the metal ions towards activating *EcMetAP*, the effect of the metal ions on the steady-state kinetic parameters of the enzyme were investigated. The data summarized in Table 5.13, page 187 indicates the k_{cat} and K_{m} values of different metalloforms of *EcMetAP* for the Met-AMC substrate. Note that both the K_{m} and k_{cat} values decrease in the order: Co²⁺ > Mn²⁺ > Ni²⁺ > Eu³⁺. The fact that the K_{m} value for the Eu³⁺-*EcMetAP* enzyme is about 2 fold lower as compared to that obtained for the Co²⁺ form of the enzyme suggests that Eu³⁺ enhances the apparent binding affinity of the substrate to the enzyme.

A survey of the cumulative experimental data obtained from this study provides an opportunity for interpreting the determinants of metal ion selectivity towards varying binding affinities and catalytic efficiencies for *EcMetAP*. The data presented in Table 5.12, page 186 reveals that the binding affinity of metal ions to *EcMetAP* decreases in the order Fe²⁺ > Fe³⁺ > Co²⁺ > Ni²⁺ > Cu²⁺ > Mn²⁺ > Ba²⁺, Sr²⁺ > Ca²⁺ > Zn²⁺ > Mg²⁺ > Cd²⁺. This order is in contrast to the binding of metal ions to small molecular weight chelates which adheres to the Irving-Williams series [156]. This is not surprising as many other metalloenzymes exhibit similar behavior [157–159] presumably because of strong influence of the micro-environment of the enzyme's active site pocket in discriminating the avidity of different metal ions. As marked in the above table, the metal ions in this study can be distinguished into two classes: (i) Class I metal ions exhibiting K_{d} values < 1 μM and, (ii) Class II metal

ions with $K_d > 1 \mu\text{M}$. Note that class I metal ions are composed entirely of transition metals whereas class II metal ions are primarily composed of the alkaline earth metals. The trend in the magnitudes of the binding affinities of each class shows a linear relationship to the ionic size (with the exceptions of Mn^{2+} and Cd^{2+}) although the relationship is reversed between the two classes as shown in Figure 6.4, page 216.

It is further evident from Table 5.12 that the distinction between these two classes extends to the catalytic nature of the metal ions in *EcMetAP*. The metal ions of class II are catalytically ineffective, while Cu^{2+} and Fe^{3+} of class I are also unable to activate *EcMetAP*. A clue to this selectivity is realized from the catalytic mechanism proposed for the mono-metalated enzyme [80], according to which, the metal ion coordination increases from 5 to 6 upon binding of the substrate via the carbonyl oxygen. The metal-bound water acts as a nucleophile and it attacks at the carbonyl group of the substrate forming a tetrahedral intermediate. Thus the catalytic effectiveness of the active site metal might be envisioned to be controlled by two factors: (i) the ability of the metal ion to undergo transition from pentacoordinate to hexacoordinate geometry to allow for the binding of the substrate and (ii) the degree of Lewis acidity of the metal ion being just appropriate to allow for the bound water to serve as a strong nucleophile. From the experimental data, it appears evident that both “softness” of metal ions (as described by Pearson’s HSAB theory [160]) and the coordination geometry are the major determinants of the catalytic functionality of the metal ions. Metal ions with “borderline soft” acidity and higher coordination states serve as desirable cofactors in catalyzing the *EcMetAP* dependent reaction. The borderline soft acidic characteristic of metal ions facilitates the deprotonation of the bound water molecule to serve as the nucleophile toward attacking the carbonyl carbon of the substrate during catalysis. Thus despite its strong binding affinity, Fe^{3+} does not show catalytic activity as it falls in the category of hard acids and

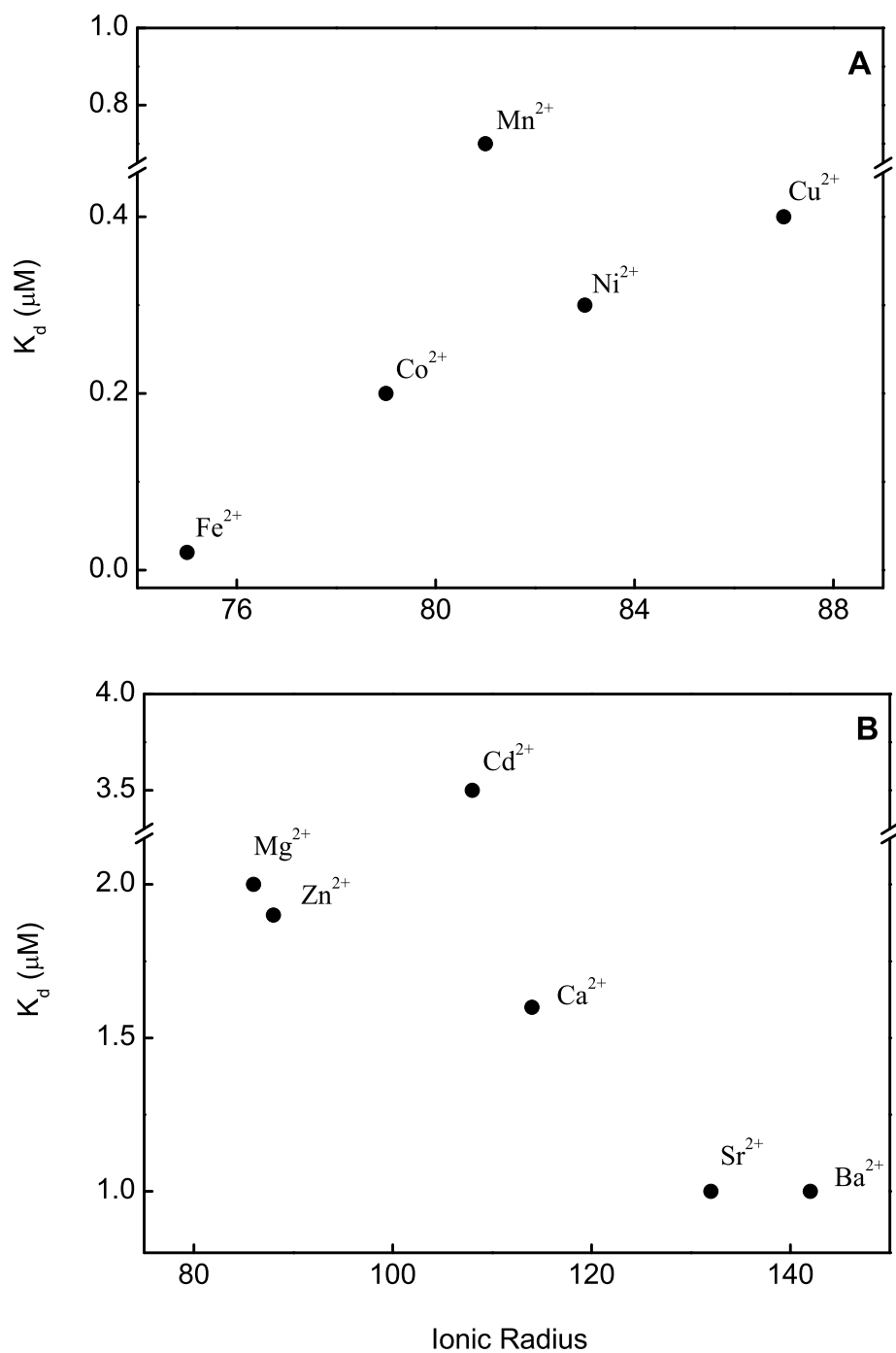


Figure 6.4. Relationship between ionic size of metal ions and binding affinity to *EcMetAP*. The binding affinity (K_d) of class I metal ions (**A**) is directly proportional to the ionic radius. The binding affinity of class II metal ions (**B**) is inversely proportional to the ionic radius.

therefore thermodynamically stabilizes the bound hydroxide anion, obviating the enzyme catalyzed hydrolytic cleavage of the peptide bond. Furthermore, metal ions with higher coordination states serve as activators of the enzyme since they stabilize the putative ground and transition states during catalysis. Thus despite its strong binding affinity to the enzyme, Cu^{2+} does not exhibit catalytic activity since it prefers the “undesirable” square planar geometry within the active site pocket of the enzyme.

In view of the above features, the ligand binding and activation role of Eu^{3+} during *EcMetAP* catalyzed reaction can be justified. The higher coordination geometry of Eu^{3+} is expected to promote the stabilization of both ground and transition states during the enzyme catalysis. Note that the Eu^{3+} bound at the *EcMetAP* active site may coordinate with multiple water (or hydroxide) molecules while being hexacoordinated with the active site residues and the substrate. The different bound water molecules can be expected to have varying nucleophilicity depending on the presence of secondary ligands. Moreover, despite its hard acid characteristics, Eu^{3+} exhibits the potential to rapidly exchange the coordinated water molecules (two to three orders of magnitude higher than other catalytically active metal ions) [161]. These features may allow the lanthanide ion to provide the nucleophilic hydroxide anion for attacking the carbonyl carbon of the substrate during catalysis.

6.3. Substrate Dependent Inhibition of MetAP by Cyclodextrin

As discussed earlier in section §6.1, although several potent inhibitors of type I MetAPs were identified through screening small organic compounds, the systematic/detailed biochemical and biological evaluation of these inhibitors was limited either by their extremely poor solubility or by their instability in aqueous media. In order to improve their viability, cyclodextrins were used as molecular carriers.

Cyclodextrins are constituted of cyclic rings contributed by 6, 7 or 8 glucopyranose units, referred to as α , β and γ cyclodextrins, respectively. These ring structures are shaped as toroids with a hydrophilic exterior surface and a lipophilic cavity. They form inclusion complexes with a wide range of compounds and, depending on the interacting guest moiety, their dissociation constants range over several orders of magnitude. Due to their non-polar cavity as well as low toxicity, cyclodextrins have been widely used as complexing and solubilizing agents in food, cosmetic and drug industries [162]. They are also known to enhance the bioavailability of drugs by facilitating their permeability (aside from solubility and stability) to cells under physiological conditions. Of the different cyclodextrins and their derivatives, 2-hydroxypropyl- β -cyclodextrin (HP- β -CD) has been found to be the most effective drug carrier, and it has been successfully used in the formulation of poorly soluble drugs [163].

While attempting to use HP- β -CD to solubilize and stabilize some of the potent MetAP inhibitors identified in the earlier sections, it was realized that the macromolecular carrier significantly impaired the catalytic activity of the enzyme (Figure 5.26, page 140). Cyclodextrins (CDs) have been known to affect the activity of many enzymes via different modes. They have been found to enhance the activity of enzymes by (a) solubilizing the product from the enzyme active site [164], (b) complexing with inhibitors [165, 166] or (c) stabilizing the enzymes under adverse conditions [167, 168]. On the other hand CDs have been known to inhibit enzyme activity primarily via reduction of the free substrate concentration due to sequestration (of the substrate) within the CD cavity. The apparent parallel to the inhibition of MetAP by HP- β -CD (as reported in this study) was first reported by Masato [169] for the inhibition of β -glucosidase by α -CD, and subsequently observed by others for various enzyme catalyzed reactions [165, 170, 171]. In each of the

reported instances of enzyme inhibition by CDs, the substrate is trapped within the cyclodextrin cavity thus reducing the availability of free substrate in the enzyme catalyzed reaction. However the experimental data presented in section §5.5 provide evidence for a unique mechanism for the inhibition of MetAP by HP- β -CD, and a review of the existing literature indicates that this mechanistic feature has not been previously demonstrated for any enzyme.

In an effort to delineate the mechanistic pathway for the inhibition of MetAP catalyzed reaction (using Met-AMC as the substrate) in the presence of HP- β -CD, it was realized that the mere sequestration of the enzyme's substrate by HP- β -CD was not adequate to explain the experimental data. This could be easily conceived by comparing the experimental rates of enzyme catalysis in the presence of HP- β -CD with those predicted on the basis of reduction in the free substrate concentration due to sequestration by HP- β -CD (Figure 5.31, page 146). Although there are some reports on the inhibition of selected enzymes by cyclodextrin due to direct interactions between them [171, 172], the experimental data reported in this study could not be explained on the basis of the direct interaction between the enzyme-cyclodextrin complex. In fact, in a surprising observation, increase in the substrate (Met-AMC) concentration enhanced the magnitude of inhibition of the enzyme by HP- β -CD as shown by Figure 6.5.

This observation is contrary to the reports of the reversal of of cyclodextrin-induced enzyme inhibition in the presence of increasing concentrations of substrate [173]. As elaborated in the results section, this feature has been due to the added inhibition of the enzyme (i.e., aside from the sequestration of the substrate) caused by the formation of the non-productive (dead-end) ternary complex involving bridged substrate between HP- β -CD and MetAP. The analysis of the substrate and CD concentration dependent enzyme catalyzed reaction data (Figure 5.32, page 149) by

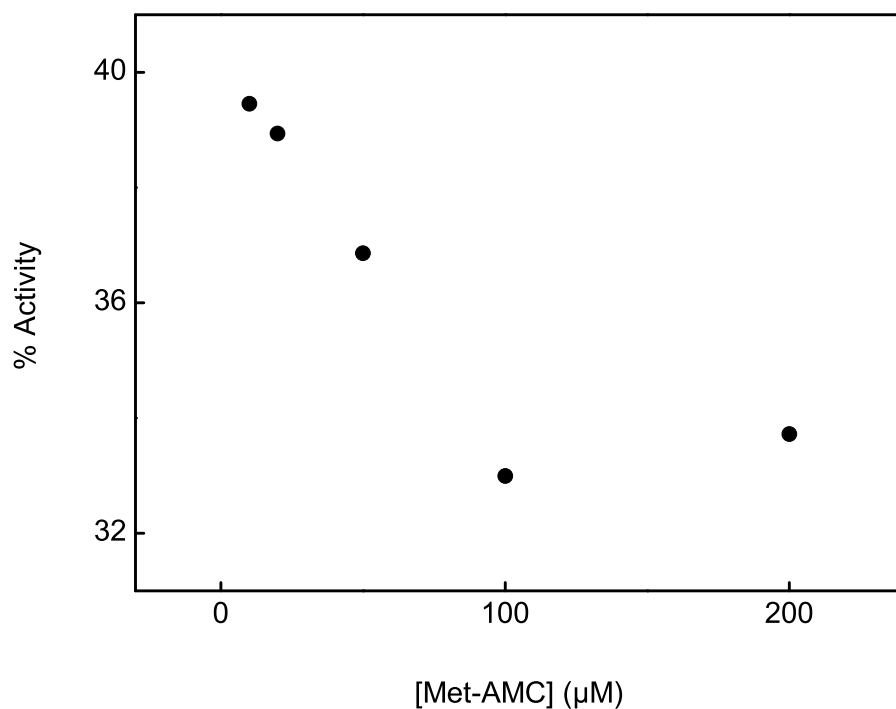


Figure 6.5. Effect of substrate concentration on Cd inhibited *EcMetAP* activity. The activity of *EcMetAP* in the presence of 5 mM HP- β -CD is plotted as a percentage of control *EcMetAP* activity (in the absence of HP- β -CD) at varying substrate (Met-AMC) concentrations. The enhanced decrease in activity at higher Met-AMC concentrations suggests that the substrate is contributing to the inhibitory effect of HP- β -CD.

alternative kinetic models unequivocally supported the model mechanism of Scheme 5.2, page 147. These results provide evidence that the HP- β -CD mediated inhibition of MetAP is not exclusively due to the sequestration of the enzyme's substrate by cyclodextrin, but is also due to the formation of HP- β -CD–Met-AMC–MetAP as the “dead-end” ternary complex. The latter is effectuated via bridging of the two ends of the substrate structure, viz., AMC and methionine moieties, between HP- β -CD and MetAP, respectively.

Although independent physical evidence for the direct interaction of the HP- β -CD–Met-AMC complex with MetAP could not be obtained (due to their relatively weak binding affinity), a combination of the X-ray crystallographic structure of the HP- β -CD–Met-AMC complex (Figure 5.34, page 152) coupled with the docking and

MD studies lead to support the prevalence of such a complex during the kinetic course of the HP- β -CD dependent inhibition of the enzyme catalyzed reaction. In view of the crystallographic structure of the HP- β -CD–Met-AMC complex, it appeared evident that the protruded methionine residue (while AMC being confined within the cyclodextrin cavity) would be unable to completely fill in the active site pocket of the enzyme. The docking data suggests that the substrate methionine side chain would fall short by about 3.5 Å from reaching the catalytic center of the enzyme. It is likely that the above void would be occupied by two water molecules such that they bridged between the active site resident metal ion and the thioether group of the methionine residue, the latter would be stabilized within the enzyme’s active site pocket both via hydrophobic interaction as well as the water mediated hydrogen bonding. However, since the HP- β -CD bound Met-AMC does not serve as direct substrate during the enzyme catalysis, it was surmised that the binding energy of the substrate within both the enzyme and cyclodextrin cavities (in the ternary complex ESC) is either greater than or equal to the binding energy of the substrate within the enzyme’s active site pocket in the ES complex alone. This was corroborated by the interaction energies obtained through the MD simulations of the complexes (see Table 5.10, page 155). The total interaction energy of the HP- β -CD–Met-AMC–MetAP complex is lower than that of each binary complex (HP- β -CD–Met-AMC, Met-AMC–MetAP and HP- β -CD–MetAP) alone. Evidently, these individual energetic contributions are modulated by the energetics of the unique interaction between the molecular surfaces involved in the formation of the HP- β -CD–Met-AMC–MetAP ternary complex, resulting in the observed inhibitory profile. The generality or frequency of such mechanism in other enzyme systems must await further studies particularly since there is an emerging trend of using cyclodextrins as the macromolecular carriers for enzyme inhibitors in the drug discovery endeavor.

6.4. Role of C-terminal Domain in PDF

The C-terminal domain of PDF has been noted for several remarkable features. It is responsible for anchoring the enzyme to the ribosome, orienting the PDF active site towards the ribosome exit tunnel [18]. The domain is dispensable for catalytic activity but detrimental for thermostability [108]. Furthermore, while it forms an α -helix when complexed with the ribosome or in crystalline form [18, 174, 175], it appears to be either mobile or disordered in solution. These properties suggested that the C-terminal domain of PDF may play an important role in regulating the function of the enzyme. In order to elucidate the properties imparted by the C-terminal domain to PDF, comparative studies were conducted with the native and truncated forms of *Ec*PDF. The data reported in section §5.9 suggest that the C-terminal domain of *Ec*PDF may be involved in the regulation of stability as well as catalytic activity of the enzyme.

6.4.1. Role of N-terminal residues in regulation of *Ec*PDF stability

The temperature induced unfolding of *Ec*PDF reported in section §5.9.1 supports the notion of different conformational states of the enzyme as proposed by Berg and Srivastava [101]. Two distinct unfolding phases of native *Ec*PDF are indicated with the transition temperatures of 51 and 75 °C (Figure 5.59, page 192). Given the thermostable nature of the truncated form of enzyme, it was expected that its unfolding would progress in a similar manner but with the transitions occurring at higher temperatures. It was therefore surprising to find that the unfolding of *Ec*PDF-C Δ 21 also displayed the transitions at the same temperatures (Figure 5.60, page 193). The thermostability of the truncated enzyme was instead manifested in a shift in the fractions of the labile and stable populations of the protein. Whereas the native enzyme exists as equal fractions of the two populations (evidenced by the

equal amplitudes of unfolding phases), the truncated enzyme exists primarily in the thermostable form ($T_m = 75^\circ\text{C}$) with only 10% of the population in the labile form ($T_m = 51^\circ\text{C}$). Note that the metal content (Zn^{2+} vs. Ni^{2+} as determined by ICP-AES) in both native and truncated forms of PDF was the same (Table 5.1, page 92). Hence it is conjectured that the two conformational states exist independent of the nature of bound metal ion.

The removal of the C-terminal domain also affected the rate constant of one of the two phases observed in the time dependent unfolding of PDF at 60°C . Whereas the rate constant of the slow unfolding phase was similar for both forms (about 0.01 min^{-1}), the fast unfolding phase of *Ec*PDF-C Δ 21 was about 8 fold slower than that of *Ec*PDF (0.07 vs. 0.54 min^{-1} respectively). In addition

The thermostability of *Ec*PDF-C Δ 21 is further discerned from the temperature dependent inactivation of PDF. The native *Ec*PDF is seen to be inactivated at 60°C in two distinct phases of equal amplitude (Figure 5.63, page 196). Note that once again, consistent with the above results, the amplitudes are skewed to 10% and 90% for the labile and stable phases respectively for the truncated form of the enzyme (Figure 5.64, page 197). Additionally, similar to the above observations, while the rate of inactivation of the stable phase remains unaffected, that of the labile phase is reduced by 3 fold for *Ec*PDF-C Δ 21.

The selective loss of the thermolabile population upon truncation of the C-terminal domain of PDF suggests that the C-terminal domain induces the whole protein molecule to exist in a high energetic state. The fact the the C-terminal domain is highly mobile or possibly disordered supports the notion that much of the entropic energy may be absorbed by the rest of the molecule resulting in its relative unstable state. Since the C-terminal domain of PDF is responsible for docking to the ribosome, it is clear that the conformation of the domain is dependent on the location of PDF in

the cell. While attached to the ribosome, the C-terminal domain will be fixed/rigid, whereas it will be flexible (dynamic or disordered) when the enzyme is free. It is therefore conceivable that the stability of PDF is at least partially determined by its location within the cell, via the state of its C-terminal domain. It has been suggested previously that the two conformational states are not interconvertible and it was not apparent if this was due to a high energy barrier [101].

6.4.2. Role of N-terminal Residues in regulation of *Ec*PDF activity

Prior to this study, the deletion of 21 amino acids from the C-terminal end of *Ec*PDF was reported to have no effect on the catalytic activity of the enzyme. However it is apparent from the data presented in Figure 5.16, page 107 that *Ec*PDF-C Δ 21 has significantly enhanced activity as compared to the native enzyme. Note that the differences in activities are not due to the presence of different metal ions in the enzyme preparations as both native and truncated forms were found to have the same composition of Ni²⁺ and Zn²⁺. Thus the deletion of the PDF C-terminal domain led to an increase in the $k_{\text{cat}}/K_{\text{m}}$ value of the enzyme by almost 18 fold for the fMet-Leu-pNA substrate. This effect may at least partly be explained by the observation of Chan et al. [174] that the C-terminal helix interacts with the loop containing the active site metal ligand Cys90, and absence of the helix not only shifts the loop by several angstroms but also orients the side chain of Cys90 differently (see Figure 6.6). In addition to the effect via the Cys90 loop, the C-terminal domain may also affect PDF catalytic activity via the above proposed induction of entropic energy to the protein molecule when in the free state. In fact the change in conformation of the Cys90 loop in the absence of the C-terminal domain indicates that the truncated enzyme may be less compact than the native form, corroborating with the observation that the native form is more susceptible to temperature.

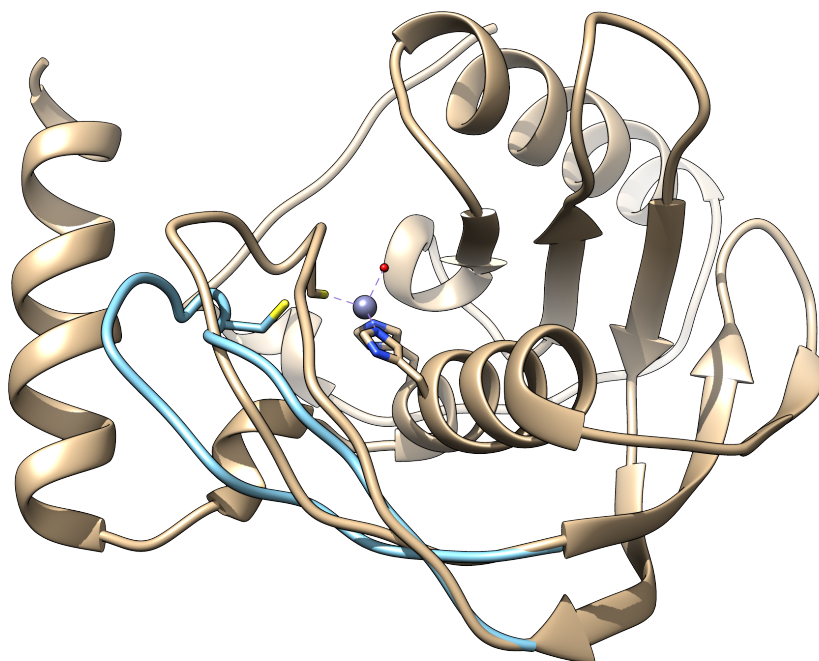


Figure 6.6. Comparison of full length and truncated Pdf structures. The X-ray crystal structure of full length *Ec*Pdf (brown, PDB ID: 1DFF) is shown with an overlay of the Cys90 loop from one conformation of the NMR structure (blue, PDB ID: 1DEF).

Prior to this study, C-terminal helix was believed to function purely as an anchor to the ribosome with no role in the catalytic function of Pdf [18, 108]. The data presented in this study however shed light on the potential role of the C-terminal domain in controlling the stability and catalytic activity of Pdf depending on its free versus ribosome-bound form. Such a mechanism for control of the enzyme can certainly be conceived to be of relevance to the cell.

REFERENCES

- (1) Bishop, J., Leahy, J., Schweet, R. (1960). Formation of the peptide chain of hemoglobin. *Proceedings of the National Academy of Sciences of the United States of America* 46, 1030–1038.
- (2) Goldstein, A., Brown, B. J. (1961). Addition of amino acid to C-terminal ends of growing protein chains in *Escherichia coli*. *Biochimica et Biophysica Acta* 53, 438–439.
- (3) Waller, J.-P., Harris, J. I. (1961). Studies on the composition of the protein from *Escherichia coli* ribosomes., en *Proceedings of the National Academy of Sciences* 47, 18–23.
- (4) Waller, J.-P. (1963). The NH₂-terminal residues of the proteins from cell-free extracts of *E. coli*. *Journal of Molecular Biology* 7, 483–496.
- (5) Marcker, K., Sanger, F. (1964). N-formyl-methionyl-S-RNA. *Journal of Molecular Biology* 8, 835–838.
- (6) Adams, J. M., Capecchi, M. R. (1966). N-formylmethionyl-sRNA as the initiator of protein synthesis. *Proceedings of the National Academy of Sciences of the United States of America* 55, 147–155.
- (7) Capecchi, M. R. (1966). Initiation of *E. coli* proteins. *Proceedings of the National Academy of Sciences of the United States of America* 55, 1517.
- (8) Fry, K. T., Lamborg, M. R. (1967). Amidohydrolase activity of *Escherichia coli* extracts with formylated amino acids and dipeptides as substrates. *Journal of Molecular Biology* 28, 423–433.
- (9) Adams, J. M. (1968). On the release of the formyl group from nascent protein. *Journal of Molecular Biology* 33, 571–589.

- (10) Yoshida, A., Watanabe, S., Morris, J. (1970). Initiation of rabbit hemoglobin synthesis: Methionine and formylmethionine at the N-terminal., en *Proceedings of the National Academy of Sciences* 67, 1600–1607.
- (11) Housman, D., Jacobs-Lorena, M., Rajbhandary, U. L., Lodish, H. F. (1970). Initiation of haemoglobin synthesis by methionyl-tRNA., en *Nature* 227, 913–918.
- (12) Yoshida, A., Lin, M. (1972). NH₂-terminal formylmethionine- and NH₂-terminal methionine-cleaving enzymes in rabbits., en *Journal of Biological Chemistry* 247, 952–957.
- (13) Ben-Bassat, A., Bauer, K., Chang, S. Y., Myambo, K., Boosman, A., Chang, S. (1987). Processing of the initiation methionine from proteins: properties of the *Escherichia coli* methionine aminopeptidase and its gene structure. *Journal of Bacteriology* 169, 751–757.
- (14) Meinnel, T., Blanquet, S. (1993). Evidence that peptide deformylase and methionyl-tRNA(fMet) formyltransferase are encoded within the same operon in *Escherichia coli*. *Journal of Bacteriology* 175, 7737–7740.
- (15) Mazel, D., Pochet, S., Marlière, P. (1994). Genetic characterization of polypeptide deformylase, a distinctive enzyme of eubacterial translation. *The EMBO Journal* 13, 914–923.
- (16) Milligan, D. L., Koshland, D. E. (1990). The amino terminus of the aspartate chemoreceptor is formylmethionine., en *Journal of Biological Chemistry* 265, 4455–4460.
- (17) Rajagopalan, P. T. R., Datta, A., Pei, D. (1997). Purification, characterization, and inhibition of peptide deformylase from *Escherichia coli*. *Biochemistry* 36, 13910–13918.

- (18) Bingel-Erlenmeyer, R., Kohler, R., Kramer, G., Sandikci, A., Antolic, S., Maier, T., Schaffitzel, C., Wiedmann, B., Bukau, B., Ban, N. (2008). A peptide deformylase-ribosome complex reveals mechanism of nascent chain processing. *Nature* 452, 108–111.
- (19) Martinez, A., Traverso, J. A., Valot, B., Ferro, M., Espagne, C., Ephritikhine, G., Zivy, M., Giglione, C., Meinnel, T. (2008). Extent of N-terminal modifications in cytosolic proteins from eukaryotes., en *PROTEOMICS* 8, 2809–2831.
- (20) Vetro, J. A., Chang, Y.-H. (2002). Yeast methionine aminopeptidase type 1 is ribosome-associated and requires its N-terminal zinc finger domain for normal function in vivo., en *Journal of Cellular Biochemistry* 85, 678–688.
- (21) Addlagatta, A., Quillin, M. L., Omotoso, O., Liu, J. O., Matthews, B. W. (2005). Identification of an SH3-binding motif in a new class of methionine aminopeptidases from *Mycobacterium tuberculosis* suggests a mode of interaction with the ribosome. *Biochemistry* 44, 7166–7174.
- (22) Pestana, A., Pitot, H. C. (1975). Acetylation of nascent polypeptide chains on rat liver polyribosomes in vivo and in vitro. *Biochemistry* 14, 1404–1412.
- (23) Varshavsky, A. (1997). The N-end rule pathway of protein degradation. *Genes to Cells* 2, 13–28.
- (24) Li, X., Chang, Y.-H. (1996). Evidence that the human homologue of a rat initiation factor-2 associated protein (p67) is a methionine aminopeptidase. *Biochemical and Biophysical Research Communications* 227, 152–159.
- (25) Noguchi, S., Komiya, T., Eguchi, H., Shirahata, A., Nikawa, J.-i., Kawamura, M. (2007). Methionine aminopeptidase II: a molecular chaperone for sarcoplasmic reticulum calcium ATPase. *Journal of Membrane Biology* 215, 105–110.

- (26) Endo, H., Takenaga, K., Kanno, T., Satoh, H., Mori, S. (2002). Methionine aminopeptidase 2 is a new target for the metastasis-associated protein, S100A4. *Journal of Biological Chemistry* 277, 26396–26402.
- (27) Sundberg, T. B., Darricarrere, N., Cirone, P., Li, X., McDonald, L., Mei, X., Westlake, C. J., Slusarski, D. C., Beynon, R. J., Crews, C. M. (2011). Disruption of Wnt Planar Cell Polarity Signaling by Aberrant Accumulation of the MetAP-2 Substrate Rab37. *Chemistry & Biology* 18, 1300–1311.
- (28) Jeong, H.-J., Shin, J. S., Ok, S. H. (2011). Barley DNA-binding methionine aminopeptidase, which changes the localization from the nucleus to the cytoplasm by low temperature, is involved in freezing tolerance. *Plant Science* 180, 53–60.
- (29) Tso, J. Y., Hermodson, M. A., Zalkin, H. (1982). Glutamine phosphoribosylpyrophosphate amidotransferase from cloned *Escherichia coli* purF. NH₂-terminal amino acid sequence, identification of the glutamine site, and trace metal analysis., en *Journal of Biological Chemistry* 257, 3532–3536.
- (30) Prchal, J. T., Cashman, D. P., Kan, Y. W. (1986). Hemoglobin Long Island is caused by a single mutation (adenine to cytosine) resulting in a failure to cleave amino-terminal methionine., en *Proceedings of the National Academy of Sciences* 83, 24–27.
- (31) Boutin, J. A. (1997). Myristoylation. *Cellular Signalling* 9, 15–35.
- (32) Chang, S. Y., McGary, E. C., Chang, S. (1989). Methionine aminopeptidase gene of *Escherichia coli* is essential for cell growth. *Journal of Bacteriology* 171, 4071–4072.

- (33) Miller, C. G., Kukral, A. M., Miller, J. L., Movva, N. R. (1989). pepM is an essential gene in *Salmonella typhimurium*. *Journal of Bacteriology* 171, 5215–5217.
- (34) Meinnel, T., Blanquet, S. (1994). Characterization of the *Thermus thermophilus* locus encoding peptide deformylase and methionyl-tRNA(fMet) formyltransferase., en *Journal of Bacteriology* 176, 7387–7390.
- (35) Li, X., Chang, Y. H. (1995). Amino-terminal protein processing in *Saccharomyces cerevisiae* is an essential function that requires two distinct methionine aminopeptidases. *Proceedings of the National Academy of Sciences of the United States of America* 92, 12357–12361.
- (36) Aasland, R., Abrams, C., Ampe, C., Ball, L. J., Bedford, M. T., Cesareni, G., Gimona, M., Hurley, J. H., Jarchau, T., Lehto, V.-P., Lemmon, M. A., Linding, R., Mayer, B. J., Nagai, M., Sudol, M., Walter, U., Winder, S. J. (2002). Normalization of nomenclature for peptide motifs as ligands of modular protein domains. *FEBS Letters* 513, 141–144.
- (37) The UniProt Consortium (2011). Reorganizing the protein space at the Universal Protein Resource (UniProt). *Nucleic Acids Research* 40, 71–75.
- (38) Sievers, F., Wilm, A., Dineen, D., Gibson, T. J., Karplus, K., Li, W., Lopez, R., McWilliam, H., Remmert, M., Söding, J., Thompson, J. D., Higgins, D. G. (2011). Fast, scalable generation of high-quality protein multiple sequence alignments using Clustal Omega., en *Molecular Systems Biology* 7, 539.
- (39) Waterhouse, A. M., Procter, J. B., Martin, D. M. A., Clamp, M., Barton, G. J. (2009). Jalview Version 2—a multiple sequence alignment editor and analysis workbench., en *Bioinformatics* 25, 1189–1191.

- (40) Huson, D. H., Scornavacca, C. (2012). Dendroscope 3: An interactive tool for rooted phylogenetic trees and networks., en *Systematic Biology*, DOI: 10.1093/sysbio/sys062.
- (41) Bradshaw, R. A., Brickey, W. W., Walker, K. W. (1998). N-Terminal processing: the methionine aminopeptidase and N α -acetyl transferase families. *Trends in Biochemical Sciences* 23, 263–267.
- (42) Alvarado, J. J., Nemkal, A., Sauder, J. M., Russell, M., Akiyoshi, D. E., Shi, W., Almo, S. C., Weiss, L. M. (2009). Structure of a microsporidian methionine aminopeptidase type 2 complexed with fumagillin and TNP-470. *Molecular and Biochemical Parasitology* 168, 158–167.
- (43) Serero, A., Giglione, C., Sardini, A., Martinez-Sanz, J., Meinnel, T. (2003). An unusual peptide deformylase features in the human mitochondrial n-terminal methionine excision pathway. *Journal of Biological Chemistry* 278, 52953–52963.
- (44) Giglione, C. (2003). Control of protein life-span by N-terminal methionine excision. *The EMBO Journal* 22, 13–23.
- (45) Bazan, J. F., Weaver, L. H., Roderick, S. L., Huber, R., Matthews, B. W. (1994). Sequence and structure comparison suggest that methionine aminopeptidase, prolidase, aminopeptidase p, and creatinase share a common fold. *Proceedings of the National Academy of Science* 91, 2473–2477.
- (46) Liu, S., Widom, J., Kemp, C. W., Crews, C. M., Clardy, J. (1998). Structure of human methionine aminopeptidase-2 complexed with fumagillin. *Science* 282, 1324–1327.

- (47) Lowther, W. T., Orville, A. M., Madden, D. T., Lim, S., Rich, D. H., Matthews, B. W. (1999). *Escherichia coli* methionine aminopeptidase: implications of crystallographic analyses of the native, mutant, and inhibited enzymes for the mechanism of catalysis. *Biochemistry* 38, 7678–7688.
- (48) Tahirov, T. H., Oki, H., Tsukihara, T., Ogasahara, K., Yutani, K., Ogata, K., Izu, Y., Tsunasawa, S., Kato, I. (1998). Crystal structure of methionine aminopeptidase from hyperthermophile, *Pyrococcus furiosus*. *Journal of Molecular Biology* 284, 101–124.
- (49) Lu, J.-P., Yuan, X.-H., Yuan, H., Wang, W.-L., Wan, B., Franzblau, S. G., Ye, Q.-Z. (2011). Inhibition of *Mycobacterium tuberculosis* methionine aminopeptidases by bengamide derivatives., eng *ChemMedChem* 6, 1041–1048.
- (50) Hu, Y.-J., Wei, Y., Zhou, Y., Rajagopalan, P. T. R., Pei, D. (1998). Determination of substrate specificity for peptide deformylase through the screening of a combinatorial peptide library. *Biochemistry* 38, 643–650.
- (51) Becker, A., Schlichting, I., Kabsch, W., Groche, D., Schultz, S., Wagner, A. F. V. (1998). Iron center, substrate recognition and mechanism of peptide deformylase., en *Nature Structural & Molecular Biology* 5, 1053–1058.
- (52) Jain, R., Hao, B., Liu, R.-p., Chan, M. K. (2005). Structures of *E. coli* peptide deformylase bound to formate: insight into the preference for Fe^{2+} over Zn^{2+} as the active site metal. *Journal of the American Chemical Society* 127, 4558–4559.
- (53) Wu, X.-H., Quan, J.-M., Wu, Y.-D. (2007). Theoretical study of the catalytic mechanism and metal-ion dependence of peptide deformylase. *The Journal of Physical Chemistry B* 111, 6236–6244.

- (54) Rajagopalan, P. T. R., Grimme, S., Pei, D. (2000). Characterization of Cobalt(II)-Substituted Peptide Deformylase: Function of the Metal Ion and the Catalytic Residue Glu-133[†]. *Biochemistry* 39, 779–790.
- (55) Deng, H., Callender, R., Zhu, J., Nguyen, K. T., Pei, D. (2002). Determination of the Ionization State and Catalytic Function of Glu-133 in Peptide Deformylase by Difference FTIR Spectroscopy[†]. *Biochemistry* 41, 10563–10569.
- (56) Leopoldini, M., Russo, N., Toscano, M. (2006). Role of the Metal Ion in FormylPeptide Bond Hydrolysis by a Peptide Deformylase Active Site Model. *The Journal of Physical Chemistry B* 110, 1063–1072.
- (57) Xiao, C., Zhang, Y. (2007). Catalytic mechanism and metal specificity of bacterial peptide deformylase: a density functional theory QM/MM study. *The Journal of Physical Chemistry B* 111, 6229–6235.
- (58) Apfel, C., Banner, D. W., Bur, D., Dietz, M., Hirata, T., Hubschwerlen, C., Locher, H., Page, M. G. P., Pirson, W., Rossé, G., Specklin, J.-L. (2000). Hydroxamic acid derivatives as potent peptide deformylase inhibitors and antibacterial agents. *Journal of Medicinal Chemistry* 43, 2324–2331.
- (59) Groche, D., Becker, A., Schlichting, I., Kabsch, W., Schultz, S., Wagner, A. F. V. (1998). Isolation and crystallization of functionally competent *Escherichia coli* peptide deformylase forms containing either iron or nickel in the active site. *Biochemical and Biophysical Research Communications* 246, 342–346.
- (60) Lazenec, C., Meinnel, T. (1997). Formate Dehydrogenase-Coupled Spectrophotometric Assay of Peptide Deformylase. *Analytical Biochemistry* 244, 180–182.
- (61) Wei, Y., Pei, D. (1997). Continuous Spectrophotometric Assay of Peptide Deformylase. *Analytical Biochemistry* 250, 29–34.

- (62) Nguyen, K. T., Hu, X., Pei, D. (2004). Slow-binding inhibition of peptide deformylase by cyclic peptidomimetics as revealed by a new spectrophotometric assay. *Bioorganic Chemistry* 32, 178–191.
- (63) Guo, X.-C., Ravi Rajagopalan, P., Pei, D. (1999). A direct spectrophotometric assay for peptide deformylase. *Analytical Biochemistry* 273, 298–304.
- (64) Berg, A. K. Conformational states and physiochemical characterizations of E. coli peptide deformylase., Ph.D. Thesis, Fargo, ND, USA: North Dakota State University, 2008.
- (65) Ragusa, S., Blanquet, S., Meinnel, T. (1998). Control of peptide deformylase activity by metal cations. *Journal of Molecular Biology* 280, 515–523.
- (66) Serero, A., Giglione, C., Meinnel, T. (2001). Distinctive features of the two classes of eukaryotic peptide deformylases. *Journal of Molecular Biology* 314, 695–708.
- (67) Huang, J., Van Aller, G. S., Taylor, A. N., Kerrigan, J. J., Liu, W.-S., Trulli, J. M., Lai, Z., Holmes, D., Aubart, K. M., Brown, J. R., Zalacain, M. (2006). Phylogenomic and Biochemical Characterization of Three Legionella pneumophila Polypeptide Deformylases. *Journal of Bacteriology* 188, 5249–5257.
- (68) Nguyen, K. T., Wu, J.-C., Boylan, J. A., Gherardini, F. C., Pei, D. (2007). Zinc is the metal cofactor of Borrelia burgdorferi peptide deformylase. *Archives of Biochemistry and Biophysics* 468, 217–225.
- (69) Nguyen, K. T., Hu, X., Colton, C., Chakrabarti, R., Zhu, M. X., Pei, D. (2003). Characterization of a human peptide deformylase: implications for antibacterial drug design. *Biochemistry* 42, 9952–9958.

- (70) Sherman, F., Stewart, J. W., Tsunasawa, S. (1985). Methionine or not methionine at the beginning of a protein., en *BioEssays* 3, 27–31.
- (71) Hirel, P. H., Schmitter, M. J., Dessen, P., Fayat, G., Blanquet, S. (1989). Extent of N-terminal methionine excision from *Escherichia coli* proteins is governed by the side-chain length of the penultimate amino acid. *Proceedings of the National Academy of Sciences of the United States of America* 86, 8247–8251.
- (72) Moerschell, R. P., Hosokawa, Y., Tsunasawa, S., Sherman, F. (1990). The specificities of yeast methionine aminopeptidase and acetylation of amino-terminal methionine in vivo. Processing of altered iso-1-cytochromes c created by oligonucleotide transformation. *Journal of Biological Chemistry* 265, 19638–19643.
- (73) Walker, K. W., Yi, E., Bradshaw, R. A. (1999). Yeast (*Saccharomyces cerevisiae*) methionine aminopeptidase I: rapid purification and improved activity assay. *Biotechnology and applied biochemistry* 29 (Pt 2), 157–63.
- (74) Xiao, Q., Zhang, F., Nacev, B. A., Liu, J. O., Pei, D. (2010). Protein N-terminal processing: substrate specificity of *Escherichia coli* and human methionine aminopeptidases. *Biochemistry* 49, 5588–5599.
- (75) Li, J.-Y., Chen, L.-L., Cui, Y.-M., Luo, Q.-l., Gu, M., Nan, F.-J., Ye, Q.-Z. (2004). Characterization of full length and truncated type i human methionine aminopeptidases expressed from *Escherichia coli*. *Biochemistry* 43, 7892–7898.
- (76) Lowther, W. T., Zhang, Y., Sampson, P. B., Honek, J. F., Matthews, B. W. (1999). Insights into the mechanism of *Escherichia coli* methionine aminopeptidase from the structural analysis of reaction products and phosphorus-based transition-state analogues. *Biochemistry* 38, 14810–14819.

- (77) Copik, A. J., Swierczek, S. I., Lowther, W. T., D'souza, V. M., Matthews, B. W., Holz, R. C. (2003). Kinetic and spectroscopic characterization of the H178A methionyl aminopeptidase from *Escherichia coli*. *Biochemistry* 42, 6283–6292.
- (78) D'souza, V. M., Holz, R. C. (1999). The methionyl aminopeptidase from *Escherichia coli* can function as an iron(ii) enzyme. *Biochemistry* 38, 11079–11085.
- (79) D'souza, V. M., Bennett, B., Copik, A. J., Holz, R. C. (2000). Divalent metal binding properties of the methionyl aminopeptidase from *Escherichia coli*. *Biochemistry* 39, 3817–3826.
- (80) Ye, Q.-Z., Xie, S.-X., Ma, Z.-Q., Huang, M., Hanzlik, R. P. (2006). Structural basis of catalysis by monometalated methionine aminopeptidase. *Proceedings of the National Academy of Sciences of the United States of America* 103, 9470–9475.
- (81) Yang, G., Kirkpatrick, R. B., Ho, T., Zhang, G.-F., Liang, P.-H., Johanson, K. O., Casper, D. J., Doyle, M. L., Marino, Thompson, S. K., Chen, W., Tew, D. G., Meek, T. D. (2001). Steady-state kinetic characterization of substrates and metal-ion specificities of the full-length and n-terminally truncated recombinant human methionine aminopeptidases (type 2). *Biochemistry* 40, 10645–10654.
- (82) Kanudia, P., Mittal, M., Kumaran, S., Chakraborti, P. K. (2011). Amino-terminal extension present in the methionine aminopeptidase type 1c of *Mycobacterium tuberculosis* is indispensable for its activity. *BMC Biochemistry* 12, 35.

- (83) Kendall, R., Bradshaw, R. (1992). Isolation and characterization of the methionine aminopeptidase from porcine liver responsible for the co-translational processing of proteins. *J. Biol. Chem.* *267*, 20667–20673.
- (84) Larrabee, J. A., Thamrong-nawasawat, T., Yee Mon, S. (1999). High-pressure liquid chromatographic method for the assay of methionine aminopeptidase activity: application to the study of enzymatic inactivation. *Analytical Biochemistry* *269*, 194–198.
- (85) Zhou, Y., Guo, X.-C., Yi, T., Yoshimoto, T., Pei, D. (2000). Two continuous spectrophotometric assays for methionine aminopeptidase. *Analytical Biochemistry* *280*, 159–165.
- (86) Li, J.-Y., Chen, L.-L., Cui, Y.-M., Luo, Q.-l., Li, J., Nan, F.-J., Ye, Q.-Z. (2003). Specificity for inhibitors of metal-substituted methionine aminopeptidase, *Biochemical and Biophysical Research Communications* *307*, 172–179.
- (87) Mitra, S., Dygas-Holz, A. M., Jiracek, J., Zertova, M., Zakova, L., Holz, R. C. (2006). A new colorimetric assay for methionyl aminopeptidases: Examination of the binding of a new class of pseudopeptide analog inhibitors. *Analytical Biochemistry* *357*, 43–49.
- (88) Shapiro, A. B., Gao, N., Thresher, J., Walkup, G. K., Whiteaker, J. (2011). A High-Throughput Absorbance-Based Assay for Methionine Produced by Methionine Aminopeptidase Using S-Adenosyl-L-Methionine Synthetase., in *Journal of Biomolecular Screening* *16*, 494–505.
- (89) Chai, S. C., Ye, Q.-Z. (2010). A cell-based assay that targets methionine aminopeptidase in a physiologically relevant environment. *Bioorganic & Medicinal Chemistry Letters* *20*, 2129–2132.

- (90) Schiffmann, R., Heine, A., Klebe, G., Klein, C. D. P. (2005). Metal ions as cofactors for the binding of inhibitors to methionine aminopeptidase: a critical view of the relevance of in vitro metalloenzyme assays. *Angewandte Chemie (International ed. in English)* 44, 3620–3623.
- (91) Huang, Q.-Q., Huang, M., Nan, F.-J., Ye, Q.-Z. (2005). Metalloform-selective inhibition: Synthesis and structure-activity analysis of Mn(II)-form-selective inhibitors of *Escherichia coli* methionine aminopeptidase. *Bioorganic & Medicinal Chemistry Letters* 15, 5386–5391.
- (92) Mitra, S., Bennett, B., Holz, R. C. (2009). Mutation of H63 and its catalytic affect on the methionine aminopeptidase from *Escherichia coli*. *Biochimica et Biophysica Acta (BBA) - Proteins & Proteomics* 1794, 137–143.
- (93) Meng, L., Ruebush, S., D'souza, V. M., Copik, A. J., Tsunasawa, S., Holz, R. C. (2002). Overexpression and divalent metal binding properties of the methionyl aminopeptidase from *Pyrococcus furiosus*. *Biochemistry* 41, 7199–7208.
- (94) Watterson, S. J., Mitra, S., Swierczek, S. I., Bennett, B., Holz, R. C. (2008). Kinetic and spectroscopic analysis of the catalytic role of H79 in the methionine aminopeptidase from *Escherichia coli*. *Biochemistry* 47, 11885–11893.
- (95) D'souza, V. M., Swierczek, S. I., Cospers, N. J., Meng, L., Ruebush, S., Copik, A. J., Scott, R. A., Holz, R. C. (2002). Kinetic and structural characterization of manganese(II)-loaded methionyl aminopeptidases. *Biochemistry* 41, 13096–13105.
- (96) Addlagatta, A., Hu, X., Liu, J. O., Matthews, B. W. (2005). Structural basis for the functional differences between type I and type II human methionine aminopeptidases. *Biochemistry* 44, 14741–14749.

- (97) Rajagopalan, P. T. R., Yu, X. C., Pei, D. (1997). Peptide deformylase: a new type of mononuclear iron protein. *Journal of the American Chemical Society* 119, 12418–12419.
- (98) Park, J. K., Kim, K.-H., Moon, J. H., Kim, E. E. (2007). Characterization of peptide deformylase2 from *B. cereus*. *Journal of biochemistry and molecular biology* 40, 1050–1057.
- (99) Li, Y., Chen, Z., Gong, W. (2002). Enzymatic properties of a new peptide deformylase from pathogenic bacterium *Leptospira interrogans*. *Biochemical and Biophysical Research Communications* 295, 884–889.
- (100) Meinnel, T., Blanquet, S. (1995). Enzymatic properties of *Escherichia coli* peptide deformylase., en *Journal of Bacteriology* 177, 1883–1887.
- (101) Berg, A. K., Srivastava, D. K. (2009). Delineation of alternative conformational states in *Escherichia coli* peptide deformylase via thermodynamic studies for the binding of actinonin. *Biochemistry* 48, 1584–1594.
- (102) Roderick, S. L., Matthews, B. W. (1993). Structure of the cobalt-dependent methionine aminopeptidase from *Escherichia coli*: a new type of proteolytic enzyme. *Biochemistry* 32, 3907–3912.
- (103) Walker, K. W., Bradshaw, R. A. (1998). Yeast methionine aminopeptidase I can utilize either Zn^{2+} or Co^{2+} as a cofactor: A case of mistaken identity? *Protein Science* 7, 2684–2687.
- (104) Leopoldini, M., Russo, N., Toscano, M. (2007). Which one among Zn(II), Co(II), Mn(II), and Fe(II) is the most efficient ion for the methionine aminopeptidase catalyzed reaction? *Journal of the American Chemical Society* 129, 7776–7784.

- (105) Chai, S. C., Wang, W.-L., Ye, Q.-Z. (2008). Fe(II) is the native cofactor for *Escherichia coli* methionine aminopeptidase. *Journal of Biological Chemistry* 283, 26879–26885.
- (106) Hu, X. V., Chen, X., Han, K. C., Mildvan, A. S., Liu, J. O. (2007). Kinetic and mutational studies of the number of interacting divalent cations required by bacterial and human methionine aminopeptidases. *Biochemistry* 46, 12833–12843.
- (107) Berg, A. K., Manokaran, S., Eiler, D., Kooren, J., Mallik, S., Srivastava, D. (2007). Energetic rationale for an unexpected and abrupt reversal of guanidinium chloride-induced unfolding of peptide deformylase. *Protein Science* 17, 11–15.
- (108) Meinnel, T., Lazennec, C., Dardel, F., Schmitter, J.-M., Blanquet, S. (1996). The C-terminal domain of peptide deformylase is disordered and dispensable for activity. *FEBS Letters* 385, 91–95.
- (109) Sin, N., Meng, L., Wang, M. Q. W., Wen, J. J., Bornmann, W. G., Crews, C. M. (1997). The anti-angiogenic agent fumagillin covalently binds and inhibits the methionine aminopeptidase, MetAP-2., en *Proceedings of the National Academy of Sciences* 94, 6099–6103.
- (110) Xu, Y., Lai, L. T., Gabrilove, J. L., Scheinberg, D. A. (1998). Antitumor activity of actinonin in vitro and in vivo., en *Clinical Cancer Research* 4, 171–176.
- (111) Selvakumar, P., Lakshmikuttyamma, A., Kanthan, R., Kanthan, S. C., Dimmock, J. R., Sharma, R. K. (2004). High Expression of Methionine Aminopeptidase 2 in Human Colorectal Adenocarcinomas., en *Clinical Cancer Research* 10, 2771–2775.

- (112) Balakrishnan, A., Wang, L., Li, X., Ohman-Strickland, P., Malatesta, P., Fan, H. (2009). Inhibition of chlamydial infection in the genital tract of female mice by topical application of a peptide deformylase inhibitor. *Microbiological Research* 164, 338–346.
- (113) Boularot, A., Giglione, C., Petit, S., Duroc, Y., Alves de Sousa, R., Larue, V., Cresteil, T., Dardel, F., Artaud, I., Meinnel, T. (2007). Discovery and refinement of a new structural class of potent peptide deformylase inhibitors. *Journal of Medicinal Chemistry* 50, 10–20.
- (114) Clements, J. M., Beckett, R. P., Brown, A., Catlin, G., Lobell, M., Palan, S., Thomas, W., Whittaker, M., Wood, S., Salama, S., Baker, P. J., Rodgers, H. F., Barynin, V., Rice, D. W., Hunter, M. G. (2001). Antibiotic Activity and Characterization of BB-3497, a Novel Peptide Deformylase Inhibitor. *Antimicrobial Agents and Chemotherapy* 45, 563–570.
- (115) Chen, D. Z., Patel, D. V., Hackbarth, C. J., Wang, W., Dreyer, G., Young, D. C., Margolis, P. S., Wu, C., Ni, Z.-J., Trias, J., White, R. J., Yuan, Z. (2000). Actinonin, a Naturally Occurring Antibacterial Agent, Is a Potent Deformylase Inhibitor. *Biochemistry* 39, 1256–1262.
- (116) Hou, C.-X., Dirk, L. M. A., Pattanaik, S., Das, N. C., Maiti, I. B., Houtz, R. L., Williams, M. A. (2007). Plant peptide deformylase: a novel selectable marker and herbicide target based on essential cotranslational chloroplast protein processing. *Plant biotechnology journal* 5, 275–281.
- (117) Chai, S. C., Wang, W.-L., Ding, D.-R., Ye, Q.-Z. (2011). Growth inhibition of *Escherichia coli* and methicillin-resistant *Staphylococcus aureus* by targeting cellular methionine aminopeptidase. *European Journal of Medicinal Chemistry* 46, 3537–3540.

- (118) Chen, X., Chong, C. R., Shi, L., Yoshimoto, T., Sullivan, D. J., Liu, J. O. (2006). Inhibitors of *Plasmodium falciparum* methionine aminopeptidase 1b possess antimalarial activity. *Proceedings of the National Academy of Sciences* 103, 14548–14553.
- (119) Lu, J.-P., Chai, S. C., Ye, Q.-Z. (2010). Catalysis and inhibition of *Mycobacterium tuberculosis* methionine aminopeptidase. *Journal of Medicinal Chemistry* 53, 1329–1337.
- (120) Lee, M. D. (2004). Human mitochondrial peptide deformylase, a new anticancer target of actinonin-based antibiotics. *Journal of Clinical Investigation* 114, 1107–1116.
- (121) Priest, R. C., Spaul, J., Buckton, J., Grimley, R. L., Sims, M., Binks, M., Malhotra, R. (2009). Immunomodulatory activity of a methionine aminopeptidase-2 inhibitor on B cell differentiation. *Clinical & Experimental Immunology* 155, 514–522.
- (122) Bernier, S. G., Lazarus, D. D., Clark, E., Doyle, B., Labenski, M. T., Thompson, C. D., Westlin, W. F., Hannig, G. (2004). A methionine aminopeptidase-2 inhibitor, PPI-2458, for the treatment of rheumatoid arthritis. *Proceedings of the National Academy of Sciences of the United States of America* 101, 10768–10773.
- (123) Cooper, A. C., Karp, R. M., Clark, E. J., Taghizadeh, N. R., Hoyt, J. G., Labenski, M. T., Murray, M. J., Hannig, G., Westlin, W. F., Thompson, C. D. (2006). A novel methionine aminopeptidase-2 inhibitor, PPI-2458, inhibits Non-Hodgkin's lymphoma cell proliferation in vitro and in vivo. *Clinical Cancer Research* 12, 2583–2590.

- (124) Lowther, W. T., McMillen, D. A., Orville, A. M., Matthews, B. W. (1998). The anti-angiogenic agent fumagillin covalently modifies a conserved active-site histidine in the *Escherichia coli* methionine aminopeptidase. *Proceedings of the National Academy of Sciences of the United States of America* 95, 12153–12157.
- (125) Sundberg, L., Porath, J. (1974). Preparation of adsorbents for biospecific affinity chromatography : I. Attachment of group-containing ligands to insoluble polymers by means of bifunctional oxiranes. *Journal of Chromatography A* 90, 87–98.
- (126) Cabrita, L., Dai, W., Bottomley, S. (2006). A family of *E. coli* expression vectors for laboratory scale and high throughput soluble protein production. *BMC Biotechnology* 6, 12.
- (127) Bradford, M. M. (1976). A rapid and sensitive method for the quantitation of microgram quantities of protein utilizing the principle of protein-dye binding. *Analytical Biochemistry* 72, 248–254.
- (128) Banerjee, A. L., Swanson, M., Roy, B. C., Jia, X., Haldar, M. K., Mallik, S., Srivastava, D. K. (2004). Protein surface-assisted enhancement in the binding affinity of an inhibitor for recombinant human carbonic anhydrase-II. *Journal of the American Chemical Society* 126, 10875–10883.
- (129) Kuzmic, P. (1996). Program DYNAFIT for the analysis of enzyme kinetic data: application to HIV proteinase. *Analytical Biochemistry* 237, 260–273.
- (130) Burnham, K. P., Anderson, D. R., *Model selection and multimodel inference: a practical information-theoretic approach*, 2nd ed.; Springer: New York, 2002.
- (131) Trott, O., Olson, A. J. (2010). AutoDock Vina: Improving the speed and accuracy of docking with a new scoring function, efficient optimization, and multithreading., en *Journal of Computational Chemistry* 31, 455–461.

- (132) Dennington, R., Keith, T., Millam, J. GaussView., 2009.
- (133) Polekhina, G., Gupta, A., van Denderen, B., Feil, S., Kemp, B., Stapleton, D., Parker, M., Polekhina, G., Feil, S., Gupta, A., O'Donnell, P., Stapleton, D., Parker, M. (2005). Structural Basis for Glycogen Recognition by AMP-Activated Protein Kinase. *Structure* 13, 1453–1462.
- (134) Sanner, M. F. (1999). Python: A programming language for software integration and development. *Journal of Molecular Graphics and Modelling* 17, 57–61.
- (135) MacKerell, Bashford, D., Bellott, Dunbrack, Evanseck, J. D., Field, M. J., Fischer, S., Gao, J., Guo, H., Ha, S., Joseph-McCarthy, D., Kuchnir, L., Kuczera, K., Lau, F. T. K., Mattos, C., Michnick, S., Ngo, T., Nguyen, D. T., Prodhom, B., Reiher, W. E., Roux, B., Schlenkrich, M., Smith, J. C., Stote, R., Straub, J., Watanabe, M., Wiórkiewicz-Kuczera, J., Yin, D., Karplus, M. (1998). All-atom empirical potential for molecular modeling and dynamics studies of proteins. *J. Phys. Chem. B* 102, 3586–3616.
- (136) Phillips, J. C., Braun, R., Wang, W., Gumbart, J., Tajkhorshid, E., Villa, E., Chipot, C., Skeel, R. D., Kalé, L., Schulten, K. (2005). Scalable molecular dynamics with NAMD., en *Journal of Computational Chemistry* 26, 1781–1802.
- (137) Humphrey, W., Dalke, A., Schulten, K. (1996). VMD: Visual molecular dynamics. *Journal of Molecular Graphics* 14, 33–38.
- (138) Zoete, V., Cuendet, M. A., Grosdidier, A., Michielin, O. (2011). SwissParam: A fast force field generation tool for small organic molecules., en *Journal of Computational Chemistry* 32, 2359–2368.
- (139) Nurminen, A., Kukkurainen, S., Kaguni, L. S., Hytonen, V. P. RMSDVT., 2012.

- (140) Wang, Z.-X., Ravi Kumar, N., Srivastava, D. K. (1992). A novel spectroscopic titration method for determining the dissociation constant and stoichiometry of protein-ligand complex. *Analytical Biochemistry* 206, 376–381.
- (141) Altschul, S. F., Gish, W., Miller, W., Myers, E. W., Lipman, D. J. (1990). Basic local alignment search tool. *Journal of molecular biology* 215, 403–410.
- (142) Ye, Q.-Z., Xie, S.-X., Huang, M., Huang, W.-J., Lu, J.-P., Ma, Z.-Q. (2004). Metalloform-selective inhibitors of *Escherichia coli* methionine aminopeptidase and x-ray structure of a Mn(II)-form enzyme complexed with an inhibitor. *Journal of the American Chemical Society* 126, 13940–13941.
- (143) Moelands, D., Karnik, N., Prankerd, R., Sloan, K., Stone, H., Perrin, J. (1992). Microcalorimetric study of the interactions of aspartame with β -cyclodextrin and hydroxypropyl- β -cyclodextrin: The anomalous heat of dilution of the latter. *International Journal of Pharmaceutics* 86, 263–265.
- (144) Beechem, J. M., Brand, L. (1985). Time-Resolved Fluorescence of Proteins. *Annual Review of Biochemistry* 54, 43–71.
- (145) Jørgensen, A. T., Norrby, P.-O., Liljefors, T. (2002). Investigation of the metal binding site in methionine aminopeptidase by density functional theory. *Journal of Computer-Aided Molecular Design* 16, 167–179.
- (146) Wang, J., Sheppard, G. S., Lou, P., Kawai, M., Park, C., Egan, D. A., Schneider, A., Bouska, J., Lesniewski, R., Henkin, J. (2003). Physiologically relevant metal cofactor for methionine aminopeptidase-2 is manganese. *Biochemistry* 42, 5035–5042.
- (147) Chai, S., Ye, Q.-Z. (2009). Analysis of the stoichiometric metal activation of methionine aminopeptidase. *BMC Biochemistry* 10, 32.

- (148) Mitra, S., Job, K. M., Meng, L., Bennett, B., Holz, R. C. (2008). Analyzing the catalytic role of Asp97 in the methionine aminopeptidase from *Escherichia coli*. *FEBS Journal* 275, 6248–6259.
- (149) Wang, W.-L., Chai, S. C., Huang, M., He, H.-Z., Hurley, T. D., Ye, Q.-Z. (2008). Discovery of inhibitors of *Escherichia coli* methionine aminopeptidase with the Fe(II)-form selectivity and antibacterial activity. *Journal of Medicinal Chemistry* 51, 6110–6120.
- (150) Horrocks, W. D., Sudnick, D. R. (1981). Lanthanide ion luminescence probes of the structure of biological macromolecules. *Accounts of Chemical Research* 14, 384–392.
- (151) Mellor, J. W., *A comprehensive treatise on inorganic and theoretical chemistry*; Longmans, Green and Co.: New York, 1935; Vol. XIX.
- (152) Lamb, A. B., Jacques, A. G. (1938). The slow hydrolysis of ferric chloride in dilute solution. I. The change in conductance, color and chloride ion concentration. *Journal of the American Chemical Society* 60, 967–981.
- (153) Cotton, F. A., Murillo, C. A., Bochmann, M., Grimes, R. N., *Advanced Inorganic Chemistry, 6th Edition*, 6th ed.; Wiley-Interscience: 1999.
- (154) Gabričević, M., Anderson, D. S., Mietzner, T. A., Crumbliss, A. L. (2004). Kinetics and mechanism of iron(III) complexation by ferric binding protein: The role of phosphate. *Biochemistry* 43, 5811–5819.
- (155) Weaver, K. D., Gabričević, M., Anderson, D. S., Adhikari, P., Mietzner, T. A., Crumbliss, A. L. (2010). Role of citrate and phosphate anions in the mechanism of iron(III) sequestration by ferric binding protein: Kinetic studies of the formation of the holoprotein of wild-type FbpA and its engineered mutants. *Biochemistry* 49, 6021–6032.

- (156) Irving, H., Williams, R. J. P. (1953). The stability of transition-metal complexes. *Journal of the Chemical Society (Resumed)*, 3192–3210.
- (157) Ray, W. J. (1969). Role of bivalent cations in the phosphoglucomutase system. *Journal of Biological Chemistry* 244, 3740–3747.
- (158) Tse, P., Scopes, R. K., Wedd, A. G. (1989). Iron-activated alcohol dehydrogenase from *Zymomonas mobilis*: isolation of apoenzyme and metal dissociation constants. *Journal of the American Chemical Society* 111, 8703–8706.
- (159) Williams, R. J. P. In *A Study of Enzymes: Mechanism of enzyme action*, Kuby, S. A., Ed.; CRC Press: 1991; Vol. 2, pp 90–91.
- (160) Pearson, R. G. (1963). Hard and soft acids and bases. *Journal of the American Chemical Society* 85, 3533–3539.
- (161) Caravan, P., Merbach, A. E. (1997). An extreme water exchange rate: the europium(II) aqua ion. *Chemical Communications*, 2147–2148.
- (162) Del Valle, E. (2004). Cyclodextrins and their uses: a review. *Process Biochemistry* 39, 1033–1046.
- (163) Challa, R., Ahuja, A., Ali, J., Khar, R. K. (2005). Cyclodextrins in drug delivery: An updated review. *AAPS PharmSciTech* 6, E329–E357.
- (164) Wacklin, H. P. (2009). Interfacial mechanism of phospholipase A2: pH-dependent inhibition and Me- β -cyclodextrin activation. *Biochemistry* 48, 5874–5881.
- (165) Orenes-Piñero, E., García-Carmona, F., Sánchez-Ferrer, A. (2007). Kinetic characterization of diphenolase activity from *Streptomyces antibioticus* tyrosinase in the presence and absence of cyclodextrins. *Journal of Molecular Catalysis B: Enzymatic* 47, 143–148.

- (166) López-Nicolás, J. M., Pérez-López, A. J., Carbonell-Barrachina, Á., García-Carmona, F. (2007). Kinetic study of the activation of banana juice enzymatic browning by the addition of maltosyl- β -cyclodextrin. *Journal of Agricultural and Food Chemistry* 55, 9655–9662.
- (167) Denadai, Â. M. L., Santoro, M. M., Lopes, M. T. P., Chenna, A., de Sousa, F. B., Avelar, G. M., Túlio Gomes, M. R., Guzman, F., Salas, C. E., Sinisterra, R. D. (2006). A supramolecular complex between proteinases and β -cyclodextrin that preserves enzymatic activity: Physicochemical characterization. *BioDrugs* 20, 283–291.
- (168) Fasoli, E., Castillo, B., Santos, A., Silva, E., Ferrer, A., Rosario, E., Griebenow, K., Secundo, F., Barletta, G. L. (2006). Activation of subtilisin Carlsberg in organic solvents by methyl- β -cyclodextrin: Lyoprotection versus substrate and product-complex effect. *Journal of Molecular Catalysis B: Enzymatic* 42, 20–26.
- (169) Masato, K. (1980). Inhibition of enzyme-reaction by α -cyclodextrin., *Japanese Kobunshi Ronbunshu* 37, 803–807.
- (170) Irwin, P. L., Pfeffer, P. E., Doner, L. W., Sapers, G. M., Brewster, J. D., Nagahashi, G., Hicks, K. B. (1994). Binding geometry, stoichiometry, and thermodynamics of cyclomalto-oligosaccharide (cyclodextrin) inclusion complex formation with chlorogenic acid, the major substrate of apple polyphenol oxidase. *Carbohydrate Research* 256, 13–27.
- (171) Núñez-Delicado, E., Mar Sojo, M., Sánchez-Ferrer, A., García-Carmona, F. (1999). Hydroperoxidase activity of lipoxygenase in the presence of cyclodextrins. *Archives of Biochemistry and Biophysics* 367, 274–280.

- (172) Koralewska, A., Augustyniak, W., Temeriusz, A., Kańska, M. (2004). Effects of cyclodextrin derivatives on the catalytic activity of tyrosine phenol-lyase. *Journal of Inclusion Phenomena and Macrocyclic Chemistry* 49, 193–197.
- (173) Alvarez-Parrilla, E., de la Rosa, L., Rodrigo-García, J., Escobedo-González, R., Mercado-Mercado, G., Moyers-Montoya, E., Vázquez-Flores, A., González-Aguilar, G. (2007). Dual effect of β -cyclodextrin (β -CD) on the inhibition of apple polyphenol oxidase by 4-hexylresorcinol (HR) and methyl jasmonate (MJ). *Food Chemistry* 101, 1346–1356.
- (174) Chan, M. K., Gong, W., Rajagopalan, P. T. R., Hao, B., Tsai, C. M., Pei, D. (1997). Crystal Structure of the Escherichia coli Peptide Deformylase^{†,‡}. *Biochemistry* 36, 13904–13909.
- (175) Becker, A., Schlichting, I., Kabsch, W., Schultz, S., Wagner, A. F. V. (1998). Structure of Peptide Deformylase and Identification of the Substrate Binding Site., en *Journal of Biological Chemistry* 273, 11413–11416.

APPENDIX

A.1. Dynafit script

The script used for data analysis and model discrimination in DynaFit 3. Comments are denoted by the ; character.

[task]

task = fit

data = velocities

model = competitive_1 ?

[mechanism]

$E + S \rightleftharpoons ES$: Ks dissociation

$ES \rightarrow E + P$: kcat

$ES + S \rightleftharpoons ESS$: Ksi dissociation

$E + C \rightleftharpoons EC$: Kd dissociation

[progress]

rapid equilibrium

[constants] ;units in mM

Ks = 0.123

kcat = 0.0034

Ksi = 1.1

Kd = 2.5 ?

[concentrations] ;unit in mM

E = 0.00075

[response] ;the change in RFU per mM of S (substrate)

SC = 2360 | ESC = 2360 | P = 1860000

[velocities]

directory <path/to/data/directory>
extension txt
variable S

plot Lineweaver-Burk

file <file name> | concentration C = 0
.
.
.
file <file name> | concentration C = 12

[output]
directory <path/to/output/directory>
;-----

[task]
task = fit
data = velocities
model = competitive_2 ?

[mechanism]
 $E + S \rightleftharpoons ES$: K_s dissociation
 $ES \xrightarrow{k_{cat}} E + P$
 $ES + S \rightleftharpoons ESS$: K_{si} dissociation
 $S + C \rightleftharpoons SC$: K_d dissociation

[progress]
rapid equilibrium

[constants]
 $K_s = 0.123$
 $k_{cat} = 0.0034$
 $K_{si} = 1.1$
 $K_d = 2.5 ?$

;-----

[task]

task = fit

data = velocities

model = uncompetitive ?

[mechanism]

$E + S \rightleftharpoons ES$: K_s dissociation

$ES \xrightarrow{k_{cat}} E + P$

$ES + S \rightleftharpoons ESS$: K_{si} dissociation

$ES + C \rightleftharpoons ESC$: K_d dissociation

[progress]

rapid equilibrium

[constants]

$K_s = 0.123$

$k_{cat} = 0.0034$

$K_{si} = 1.1$

$K_d = 2.5 ?$

;-----

[task]

task = fit

data = velocities

model = noncompetitive_1 ?

[mechanism]

$E + S \rightleftharpoons ES$: K_s dissociation

$ES \xrightarrow{k_{cat}} E + P$

$ES + S \rightleftharpoons ESS$: K_s'' dissociation

$S + C \rightleftharpoons SC$: K_d dissociation

$E + SC \rightleftharpoons ESC$: K_s' dissociation

[progress]
rapid equilibrium

[constants]
Ks = 0.123
kcat = 0.0034
Ks" = 1.1
Kd = 2.5 ?
Ks' = 0.123 ?

;------

[task]
task = fit
data = velocities
model = noncompetitive_2 ?

[mechanism]
E + S <=> ES : Ks dissociation
ES --> E + P : kcat
ES + S <=> ESS : Ks" dissociation
S + C <=> SC : Kd dissociation
E + SC <=> ESC : Ks dissociation
ES + C <=> ESC : Kd dissociation

[progress]
rapid equilibrium

[constants]
Ks = 0.123
kcat = 0.0034
Ks" = 1.1
Kd = 2.5 ?

;------

[task]
task = fit

```
data = velocities
model = noncompetitive_3 ?
```

```
[mechanism]
```

```
E + S <=> ES : Ks  dissoc
ES --> E + P : kcat
ES + S <=> ESS : Ksi  dissoc
E + C <=> EC : Ki  dissoc
S + C <=> SC : Kd  dissoc
E + SC <=> ESC : Ks  dissoc
ES + C <=> ESC : Kd  dissoc
EC + S <=> ESC : Kis  dissoc
```

```
[progress]
```

```
rapid equilibrium
```

```
[constants]
```

```
Ks = 0.123
kcat = 0.0034
Ksi = 1.1
Ki = 5 ?
Kd = 2.9
Kis = 0.25 ?
```

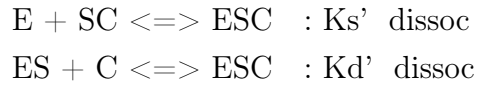
```
;-----
```

```
[task]
```

```
task = fit
data = velocities
model = mixed_1 ?
```

```
[mechanism]
```

```
E + S <=> ES : Ks  dissoc
ES --> E + P : kcat
ES + S <=> ESS : Ksi  dissoc
S + C <=> SC : Kd  dissoc
```



[progress]

rapid equilibrium

[constants]

$$Ks = 0.123$$

$$kcat = 0.0034$$

$$Ksi = 1.1$$

$$Kd = 2.9$$

$$Ks' = 0.123 ?$$

$$Kd' = 2.9 ?$$

;-----

[task]

task = fit

data = velocities

model = mixed_2 ?

[mechanism]



[progress]

rapid equilibrium

[constants]

$$Ks = 0.123$$

$k_{cat} = 0.0034$

$K_{si} = 1.1$

$K_i = 5 ?$

$K_d = 2.9$

$K_{s'} = 0.132 ?$

$K_{d'} = 2.9 ?$

$K_{is} = 0.25 ?$

;-----

[end]

A.2. NAMD scripts

A typical script for an energy minimization routine in NAMD 2. Comments are denoted by the # character.

```
#input files
coordinates      <filename>.pdb
#structure file generated by psfgen
structure        <filename>.psf
#custom parameter file for MetAMC
parameters       <path/filename>.inp
#custom parameter file for cyclodextrin
parameters       <path/filename>.inp
#standard parameter file for MetAP
parameters       <path/>par_all22_prot.inp
#standard parameter file for water and ions
parameters       <path/>toppar_water_ions.str
paratypecharmm   on
fixedAtoms       on
fixedAtomsFile   <filename>.pdb
fixedAtomsCol    B

#output file
outputname       <filename>

#output parameters
binaryoutput     no
DCDFreq          1000
restartfreq      10000
outputenergies   1000
outputTiming     1000

#timestep parameters
firsttimestep    0
timestep         1
stepspercycle    10
```

```
#space partitioning
cutoff          12
switching       on
switchdist      10
pairlistdist     16
margin          0

#dynamics parameters
exclude         scaled1-4
temperature     300
1-4scaling      1.0
rigidbonds      water
rigidTolerance  0.00001

#spherical boundary conditions
sphericalBC     on
  #center of sphere
  sphericalBCcenter  <x coord.>, <y coord.>, <z coord.>
  #radius of sphere
  sphericalBCr1      <angstroms>
sphericalBCk1   10
sphericalBCexp1  2

#run
minimize        250000
```

A typical script for an equilibration routine in NAMD 2. Comments are denoted by the # character.

```
#input files
#file from minimization output
coordinates      <filename>.pdb
#file from minimization output
structure        <filename>.psf
#custom parameter file for MetAMC
parameters       <path/filename>.inp
#custom parameter file for cyclodextrin
parameters       <path/filename>.inp
#standard parameter file for MetAP
parameters       <path/>par_all22_prot.inp
#standard parameter file for water and ions
parameters       <path/>toppar_water_ions.str
paratypecharmm   on
fixedAtoms       on
fixedAtomsFile   <filename>.pdb
fixedAtomsCol    B
#restart file from minimization output
set inputname    <filename>
binCoordinates   $inputname.restart.coor
binVelocities    $inputname.restart.vel

#output file
outputname       <filename>
binaryoutput     no
DCDfreq         1000
restartfreq      10000

#standard output
outputenergies   1000
outputTiming     1000

#timestep parameters
```



```

#frame number from minimization run
  firsttimestep <frame number>
timestep          1
stepspercycle     10

#space partitioning
cutoff            12
switching         on
switchdist        10
pairlistdist      16
margin            0

#basic dynamics
exclude           scaled1-4
1-4scaling        1.0
rigidbonds        water
rigidTolerance    0.00001

#temperature control and equilibration
langevin          on
langevinTemp      300
langevinDamping   1

#spherical boundary conditions
sphericalBC       on
#center of sphere
  sphericalBCcenter <x coord.>, <y coord.>, <z coord.>
#radius of sphere
  sphericalBCr1     <angstroms>
sphericalBCk1     10
sphericalBCexp1   2

#run
run 150000

```